Cooper pair box circuits: two-qubit gate, qubit single-shot readout, and current to frequency conversion

François Nguyen

THESE DE DOCTORAT DE
L'UNIVERSITE PIERRE ET MARIE CURIE

Spécialité :
Physique quantique
ED107

Présentée par

M. NGUYEN

Pour obtenir le grade de

DOCTEUR de l'UNIVERSITÉ PIERRE ET MARIE CURIE

Sujet de la thèse :

COOPER PAIR BOX CIRCUITS: TWO-QUBIT GATE, SINGLE-SHOT READOUT, AND CURRENT TO FREQUENCY CONVERSION

soutenue le 15 décembre 2008

devant le jury composé de :

O. Buisson (Rapporteur)
R. Combescot
D. Estève (Directeur de thèse)
D. Haviland (Rapporteur)
F. Piquemal
R. Simmonds

Thèse préparée au sein du Service de Physique de l'Etat Condensé,
CEA-Saclay

Contents

Introduction

What makes quantum mechanics so interesting?

The theory of quantum mechanics was elaborated in the early 20th century for the sake of understanding experimental facts that could not be explained within the framework of classical physics: black-body radiation and atomic spectra. Soon after, the quantum framework was invoked for explaining other phenomena. In particular, superfluidity was explained as a manifestation of the quantum properties of liquid He_4 at low temperature [1, 2, 3], i.e. the condensation of weakly bounded atoms that occurs when thermal fluctuations are weak enough. Superfluidity was thus the first many-body phenomenon explained by quantum mechanics. A few decades later, in the 1950s, Bardeen, Cooper, and Schriefer proposed a quantum theory [4, 5] based on the pairing of electrons in so-called Cooper pairs to explain superconductivity. At about the same period, quantum mechanics was at the origin of two major inventions of the 20th century physics: the laser and the transistor.
But, even if quantum mechanics was undoubtedly successful in all the domains where it was applied, many essential issues and "gedanken experiments" raised by the founding fathers of quantum mechanics had remained unsolved.

The puzzle of entanglement

An important gedanken experiment is the celebrated EPR paradox [6] raised by Einstein, Podolsky and Rosen in the nineteen-thirties. In the early nineteen-eighties, A. Aspect [7] demonstrated that two distant photons originating from a single quantum process and forming a non factorizable quantum state violate Bell inequalities for hidden variable theories. By shedding shed light on the properties of entangled states, this experiment conveyed a status of quantum resource to the phenomenon of entanglement. Previously, entanglement was merely considered as an illustration of quantum weirdness. This important change of mind paved the way to quantum information.

Quantum mechanical effects in electrical circuits

In the early nineteen-eighties, different groups tried to push ahead quantum mechanics by performing experiments on more complex systems, and in particular on macroscopic systems described by collective variables implying a large number of underlying microscopic degrees of freedom. Noticibly, the quantum properties of superconducting electrical circuits based on Josephson junctions were probed. J. Clarke et *al.* demonstrated in 1984 [8] the quantization of the energy levels for the superconducting phase difference across a Josephson junction. This experiment proved unambiguously that a collective degree of freedom such as the superconducting phase can behave quantum mechanically, and that an appropriate Josephson circuit can be seen as artificial atom with well-defined quantum levels.
In a different direction, K. von Klitzing demonstrated the quantization with metrological accuracy [9] of the Quantum Hall Conductance in a 2D electron gas system. The conductance of a simple quantum point contact was also found to be related to the conductance quantum e^2/h, as predicted by T. Ando [10]. All these experiments demonstrated that quantum mechanics is relevant in mesoscopic electrical circuits both for transport properties and for the quantum state of the whole circuit.

The advent of quantum information

The first success of quantum information for exploiting the resource provided by entanglement was the quantum cryptography protocol based on entangled photons proposed by C. Bennett and G. Brassard [11]. The first quantum algorithm outperforming a sequential one was proposed by R. Jozsa and D. Deutsch [12]. It proved that entanglement offers a powerful ability for storing and parallel processing of quantum information beyond range of classical information processing. In 1995, P. Shor proved that a quantum algorithm can be much much more efficient than a classical one by proposing a method for the factorization of large numbers [13], which is considered as a hard problem.

Quantum information processing with superconducting circuits

On the experimental side, Josephson circuits were natural candidates for providing the quantum resources needed for processing quantum information, namely quantum bits and quantum logical gates. This thesis is part of the effort for implementing the building blocks of a quantum processor. Our experiments are based on a specific qubit circuit, the quantronium [14], a variant of the Cooper pair box circuit developed during the years 2001-2002 by the Quantronics group. A strategy for reducing the dephasing arising from the noise in the circuit control parameters provided to this qubit a better coherence than that of the Cooper pair box operated at NEC in 1999 [15].

Good coherence properties and the possibility to readout the quantum state allowed to perform qubit manipulation and to demonstrate single quantum gates [16, 17].
Our initial goal was thus to proceed to the next step: implementing a universal gate in a two-qubit circuit. A universal gate is a two qubit gate that allows to perform any unitary evolution when combined with single-qubit gates. The most natural universal gate for quantroniums is the $\sqrt{ISWAP}$ gate. This gate can fully entangle the two qubits, and produce Bell states that violate Bell inequalities.
We have successfully implemented a suitable coupling between two quantronium qubits, and demonstrated it yields the predicted swapping between the qubits. However, the coherence times were too small to characterize the gate and the fidelity of the entanglement produced. Furthermore, an unexpected outcome of these experiments was the discovery that our quantronium samples suffer from severe defects detrimental for advanced experiments on coupled qubits.
We have then decided to switch from quantronium qubits to "transmon" qubits, initially developed at Yale University by R. Schoelkopf [18]. The transmon is a Cooper Pair Box operated in the phase regime, and embedded in a 1d microwave cavity that provides a controlled electromagnetic environment. Its coherence properties are presently the best of all Josephson qubits. However, the transmon was lacking of a high fidelity readout, and we focused our effort on developing one. For readout, we have designed and implemented a variant of the Bifurcation readout method initially developed for the quantronium by M. Devoret [19]. The first results obtained indicate that this new strategy does provide a readout with high fidelity and little back-action, while maintaining good quantum coherence. These results yield to a scalable architecture for transmon qubits.

Towards a quantum-based definition of electrical units

Besides developing qubits for quantum information, Josephson devices were also proposed for the metrology of the electrical current. In 1985, K. Likharev, A. Zorin, and D. Averin [20] showed theoretically that a current-biased Josephson junction exhibits Bloch oscillations analogous to those initially proposed for electrons in solids, and with a frequency f related to the bias current I by the relation $I = 2ef$. Together with the Quantum Hall Effect and the Josephson effect, this experiment could provide a solution for closing the triangle of quantum metrology that relates the time, current and voltage units. This closure is important since its success could lead to a redefinition of the SI system based on electrical units, and even possibly to a redefinition of the kilogramme.
In this thesis, we have demonstrated that the phenomenon of Bloch oscillations initially proposed for the current biased Josephson junction also occurs in a simpler setup involving a quantronium. When an alternating current $\pm I$

is injected in the gate electrode of this device, We have found that Bloch oscillations develop with a frequency f very accurately related to the current I by the relation $I = 2ef$. This work can be considered as a first step along the programme proposed long ago for the current-biased Josephson junction.

Chapter 1

The Quantroswap: a two qubit gate based on the Cooper Pair Box

Contents

1.1 The Cooper Pair Box

1.1.1 A brief survey of quantum bit circuits based on the Cooper pair box

The Cooper Pair Box (CPB), described in Fig. 1.1, is a very simple quantum electrical circuit based on a single Josephson junction. It was initially proposed M. Büttiker in 1987 [21] in the context of Coulomb blockade and of Bloch oscillations in Josephson junctions, and first implemented in 1996 by the Quantronics group to investigate the competition between charging and Josephson effects [22].

At that time, the amazing theoretical breakthroughs just obtained in the domain of quantum computing, such as the discovery of a quantum factorization algorithm [23], triggered an intense search of quantum devices suitable for providing the elementary building blocks of a quantum processor, the so-called quantum bits. Ideally, quantum bits are two level systems whose quantum state can be manipulated and read, and that can be coupled in a controlled way to implement a quantum algorithm. In the field of superconducting circuits, the Cooper pair box soon became an attractive candidate investigated by a few research groups. Its quantum states, manipulation and readout methods are described in the next sections. The research group of Tsai and Y. Nakamura at NEC first demonstrated in 1999 [24, 15] the coherent manipulation of the quantum state of a CPB. However, the achieved coherence time was rather short (a few ns), and the experiment could not determine the quantum state for each realization of the experiment. The signal to noise ratio was much smaller than one in a single measurement, which imposed heavy averaging. A readout method able to discriminate the qubit states in a single readout is called a single-shot readout, and is characterized by its readout fidelity. To provide such a single-shot readout, the research group of P. Delsing at Chalmers University developed a CPB coupled to a radio-frequency Single Electron Transistor [25] .

In parallel, the Quantronium circuit [14], derived from the Cooper pair box, was developed in 2001 by the Quantronics group with the purpose of implementing a strategy for reducing decoherence. Decoherence mainly arises from the coupling of the quantum bit to its electrical environment. Ideally, a quantum bit circuit should be decoupled from its environment during its operation, and coupled to it only at readout time. This goal can be partly reached by operating the circuit at an optimal point where the transition frequency of the quantum bit is stationary respectively to variations of the control parameters. At such a point, the dephasing is suppressed at first order, which allowed to gain two orders of magnitude in the coherence time. A single-shot readout method for the quantronium was obtained by controlling the switching of a Josephson junction by the quantum state of the Cooper pair box. The achieved coherence time, 0.5 μs, and readout fidelity, at best 0.4, obtained with the original quantronium circuit were sufficient for performing

interesting and useful experiments on qubit manipulation and on decoherence [26, 27], but still far from meeting the criteria requested for quantum computing.

The coherence of Cooper pair box circuits was then significantly improved in 2004 by placing a Cooper pair box in a microwave resonator that provides a well characterized electromagnetic environment, as proposed and demonstrated by the group of R. Schoelkopf at Yale [18]. Recently, this group further demonstrated that making the Cooper pair box almost insensitive to charge noise significantly improves its coherence. For readout, a new microwave readout strategy was first developed by the group of M. Devoret at Yale in 2004 [28]. This new readout, based on the Josephson Bifurcation Amplifier (JBA), exploits the dynamical switching of a Josephson junction between two different dynamical states. It allows to measure the quantronium at its optimal point, and, ideally, to perform a QND readout. It also allows to measure different qubits with a single readout circuit by addressing them at different readout frequencies, which is truly essential for operating even an elementary quantum processor. Presently, the application of this multiplexed readout method based on the JBA to qubits embedded in microwave resonators is a promising research direction for Cooper pair boxes.

During this thesis work, in 2006, the group of O. Buisson in Grenoble coupled a CPB to an other Josephson qubit (phase qubit) and demonstrated the coherence of the system by spectroscopic measurement [29]. Besides the Yale groups demonstrated in the time domain the coherent coupling between two CPBs embedded in a microwave resonator [30].

1.1.2 Discrete anharmonic energy spectrum allows to define a qubit

The Cooper Pair Box is made of two superconducting electrodes connected together by one or two Josephson junctions. In its simplest version, it consists in a superconducting island connected to a superconducting reservoir (see Fig. 1.1) by a single Josephson junction with capacitance C_J and Josephson energy $E_J = I_0\varphi_0$, where $\varphi_0 = \hbar/2e$ is the reduced flux quantum and I_0 is the critical current of the junction given by the Ambegaokar-Baratoff formula [31]

$$I_0 = \frac{\pi}{2}\frac{\Delta}{eR_T}, \tag{1.1}$$

where Δ is the superconducting gap of the superconductor and R_T the tunnel resistance of the junction. The island is electrostatically biased by a gate voltage source V_g in series with a capacitance C_g. In addition to E_J, the box has a second characteristic energy, the charging energy [1]

$$E_C = \frac{(2e)^2}{2C_\Sigma}, \tag{1.2}$$

[1] The charging energy is defined for a Cooper pair in this thesis work.

where $C_\Sigma = C_g + C_J$ is the total capacitance of the island and $2e$ the charge of a Cooper pair. At sufficiently low temperature, such that no quasiparticle excitations exist in the superconductors (i.e. all the electrons in the electrodes are paired), the system has a single degree of freedom corresponding to two conjugate observables: the gauge invariant phase difference $\widehat{\theta}$ across the junction, and the number $\widehat{N}$ of Cooper pairs in excess to electroneutrality in the island. The Hamiltonian of the whole CPB circuit, including the gate voltage source, is

$$\begin{aligned} \widehat{H} &= E_C(\widehat{N} - N_g)^2 - E_J \cos\left(\widehat{\theta}\right), \\ \left[\widehat{N}, \widehat{\theta}\right] &= i, \end{aligned} \tag{1.3}$$

with $N_g = C_g V_g / 2e$ the reduced gate charge. The first term corresponds to the electrostatic energy of the circuit, while the second one is the Josephson Hamiltonian that depends on the phase difference θ. This Josephson term is the residual BCS pairing interaction between the electrodes, mediated by electron tunneling across the junction.
It is often useful to make the Josephson energy tunable. For that purpose, the CPB junction can be split into two junctions (see Fig.1.1) with energies $E_J(1+d)/2$ and $E_J(1-d)/2$ respectively, where $d \in [0,1]$ is the asymmetry coefficient between them. The island and the reservoir now form a superconducting loop that encloses a magnetic flux Φ. This loop has a geometrical inductance negligible with respect to the Josephson inductance $2\varphi_0/I_0$ of the two junctions in series. Neglecting this geometrical inductance, the Hamiltonian of the split CPB writes

$$\widehat{H_0} = E_C(\widehat{N} - N_g)^2 - E_J \left[\cos\left(\frac{\widehat{\delta}}{2}\right)\cos\widehat{\theta} + d\sin\left(\frac{\widehat{\delta}}{2}\right)\sin\left(\widehat{\theta}\right)\right], \tag{1.4}$$

with

$$\begin{aligned} \widehat{\theta} &= \frac{\widehat{\theta}_1 - \widehat{\theta}_2}{2}, \\ \widehat{\delta} &= \widehat{\theta}_1 + \widehat{\theta}_2, \end{aligned} \tag{1.5}$$

where $\widehat{\theta}_{1,2} \in [0, 2\pi]$ are the superconducting phase differences across each Josephson junctions. In most cases [16], $\widehat{\delta}$ undergoes small quantum fluctuations, so that it can be considered as a classical parameter, equal to $\delta = \Phi/\varphi_0$.

For the purpose of computing the eigenstates and the corresponding eigenenergies, the Hamiltonian (5.2) can be equivalently written either in the discrete charge state basis $\{|N\rangle_C\}$ of the eigenvectors of $\widehat{N}$, or in the continuous phase state basis $\{|\theta\rangle\}$ of the eigenvectors of $\widehat{\theta}$. Using the commutation relation between $\widehat{\theta}$ and $\widehat{N}$, one has [16]

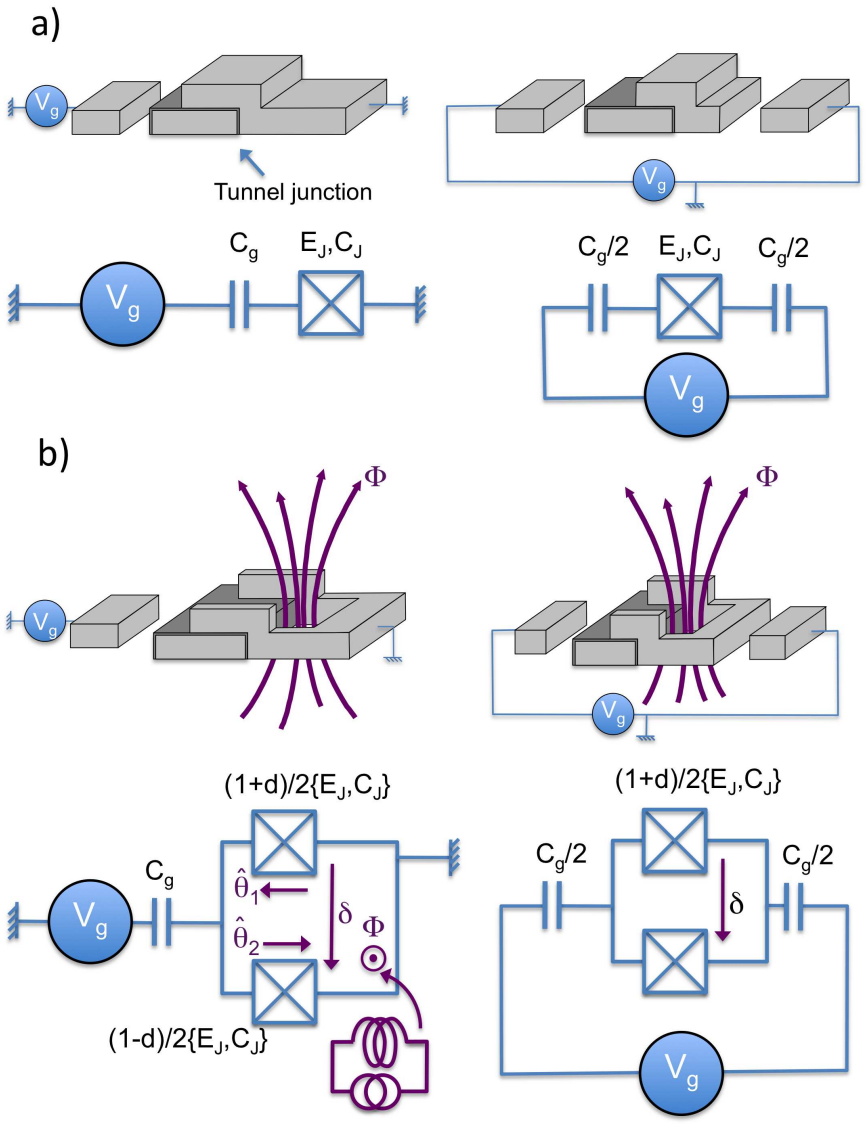

Fig. 1.1. Schematic representation and electrical schemes of the basic CPB (a) and split CPB (b), in its original version with one island and a reservoir (left) and in its symmetrized version (right).

$$e^{\pm i\widehat{\Theta}}\left|N\right\rangle_C = \left|N \pm 1\right\rangle_C \text{ and } \widehat{N} = \frac{1}{i}\frac{\partial}{\partial\widehat{\theta}}. \tag{1.6}$$

Thus, the Hamiltonian (5.2) writes

$$\begin{aligned}\widehat{H} = E_C(\widehat{N} - N_g)^2 - \tfrac{E_J}{2}\textstyle\sum_N \Big\{ \left[\cos\left(\tfrac{\delta}{2}\right) - id\sin\left(\tfrac{\delta}{2}\right)\right]\left|N+1\right\rangle_C\left\langle N\right|_C \\ + \left[\cos\left(\tfrac{\delta}{2}\right) + id\sin\left(\tfrac{\delta}{2}\right)\right]\left|N\right\rangle_C\left\langle N+1\right|_C \Big\}\end{aligned} \tag{1.7}$$

or

$$\widehat{H} = E_C\left(\frac{1}{i}\frac{\partial}{\partial\widehat{\theta}^*} - N_g\right)^2 - E_J^*(d,\delta)\cos\left(\widehat{\theta}^*\right) \tag{1.8}$$

in the charge and phase representations, respectively. In Eq. (1.8), $E_J^*(d,\delta) = E_J\sqrt{(1+d^2+(1-d^2)\cos(\delta)/2}$ plays the role of a magnetically tunable Josephson energy, and $\widehat{\theta}^* = \widehat{\theta} + \zeta(d,\delta)$ with $\tan[\zeta(d,\delta)] = -d\tan(\delta/2)$ [16]. The Hamiltonian (1.7) can be easily diagonalised by truncating the charge basis, but the phase representation allows to obtain exact results. Indeed, the Schrödinger equation associated to Hamiltonian (1.8) is a solvable Mathieu equation with periodic boundary conditions. The wavefunctions Ψ_k have eigenenergies that form discrete energy bands 2π-periodic in δ, and even and 1-periodic in N_g. In the range $N_g \in]0, 0.5[$, the eigenenergies and wavefunctions are given by the expressions [16]:

$$\begin{aligned} E_k &= \tfrac{E_C}{4}\mathcal{M}_A[k+1-(k+1)mod2+2N_g(-1)^k, -\tfrac{2E_J^*}{E_C}] \\ \langle\theta^*|k\rangle &= \Psi_k(\theta^*) \\ &= \tfrac{e^{iN_g\theta^*}}{\sqrt{2\pi}}\left[\mathcal{M}_C\left(\tfrac{4E_k}{E_C}, \tfrac{-2E_J^*}{E_C}, \tfrac{\theta^*}{2}\right) + i(-1)^{k+1}\mathcal{M}_S\left(\tfrac{4E_k}{E_C}, \tfrac{-2E_J^*}{E_C}, \tfrac{\theta^*}{2}\right)\right] \end{aligned} \tag{1.9}$$

The CPB can thus be regarded as an artificial atom subject to Zeeman (δ) and Stark (N_g) fields. Figure 1.2 shows the three lowest energy bands for different E_J/E_C ratios. The two lowest energy states $|0\rangle$ and $|1\rangle$ define the qubit. When inducing a resonant transition between $|0\rangle$ and $|1\rangle$, one has to avoid excitation of the upper energy state $|2\rangle$. The anharmonicity $\nu_{12}/\nu_{01} - 1$, where $\nu_{12} = (E_2 - E_1)/h$ and $\nu_{01} = (E_1 - E_0)/h$ are the two first transition frequencies, needs thus to be sufficiently large. More precisely [16], the anharmonicity has to be much larger than $1/\nu_{01}\tau$, where τ is the duration of the excitation (see next section). The variations of the anharmonicity with the ratio E_J/E_C for a constant transition frequency is shown in Fig. 1.2 at the optimal working point $N_g = 1/2$ and $\delta = 0$. Three different regimes noted 1, 2 and 3 in Fig. 1.2 can be distinguished. The first one corresponds to the charge regime $E_J/E_C << 1$. The CPB operated in 1999 by Nakamura at NEC [24, 15] to demonstrate the first coherent manipulation of an electrical circuit, and the CPB operated at Chalmers university in 2004 [25] were in this regime. Except in the vicinity of $N_g = 1/2 \mod 1$, the CPB eigenstates are

almost pure charge states $|N\rangle_C$ with eigenenergies $E_C(N-N_g)^2$ in this case. At $N_g = 1/2 \mod 1$, the eigenstates are the symmetric and antisymmetric superpostions of $|N\rangle_C$ and $|N+1\rangle_C$ with energies $E_C/4 \pm E_J/2$. As shown on Fig. 1.2 the anharmonicity is always large in this regime.
The opposite regime, $E_J/E_C >> 1$, can be called a phase regime. We will explain later how this regime allows to suppress the effect of charge noise, as demonstrated by the group of R. Schoelkopf at Yale[18]. The qubit eigen wavefunctions are now well localised in phase and the transition energy is independant of the gate charge, and equal to the plasma frequency of the junction $\sqrt{2E_J^* E_C}$ at $\delta = 0$. The anharmonicity is much lower and tends towards $\sqrt{2E_C/E_J^*}$.
The Quantronium qubit, developed at Saclay since 2001 [14] lies in the intermediate regime $E_J \sim E_C$. In this regime, the eigenstates are superpositions of typically 5 to 10 charge states (with weight larger than 1%) and the energy bands depend on both N_g and δ (see Fig. 1.2). The anharmonicity varies strongly and vanishes at a certain ratio $E_J/E_C = r_c$ that depends on $\nu_{01}(\delta = 0)$. A narrow window in E_J/E_C around r_c is thus unappropriate for making qubits.

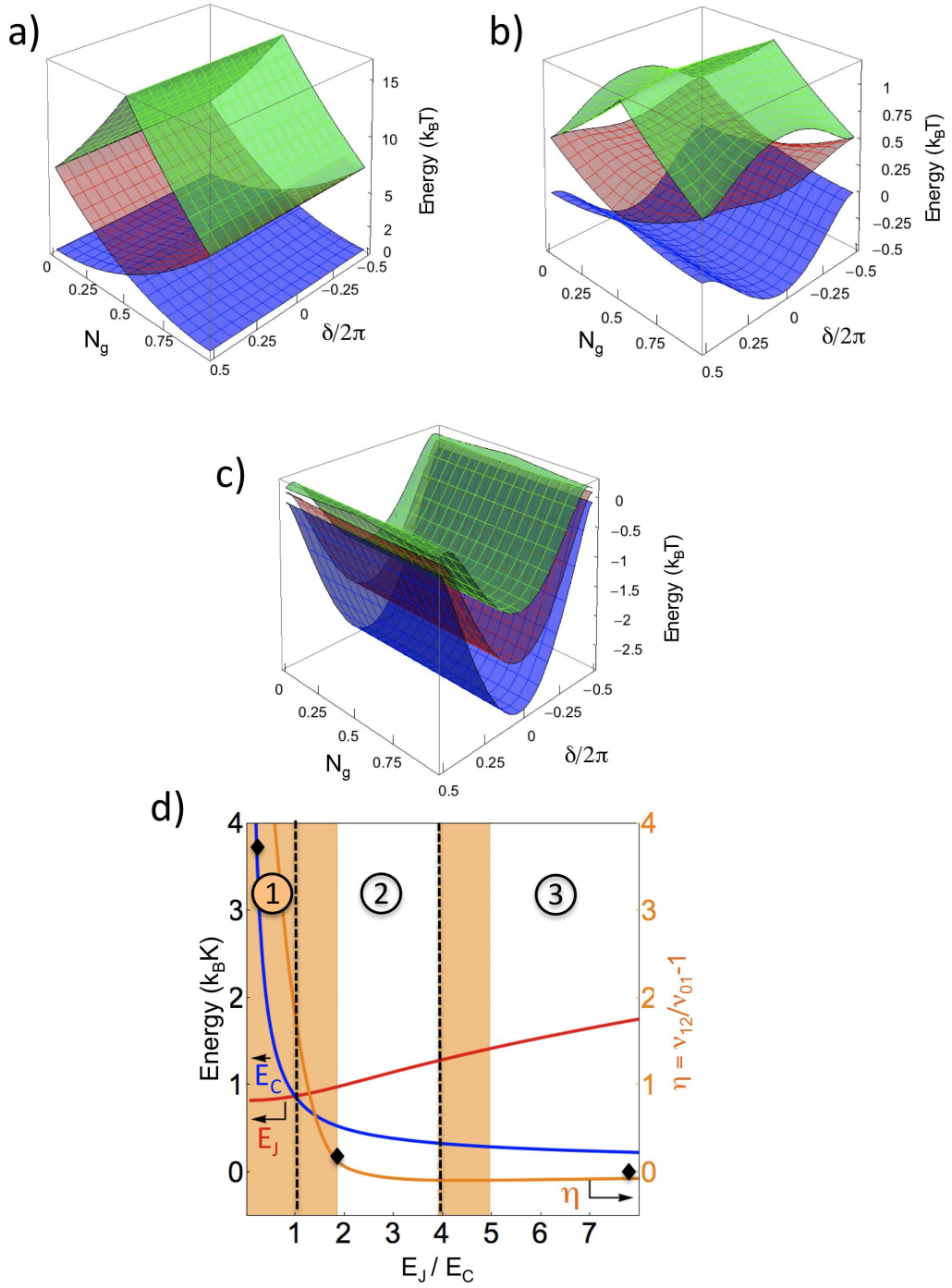

Fig. 1.2. Energy spectra and anharmonicity of the split CPB as a function of E_J/E_C. Top: First three energy bands of a CPB with a transition frequency $\nu_{01} =$ 17 GHz and an asymmetry $d = 5\%$, as a function of δ and N_g, and for $E_J/E_C = 0.12$ (a), 1.9 (b), and 30 (c). d) Anharmonicity $\eta = \nu_{12}/\nu_{01} - 1$ at the working point $\delta = 0$ and $N_g = 1/2$ for a constant transition frequency 17GHz. The charge (1) , intermediate (2) and phase (3) regimes are indicated as well as the region (hatched) where the anharmonicity is above 10%. Josephson and charging energies E_J (red) and E_C (blue) are also shown. The diamonds indicate the E_J/E_C ratios of the three upper plots.

1.1.3 Coherent manipulation and single qubit gate

The coherent manipulation of a qubit is realized by performing a non adiabatic evolution with a time-dependent Hamiltonian. The qubit manifold can then be regarded as a pseudo-spin 1/2 evolving in a fictitious magnetic field $\overrightarrow{H}$ representing its Hamiltonian, and its evolution is conveniently visualized on the Bloch sphere picture. Different non-adiabatic manipulation schemes can be applied. In the first CPB manipulation experiment[15], Y. Nakamura and coworkers applied ultrafast trapezoidal N_g pulses on a CPB in the charge regime. In that case, the Hilbert space can be restricted to two pure charge states $|0\rangle_C$ and $|1\rangle_C$ provided that N_g is kept in the range $[0.2, 0.8]$. These two states respectively point to the north and south poles of the Bloch sphere (see. Fig 1.3), while the fictitious magnetic field is

$$\overrightarrow{H} = Ec(N - N_g)\overrightarrow{z} + Ej\overrightarrow{x}. \tag{1.10}$$

The qubit was initially prepared in its ground state at $N_g \simeq 0.3$ (very close to the north pole); then the longitudinal component of the field was suddenly suppressed to bring the qubit at the degeneracy point $N_g = 1/2$. Since the risetime of this pulse was shorter than h/E_J, the qubit state did not evolve during this step. Then, the remaining transverse Josephson field induced coherent oscillations between the two charge states (see Fig. 1.3). Finally the qubit was brought back to the initial N_g to be measured in the pure charge states basis (see next section). Rabi oscillations were observed as a function of the time spent at $N_g = 1/2$.

A more versatile and more accurate manipulation method consists in applying an AC perturbation of the Hamiltonian on resonance with the qubit frequency, as done in atomic physics or in Nuclear Magnetic Resonance [24]. With CPBs, it consists in applying a small harmonic perturbation $\Delta N_{rf} \cos(2\pi\nu_{rf}t + \varphi_{rf})$ to the gate charge [14] at a frequency ν_{rf} resonant or nearly resonant with the qubit frequency ν_{01}. The north and south pole are now the two energy eigenstates $|0\rangle$ and $|1\rangle$ at a fixed N_g (usually $N_g = 1/2$) (see Fig. 1.3). At $N_g = 1/2$ the small harmonic perturbation in $\overrightarrow{H}$ is equivalent to a purely transverse field $4E_C\Delta N_{rf}|\langle 1|\widehat{N}|0\rangle|\cos(2\pi\nu_{rf}t + \varphi_{rf})\overrightarrow{x}$. It is convenient to represent the dynamics in a frame rotating at the microwave frequency ν_{rf}. Indeed, within the rotating wave approximation [32], the AC field becomes static in the rotating Bloch sphere:

$$\overrightarrow{H} = 2E_C\Delta N_{rf}|\langle 1|\widehat{N}|0\rangle|(\cos\varphi_{rf}\overrightarrow{x} + \sin(\varphi_{rf})\overrightarrow{y} + \delta\nu\overrightarrow{z}), \tag{1.11}$$

where $\delta\nu = \nu_{01} - \nu_{rf}$ (see Fig. 1.3). This field induces the Rabi precession of the spin at the Rabi frequency $\nu_{Rabi} = \sqrt{\nu_{r0}^2 + \delta\nu^2}$, the angle of precession being adjustable by tuning the amplitude or the duration of the microwave pulse. Note that ν_{r0} should not be too high in order to avoid spurious population

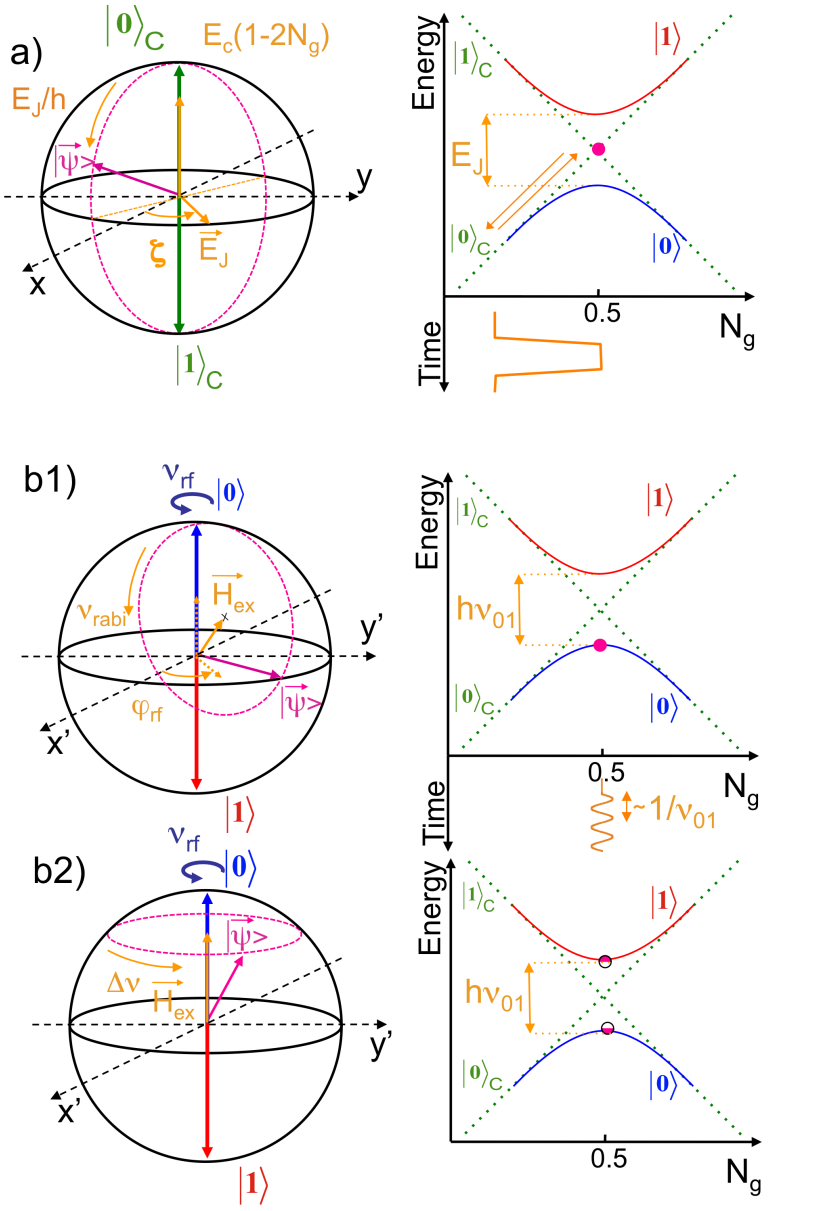

Fig. 1.3. Coherent manipulation of the CPB in the Bloch sphere picture. a) Case of a CPB in the charge regime (1 in Fig. 1.2). The qubit states are pure charge states at the poles of the Bloch sphere. An ultrafast trapezoidal gate pulse to $N_g = 1/2$ (bottom right) brings the system at the degeneracy point (magenta disk) of the energy diagram (top right); the field H_{ex} (orange arrow in the Bloch sphere) is sent to the equatorial plane, which induces a precession of the spin (magenta arrow) along a meridian (magenta circle). b) Manipulation of the CPB at the degeneracy point $N_g = 1/2$ by a sinusoidal N_g perturbation nearly resonant with the qubit frequency ν_{01}. The Bloch sphere is now rotating at the microwave frequency and the field H_{ex} is static. In presence of microwave (b1), the field lays in a longitudinal plane making an angle φ_{rf} with the reference X' axis and induces Rabi oscillations of the spin at the Rabi frequency ν_{Rabi}. In the absence of microwave (b2), the field is oriented along the z axis, and the spin precesses freely around z at the detuning frequency $\Delta\nu$.

of the third CPB level $|2\rangle$. Indeed, the matrix element $m = 2\nu_{r0}E_C \langle 2| \widehat{N} |1\rangle$ responsible for such a spurious population p_2 is equal to $\alpha 2\nu_{r0}E_C \langle 1| \widehat{N} |0\rangle$ with $\alpha \in [1, \sqrt{2}]$ for $E_J/E_C > 0.5$. We have calculated p_2 due to the perturbation applied to unperturbed evolution $\cos(\pi\nu_{r0}t)|0\rangle + \sin(\pi\nu_{r0}t)|1\rangle$. For $(\nu_{r0})/(\nu_{12} - \nu_{01}) << 1$, we find

$$p_2 = ((\alpha\nu_{r0}/2)/(\nu_{12} - \nu_{01}))^2 \tag{1.12}$$

Then combining three resonant pulses inducing rotations around x ($\varphi_{rf} = \pi/2$), y and x, implements any single qubit operator [33, 26]. Alternatively, adiabatic changes of N_g or δ increases the z component of the fictious field, and so induces rotation around the z-axis [26]. All these gates can be characterized by quantum tomography as demonstrated by M. Devoret on the quantronium, following the experiment on phase qubit by J. Martinis [34].
It is important to notice that all these methods inspired from NMR and atomic physics also apply to CPBs deep in the phase regime (region 3 of Fig. 1.2). Indeed, the smallness of E_C can be compensated by a larger microwave amplitude or a larger gate capacitance C_g, as demonstrated by the successful manipulation of transmon devices at Yale [35].

1.1.4 Readout of Cooper Pair Boxes

Many strategies, which differ in many respects, have been proposed to discriminate the $|0\rangle$ and $|1\rangle$ states of a CPB. A first essential distinction is whether or not the readout is single-shot, that is whether or not the two qubit states can be discriminated in a single measurement with a "reasonable" fidelity. This definition is of course subjective, and any single-shot measurement has to be characterized by its error rates $e_{|0\rangle,|1\rangle}$ or fidelities $1 - e_{|0\rangle,|1\rangle}$ for the two qubit states, or by its readout contrast $1 - (e_{|0\rangle} + e_{|1\rangle})$ between the two states. Note that achieving a good readout fidelity requires to complete the measurement in a time shorter than the relaxation time. In the case of a low signal to noise measurement, the state preparation and measurement sequence has to be repeated numerous times in order to determine the average value of the qubit at the end of the sequence. A single-shot readout is further characterized by its projective or destructive character. Ideally, a single-shot measurement is projective, i.e. it is associated to a Quantum Non Demolition (QND) measurement that leaves the qubit in a state corresponding to the outcome of the readout performed. For a perfect QND readout, subsequent readouts yield the same result. The projection fidelity measures the QND character of a readout. Similarly, a non single-shot readout, which takes only a partial information on the qubit state, can have a back-action corresponding to the minimal decoherence imposed by quantum mechanics, or a larger one. A readout that completely scrambles the qubit is said to be destructive.
Last but not least, one has to consider which variable of the qubit is involved in the readout. In the case of CPBs, the measurements used so

far for readout of the quantum state involve either the CPB island charge $\widehat{N} = (\partial\widehat{H}/\partial N_g + N_g)/(2E_C)$, or, for the split CPB, the persistent current in the loop given by $\widehat{I} = \varphi_0^{-1}\partial\widehat{H}/\partial\delta$ [36]. The physical quantities actually measured can be $< N >$ or $< I >$, or further derivatives respectively to the control parameters N_g and δ:
-the so-called quantum capacitance $\widehat{C} = 2e(\partial\widehat{V}/\partial N_g)^{-1}$;
-the quantum inductance $\widehat{L} = (\varphi_0\partial\widehat{I}/\partial\delta)^{-1}$ [28, 37].

The dependance of these measurable quantities are shown in Fig. 1.4 for CPBs with different E_J/E_C ratios. We now briefly review the various CPB readouts implemented up to now.

1.1.5 Readout of a CPB through the charge

In their first experiment performed in 1999 [24], Y. Nakamura and coworkers measured directly the island charge. A small and very opaque additional tunnel junction was connected to the island and voltage biased. In this setup, when the qubit is in the state $|1\rangle = |1\rangle_C$, the extra Cooper Pair in the island can be broken into two electrons tunneling sequentially through the measuring junction (see Fig. 1.5a)[24]. By repeating the preparation and measurement sequence, a current of a few picoamps builds up and can be measured. This readout method is intrinsically destructive as the qubit is always reset in state $|0\rangle$ after the measurement. Moreover it is also non-single shot because current meters do not resolve a single Cooper pair.

In the experiment [38, 39, 25] of P. Delsing and coworkers, a CPB in the charge regime was coupled capacitively to a Radio Frequency Single Electron Transistor (RFSET) used as a fast sensitive electrometer for measuring the island potential $\langle V\rangle$, proportional to the average island charge. Figure 1.5b shows the setup with the RFSET made of a voltage biased SET in parallel with a resonant tank circuit. Since the RFSET circuit resonance varies with the charge coupled to its island, this results in a state dependent frequency shift which can then measured by microwave reflectometry. This readout was not found to be single-shot due to a too short qubit relaxation time, but could be in principle be QND and projective.

More recently, in the experiments [35] implemented at Yale, a split CPB was placed at the electric field antinode of a coplanar stripline resonator (see Fig.1.5c). The CPB acts as an electric dipole that modifies locally the dielectric constant in the resonator and displaces its resonance frequency ν_{cav}. This frequency shift translates in a change of the amplitude and phase of the microwave signal transmitted through (or reflected by) the resonator [18]. This dispersive method is by nature projective and QND, provided the number of photons injected in the resonator is low enough to avoid excitation and relaxation of the CPB. Using microwave amplifiers with a noise temperature lower

than presently available, this dispersive readout method would be single-shot and QND.

1.1.6 Readout of a split CPB through the loop current

In 2001 the Quantronics group developed a new circuit [14, 16] called the Quantronium (see Fig. 1.6) made of a split CPB, in which the persistent loop current i_k is exploited to discriminate the qubit states. An additional current biased large Josephson junction with critical current I_0 is inserted in the CPB loop. During qubit manipulation, the bias current I_b is kept small compared to I_0, so that the quantum fluctuations of the phase γ across the readout junction are small. This phase then behaves as a classical variable given by $\gamma = \arcsin(I_b/I_0)$. The bias current plays the role of an additional knob that controls the CPB phase

$$\delta(\phi, I_b) = \phi/\varphi_0 + \gamma(I_b). \tag{1.13}$$

For readout, the bias current is adiabatically increased up to a plateau with duration τ and peak value I_p close enough to I_0 (see Fig.1.6) to induce the switching of the readout junction to its voltage state. Since the state dependent persistent current $i_k(\delta)$ adds algebraically to the bias current I_b, the switching rate of the readout junction depends on the qubit state. The readout junction thus behaves as a threshold detector that switches to a voltage state with a high or low probability depending on the qubit state. The stochastic dynamics of the junction phase γ during the readout time τ determines the switching rate Γ. In the thermal regime $\hbar\omega_p/k_BT << 1$, this rate Γ writes [40]:

$$\Gamma(s) = \omega_p(1-s^2)^{1/4} e^{-\frac{4\sqrt{2}}{3}\frac{\xi_J(1-s)^{3/2}}{k_BT}}, \tag{1.14}$$

with $s = I/I_0$, the plasma frequency $\omega_p = \sqrt{I_0/\phi_0 C_J}$, the Josephson energy $\xi_J = I_0\varphi_0$. Integrated over τ, this rate leads to a switching probability

$$P_S(s) = 1 - e^{\Gamma(I_p/I_0)\tau} \tag{1.15}$$

where $I_p = I_p + i_k(\delta_p)$ and the index p denotes quantities taken at the plateau. By precisely adjusting I_p and τ, the switching probability P_S can be tuned such that the probability p_1 (qubit in state $|1\rangle$) is much larger than the probability p_0 (qubit in state $|0\rangle$). The difference $\eta = p_1 - p_0$ depends strongly on I_p, as shown on Fig. 1.7a. Its maximum in I_p defines the readout constrast, which depends on δ_p (see Fig. 1.7b). The fidelity is maximun betwen 0.8π and 0.9π. Since the quantronium is usually manipulated close to $\delta = 0$, and since γ can be ramped only up to $\pi/2$, it can be interesting to ramp I_b starting from a negative value I_{b_in} in order to reach the optimal phase range for δ_p. The applied flux ϕ, and the bias currents I_{b_in} and I_p should then be

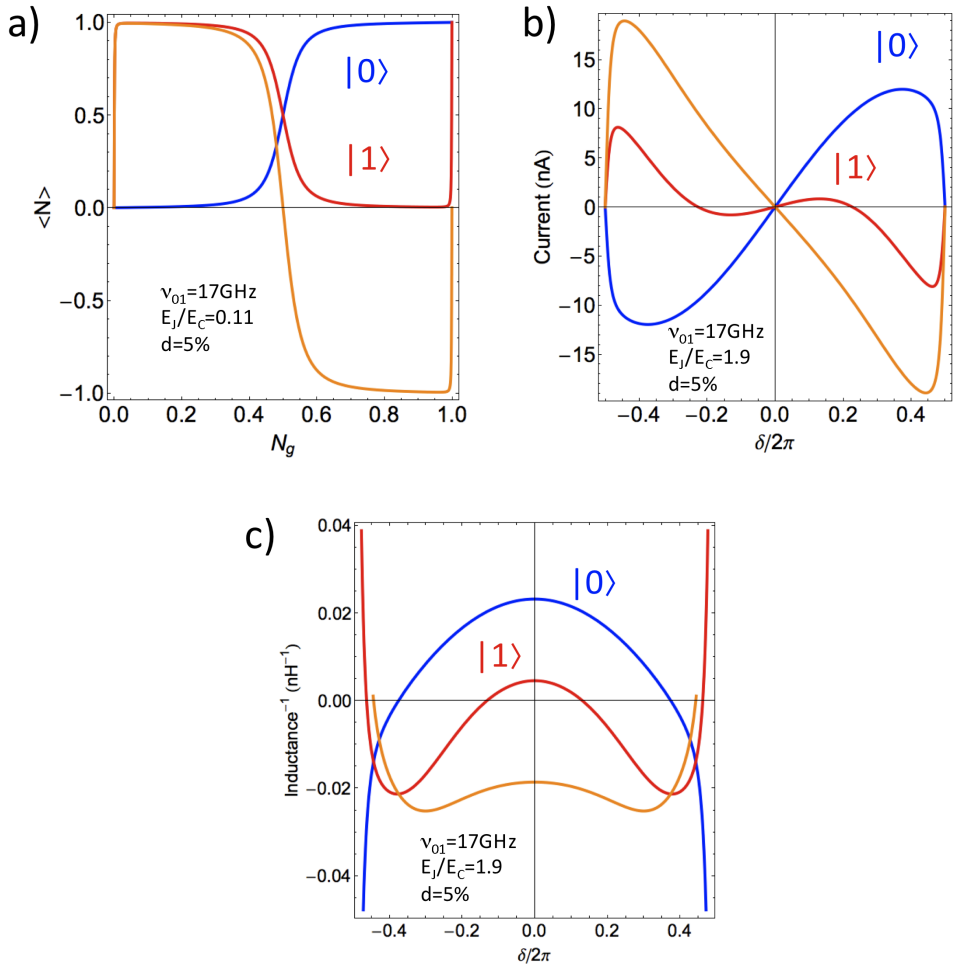

Fig. 1.4. Different properties of the CPB qubit can serve to discriminate its $|0\rangle$ (blue curves) and $|1\rangle$ (red curves) states. The difference in a given property between the two qubit states is shown in orange. a) Average charge $\langle N \rangle$ of the island in the charge regime (same parameter as in Fig. 1.2a), as a function of the reduced gate charge N_g. b) Persistent loop current of the split CPB in the intermediate regime (same parameter as in Fig. 1.2b), as a function of δ . c) Quantum inductance of the CPB in the intermediate regime (same parameter as in Fig. 1.2b), as a function of δ.

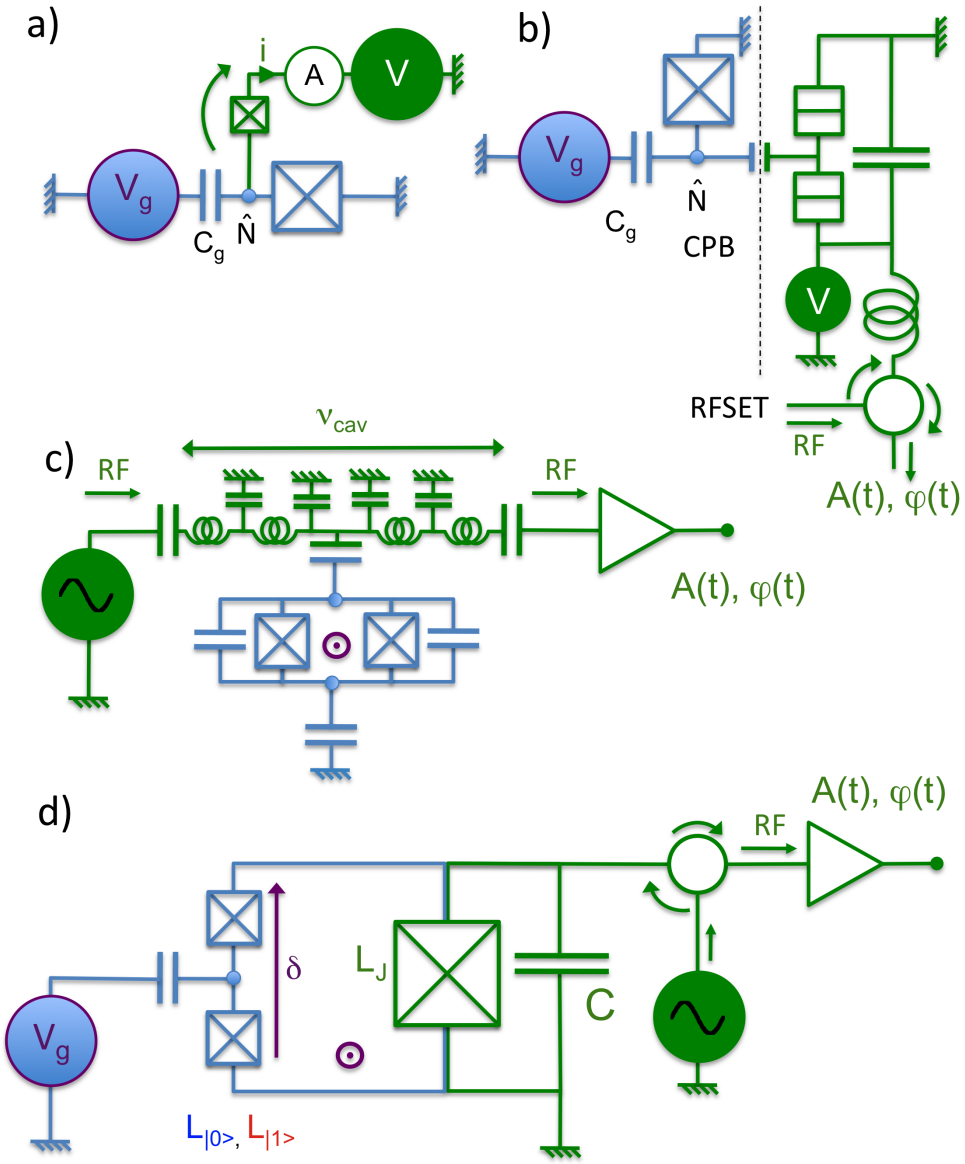

Fig. 1.5. Several readout schemes for a CPB. a) The island of the CPB is connected to a voltage biased opaque Josephson junction. When the qubit is in state $|1\rangle$, the excess Cooper pair in the island can break into two electrons passing through the readout junction and building a current i when the experiment is repeated. b) The CPB is capacitively coupled to an RFSET, a sensitive electrometer whose impedance depends on the average charge on the CPB island. The qubit state is determined by measuring the amplitude A or phase φ of the reflected microwave. c) The CPB is placed in a coplanar waveguide resonator with resonance frequency ν_{cav} shifted by the qubit. The qubit is read by measuring the amplitude or phase of a microwave transmitted through the cavity. d) The split CPB, which can be regarded as a state dependent inductance L_k, is connected in parallel with a tank circuit to form a resonator whose resonance frequency is measured by microwave reflectometry.

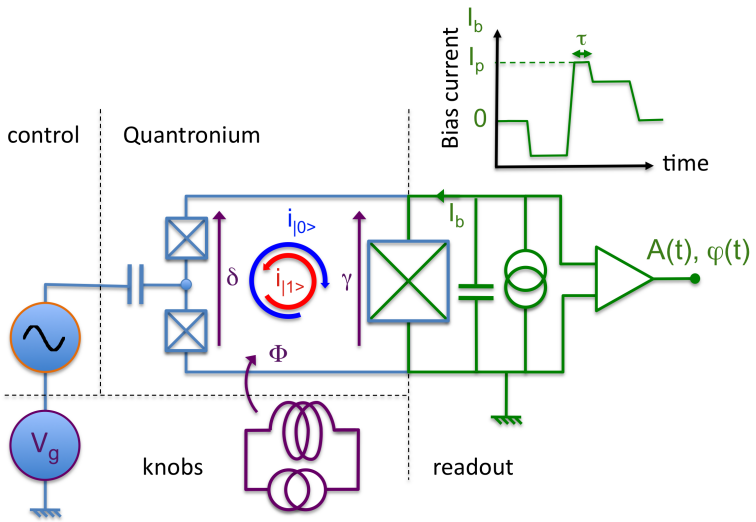

Fig. 1.6. Electrical scheme of the quantronium qubit. The qubit is in blue and the readout circuit in green. A large Josephson junction is inserted in the split CPB loop to serve as a threshold detector: a current pulse $I_b(t)$ (top right) with a peak value I_p applied during a duration τ induces the switching of the junction to a finite voltage with a probability that depends on the qubit state.

such that $\delta(\phi, I_{b_in}) \simeq 0$ and $\delta(\phi, I_p) \simeq 0.85\pi$. This method requires to compensate the negative bias current by an appropriate magnetic flux Φ. Using this technique, the maximum theoretical fidelity is about 95% for a critical current I_0 of about $1\mu A$. Experimentally the maximum fidelity was smaller, about 40%, the discrepancy being only partly explained by level-crossings and relaxation occuring during the readout ramp. This readout fidelity is insufficient for quantum information processing. Furthermore, the large amount of quasiparticles generated in the superconducting leads during the switching destroys the qubit state. In a quantum processor this destruction would prevent using the measured qubit later in the algorithm. Despite the qubit state could be "copied" using an extra two-qubit gate before readout, a QND readout method is clearly useful.

1.1.7 Towards a QND readout for the quantronium

In 2004, M. Devoret and coworkers [28] measured the quantum inductance L of the CPB using a microwave readout method. More precisely, the series inductance of the two CPB junctions, which depends on the qubit state, slightly contributes to the effective inductance of the quantronium circuit mainly determined by the inductance φ_0/I_0 of the readout junction. With the capacitor

C, the quantronium thus forms a resonant circuit whose resonance frequency ω_p depends on the qubit state. Since the readout junction is furthermore a non linear inductor, this resonator is a non linear system with several dynamical states (for the same excitation) that can be exploited to discriminate the qubit states. When driven at a frequency ω_{rf} close to the circuit resonance frequency ω_p, the phase γ develops oscillations, which obey the following equation of motion

$$\ddot{\gamma} + \frac{\omega_p}{Q}\dot{\gamma} + \omega_p^2 \sin(\gamma) = \frac{V}{ZI_0}\cos(\omega_{rf}t) \tag{1.16}$$

with $Q = ZC\omega_P$ the quality factor of the resonator and Z the impedance of the measuring line. With a drive frequency sufficiently detuned from ω_p ($1 - \omega_{rf}/\omega_p > \sqrt{3}/2Q$), increasing the drive amplitude V induces a switching or bifurcation from a regime with low amplitude oscillations to a regime with large amplitude oscillations [37], and with a different phase. As the bifurcation drive amplitude V_b depends strongly on the ratio ω_{rf}/ω_p [41], the drive amplitude V can be set such that the bifurcation occurs only when the qubit is in state $|1\rangle$. This AC switching method is expected to be single-shot. Experimentally, the largest observed contrast for Rabi oscillations was about 60% [28], which is already better than the one obtained with the DC switching method. When the drive is not too large, the method is furthermore expected to be projective. Its QND character was probed by performing successive measurements. By measuring the conditional probability of obtaining an outcome corresponding to state $|0\rangle$ (resp. $|1\rangle$) after a first readout having given the outcome $|0\rangle$ (resp. $|1\rangle$), one can determine the QND fractions for both qubit states. It was found that this QND fraction is about 35% for state $|1\rangle$, and close to 100% for state $|0\rangle$ [42]. This bifurcation method has also been implemented in flux qubits by the group of H. Mooij at T.U. Delft [43, 44], and excellent QND behavior was demonstrated.

In the present thesis, we have designed a two-qubit circuit using either the DC switching or the JBA readout method (see next chapter). Although we have only implemented experimentally the first one, the JBA method was also used in the "transmon" experiment reported (see chapter 4) and in the experiment on current to frequency conversion for characterizing the detector (see chapter 5).

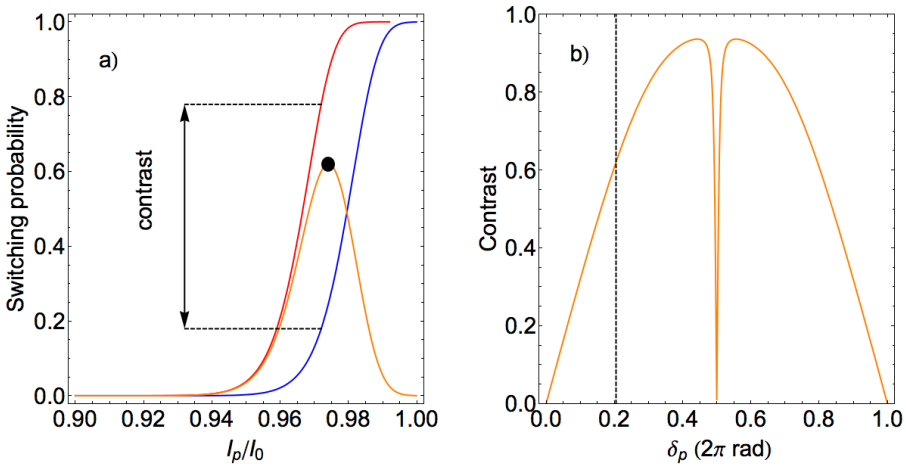

Fig. 1.7. Theoretical readout fidelity of the quantronium. a) Theoretical switching probabilities for the two qubits states $|0\rangle$ (blue curve) and $|1\rangle$ (red curve) as a function of the peak bias current I_p for $\delta = \gamma = 0$ before the readout pulse (ramp from $I_b = 0$), and for typical experimental parameters: Ej=0.96K, Ec=0.54K, d=0.05, I_0=650nA, ν_p=5GHz, τ = 10ns, and T = 50mK. The maximum difference in the two switching probabilities (as a function of I_p) is the readout constrast (orange curve). b) Theoretical readout contrast as a function of δ_p. The dashed line corresponds to graph (a)

1.1.8 Decoherence

As any quantum object, the CPB is subject to an interaction with its environment, which yields the decay of an initial density matrix towards the thermal equilibrium density matrix. One makes the distinction between relaxation, that describes the evolution of the longitudinal part of the density matrix, and decoherence that pertains to the transverse part. Relaxation involves an energy transfer $h\nu_{01}$ between the qubit and its environment, and is characterized by an exponential decay with rate Γ_1. Decoherence combines two independent phenomena: relaxation and dephasing. Relaxation yields an exponential decay factor of the coherence term with a rate $\Gamma_1/2$. Dephasing occurs without energy transfer, and consists in a progressive loss of coherence for the phase φ of a coherent superposition $|0\rangle + e^{i\varphi}|1\rangle$, due to fluctuations of the qubit frequency ν_{01} induced by the noise from environmental degrees of freedom. Dephasing does not always yield to an exponential decay. The decay of quantum coherence is best measured with the two-pulse Ramsey sequence followed by qubit readout [14].

Relaxation and dephasing have been widely studied both experimentally [45, 46, 47, 48, 27] and theoretically [49, 50] in CPBs, and in other supercon-

ducting qubits [51, 52, 53, 54]. We summarize the most relevant results about theoretical and experimental decoherence rates of the quantronium, following the treatment of Ithier *et al* [27]. These results will be used in the next chapter for designing a two-quantronium experiment.

The different sources S of decoherence acting in the quantronium are presented in Fig. 1.8. They induce quantum and classical noise in the external parameters λ entering Hamiltonian (1.3), i.e. N_g, $\delta/2\pi$ and E_J. The noise in N_g can be due to charged two-level fluctuators (TLFs) present in the substrate, in tunnel barriers of the CPB junctions, or at the surface of the device; another source of charge noise arises from the impedance of the gate line, assumed at thermal equilibrium. The δ phase noise can be due to fluctuations of the magnetic field threading the quantronium loop (possibly induced by moving magnetic vortices), and to bias current fluctuations produced by the impedance of the readout circuit. Additionally, fluctuations of the critical current I_0 of the readout junction could also induce δ noise. Finally, noise in E_J can be due to microscopic defects present in the CPB tunnel barriers that change slightly their critical current. Each of these sources generates a $\boldsymbol{\delta\lambda}_S = \boldsymbol{\lambda}_S - \langle\lambda\rangle$ noise[2] which is in most cases gaussian, and is characterized by a generalized quantum spectral density

$$\mathcal{S}_{S,\lambda}(\omega) = \frac{1}{2\pi}\int_{-\infty}^{+\infty} d\tau < \boldsymbol{\delta\lambda}_S(t)\boldsymbol{\delta\lambda}_S(t+\tau) > e^{i\omega\tau}. \tag{1.17}$$

This spectral density contains both the classical and quantum fluctuations of $\delta\lambda$, $S_{S,\lambda}(\omega > 0)$ and $S_{S,\lambda}(\omega < 0)$ corresponding to the absorption and emission of energy by the source S, respectively.
At thermal equilibrium, the contribution to N_g fluctuations from the gate line impedance $Z_g(\omega)$, as seen from the gate capacitance, is characterized by the spectral density [27]

$$\mathcal{S}_{S,\lambda}(\omega) = \kappa_g^2 \frac{\hbar^2\omega}{E_C^2}\frac{Re[Z_g(\omega)]}{R_k}\left[1 + \coth\left(\frac{\hbar\omega}{2k_BT}\right)\right], \tag{1.18}$$

where R_k is the quantum of resistance, $\kappa_g = C_g/C_\Sigma$. Microscopic N_g fluctuations (due to TLFs) were measured in previous quantronium experiment [27]. They were found to be characterized by a spectral density (see Fig. 1.9)

$$\mathcal{S}_{S,\lambda}(\omega) = A/\omega \text{ with } A \simeq 1.6\ 10^{-6}, \text{ for } \omega < 0.4 \text{ MHz}. \tag{1.19}$$

In the same way, at thermal equilibrium, the contribution to δ fluctuations from the readout line admittance $Y_R(\omega)$, as seen from the readout junction, is characterized by the spectral density [27]

[2] We use here a simplified notation $\boldsymbol{O}$ for operator $\widehat{O}$. The operator vector $\overrightarrow{\widehat{\sigma}}$ is noted $\overrightarrow{\boldsymbol{\sigma}}$

$$S_{\delta/2\pi}(\omega) = \frac{1}{64\pi^4}\frac{\hbar^2\omega}{2\pi\xi_J^2}R_k\frac{Re[Y_R(\omega)]}{|1+i2\pi\mathcal{L}_J Y_R(\omega)\omega|^2}\left[1+\coth\left(\frac{\hbar\omega}{2k_BT}\right)\right],$$

where $\xi_J = I_0\varphi_0$ and $\mathcal{L}_J = \varphi_0/I_0$ are Josephson energy and inductance of the readout junction, respectively . Besides, microscopic δ fluctuations [27] are characterized by the spectral density (see Fig. 1.9)

$$\mathcal{S}_{S,\lambda}(\omega) = A/\omega \text{ with } A = 11\ 10^{-8}, \text{ when } \omega < 0.1 \text{ MHz}. \tag{1.20}$$

Note that for dephasing (low frequencies) and relaxation ($\omega = \omega_{01}$), the $1+\coth\left(\frac{\hbar\omega}{2k_BT}\right)$ term in Eqs. (1.18) and (1.20) is equal to $2k_BT/\hbar\omega$ and 2, respectively.

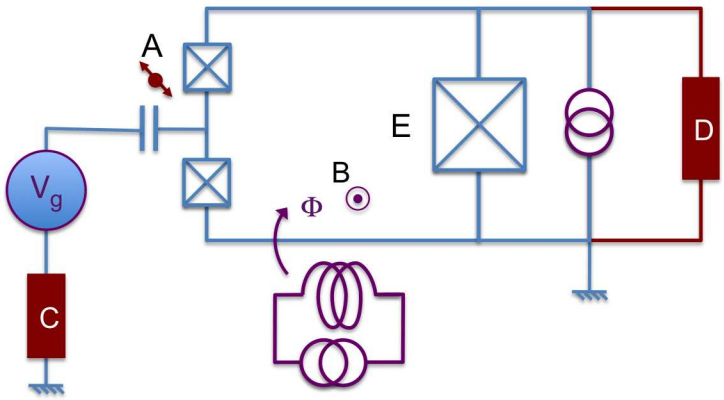

Fig. 1.8. Main decoherence sources in a quantronium device. Noise in N_g is generated by charged two-level fluctuators (A) in the vicinity of the island and by voltage fluctuations of series impedance (C) in the gate line. Noise in δ is generated by fluctuations in the flux ϕ (B), by current fluctuations in the finite impedance (D) of the readout bias source. Noise in E_J is induced by critical current fluctuations of the CPB junctions (E).

The spectral densities presented above enter the expressions of decoherence rates, which we derive now. When the coupling between the environment and the qubit is weak, the Hamiltonian

$$\boldsymbol{H} = -1/2\vec{\boldsymbol{\sigma}}.\overrightarrow{H(\lambda)} \tag{1.21}$$

can be expanded at first order for each external parameter λ. Each of the noise source S in λ yields a perturbation of the Hamiltonian

$$\boldsymbol{\delta H}_{\lambda,S} = -\frac{\hbar}{2}\left(\overrightarrow{D_\lambda}.\vec{\boldsymbol{\sigma}}\right)\boldsymbol{\delta\lambda}_S. \tag{1.22}$$

where $\overrightarrow{D_\lambda}.\overrightarrow{\boldsymbol{\sigma}}$ is the restriction of $-(2/\hbar)\partial \boldsymbol{H}/\partial\lambda$ to the $\{|0\rangle, |1\rangle\}$ Hilbert space. The longitudinal and transverse parts of $\overrightarrow{D_\lambda}$, i.e. $D_{\lambda,z}$ and $D_{\lambda,\perp}$ respectively, are thus

$$\begin{aligned} D_{N_g,z} &= -2\frac{E_C}{\hbar}\left(\langle 1|\,\widehat{N}\,|1\rangle - \langle 0|\,\widehat{N}\,|0\rangle\right) \\ D_{N_g,\perp} &= 4\frac{E_C}{\hbar}\left|\langle 0|\,\widehat{N}\,|1\rangle\right| \\ D_{\delta/2\pi,z} &= \frac{2\pi\varphi_0}{\hbar}\left(\langle 1|\,\widehat{I}\,|1\rangle - \langle 0|\,\widehat{I}\,|0\rangle\right) \\ D_{\delta/2\pi,\perp} &= \frac{4\pi\varphi_0}{\hbar}\left|\langle 0|\,\widehat{I}\,|1\rangle\right|. \end{aligned} \tag{1.23}$$

Relaxation rates

Following Fermi's golden rule, one finds the relaxation rate

$$\Gamma^{rel}_{S,\lambda} = \frac{1}{T_1} = \frac{\pi}{2}|D_{\lambda,\perp}|^2 \mathcal{S}_{S,\lambda}(\omega = \omega_{01}), \tag{1.24}$$

where T_1 is the relaxation time. At finite temperature, the qubit relaxation and excitation rates follow the detailed balance.
In the Quantronium circuit, when the asymmetry d is zero, the first derivative $\partial H/\partial\delta$ vanishes at $\delta = 0$, and one has to take into account the second derivative $\partial^2 H/\partial\delta^2$ (which does not depend on d) to evaluate the relaxation. In this case, relaxation involves the absorption by the environment of two photons $h\nu_1$ and $h\nu_2$, such that $\nu_1 + \nu_2 = \nu_{01}$. The corresponding rate is given by [55]

$$\Gamma^{rel}_{S,\delta} = |D^{(2)}_{\lambda\perp}|^2 \int_{\omega=0}^{\omega_{01}} \mathcal{S}_{S,\delta}(\omega)\mathcal{S}_{S,\delta}(\omega_{01} - \omega)d\omega, \tag{1.25}$$

where

$$\begin{aligned} D^{(2)}_{\delta,\perp} &= -1/\hbar|\,\langle 0|\,\frac{\partial^2 \widehat{H}}{\partial\delta^2}\,|1\rangle\,| \\ &= -\pi/(h\varphi_0^2)|\,\langle 0|\,\frac{1}{\widehat{L}}\,|1\rangle\,| \end{aligned} \tag{1.26}$$

Dephasing rates

When the noise is regular at low frequency, $\left\langle e^{i\varphi}\right\rangle$ decays exponentially with a pure dephasing rate

$$\Gamma^{\varphi}_{S,\lambda} = \frac{1}{T_\varphi} = \pi D^2_{\lambda,z} S_{S,\lambda}(\omega = 0), \tag{1.27}$$

with T_φ the pure dephasing time.

In the case of a singular spectral density of the form $A/|\omega|$ for $\omega \in [\omega_{ir}, \omega_{uv}]$ and zero elsewhere, the decay of the phase factor is gaussian:

$$\left\langle e^{i\varphi} \right\rangle (t) = e^{-t^2 D_{\lambda,z}^2 \frac{<\delta\lambda^2>}{2}}. \tag{1.28}$$

The dephasing time T_φ is in this case defined as the time after which $\left\langle e^{i\varphi} \right\rangle$ has decayed by a factor $1/e$. Furthermore, two cases have to be distinguished: the static case, where ω_{uv} is below the decoherence rate and the parameter λ can be considered as constant during T_φ, and the non static-case, where λ fluctuates during T_φ [50, 56, 57]. For the static case,

$$< \delta\lambda^2 >= 2A \ln\left(\frac{\omega_{uv}}{\omega_{ir}}\right), \tag{1.29}$$

and

$$T_{\varphi,\lambda} = \frac{1}{|D_{\lambda,z}| \sqrt{A \ln\left(\frac{\omega_{uv}}{\omega_{ir}}\right)}}. \tag{1.30}$$

At the working point $\{N_g = 1/2[\mod 1], \delta = 0[\mod 2\pi]\}$, $D_{N_g,z}$ and $D_{\delta/2\pi,z}$ vanishes. The dephasing rate is thus minimum, which makes this point optimal to operate a split CPB, as demonstrated in the first quantronium experiment [16]. At the optimal point, dephasing is governed by the second order contribution $\partial^2\omega_{01}/\partial\lambda^2$ in the expansion of $H(\lambda)$. The decay of $\left\langle e^{i\varphi} \right\rangle$ is then not universal. The static approximation yields to

$$\begin{aligned} |\left\langle e^{i\varphi} \right\rangle (t)|^{lf} &= \left| \frac{1}{\sqrt{1 - i\frac{\partial^2\omega_{01}}{\partial\lambda^2}\sigma_{\delta\lambda}^2 t}} \right| \\ &= \left\{ 1 + \left[\frac{\partial^2\omega_{01}}{\partial\lambda^2} tA \ln(1/\omega_{ir}t) \right]^2 \right\}^{-1/4} \end{aligned} \tag{1.31}$$

and

$$T_{\varphi,N_g}^{lf} = \frac{7.2}{2\frac{\partial^2\omega_{01}}{\partial N_g^2} A \ln(1/\omega_{if}T_\varphi)}. \tag{1.32}$$

In the non-static case, for time $t >> [(\partial^2\omega_{01}/\partial\lambda^2)A/2]^{-1}$, the high-frequency contributions dominate the decay, and one has [17]

$$|\left\langle e^{i\varphi} \right\rangle (t)|^{hf} = e^{-\frac{\pi}{2}\frac{\partial^2\omega_{01}}{\partial\lambda^2}At} \tag{1.33}$$

and

$$T_{\varphi,\lambda}^{hf} = \frac{1}{\frac{\pi}{2}\frac{\partial^2\omega_{01}}{\partial\lambda^2}A}, \tag{1.34}$$

provided $[\pi(\partial^2\omega_{01}/\partial\lambda^2)A]^{-1} >> 1/\omega_c$.

Figure 1.9 shows the measured coherence times [27] that are compared to the above theoretical expressions. These results as well as measurements obtained on other sCPBs show that for E_J/E_C ratios corresponding to regimes 1 and 2 (see Fig. 1.2), decoherence at the optimal point is clearly limited by charged TLFs. In the case of the quantronium sample of Ithier *et al* [27], relaxation was attributed at least partly to the gate line impedance , whereas the NEC group [45] attributed it in their samples to energy exchange between the CPB and charged TLFs.
Recent experiment made at Yale [47, 46] with symmetrized CPBs in the regime $E_J/E_C >> 1$ (regime 3 of Fig. 1.2) and embedded in microwave resonators have demonstrated that the contribution of dephasing to decoherence can be made small compared to that of relaxation.

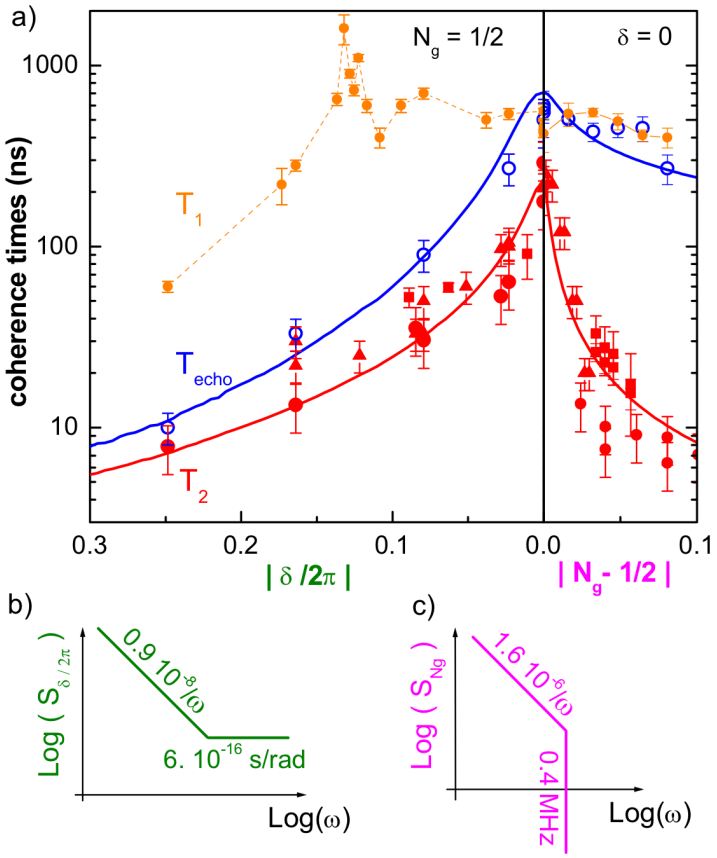

Fig. 1.9. a) Relaxation time T_1 (orange), echo time T_E (blue - see Annex 1) and coherence time T_2 (red) measured in a quantronium sample during G. Ithier's thesis [17]. Dots are measured data while solid lines are theoretical fits using the expressions presented in this section. Fitting parameters are detailed in [27]. The dashed orange line is only a guide for the eyes. b) Charge and phase noise spectral densities resulting from the fit. Note that the spectra are even functions of ω.

1.2 A two quantronium gate: the Quantroswap

Implementing a quantum algorithm corresponding to an arbitrary unitary evolution requires adding to single qubit gates at least one two-qubit gate, such that the ensemble forms a so-called "universal" set of quantum gates [23]. While any two-qubit gate that entangles two qubits can be considered universal, the most convenient ones are those which fully entangle them. The most well-known examples are the Controlled-Phase gate, the CNOT gate, and the $\sqrt{ISWAP}$ gate. Contrarily to the CNOT, which can be characterized by a truth table as a classical logical gate, $\sqrt{ISWAP}$ has no classical analogue. It is obtained by operating a swapping interaction during half the time needed for a complete exchange of an energy quantum between the two qubits. This gate transforms the computational basis $\{|00\rangle, |01\rangle, |10\rangle, |11\rangle\}$ into the Bell state basis $\{|00\rangle, (|01\rangle - |10\rangle)/\sqrt{2}, (|01\rangle + |10\rangle)/\sqrt{2}, |11\rangle\}$, which demonstrates its entangling character.
Different strategies have been developed to couple two superconducting qubits. The first implementation [58] was demonstrated at NEC in 2003. It was a CNOT gate with two capacitively coupled CPBs in the charge regime, driven by fast trapezoidal gate pulses. The truth table was measured, but the lack of single shot readout hindered the observation of correlations between the two final qubit states and the characterization of the gate operator. Then, several groups initiated a big effort on different Josephson qubits in order to demonstrate a gate in a two-qubit circuit fitted with single shot readout. The present work is part of this effort, focusing here on an ISWAP gate with two quantronium qubits. Two groups have published results on such two qubit circuits during the recent years:

- The complete tomography [59, 60] of coupled phase qubits was obtained in J. Martinis'group at U.C.S.B. in 2006. The capacitive coupling between the qubits induces the SWAP operation between the qubits. The correlations between the two interacting qubits were demonstrated. The fidelity for the production of Bell states was determined at $F = 0.87$ by performing the state tomography of the entangled qubits after operation of the $\sqrt{ISWAP}$ gate.
- A CNOT gate was demonstrated on flux qubits in 2007, in H. Mooij's group [61] at T.U. Delft. The gate fidelity was determined at about $F = 0.4$, but the reduced readout fidelity hindered to perform the full gate tomography. These two works have used a fix coupling between the qubits. Although, the effective coupling can generally be tuned by changing the difference between the qubit frequencies, it is highly desirable to change or switch on/off the coupling without changing the qubit frequencies, by using a tunable coupler. Such couplers have been demonstrated:
  - with CPB qubits coupled by a Josephson junction [62, 63] or by a microwave coplanar resonator [30];
  - with flux qubits coupled by a SQUID [64, 65];

- and with phase qubits coupled by a resonator[66].

We present in this section the circuit we have designed for operating a $\sqrt{ISWAP}$ gate. It consists of two quantroniums coupled by a fixed capacitor, and is nicknamed quantroswap. We first derive its Hamiltonian, then discuss how to operate a gate, and address the issue of simultaneous readout of the qubits.

1.2.1 The two quantronium circuit and its Hamiltonian

As shown on Fig. 1.10, the quantroswap is based on two quantroniums labelled A and B whose islands are capacitively coupled. Each CPB is connected to its own voltage source $V_{g_{A,B}}$ through its gate capacitances $C_{g_{A,B}}$, and has its own readout junction. Experimentally, the magnetic flux is produced by a macroscopic coil above the circuit that induces the same flux Φ through each loop. Thus, using the usual sign convention for voltages, currents and superconducting phase differences (see Fig. 1.10), the phases and the flux are related by $\delta_A = \gamma_A + \Phi/\varphi_0$ and $\delta_B = \gamma_B - \Phi/\varphi_0$.

The Hamiltonian of the system can be calculated following the method proposed by B.Yurke [67] and developed in [68, 69]. We briefly summarize it now. Starting from Kirchoff's laws, which play the role of the equations of motions for the electrical variables, one determines the Lagrangian. The Hamiltonian is then derived from this Lagrangian. One has first to analyse the topology of the circuit in terms of a spanning tree, i. e. a minimum set of circuit branches XY (between two nodes X and Y) connecting ground to all the other nodes X (without using twice the same branch). The number of degrees of freedom of the circuit is the number of branches in the tree, not counting those with a voltage or a current source. Each branch XY is characterized by its voltage v_{XY} and its current i_{XY}. One defines the generalized branch fluxes

$$\Phi_{XY}(t) = \int_{-\infty}^{t} v_{XY}(t')dt', \tag{1.35}$$

and the branch charges

$$Q_{XY}(t) = \int_{-\infty}^{t} i_{XY}(t')dt'. \tag{1.36}$$

A branch with a capacitor C is characterized by the constitutive relation $\dot{\Phi}_{XY} = Q_{XY}/C$, whereas a branch with an inductor L is characterized by $\dot{Q}_{XY} = \Phi_{XY}/L$. For a Josephson junction with critical current I_0, the constitutive relation is the Josephson relation $\dot{Q}_{XY} = I_0 \sin\theta$, with θ the jauge invariant superconducting phase difference across the junction. The second

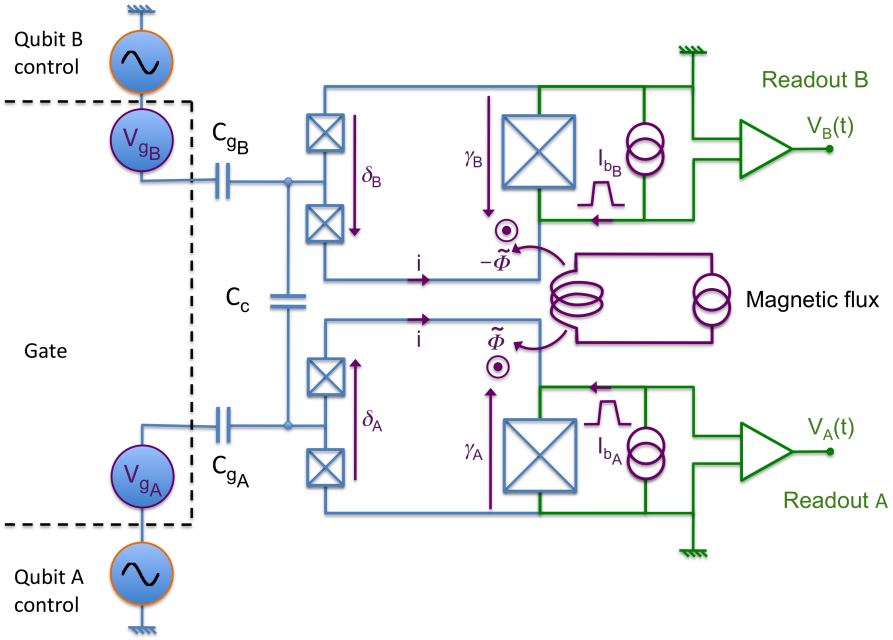

Fig. 1.10. Simplified diagram of the Quantroswap circuit with 2 quantroniums whose islands are capactively coupled. Each qubit has its own gate and readout. The fluxes through the loops are applied using the same coil and have consequently opposite signs, considering the orientation of the different phases, voltages and loop current.

Josephson relation $V = \varphi_0 \dot{\theta}$ (with V the voltage across the junction) and our definition 1.35 lead to

$$\dot{Q}_{XY} = I_{0_{XY}} \sin\left(\frac{\Phi_{XY}}{\varphi_0} + cst\right). \tag{1.37}$$

A branch with a current source i is modeled as an infinite reservoir of flux Φ_{XY} (infinite inductance $L = \Phi_{XY}/i$), whereas a branch with a voltage source v is modeled as an infinite reservoir of charge Q_{XY} (infinite capacitance $C = Q_{XY}/v$). We also introduce node fluxes ϕ_X, which are equal to the sum of all tree branch fluxes going from ground to node X; similarly, we define node charges q_X equal to the sum of the charges brought by all branches reaching the node X.

In Annex A, we apply this method to show that a single quantronium can be replaced by a basic CPB with effective Josephson energy $E^*_{J_{A,B}}$, capacitance C_J, and island phase

$$\theta^*(d_{A,B}, \pm\tilde{\Phi}, \gamma) = \theta_{A,B} + \zeta(d_{A,B}, \pm\tilde{\Phi}, \gamma_{A,B}), \tag{1.38}$$

as introduced in section 1.1.2.
Then, we apply the method to the quantroswap circuit shown in Fig. 1.11, which has four nodes M,N,P,Q. Since all of these nodes are connected to ground by only one branch, node fluxes ϕ_X are equal to branch fluxes $\Phi_{XGround}$. As P and Q are connected to ground through voltage sources, the system has only two degrees of freedom, which we take as the node fluxes ϕ_M and ϕ_N (and their conjugate variables, the corresponding nodes charges q_M and q_N).

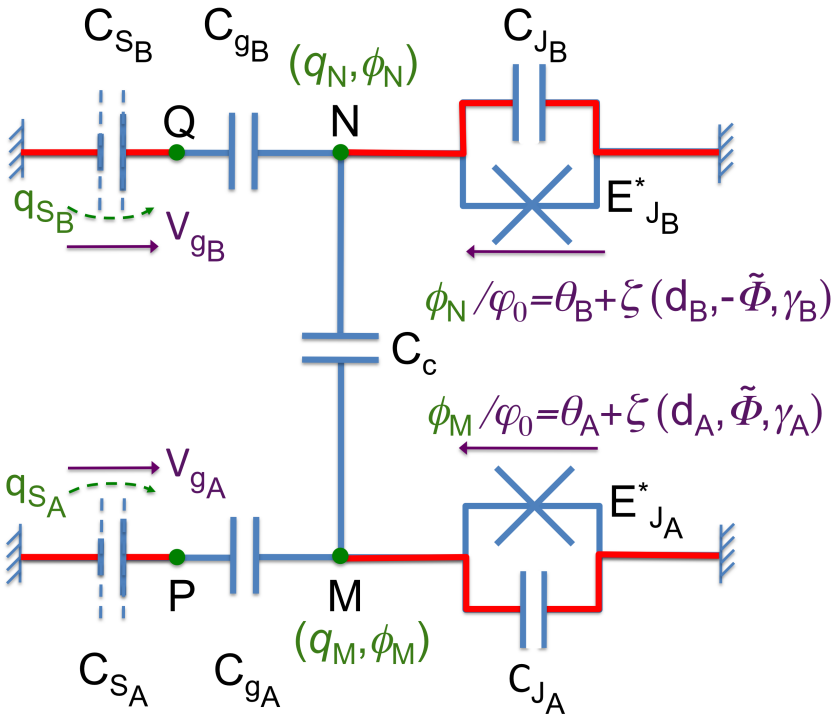

Fig. 1.11. Model electrical circuit of the quantroswap: the chosen spanning tree leading to the four M,N,P,Q nodes is indicated in red. The two couples $\{q_M, \phi_M\}$ $\{q_N, \phi_N\}$ of conjugated node variables chosen as the degrees of freedom of the system are shown. The voltage sources $V_{g_{A,B}}$ are modeled by infinite capacitor $C_{S_{A,B}}$ having delivered a charge $q_{S_{A,B}}$.

Using these definitions, one writes the Kirchhoff's current law at all nodes.

$$
\begin{aligned}
\text{Node M:}\quad & C_{J_A}\ddot{\phi}_M + C_c\left(\ddot{\phi}_M - \ddot{\phi}_N\right) + C_{g_A}\left(\ddot{\phi}_M - \ddot{\phi}_P\right) \\
& \qquad -I_{0_A}\sin\left(\tfrac{\phi_M}{\varphi_0} - \zeta_A\right) = 0 \\
\text{Node N:}\quad & C_{J_B}\ddot{\phi}_B + C_c\left(\ddot{\phi}_N - \ddot{\phi}_M\right) + C_{g_B}\left(\ddot{\phi}_N - \ddot{\phi}_Q\right) \\
& \qquad -I_{0_B}\sin\left(\tfrac{\phi_N}{\varphi_0} - \zeta_B\right) = 0 \qquad (1.39) \\
\text{Node P:}\quad & C_{g_A}\left(\ddot{\phi}_P - \ddot{\phi}_M\right) + \partial(C_{S_A}\dot{\phi}_P)/\partial t \qquad = 0 \\
\text{Node Q:}\quad & C_{g_B}\left(\ddot{\phi}_Q - \ddot{\phi}_N\right) + \partial(C_{S_B}\dot{\phi}_Q)/\partial t \qquad = 0
\end{aligned}
$$

Here we have used the simplified notation $\zeta_{A,B} = \zeta_{A,B}(d_{A,B}, \pm\tilde{\Phi}, \gamma_{A,B})$. These equations of motion take the form of Euler-Lagrange equations

$$
\frac{\partial \mathcal{L}}{\partial \phi} = \frac{\partial}{\partial t}\frac{\partial \mathcal{L}}{\partial \dot{\phi}} \text{ with } \dot{\phi} = \frac{\partial \phi}{\partial t}, \tag{1.40}
$$

associated to the Lagrangian

$$
\begin{aligned}
\mathcal{L} = & \frac{C_{J_A}}{2}\dot{\phi}_M^2 + \frac{C_{J_B}}{2}\dot{\phi}_N^2 + \frac{C_c}{2}\left(\dot{\phi}_M - \dot{\phi}_N\right)^2 \\
& + \frac{C_{g_A}}{2}\left(\dot{\phi}_M - \dot{\phi}_P\right)^2 + \frac{C_{g_B}}{2}\left(\dot{\phi}_N - \dot{\phi}_Q\right)^2 \\
& + \int_{-\infty}^{t} C_{S_A}\dot{\phi}_P d\dot{\phi}_P + \int_{-\infty}^{t} C_{S_B}\dot{\phi}_Q d\dot{\phi}_Q \qquad (1.41) \\
& - \int_{-\infty}^{t} I_{0_A}\sin\left(\frac{\phi_M}{\varphi_0} - \zeta_A\right) d\phi_M - \int_{-\infty}^{t} I_{0_B}\sin\left(\frac{\phi_N}{\varphi_0} - \zeta_B\right) d\phi_N.
\end{aligned}
$$

This Lagrangian is the difference between the electrostatic energy stored on all capacitors ("kinetic" energy), and the magnetic energy of all inductive elements ("potential" energy). Using the definitions (1.38) of Josephson inductances $L_{J_{A,B}}$, the last terms in (1.41) are

$$
\int_{-\infty}^{t} I_{0_{A,B}}\sin\left(\frac{\phi_{M,N}}{\varphi_0} - \zeta_{A,B}\right) d\phi_{M,N} = -E^*_{J_{A,B}}\cos\left(\frac{\phi_{M,N}}{\varphi_0} - \zeta_{A,B}\right) \tag{1.42}
$$

Besides, after introducing the charges $q_{S_{A,B}}$ passed through the voltage sources to the gate capacitor $C_{g_{A,B}}$ since $t = -\infty$, taking the limit $Q_{S_{A,B}} \to \infty$, and using the constitutive relation for capacitors, the terms of third lines in Eq. (1.41) become

$$
\int_{-\infty}^{t} C_{S_{A,B}}\dot{\phi}_{P,Q} d\dot{\phi}_{P,Q} = \frac{1}{2C_{S_{A,B}}}\left[(C_{S_{A,B}}\dot{\phi}_{P,Q})^2\right]_{Q_{S_{A,B}}}^{Q_{S_{A,B}}+q_{S_{A,B}}} = V_{g_{A,B}} q_{S_{A,B}}.
$$

Using Eq. (1.39) at node P and Q, one has also

$$q_{S_{A,B}} = C_{g_A}\left(\dot{\phi}_{M,N} - \dot{\phi}_{P,Q}\right).$$

The Lagrangian (1.41) can be re-expressed as

$$\begin{aligned}\mathcal{L} = &\frac{C_{\Sigma A}}{2}\dot{\phi}_M^2 + \frac{C_{\Sigma B}}{2}\dot{\phi}_N^2 - \frac{C_{g_A}}{2}\dot{\phi}_P^2 - \frac{C_{g_B}}{2}\dot{\phi}_Q^2 - C_c\dot{\phi}_M\dot{\phi}_N \\ &+E^*_{J_A}\cos\left(\frac{\phi_M}{\varphi_0} - \zeta_A\right) + E^*_{J_B}\cos\left(\frac{\phi_N}{\varphi_0} - \zeta_B\right).\end{aligned} \tag{1.43}$$

where $C_{\Sigma_{A,B}} = C_{J_{A,B}} + C_{g_{A,B}} + C_c$.
By subtracting $C_{g_A}\dot{\phi}_P\dot{\phi}_M + C_{g_B}\dot{\phi}_Q\dot{\phi}_N$, $\mathcal{L}$ can be transformed in an equivalent Lagrangian

$$\begin{aligned}\mathcal{L}' = &\frac{C_{\Sigma_A}}{2}\dot{\phi}_M^2 + \frac{C_{\Sigma_B}}{2}\dot{\phi}_N^2 - \frac{C_{g_A}}{2}V_{g_A}^2 - \frac{C_{g_B}}{2}V_{g_B}^2 \\ &-C_c\dot{\phi}_M\dot{\phi}_N - C_{g_A}V_{g_A}\dot{\phi}_M - C_{g_B}V_{g_B}\dot{\phi}_N \\ &+E^*_{J_A}\cos\left(\frac{\phi_M}{\varphi_0} - \zeta_A\right) + E^*_{J_B}\cos\left(\frac{\phi_N}{\varphi_0} - \zeta_B\right)\end{aligned} \tag{1.44}$$

that lets the equations Eq. (1.39) unchanged. $\mathcal{L}'$ is now explicitly the Lagrangian of a two degree of freedom system with time independent sources. The Lagrange conjugation relations yield the node charge

$$q_{M,N} = \frac{\partial\mathcal{L}'}{\partial\dot{\phi}_{M,N}} = C_{\Sigma_{A,B}}\dot{\phi}_{M,N} - C_c\dot{\phi}_{N,M} - C_{g_{A,B}}V_{g_{A,B}} \tag{1.45}$$

and to the Hamiltonian

$$H = \sum_{i=\{M,N\}} q_i\dot{\phi}_i - \mathcal{L}' =$$

$$\begin{aligned}= &\frac{1}{2}C_{\Sigma_A}\dot{\phi}_M^2 + \frac{1}{2}C_{\Sigma_B}\dot{\phi}_N^2 + \frac{1}{2}C_{g_A}V_{g_A}^2 + \frac{1}{2}C_{g_B}V_{g_B}^2 - C_c\dot{\phi}_M\dot{\phi}_N \\ &-E^*_{J_A}\cos\left(\frac{\phi_M}{\varphi_0} - \zeta_A\right) - E^*_{J_B}\cos\left(\frac{\phi_N}{\varphi_0} - \zeta_B\right).\end{aligned} \tag{1.46}$$

We now switch from the conjugate variables $\{q_{M,N}, \phi_{M,N}\}$ to the conjugate superconducting variables

$$\{N_{A,B} = q_{M,N}/2e, \theta^*_{A,B} = \frac{\phi_{M,N}}{\varphi_0} - \zeta_{A,B}\}: \tag{1.47}$$

equation B.3

$$\begin{bmatrix} -2eN_A + C_{g_A}\dot{\phi}_C \\ -2eN_B + C_{g_B}\dot{\phi}_Q \end{bmatrix} = \begin{bmatrix} C_{\Sigma_A} & -C_c \\ -C_c & C_{\Sigma_B} \end{bmatrix}\begin{bmatrix} \dot{\phi}_M \\ \dot{\phi}_N \end{bmatrix}.$$

Inverting this system, one obtains

$$\begin{aligned}
\dot{\phi}_M &= \alpha\frac{1}{C_{\Sigma_A}}\left[(-2eN_A + C_{g_A}V_{g_A}) + \frac{C_c}{C_{\Sigma_B}}(-2eN_B + C_{g_B}V_{g_B})\right] \\
&= \alpha\frac{-2e}{C_{\Sigma_A}}\left[(N_A - N_{g_A}) + \frac{C_c}{C_{\Sigma_B}}(N_B - N_{g_B})\right] \\
\dot{\phi}_N &= \alpha\frac{1}{C_{\Sigma_B}}\left[(-2eN_B + C_{g_B}V_{g_B}) + \frac{C_c}{C_{\Sigma_A}}(-2eN_A + N_{g_A})\right] \\
&= \alpha\frac{-2e}{C_{\Sigma_B}}\left[(N_B - N_{g_B}) + \frac{C_c}{C_{\Sigma_A}}(N_A - N_{g_A})\right]
\end{aligned} \tag{1.48}$$

with $\alpha = 1/(1 - C_{cc}^2/(C_{\Sigma a}C_{\Sigma b}))$ and $N_{g_{A,B}} = C_{g_{A,B}}V_{g_{A,B}}/2e$.
Substituting Eq. in Eq. (1.46), we finally obtain

$$\begin{aligned}
\widehat{H} &= E_{\Sigma_A}(\widehat{N_A} - N_{g_A})^2 - E_{J_A}^* \cos\left(\widehat{\theta_A^*}\right) \\
&+ E_{\Sigma_B}(\widehat{N_B} - N_{g_B})^2 - E_{J_B}^* \cos\left(\widehat{\theta_B^*}\right) \\
&+ 2\frac{E_{\Sigma_A}E_{\Sigma_B}}{E_{cc}}(\widehat{N_A} - N_{g_A})(\widehat{N_B} - N_{g_B}) \\
&+ \frac{C_{g_A}}{2}V_{g_A}^2 + \frac{C_{g_B}}{2}V_{g_B}^2
\end{aligned} \tag{1.49}$$

with

$$\begin{aligned}
E_{\Sigma a} &= \alpha(2e)^2/2C_{\Sigma_A}, \\
E_{\Sigma b} &= \alpha(2e)^2/2C_{\Sigma_B}, \\
E_{cc} &= \alpha(2e)^2/2C_c.
\end{aligned}$$

Note that as junction capacitances C_J are in general much larger than gate and coupling capacitances, $\epsilon = \alpha - 1 = C_{cc}^2/(C_{\Sigma_A}C_{\Sigma_B}) << 1$. The Hamiltonian (1.49) reads as the sum of the Hamiltonian of both qubits (with a charging energy slightly renormalized by the presence of the other qubit) and of a coupling term proportional to $(\widehat{N_A} - N_{g_A})(\widehat{N_B} - N_{g_B})$. Physically, each qubit can behave as an extra gate for the other qubit. Indeed the charge stored on an island plays for the other island exactly the same role as its own gate charge.

When restricting the Hilbert space to the space spanned by the uncoupled basis ($|00>, |01>, |10>$, and $|11>$), the Hamiltonian (1.49) simplifies:

$$\begin{aligned}
\widehat{H_0} = &\frac{h}{2}\nu_A(N_{g_A}, \delta_A)\widehat{\sigma}_{z_A} + \frac{h}{2}\nu_B(N_{g_B}, \delta_B)\widehat{\sigma}_{z_B} \\
&+2\frac{E_{\Sigma_A}E_{\Sigma_B}}{E_{cc}}(\widehat{N_A} - N_{g_A})(\widehat{N_B} - N_{g_B})
\end{aligned} \tag{1.50}$$

with $\nu_{A,B}$ the qubit frequencies.
At the charge degeneracy point $N_{g_{A,B}} = 1/2$, where decoherence is minimum, the Hamiltonian reduces to

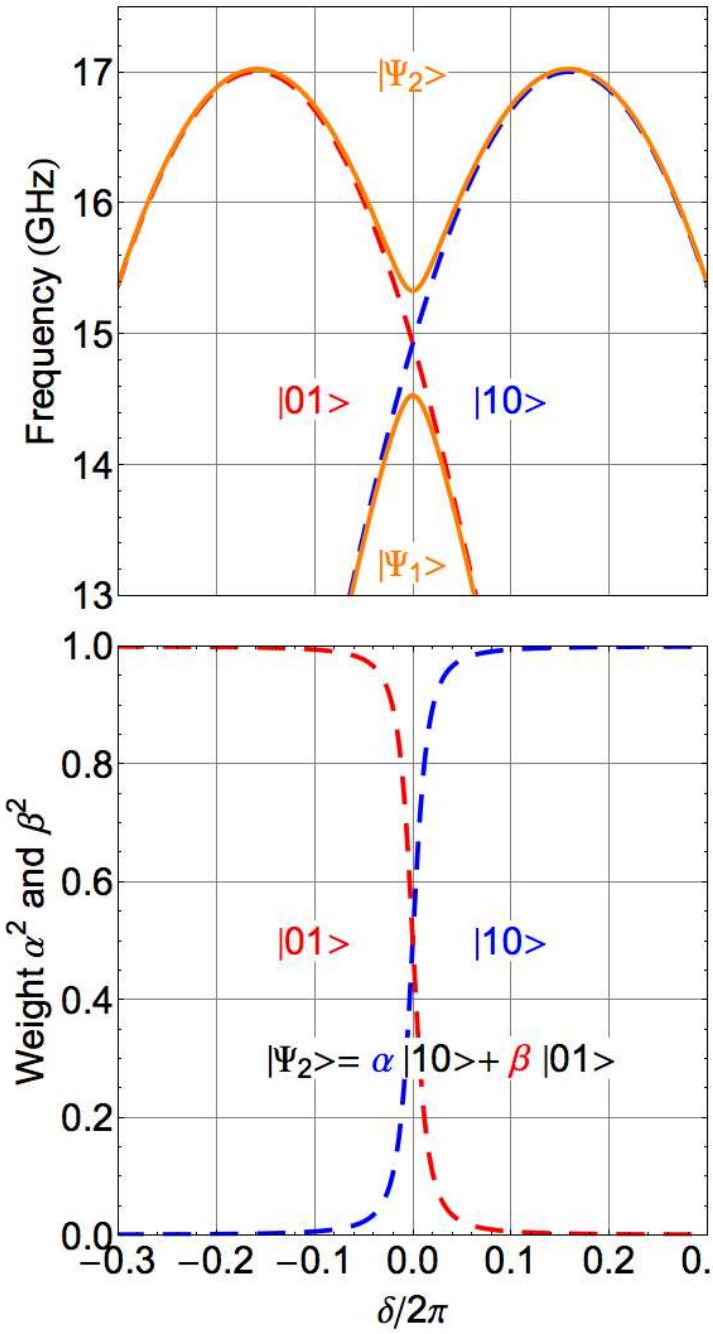

Fig. 1.12. Eigenenergies and eigenstates of two coupled quantroniums. a): Transition frequencies $\nu_{A,B}$ of the qubit A and B alone, and transition frequencies ν_{Φ_0,Φ_1} ν_{Φ_0,Φ_2} of the coupled system as a function of δ with $\nu_A = \nu_B = 17$GHz, $E_{J_A}/E_{C_A} = E_{J_B}/E_{C_B} = 1.9$, $\nu_{cc} = 800$MHz and a phase difference $\delta_A - \delta_B = 2$rad. b): Weights α^2 (blue) and β^2 (red) of $|\Psi_2\rangle = \alpha\,|10\rangle + \beta\,|01\rangle$ with respect to δ.

$$\frac{2}{h}\widehat{H_0} = \nu_A(N_{g_A} = 1/2, \delta_A)\widehat{\sigma}_{z_A} + \nu_B(N_{g_B} = 1/2, \delta_B)\widehat{\sigma}_{z_B} + \nu_{cc}\widehat{\sigma}_{x_A}\widehat{\sigma}_{x_A}. \quad (1.51)$$

where $\nu_{cc} = 4\left|< 0|\widehat{N_A}|1 >< 1|\widehat{N_B}|0 >\right| E_{\Sigma_A}E_{\Sigma_B}/hE_{cc}$ is the coupling frequency between the qubits.
In the uncoupled basis mentioned above, the matrix representation of $\widehat{H_0}$ is

$$\widehat{H}_0 = \frac{h}{2}\begin{bmatrix} -(\nu_A+\nu_B) & & & \nu_{cc} \\ & \nu_B-\nu_A & \nu_{cc} & \\ & \nu_{cc} & -\nu_B+\nu_A & \\ \nu_{cc} & & & \nu_B+\nu_A \end{bmatrix} = \frac{h}{2}\begin{bmatrix} -\nu & & & \nu_{cc} \\ & -\Delta\nu & \nu_{cc} & \\ & \nu_{cc} & \Delta\nu & \\ \nu_{cc} & & & \nu \end{bmatrix}.$$

with $\nu = \nu_A + \nu_B$, $\Delta\nu = \nu_A - \nu_B$, and where missing elements are zeroes.
The physical meaning of this Hamiltonian is enlightened by re-expressing it in the frame rotating around z_b at frequency ν_B:

$$\begin{aligned}\widehat{H_0'} &= \frac{h}{2}\nu_A\widehat{\sigma}_{z_A} + \nu_{cc}\widehat{\sigma}_{x_A}e^{\imath\pi\nu_B\widehat{\sigma}_{z_B}t}\widehat{\sigma}_{x_B}e^{-\imath\pi\nu_B\widehat{\sigma}_{z_B}t} \\ &= \frac{h}{2}\nu_A\widehat{\sigma}_{z_A} + \left(\nu_{cc}\widehat{\sigma}_{x_B}e^{-\imath 2\pi\nu_B\widehat{\sigma}_{z_B}t}\right)\widehat{\sigma}_{x_A}. \end{aligned} \quad (1.52)$$

The last term in Eq. (1.52) is similar to an RF excitation of qubit A with a driving field being an operator of qubit B oscillating at frequency ν_B (see section 1.1.3): as in a Rabi precession, when ν_B is close to ν_A, the qubit A precesses at the coupling frequency ν_{cc}. As explained in the next section, the main difference is that the excitation field is not a coherent field but a spin [70].
From Hamiltonian (1.51), one calculates the eigenenergies E_i and the corresponding eigenstates $|\Psi_i\rangle$ in the uncoupled basis:

$$\begin{aligned} E_0 &= -\frac{h\nu}{2}\sqrt{1+r} \\ E_1 &= -\frac{h\nu_{cc}}{2}\sqrt{1+s^2} \\ E_2 &= \frac{h\nu_{cc}}{2}\sqrt{1+s^2} \\ E_3 &= \frac{h\nu}{2}\sqrt{1+r} \end{aligned} \quad (1.53)$$

$$\begin{aligned} |\Psi_0\rangle &= \{-\frac{1+\sqrt{1+r^2}}{r}, 0, 0, 1\} \\ |\Psi_1\rangle &= \{0, s-\sqrt{1+s^2}, 1, 0\} \\ |\Psi_2\rangle &= \{0, s+\sqrt{1+s^2}, 1, 0\} \\ |\Psi_3\rangle &= \{-\frac{1-\sqrt{1+r^2}}{r}, 0, 0, 1\}. \end{aligned} \quad (1.54)$$

with $r = \nu_{cc}/\nu$ and $s = \Delta\nu/\nu_{cc}$.
In the regime where $\nu_{cc}/\nu << 1$, the eigenstates Ψ_0 and Ψ_3 are close to states $|00\rangle$ and $|11\rangle$.
As an example Figure 1.12 shows the eigenenergies of the system with respect to δ for $\nu_{cc} = 800$ MHz, when the two qubits have a phase difference $\delta_A - \delta_B = 2$ rad. When both qubits have exactly the same energies ($\Delta\nu = 0$), the degeneracy of the $|01\rangle$ and $|10\rangle$ levels is lifted by the coupling, and the two eigenstates $|\Psi_1\rangle = \{0, -1, 1, 0\}$ and $|\Psi_2\rangle = \{0, 1, 1, 0\}$ are two maximally entangled states. As shown in the inset of Fig. 1.12, away from $\delta = 0$, s increases and the eigenstates tend to be the eigenstates of the uncoupled system.
Thus, the frequency difference between the two qubits acts as the parameter which controls the coupling between the two qubits: in principle, even if the coupling is fixed, one can define a tunable effective coupling term s between states $|10\rangle$ and $|01\rangle$.

1.2.2 Coherent manipulation of the quantroswap and two qubit gates

Depending on the coupling strength ν_{cc}, the quantroswap circuit can be regarded either as an artificial molecule; whose discrete energy levels can be directly addressed, or as a system of two artificial atoms sufficiently weakly coupled to be manipulated independently. More precisely, these two cases correspond to $\nu_{cc}\sqrt{1+s^2}$ being larger or smaller than the maximum Rabi frequency $\nu_{r\ \max}$, respectively.
In the latter case, different strategies have been proposed to implement two-qubit logic gates. The simplest one consists in bringing the two qubits close to resonance. Unless one is able to fabricate two quantroniums with the very same parameters, this method requires moving at least one qubit away from its optimal working point, which is detrimental to coherence. An alternative strategy consists in keeping the two quantroniums at their respective optimal points, and in inducing an effective coupling by AC driving both qubits.
In this section, we first explain how to address the "molecular" energy levels of two quantroniums strongly coupled; then we present two different two-qubit gates made up of two quantroniums in or out of resonance.

1.2.2.1 Addressing the energylevels of the molecule

When $\nu_{cc}\sqrt{1+s^2} >> \nu_r$, one can only address the energy levels of the whole two-qubit molecule. This can be done by driving resonantly a molecular transition from any side of the "molecule", i.e. through gate A and/or B.
Let us consider first the case of the transition between the ground state Φ_0 and the first "molecular" state Φ_1, excited through gate B with a signal $\Delta N_{g_B} = \Delta N_{g_{B0}} \cos(2\pi\nu_{\mu w}t + \varphi_B)$ with $\nu_{\mu w} = (E_1 - E_0)/h = \nu(1 - r\sqrt{1+s^2})/2$. In the coupled (molecular) basis (1.53), the Hamiltonian (1.49) writes

$$\frac{2}{h}\widehat{H} = \nu_A\widehat{\sigma}_{z_A} + \nu_B\widehat{\sigma}_{z_B} + \nu_{cc}\widehat{\sigma}_{x_A}\widehat{\sigma}_{x_B} + 2\nu_{r_B}\cos(2\pi\nu_{\mu w}t + \phi)\,\widehat{\sigma}_{x_B}, \tag{1.55}$$

which gives in the rotating wave approximation

$$\frac{2}{h}\widehat{H} = \begin{pmatrix} -\nu & \alpha(s)\tilde{\nu}^*_{r_B} & \beta(s)\tilde{\nu}^*_{r_B} & 0 \\ \alpha(s)\tilde{\nu}_{r_B} & -\nu_{cc}\sqrt{1+s^2} & 0 & \alpha(s)\tilde{\nu}^*_{r_B} \\ \beta(s)\tilde{\nu}_{r_B} & 0 & \nu_{cc}\sqrt{1+s^2} & \beta(s)\tilde{\nu}^*_{r_B} \\ 0 & \alpha(s)\tilde{\nu}_{r_B} & \beta(s)\tilde{\nu}_{r_B} & \nu \end{pmatrix}_{\{|\Psi_0\rangle,..,|\Psi_3\rangle\}} \tag{1.56}$$

where $\tilde{\nu_B} = \nu_{r_B}e^{i(2\pi\nu_{\mu w}t+\varphi_B)}$ (ν_{r_B} would be Rabi frequency of qubit B if it were alone), $\tilde{\nu}^*_{r_B}$ notes for the conjugate of $\tilde{\nu}_{r_B}$, and

$$\begin{aligned}\alpha(s) &= \frac{1}{\sqrt{2}}\frac{\sqrt{1+g(s)}}{\sqrt{1+s^2}},\\ \beta(s) &= \frac{1}{\sqrt{2}}\frac{1}{\sqrt{1+g(s)}},\\ &\text{and}\\ g(s) &= s^2(1+\text{sign}(s)\sqrt{1+1/s^2}).\end{aligned} \tag{1.57}$$

Going first to the frame rotating at the excitation frequency, and applying then the unitary operator

$$U = e^{i2\pi\frac{\nu(-|\Psi_0\rangle\langle\Psi_0|+|\Psi_3\rangle\langle\Psi_3|)-\nu_{cc}\sqrt{1+s^2}[|\Psi_1\rangle\langle\Psi_1|+|\Psi_2\rangle\langle\Psi_2|]}{2}t} \tag{1.58}$$

to eliminate most oscillating terms, Hamiltonian (1.56) becomes

$$\widehat{H_I} = \frac{h}{2}\begin{pmatrix} \boxed{\begin{matrix}0 & \alpha(s)\nu_{r_B}\\ \alpha(s)\nu_{r_B} & 0\end{matrix}} & \begin{matrix}\beta\nu_{r_B} & 0\\ 0 & \alpha\tilde{\tilde{\nu}}^*_{r_B}\end{matrix}\\ \begin{matrix}\beta\nu_{r_B} & 0\\ 0 & \alpha\tilde{\tilde{\nu}}_{r_B}\end{matrix} & \boxed{\begin{matrix}2\nu_{cc}\sqrt{1+s^2} & \beta\tilde{\tilde{\nu}}^*_{r_B}\\ \beta\tilde{\tilde{\nu}}_{r_B} & 0\end{matrix}}\end{pmatrix}_{\{|\Psi_0\rangle,..,|\Psi_3\rangle\}} \tag{1.59}$$

with $\tilde{\tilde{\nu}}_{r_B} = e^{i2\pi\sqrt{1+s^2}\nu_{cc}t}$.

In matrix (1.59), the upper left block is responsible for the main transition $|\Psi_0\rangle \rightarrow |\Psi_1\rangle$ at frequency $\alpha\nu_{r_B}$. In addition, the red terms induce the spurious transition $|\Psi_0\rangle \rightarrow |\Psi_2\rangle$ at frequency $\sqrt{(\beta\nu_{r_B})^2+4\nu_{cc}^2(1+s^2)}$ leading to a maximum population $1-2\nu_{cc}\sqrt{1+s^2}/(\beta\nu_{r_B})$ of level $|\Psi_2\rangle$. As an example, for two resonant qubits ($\Delta\nu = 0$) and $\nu_{cc}/\nu_{r_B} > 5$, this maximum population of $|\Psi_2\rangle$ is below 5%. Neglecting this leakage to $|\Psi_2\rangle$ and noticing that the other terms do not couple to states $|\Phi_0\rangle$ and $|\Phi_1\rangle$, Hamiltonian (1.59) simplifies to

$$\widehat{H}_I = h\alpha\nu_{r_B}(e^{i\phi_B}|\Psi_1><\Psi_0| + e^{-i\phi_B}|\Psi_0><\Psi_1|). \tag{1.60}$$

We now consider the case of addressing the system through both gates at the same frequency, but with different amplitudes $\nu_{r_{A,B}}$ and possibly different phases $\phi_{A,B}$. This situation pertains to the capacitive crosstalk that exists between gates A (resp. B) and island B (resp. A). Within the same approximation, Hamiltonian is now

$$\widehat{H}_I = h(\nu_r|\Psi_1><\Psi_0| + \nu_r^*|\Psi_0><\Psi_1|).$$

with $\nu_r = \alpha\nu_{r_A}e^{i\phi_A} + \beta\nu_{r_B}e^{i\phi_B}$. So by carefully adjusting $\nu_{r_{A,B}}$ and $\delta\phi = \phi_B - \phi_A$, it is possible to tune the frequency ν_r of the coherent oscillations.

1.2.2.2 An ISWAP gate with two resonant quantroniums

We now consider the case of two quantroniums that can be manipulated individually ($\nu_{cc}\sqrt{1+s^2} << \nu_r$), and that are then brought on resonance to turn on their coupling and make a two-qubit gate. After the resonant condition has been established ($\Delta\nu = 0$), the Hamiltonian (1.51) is

$$\begin{aligned}\widehat{H} &= \frac{\nu-\Delta\nu}{4}\widehat{\sigma}_{z_A} + \frac{\nu+\Delta\nu}{4}\widehat{\sigma}_{z_B} + \frac{\nu_{cc}}{2}\widehat{\sigma}_{x_A}\widehat{\sigma}_{x_B} \\ &= \frac{h}{2}\begin{bmatrix} -\nu & & & \nu_{cc} \\ & 0 & \nu_{cc} & \\ & \nu_{cc} & 0 & \\ \nu_{cc} & & & \nu \end{bmatrix}_{\{|00\rangle,..,|11\rangle\}} \\ &= \frac{h}{2}\begin{bmatrix} -\sqrt{\nu^2+\nu_{cc}^2} & & & \\ & -\nu_{cc} & & \\ & & \nu_{cc} & \\ & & & \sqrt{\nu^2+\nu_{cc}^2} \end{bmatrix}_{\{|\Psi_0\rangle,..,|\Psi_3\rangle\}},\end{aligned}$$

where the uncoupled basis $|00\rangle\,..\,|11\rangle$ is considered as the computational basis for the qubit register.

Within the rotating wave approximation [32], in the doubly Larmor-precessing frame $\mathcal{R}^{(2)}$ rotating at $\nu_{A,B}$ around $\sigma_{z_{A,B}}$, the Hamiltonian is transformed into

$$\widehat{H}_I = \frac{h}{2}\begin{bmatrix} 0 & & & \\ & & -\nu_{cc} & \\ & \nu_{cc} & & \\ & & & 0 \end{bmatrix}_{\{|00\rangle,..,|11\rangle\}}. \tag{1.61}$$

According to Schrödinger equation [71], the system initially prepared in state $|\Psi(0)\rangle$ evolves as

$$|\Psi(t)\rangle = \widehat{U}(t)\,|\Psi(0)\rangle\,, \tag{1.62}$$

where

$$\begin{aligned}\widehat{U}(t) &= e^{-\imath\frac{\widehat{H}_I t}{\hbar}} = e^{-\imath\pi\nu_{cc}t(|10\rangle\langle 01|+|01\rangle\langle 10|)} \\ &= \begin{bmatrix} 1 & & & \\ & \cos(\pi\nu_{cc}t) & i\sin(\pi\nu_{cc}t) & \\ & i\sin(\pi\nu_{cc}t) & \cos(\pi\nu_{cc}t) & \\ & & & 1 \end{bmatrix}.\end{aligned} \tag{1.63}$$

This evolution operator leaves states $|00\rangle$ and $|11\rangle$ unchanged, while it induces coherent oscillations between $|10\rangle$ and $|01\rangle$ with period $2/\nu_{cc}$. After half a period, a quantum of energy has been swapped between the qubits, hence the word SWAP in the name of the gates.
More precisely, the three durations $t_1 = 1/4\nu_{cc}$, $t_2 = 1/2\nu_{cc}$ and $t_3 = 1/\nu_{cc}$ lead to the following quantum gates:

$$\widehat{U}(t_1 = 1/4\nu_{cc}) = \frac{1}{\sqrt{2}} \begin{bmatrix} 1 & & & \\ & 1 & i & \\ & i & 1 & \\ & & & 1 \end{bmatrix} \equiv \sqrt{iSWAP}, \tag{1.64}$$

$$\widehat{U}(t_2) = \begin{bmatrix} 1 & & & \\ & 0 & i & \\ & i & 0 & \\ & & & 1 \end{bmatrix} \equiv iSWAP, \tag{1.65}$$

$$\widehat{U}(t_3) = \begin{bmatrix} 1 & & & \\ & -1 & & \\ & & -1 & \\ & & & 1 \end{bmatrix}. \tag{1.66}$$

The $\sqrt{ISWAP}$ gate transforms $|01\rangle$ in the maximally entangled state $|01\rangle + i\,|10\rangle$, and is universal. The operator $\widehat{U}(t_2)$, nicknamed ISWAP, transforms $|01\rangle$ in $i\,|10\rangle$.

In case the two qubits are not strictly on resonance, the evolution is slightly modified, but still keeps the separation between the $|00\rangle, |11\rangle$ and $|01\rangle, |10\rangle$. The evolution can be visualized in the Bloch sphere corresponding the $|01\rangle, |10\rangle$ subspace as shown in Fig. 1.13a.

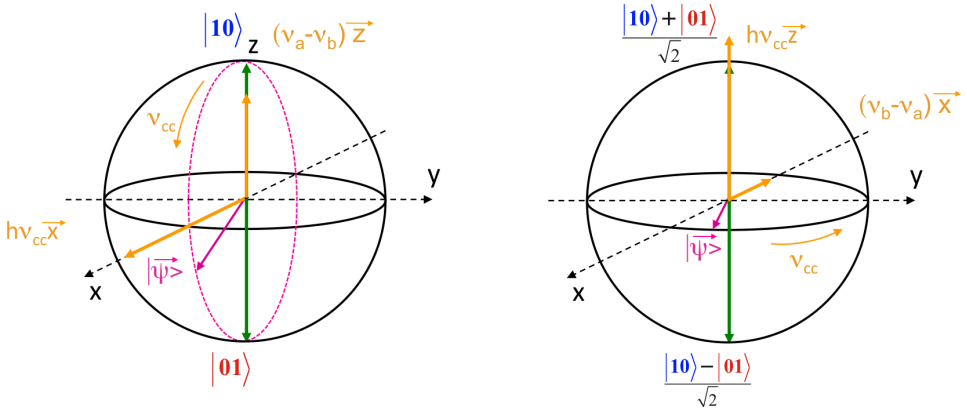

Fig. 1.13. Bloch sphere representation of the free evolution of quasi-resonant quantroniums in the $|01\rangle, |10\rangle$ subspace. a): Bloch sphere in the computational basis. The fictitious spin precesses around the $h(\nu_A - \nu_B)\overrightarrow{z} + h\nu_{cc}\overrightarrow{x}$. b): Bloch sphere in the energy eigenstate basis. The fictitious magnetic field is now $h\nu_{cc}\overrightarrow{z} - h(\nu_A - \nu_B)\overrightarrow{x}$.

1.2.2.3 Gate based a non-resonant coupling induced by irradiation of two quantroniums

We now present a two-qubit gate with non-resonant quantroniums, both of them being driven resonantly with drive amplitude properly chosen to introduce an effective coupling between them. This method is well-known in NMR [70] to induce an effective coupling between two spins with different Larmor frequencies. Although, it has been described for qubits [72] in terms of qubit dressed states, it can be derived in a semi-classical way as we do now. Figure 1.14 illustrates the idea behind this coupling scheme. It consists in introducing terms at the same frequency in the dynamics of the two qubits. This is done by choosing their Rabi frequencies such that $\nu_A - \nu_{r_A} = \nu_B + \nu_{r_B}$, or more precisely $\nu_{r_A} = \nu_{r_B} = \Delta\nu/2$ (we suppose here $\nu_A > \nu_B$) .

The Hamiltonian of the two "spins", including their resonant driving terms, is

$$\begin{aligned}\widehat{H} = & \frac{h\nu_A}{2}\widehat{\sigma}_{z_A} + \frac{h\nu_B}{2}\widehat{\sigma}_{z_B} \\ & + h\nu_{r_A}\cos\left(2\pi\nu_A t + \varphi_A\right)\widehat{\sigma}_{x_A} + h\nu_{r_b}\cos\left(2\pi\nu_B t + \varphi_B\right)\widehat{\sigma}_{x_B} \\ & + \frac{h\nu_{cc}}{2}\widehat{\sigma}_{x_A}\widehat{\sigma}_{x_B},\end{aligned} \tag{1.67}$$

with $\nu_{r_{A,B}}$ the Rabi frequency of each qubit.
In the doubly Larmor-precessing frame $\mathcal{R}^{(2)}$ rotating at $\nu_{A,B}$ around $\overrightarrow{z}_{A,B}$, this Hamiltonian becomes

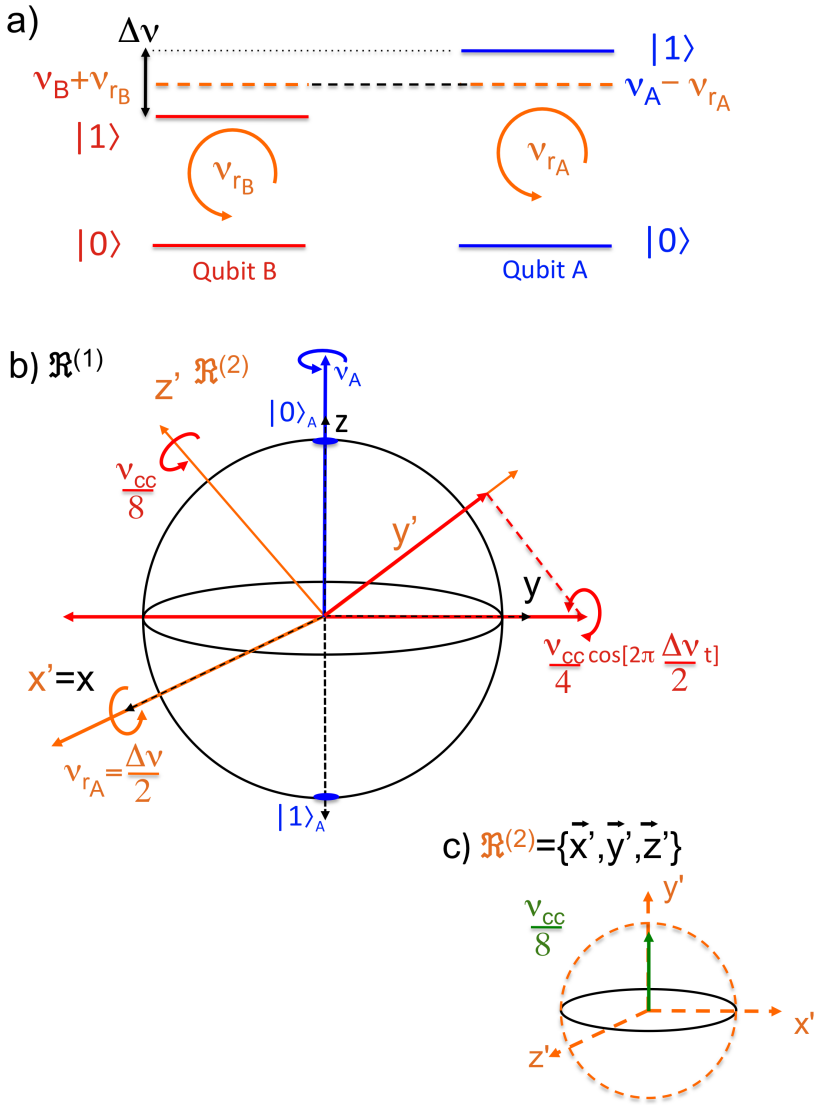

Fig. 1.14. Principle of a SWAP gate made with two non-resonant qubits. a) Energy diagram showing how an effective coupling is introduced between the qubits by driving both of them resonantly at Rabi frequencies $\nu_{R_A} = \nu_{R_B}$ equal to half their energy difference $\Delta nu = \nu_A - \nu_B$. The qubits share a common frequency $\nu_A - \nu_{R_A} = \nu_B + \nu_{R_B}$ in their dynamics, which introduces the effective coupling. b) Physical intuition on the effective coupling can be gained by looking semi-classically at the dynamics of qubit A in its Bloch sphere rotating at microwave frequency ν_A. In this frame called $\mathcal{R}^{(2)}$ (see text), qubit A is subject to a transverse, static, classical, and coherent field ν_{R_A} (represented by an orange arrow along x) and to the qubit B induced "qantum field" $\nu_{cc}/4 \cos(2\pi\Delta\nu/2t)$ (represented here by a red double arrow along y) that oscillates at the very same frequency ν_{R_A}. Within the rotating wave approximation applied to the frame $\mathcal{R}^{(4)}$ that corresponds to $\mathcal{R}^{(2)}$ rotating around y at $\Delta\nu/2 = \nu_{R_A}$, this oscillating quantum field becomes static with an amplitude $\nu_{cc}/16$. So the effective coupling induces rotation of qubit A at frequency, $\nu_{cc}/16$, while symetrically, qubit B undergoes the same oscillation with opposite phase, so that the net interaction is of the SWAP type.

$$\widehat{H_1} = U_1 H U_1^+ - \tfrac{\hbar}{i} U_1 \tfrac{dU_1^+}{dt} \tag{1.68}$$

where $U_1(t) = e^{\imath\pi[(\nu_A t+\varphi_A)\widehat{\sigma}_{z_A}+(\nu_B t+\varphi_B)\widehat{\sigma}_{z_B}]}$

$$\begin{aligned} U_1 &= e^{\imath\pi(\nu_A\widehat{\sigma}_{z_A}+\nu_B\widehat{\sigma}_{z_B})t} \\ &= e^{\imath\pi\nu_A\widehat{\sigma}_{z_A}t}.e^{\imath\pi\nu_B\widehat{\sigma}_{z_B}t} \\ &= (\cos(\pi\nu_A t) + i\widehat{\sigma}_{z_A}\sin(\pi\nu_A t))(\cos(\pi\nu_B t) + i\widehat{\sigma}_{z_B}\sin(\pi\nu_B t)) \end{aligned} \tag{1.69}$$

is the transformation operator from the laboratory frame to $\mathcal{R}^{(2)}$. By neglecting all terms oscillating at the frequency $2\nu_{A,B}$ (rotating wave approximation),

$$\frac{2}{h}\widehat{H_1} = \nu_{r_A}\widehat{\sigma}_{x_A} + \nu_{r_B}\widehat{\sigma}_{x_B} + \nu_{cc}U_1\widehat{\sigma}_{x_A}\widehat{\sigma}_{x_B}U_1^+, \tag{1.70}$$

with

$$U_1\widehat{\sigma}_{x_A}\widehat{\sigma}_{x_B}U_1^+ = \cos(\Delta\nu t + \Delta\varphi)\,\frac{\widehat{\sigma}_{x_A}\widehat{\sigma}_{x_B} + \widehat{\sigma}_{y_A}\widehat{\sigma}_{y_B}}{2} + \sin(\Delta\nu t + \Delta\varphi)\,\frac{\widehat{\sigma}_{x_A}\widehat{\sigma}_{y_B} - \widehat{\sigma}_{y_A}\widehat{\sigma}_{x_B}}{2}$$

and $\Delta\varphi = \varphi_B - \varphi_A$.
Choosing $\nu_{r_A} = \nu_{r_B} = \Delta\nu/2$ as explained above, one gets

$$\begin{aligned} \frac{4}{h}\widehat{H_I} &= \Delta\nu\,[\widehat{\sigma}_{x_A} + \widehat{\sigma}_{x_B}] \\ &\quad + \nu_{cc}\left[\cos(\Delta\nu t + \Delta\varphi)\,\frac{\widehat{\sigma}_{x_A}\widehat{\sigma}_{x_B} + \widehat{\sigma}_{y_A}\widehat{\sigma}_{y_B}}{2} + \sin(\Delta\nu t + \Delta\varphi)\,\frac{\widehat{\sigma}_{x_A}\widehat{\sigma}_{y_B} - \widehat{\sigma}_{y_A}\widehat{\sigma}_{x_B}}{2}\right]. \end{aligned}$$

We now switch to the quadruply rotating frame $\mathcal{R}^{(4)}$ that corresponds to $\mathcal{R}^{(2)}$ rotating around $\overrightarrow{x}_A$ and $\overrightarrow{x}_B$ at frequencies $\nu_{r_{A,B}}$, respectively. The corresponding transformation operator from frame $\mathcal{R}^{(2)}$ to frame $\mathcal{R}^{(4)}$ is

$$\begin{aligned} U_2(t) &= e^{\imath 2\pi(\frac{\nu_{r_A}}{2}\widehat{\sigma}_{x_A}+\frac{\nu_{r_B}}{2}\widehat{\sigma}_{x_B})t} \\ &= e^{\imath 2\pi\frac{\Delta\nu}{4}(\widehat{\sigma}_{x_A}+\widehat{\sigma}_{x_B})t}, \end{aligned}$$

and leads to the new interaction Hamiltonian

$$\widehat{H}_2 = \frac{h\nu_{cc}}{4}U_2\left[\cos(2\pi\Delta\nu t + \Delta\varphi)\,\frac{\widehat{\sigma}_{x_A}\widehat{\sigma}_{x_B} + \widehat{\sigma}_{y_A}\widehat{\sigma}_{y_B}}{2} + \sin(2\pi\Delta\nu t + \Delta\varphi)\,\frac{\widehat{\sigma}_{x_A}\widehat{\sigma}_{y_B} - \widehat{\sigma}_{y_A}\widehat{\sigma}_{x_B}}{2}\right]U_2^+.$$

Now one has

$$U_2\widehat{\sigma}_{x_A}\widehat{\sigma}_{x_B}U_2^+ = \widehat{\sigma}_{x_A}\widehat{\sigma}_{x_B},$$

$$\begin{aligned} U_2\widehat{\sigma}_{y_A}\widehat{\sigma}_{y_B}U_2^+ &= e^{\imath\frac{2\pi\Delta\nu}{4}\widehat{\sigma}_{x_A}t}\widehat{\sigma}_{y_A}e^{-\imath\frac{2\pi\Delta\nu}{4}\widehat{\sigma}_{x_A}t}e^{\imath\frac{2\pi\Delta\nu}{4}\widehat{\sigma}_{x_B}t}\widehat{\sigma}_{y_B}e^{-\imath\frac{2\pi\Delta\nu}{4}\widehat{\sigma}_{x_B}t} \\ &= \left[\cos\left(\frac{2\pi\Delta\nu}{2}t\right)\widehat{\sigma}_{y_A} + \sin\left(\frac{2\pi\Delta\nu}{2}t\right)\widehat{\sigma}_{z_A}\right]\left[\cos\left(\frac{2\pi\Delta\nu}{2}t\right)\widehat{\sigma}_{y_B} + \sin\left(\frac{2\pi\Delta\nu}{2}t\right)\widehat{\sigma}_{z_B}\right], \end{aligned}$$

and

$$U_2\widehat{\sigma}_{x_A}\widehat{\sigma}_{y_B}U_2^+ = \widehat{\sigma}_{x_A}\left[\cos\left(\frac{2\pi\Delta\nu}{2}t\right)\widehat{\sigma}_{y_B} + \sin\left(\frac{2\pi\Delta\nu}{2}t\right)\widehat{\sigma}_{z_B}\right].$$

Thus, by considering $\nu_{cc} << \Delta\nu$ and suppressing all fast oscillating terms that average to zero,

$$\widehat{H}_2 = \frac{h\nu_{cc}}{16}\left[(\widehat{\sigma}_{y_A}\widehat{\sigma}_{y_B} - \widehat{\sigma}_{z_A}\widehat{\sigma}_{z_B})\cos(\Delta\varphi) + (\widehat{\sigma}_{y_A}\widehat{\sigma}_{z_B} + \widehat{\sigma}_{z_A}\widehat{\sigma}_{y_B})\sin(\Delta\varphi)\right].$$

As $U_2(t = 4m/\Delta\nu) = \mathbf{I}$ with $m \in \mathbb{N}$, the two frames $\mathcal{R}^{(2)}$ and $\mathcal{R}^{(4)}$ coincide every $4m/\Delta\nu$ periods. By adjusting $\Delta\varphi$ to 0 and $\Delta\nu$ such that $\nu_{cc}/4 = \Delta\nu/m$, Hamiltonian is

$$\widehat{H}_2(4m/\Delta\nu) = \frac{h\nu_{cc}}{16}(\widehat{\sigma}_{y_A}\widehat{\sigma}_{y_B} - \widehat{\sigma}_{z_A}\widehat{\sigma}_{z_B})$$

The evolution operator $e^{i\widehat{H}_2 t/\hbar}$ corresponds at $t = 16/\nu_{cc}$ to the universal two qubit gate $1 + \widehat{\sigma}_{y_A}\widehat{\sigma}_{y_B}$, which transforms, for example, $|00\rangle$ in a maximally entangled state $|00\rangle - |11\rangle$[73].

A few remarks need to be made at that level. Note first that suppressing non-secular terms as we have done implies two strong conditions: $\Delta\nu/2 = \nu_{r_{A,B}} << \nu_{A,B}$ and $\nu_{cc} << \nu_{r_{A,B}} = \Delta\nu/2$. Condition 1 is easily satisfied since $\Delta\nu$ can easily be made one order of magnitude smaller than the qubit frequencies. The second condition is more drastic, as it requires to induce Rabi oscillations at high frequency, which implies working with CPB with large anharmonicity in order not to populate higher excited levels. Finally, note that this protocol can not be implemented on CPBs circuit with large gate crosstalk.

1.2.3 Readout of two coupled quantroniums by DC switching

A natural requirement for the quantroswap readout is to be able to project the two quantroniums onto the computational basis states ($|00\rangle$,..,$|11\rangle$), with the correct probabilities that correspond to the two-qubit state just before the readout was switched on. Then, the states of the two quantroniums are determined quasi-simultaneously and independently. This requirement applied to the DC switching readout method, rises a technical issue and a more fundamental one. The technical one is called "readout crosstalk", and corresponds to a possible perturbation of the switching of readout junction A, due to the simultaneous operation of readout junction B, and vice and versa. We do not address this problem in this theoretical chapter. The more fundamental issue is the unwanted evolution of the two-qubit state while ramping the readout currents $i_{b_{A,B}}$, and consequently the frequencies $\nu_{A,B}[\delta_{A,B}(I_{b_{A,B}})]$.As shown by Eq. (1.53), this spurious evolution occurs as soon as $\Delta\nu \lesssim \nu_{cc}$. It thus occurs at the beginning of the readout ramp if the two qubits were invloved in a swap operation just before, or when ν_A and ν_B cross each other during the ramp.
We now evaluate quantitatively the probabilitiy that the two qubits stay in the initially prepared state $|10\rangle$ or $|01\rangle$, in the simple case where only readout B is ramped, as illustrated in Fig. 1.15. The time dependent Schrondinger equation for the system is

$$\frac{i}{\pi}\frac{\partial}{\partial\tau} = \begin{bmatrix} -\tau/x & 1 \\ 1 & \tau/x \end{bmatrix}_{|10\rangle,|01\rangle} \tag{1.71}$$

where $\tau = \nu_{cc}t$ and $x = \nu_{cc}^2/(\partial\Delta\nu/\partial t)$ is the only dynamical parameter. This equation was integrated numerically starting either well before or at the crossing point defined by $\nu_A = \nu_B$. Results are shown in Fig. 1.15 for these two cases and for the initial state $|10\rangle$. In case the two qubits cross each other during the ramp, $P_{|10\rangle}$ coincides with the Landau-Zener tunneling probability [74]

$$P_{LZ} = e^{-2\pi^2 x}, \tag{1.72}$$

within a precision better than 1%. Figure 1.15 shows that the two qubit state, and consequently the contrast of Rabi or SWAP oscillations, can be tremendously modified at readout depending on the ramping speed. More precisely the state is preserved with a probability better than 95% only when $\partial\Delta\nu/\partial t >> 250\nu_{cc}^2$. Note also that any two-level-system with a frequency crossing the frequency of the qubits can induce exactly the same problem, as already pointed out for other Josephson qubits.

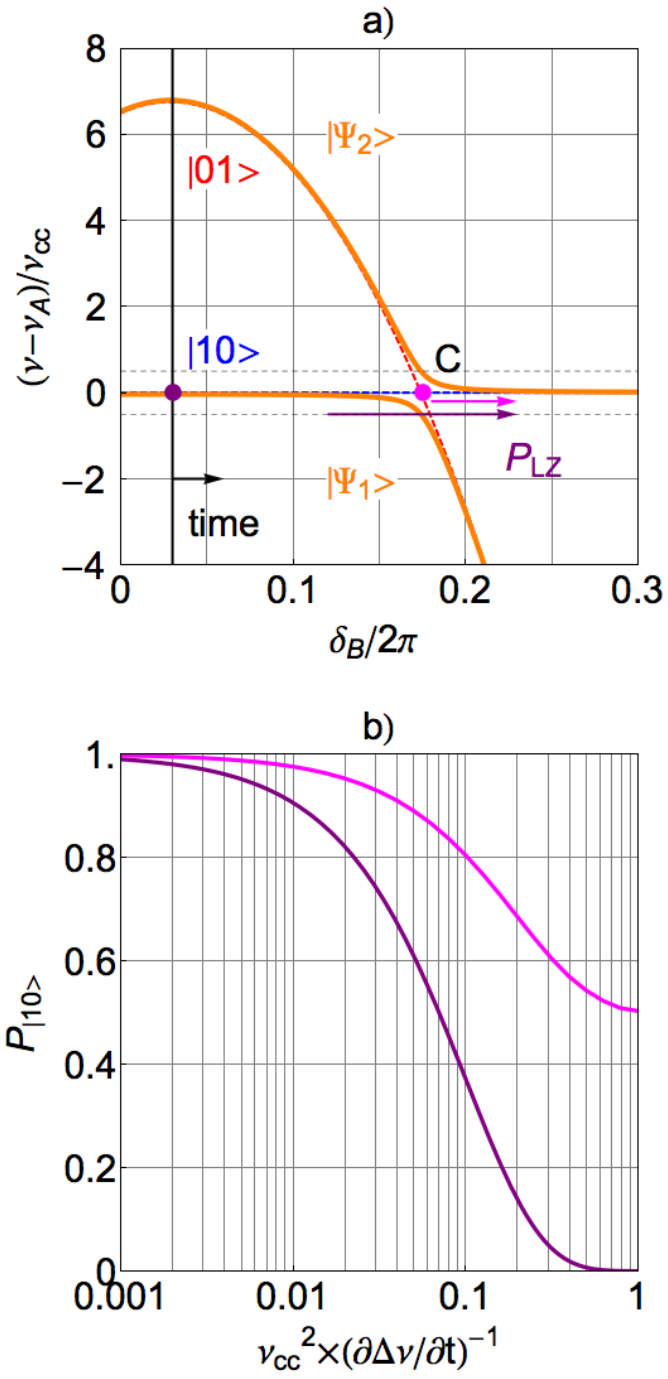

Fig. 1.15. Evolution of the two qubit states during a readout ramp of qubit B alone. a) Time-dependant energy diagram of the system during a δ_B ramp over a range of about $0.2\times2\pi$ rad. Uncoupled states $|01\rangle$ and $|10\rangle$ are indicated by red and blue dashed lines, while energies of eigenstates $|\Psi_1\rangle$ and $|\Psi_2\rangle$ are in orange. All energies are expressed in ν_{cc} units. The system is initially prepared in the $|10\rangle$ state, and the ramp is started either well before or at the crossing point C defined by $\nu_A = \nu_B$. b) Probability $P_{|10\rangle}$ that the system is still in the $|10\rangle$ state at the end of the ramp as a function of $\nu_{cc}/(\partial\Delta\nu/\partial t)$, when the ramp is started well before (purple line) or at the crossing point C (magenta line). In the first case, $P_{|10\rangle}$ coincides with the probability of Landau-Zener tunneling across C. In the second case, when the energy evolution is very slow compare to ν_{cc}^2, the system is either in state $|10\rangle$ or $|01\rangle$ with 50% probability, and all the information about the initial state is lost.

Chapter 2

The Quantroswap: design and implementation

Contents

2.1 Quantum engineering and design of a two quantronium qubit experiment

In this chapter we report on our design of a two-quantronium experiment for demonstrating the coherent coupling between the qubits, and for implementing the universal quantum gate $(ISWAP)^{1/2}$, hence the name Quantroswap. More precisely, the planned experiment involves two quantroniums A and B whose islands are connected by a small capacitance as described in Fig. 1.10. The quantroniums have slightly different frequencies at their optimal working points in order to have a negligible interaction there, which allows their independent preparation in a first step. Then, the interaction is switched on by placing the quantroniums in resonance, which is achieved by tuning the phase of the quantronium with the highest frequency. In the simplest implementation, a trapezoidal current pulse with fast rise and fall times T_b is applied to its readout circuit, as described in Fig. 2.1b. Shifting the qubit from its optimal point reduces its coherence time, and should be done in a time shorter than the coherence time at the arrival point. Then the two qubits are coupled and decoherence follows a different law explained at the end of the present section. During the in-resonance step, the capacitive interaction yields a periodic swapping of the two qubits, and the universal gate $(ISWAP)^{1/2}$ is obtained after a quarter of period. An alternative implementation would consist in keeping the two quantroniums at their optimal point, while coupling them using the FLICFORQ method described in section 1.2.2.2. After the swapping step, either one or both qubits are measured by DC switching of their readout junctions (see section 1.1.6), or by bifurcation of their readout oscillators (see section 1.1.7). When reading out the two qubit states, the measurement pulses are applied independently and simultaneously. However, the readout measures the σ_Z component of the fictitious spin representing each qubit, which does not fully characterize the two-qubit quantum state produced by the gate. Ideally, the quantum tomography of the final quantum state should be performed by applying suitable qubit rotations $(\pi/2)_{X,-Y}$ before readout in order to determine the nine average values of $\sigma_{U_A}\sigma_{U_B}$, where U stands for X, Y or Z.

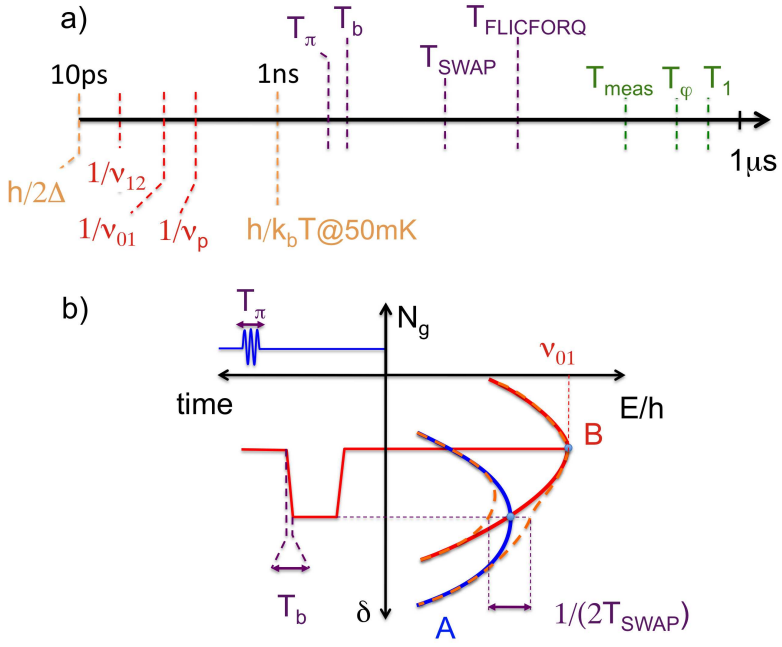

Fig. 2.1. Different characteristic times and energies involved in a Quantroswap experiment. a) Characteristic times for coherence and readout (green), qubit manipulation (purple), material properties and temperature (orange), and qubit and readout oscillator frequencies (red). T_1, T_φ, and T_{meas} are the relaxation, dephasing and measurement times respectively. T_{SWAP} and $T_{FLICFLORQ}$ are the two-qubit gate durations for the two coupling schemes discussed. T_π and T_b are the duration of a π pulse, and the rise and fall time of the current pulse bringing the two qubits in resonance in the first coupling scheme. Frequencies ν_{01}, ν_{12} and ν_p are the first two transition frequencies and the plasma frequency of the readout oscillator. T and Δ are the typical electronic temperature of the circuit and the Al superconducting gap. b): Simple experimental protocol for demonstrating a SWAP gate within the resonant coupling scheme. Both qubits are initially at their optimal point. One of them (A for instance) is prepared in state $|1\rangle$ by a π pulse. Then the qubit with the highest frequency (here B) is brought in resonance with the other qubit by a pulse in δ. The two qubits swap in a time $T_{SWAP} = 1/2\nu_{cc}$, with ν_{cc} the difference of frequencies between the eigenenergies (dashed orange) of the system.

With this quantrowap experiment in mind, one has to optimize the various parameters involved in the different building blocks of the circuit. A key concept in this optimization is to achieve the desired hierarchy between the different characteristic times involved in the experiment (see Fig. 2.1). First, the duration of single qubit gates should be shorter than the duration of a two-qubit gate in order to manipulate the qubits independently whether they

are in resonance or not. Second, the two-qubit gate duration should be shorter than the qubit coherence time in order to perform as much gate operations as possible before quantum coherence is lost. Then, single qubit gates, represented in Fig. 2.1 by the duration T_π of a π pulse, are of course much longer than the qubit period. The time needed to reach the resonance condition T_b should be shorter than T_{SWAP} in order to avoid complex evolution of the system during the rise and fall. The two qubit swapping time (either T_{SWAP} or $T_{FLICFORQ}$ for the resonant and FLICFORQ coupling schemes, respectively) governed by the capacitive coupling between the quantroniums should then be shorter than the times T_1 and T_φ that characterize coherence. Finally, the measurement time T_{meas} should be shorter than T_1 in order to avoid spurious relaxation during measurement.

This hierarchy between the timescales is not the only requirement to be fulfilled. Indeed, other issues come into play: the electronic temperature of the circuit, the sensitivity of the readout circuit, the fabrication process, and the availability of microwave components. When several requirements contradict one another, which often happens, trade-offs have to be found. By using the results of chapter 1 to evaluate quantitatively these requirements and trade-offs, we determine below the parameters of the various circuit blocks.
The section is organized as follows:

- We first select qubit parameters ensuring a sufficient anharmonicity and the absence of thermal excitation of the qubit.
- Then, we determine the gate line parameters of each qubit in order to achieve fast single qubit gates, with limited relaxation due to the gate impedance.
- In a third step, the DC switching readout is designed for reaching a high sensitivity, a short measurement time, a frequency decoupling to the qubit, and limited relaxation due to the impedance of the readout circuit.
- Finally, we determine the coupling capacitance between the quantronium to ensure the adequate timescale separation.

2.1.1 Determination of qubit parameters

We determine in this section the qubit parameters, i.e. the Josephson energy E_J, the charging energy E_C, and the CPB asymmetry d.

2.1.1.1 Choice of the qubit frequency

The first requirement is to maintain the qubit energy $h\nu_{01}(\delta = 0, N_g = 0.5)$ well above the thermal energy scale $k_B T \approx 40$ mK in order to limit the probability $e^{-h\nu/k_B T}$ for thermal excitation of state $|1\rangle$. However, due to the limited frequency range of commonly available microwave components and

equipments, this frequency has to be lower than 20 GHz. In order to ensure a sufficient safety margin, a suitable value for the qubit frequency is about 17 GHz. Given this value of ν_{01}, the possible values of E_J and E_C are shown in Fig. 2.2.

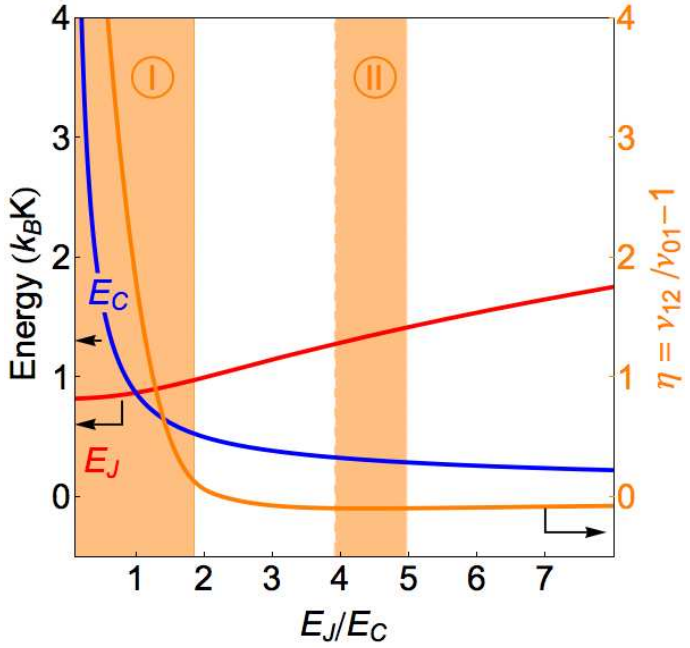

Fig. 2.2. Josephson (red line) and charging (blue line) energies, as well as anharmonicity η (orange line) as a function of E_J/E_C for $\nu_{01}(\delta = 0, N_g = 1/2) = 17$ GHz. Orange areas correspond to an anharmonicity larger than 10%, which is the minimum target value for the experiment.

2.1.1.2 Single qubit gate, speed, and anharmonicity

As explained in section 1.1.3, the second requirement is to be able to operate the qubit in a time much shorter than the qubit decoherence time and much shorter than the swapping time. More precisely, microwave excitation pulses have to induce selectively the transition between states $|0\rangle$ and $|1\rangle$, avoiding excitation of the third level. Equation (1.12) leads to a minimum difference of frequency $\nu_{12} - \nu_{01}$ in order to populate the third level by less than 3% during a π pulse of 1 ns. This corresponds to an anharmonicity larger than 10% for a qubit at 17 GHz, and thus to possible values of E_J/E_C ratio below 1.9 (area I in Fig. 2.2) or in the range 4 to 5 (area II in Fig. 2.2). Area

II was already explored experimentally before this thesis work by making quantroniums with large and weakly oxidized junctions. Unfortunately, these qubits always exhibited many spurious two-level systems coupled to the qubit. Therefore, we have decided to limit our optimization to area I of Fig. 2.2.

2.1.1.3 Readout discrimination

As explained in section 1.1.6, the "DC switching" readout is based on the discrimination of the persistent currents $i_{|0\rangle}$ and $i_{|1\rangle}$. The phase dependance of the signal, i.e. $i_{|1\rangle} - i_{|0\rangle}(\delta)$, is shown in Fig. 2.3a. The two specific values of δ spotted on the figure correspond to two different values of the current bias prepulses (see section 1.1.6). Figure 2.3b shows the iso-signal lines as well as the regions with anharmonicity larger than 10%, in the E_J-E_C plane and at the optimal value of δ. When moving in region I along the target line $\nu_{01} = 17$ GHz (blue line in Fig. 2.3), the signal happens to be maximum at the border, i.e. at $E_J = 1 k_B$K. This value is thus optimal, which is still the case for limiting decoherence, as we now show.

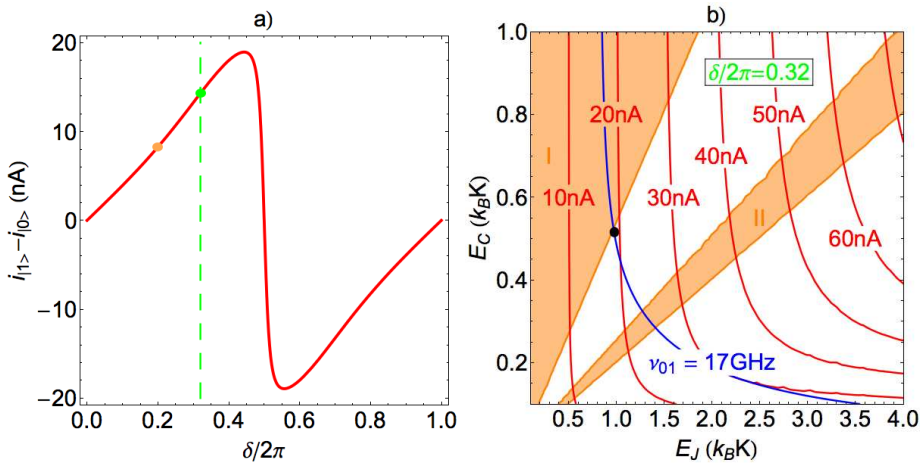

Fig. 2.3. Maximization of the readout signal at $N_g = 1/2$. a) Difference between persistent currents of the two qubit states with respect to δ for $\nu_{01}(N_g = 0.5, \delta = 0) = 17GHz$. The orange and green dots correspond to phases δ_p reached at the top of the readout pulse when starting from the optimal working point with no pre-bias pulse ($\delta = 0$) and with the optimal possible prepulse ($\delta = 0.12 \times 2\pi$ rad), respectively. b) Iso-values (red lines) of the maximum reachable signal $i_{|1\rangle} - i_{|0\rangle}$ in the E_J-E_C plane for $\delta = 0.32 \times 2\pi$ rad (dotted vertical line in graph a). The blue line corresponds to the target value $\nu_{01} = 17GHz$. Orange areas correspond to regions where anharmonicity is larger than 10% (see Fig. 2.2)

2.1.1.4 Dephasing time

The last constraint in the choice of (E_J, E_C) is the maximisation of the decoherence time due to microscopic fluctuators. We thus calculate the charge and phase noise contributions to dephasing time using Eqs.(1.32)-(1.30)-(1.34) at and away from the optimal point, respectively, as well as the noise spectral densities determined in experiment [27] ($A_{N_g} \simeq 1.6\ 10^{-6}$ and $A_\delta \simeq 0.9\ 10^{-8}$). The results are shown in Fig. 2.4 as a function of E_J/E_C and of the working point. Panel c) of the figure shows that close to the optimal point and below $E_J/E_C = 1.9$, T_φ decreases quickly as E_J decreases, which is not a surprise when remembering that N_g noise dominates decoherence in regimes 1 and 2 of Fig. 1.2. The optimal E_J/E_C is consequently 1.9, which leads to an expected T_φ of about 1 μs.

Partial conclusion

As a conclusion, considering the constraints of operability and sensitivity, the optimal frequency of 17 GHz leads to $E_J = 0.97$ K and $E_C = 0.51$ K (black dot in Fig. 2.3b).
These two energies depend on three fabrication parameters of the Josephson junctions: their area A, their specific tunnel conductance G_{Tu}, or equivalently their critical current density I_{0u}, and their capacitance C_{Ju} per unit area. Using the Ambegaokar-Baratoff relation [31] and the definition of E_C, one has indeed:

$$E_J = I_0\varphi_0 = I_{0u}\varphi_0 A = \frac{\pi\varphi_0}{2e}\Delta G_{Tu} A,$$
$$E_C = \frac{(2e)^2}{2C_J} = \frac{(2e)^2}{2C_{Ju}}\frac{1}{A},$$

where $\Delta \simeq 180\mu$eV is the value of the superconducting gap usually measured on aluminum thin films (above 40 nm), and $C_{Ju} \simeq 100$ fF/μm^2 (value measured for Aluminum oxide grown at room temperature).
The value $E_C = 0.51$ K then gives a junction area of $0.2 \times 0.18\mu$m^2, whereas $E_J = 0.97$ K yields a critical current density of 113 A/cm^2, or equivalently a tunnel conductance $1/(500\ \Omega.\mu\text{m}^2)$.

2.1.2 Design and parameters of the gate line circuit

The second design step consists in determining a suitable gate capacitance that limits relaxation due to the gate line, given its standard 50 Ω impedance, without loosing too much in qubit operability.

2.1.2.1 Maximization of the Rabi frequency

As explained in section 1.1.3, the Rabi frequency $\nu_{r_0} = 2E_C\Delta N_g |\langle 0|\,\widehat{N}\,|1\rangle|$ is is proportional to $E_C C_g V_{g_{\mu w}}$, where $V_{g_{\mu w}}$ is the microwave amplitude of the

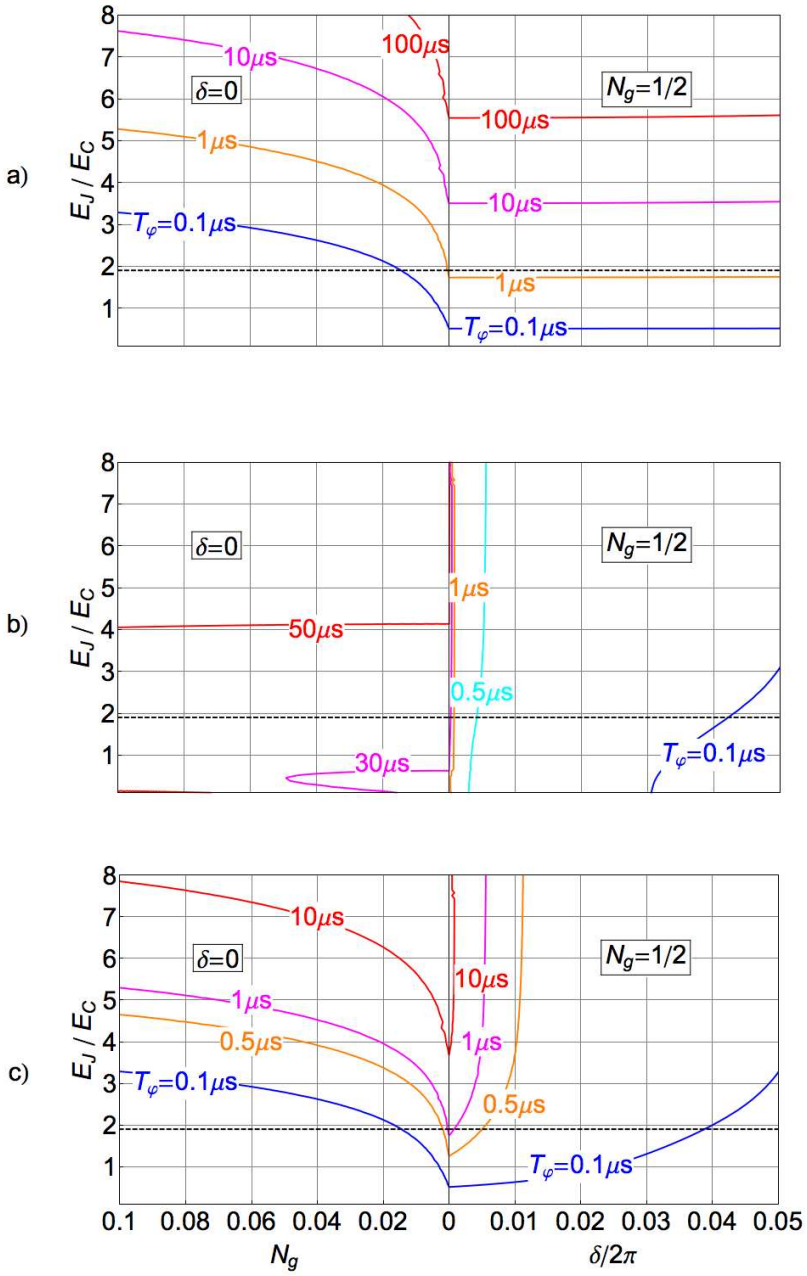

Fig. 2.4. Dephasing time T_φ as a function of E_J/E_C and of the working point for $\nu_{01} = 17GHz$ and $d = 5\%$. Color lines are calculated iso-T_φ contours in the $N_g - E_J/E_C$ plane (at $\delta = 0$) in left panels, and in the $\delta - E_J/E_C$ plane (at $N_g = 1/2$) in right panels. a), b) and c) correspond to the charge noise contribution only, to the phase noise contribution, and to the sum of them, respectively. The horizontal dashed lines indicates the E_J/E_C value chosen for the design. The calculation use expressions given in section 1.1.8, and charge and phase noise spectral densities characterized by $A_{N_g} \simeq 1.6\ 10^{-6}$ and $A_\delta \simeq 0.9\ 10^{-8}$.

gate pulse. Note that this dependance allows to drive the Cooper pair box even when E_C is small [1], by increasing C_g or $V_{g_{\mu w}}$ within the limits of the available power. Although commercial continuous microwave sources can deliver up to +20 dBm (up to 20 GHz), some power is lost when creating pulses by mixing their CW output with DC pulses supplied by arbitrary waveform generators. The available power in the pulse is in pratical about 10dBm. Moreover, the microwave generators have noise temperatures of several 10^4K, and have to be heavily attenuated to reduce the noise on the quantronium gate. More precisely, as explained in section 1.1.8, the effective electronic temperature T_{eff} as seen from the gate has to be lower than $T_q = h\nu_{01}/k_B$ in order to prevent excitation of the qubit. This leads to a minimal attenuation of -60 dB to decrease the noise below T_q. This attenuation is provided by several attenuators placed at proper locations all along the gate line to prevent heating of the fridge and to thermalize gradually the electrons (this point will be explained in more details in section 2.2). This leads to a maximal microwave power available on the gate capacitance of the order of -50 dBm $= 0.7$ mV $\simeq$ 0.2%Cooper pair / aF.
Figure 2.5 shows the Rabi frequency ν_{r0} as a function of C_g for the chosen E_J and E_C values. Taking our target value of $\nu_{r0} = 0.5$ GHz, we read on the figure that C_g has to be larger than 1 aF. We now chose a more precise value based on the evaluation of the gate line induced decoherence.

2.1.2.2 Gate line induced decoherence

The relaxation and dephasing times are given by Eqs. (1.18)-(1.23)-(1.24)-(1.27), which lead for $h\nu_{01}/(k_BT) >> 1$ to

$$T_{1,N_g} = \frac{1}{32\pi^2 \left|\langle 0|\,\widehat{N}\,|1\rangle\right|^2 \kappa^2 \frac{Re[Z_g(2\pi\nu_{01}]}{R_k}\nu_{01}} \tag{2.1}$$

and

$$T_{\varphi,N_g} = \frac{1}{16\pi^2|\,\langle 0|\,\widehat{N}\,|0\rangle - \langle 1|\,\widehat{N}\,|1\rangle\,|^2\kappa^2\frac{Re[Z(\nu=0]}{R_k}\frac{k_BT}{h}}. \tag{2.2}$$

Given the values chosen for E_J and E_C, and assuming that the 50Ω impedance of the line is at $T = 100$ mK, one gets $T_{1,N_g} \simeq 12/C_g^2$ ms/aF^2 and $T_{\varphi,N_g} \simeq 0.026(N_g - 0.5)^{-2}/C_g^2$ s/aF^2. These functions are plotted on Fig. 2.6, which shows that dephasing is completely negligible in the range of capacitance considered above. Besides, T_1 decreases with C_g, which should be kept below 30 aF to get $T_1 > 10$ μs. We are thus left with $C_g \in [1, 30]$ aF and chose $C_g = 10$ aF.

[1] This property is exploited in the transmon version of the Cooper pair box

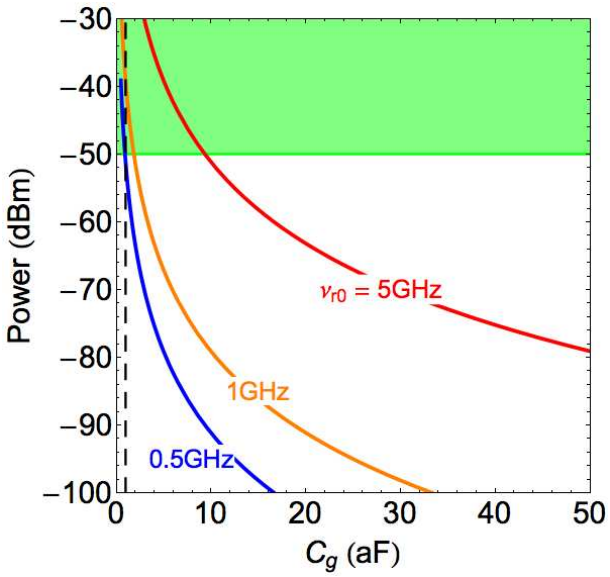

Fig. 2.5. Iso-values of the Rabi frequency as a function of gate capacitance C_g and of the microwave power applied to the gate for the selected values $E_J = 0.51$ K $E_C = 0.97$ K. The green area corresponds to a gate power higher than available. Dashed vertical line indicates the minimal value for C_g in order to apply a π pulse in 1ns.

2.1.3 Design and parameters of the readout circuit

The design of the readout line is a bit more complicated than that of the gate line. In this section, we only discuss the DC switching readout, which is the only one we have actually used in Quantroswap experiments. The case of the Josephson bifurcation amplifier is treated in chapter 4, devoted to current to frequency conversion with a Quantronium. As far as DC switching is concerned, we want to be able to apply fast readout pulses with a rise time and a plateau duration (see Fig. 2.1b) as short as 10 ns, and with a noiseless peak value I_p. Thus, we choose (see Fig. 2.7) to attenuate strongly the pulses with several 50Ω attenuators (at different places along the readout line as for the gate line), to place the bias resistor R_b of the current source I_b at milliKelvin temperature, and to match the line to 50Ω above and below R_b. As the readout oscillator (readout junction in parallel with capacitance C_r) would behave as a short at the end of the line if it was alone, we insert a $R_l = 50$ Ω load resistance in front of it. With such a design, R_b is the only non 50Ω component, and the reflected and transmitted pulses are absorbed completely. Besides, the impedance of the line as seen from the qubit (or from the readout oscillator) has to be kept under control up to 20 GHz. However, since R_b is made big for thermalization purpose, its impedance is not known at

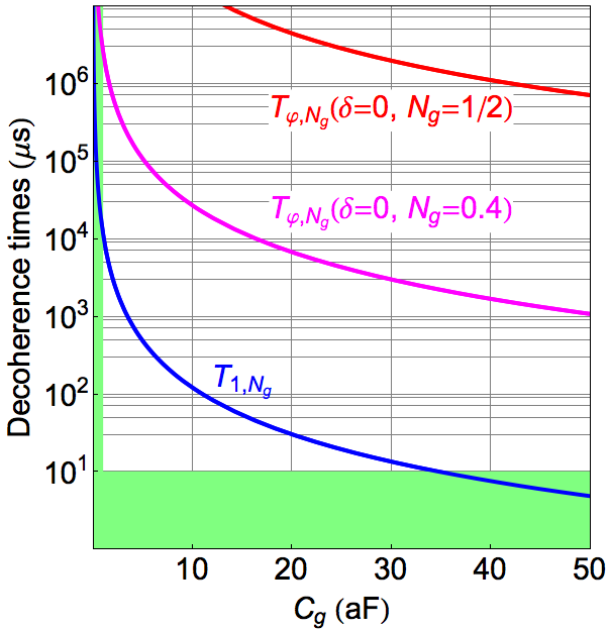

Fig. 2.6. Gate line contribution to decoherence as a function of C_g for $E_J = 0.51$ K $E_C = 0.97$ K: T_1 (blue) is calculated at the optimal point whereas T_φ is calculated at $\delta = 0$ in the relevant range $N_g \in [0.4, 0.5]$. The left green area is discarded for power availability reason, while the bottom one corresponds to T_1 shorter than our target value 10μs.

high frequency, so that we choose to prevent the qubit from seeing it. Thus, we place a capacitor to ground immediately after R_l. The value of this capacitor is chosen so that it terminates the impedance as seen from the readout above a few GHz, but does not disturb a 10 ns long readout pulse propagating down the line. Finally, two high impedance voltage probes are connected to ground and above the capacitor, respectively (more details will be given in the next section).

With this structure of the readout line in mind, we have now to determine the parameters of the readout oscillator, i.e. its critical current I_0 and parallel capacitance C_r, in order to maximize the readout fidelity and minimize the readout line induced decoherence.

Let us first notice that C_r plays several roles in the quantronium circuit. First, it reduces the plasma frequency $\nu_p = 1/2\pi\sqrt{\mathcal{L}C_r}$ of the oscillator [2] well below the qubit transition frequency, during manipulation and readout ramp.

[2] $\mathcal{L} = \varphi_0/\sqrt{I_0^2 - I_b^2}$ is the inductance of the junction biased by a current I_b.

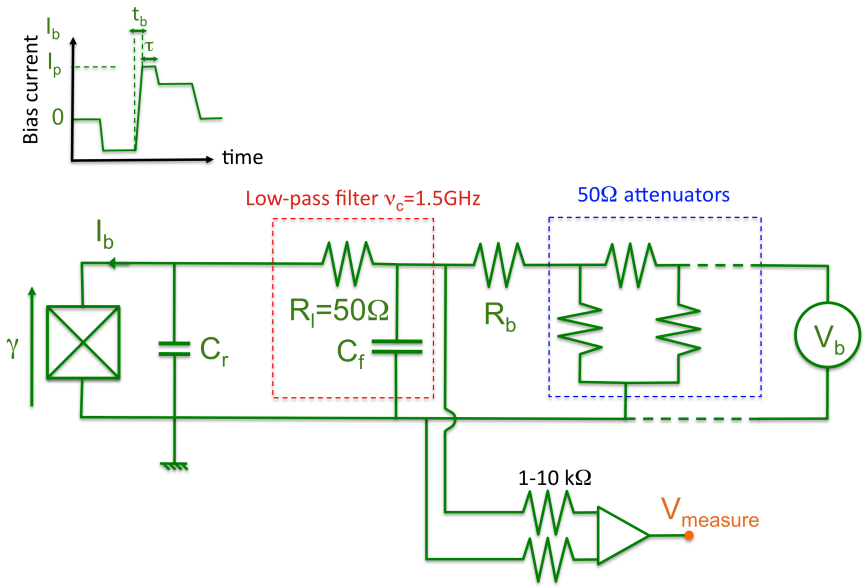

Fig. 2.7. Schematic of the readout line with its readout oscillator (on the left), an R_lC_f filter that matches the line to 50Ω and prevents the top part of the line from being seen by the qubit, the bias line resistor R_b, and 50Ω attenuators. A differential high-impedance voltage probe is inserted between the filter and R_b. The environment seen by the qubit reduces to the Josephson oscillator in parallel with R_l at high-frequency, and to Josephson junction in parallel with R_l+R_b+50 Ω at low frequency.

It also reduces the δ phase noise by filtering the current noise produced by the admittance $Y(\nu)$ of the line. Finally, it influences the quality factor Q of the oscillator, and thus the physics of the switching.

2.1.3.1 Maximization of the readout fidelity

The switching probability $P_S(I_b + i_{|0\rangle,|1\rangle})$ of the readout junction during a readout pulse with duration τ is given by Eq. 1.7, asssuming a quality factor Q of the readout oscillator above 1 [75, 76, 77]. In this regime the escape is dominated by quantum tunneling below the crossover temperature $T_{CO} = h\nu_p/7.2k_B$, and by thermal activation above. The readout sensitivity improves thus upon cooling down till the crossover temperature is reached. As the effective temperature of the dissipative elements of the readout line is about 40 mK, it is convenient to have T_{CO} in this range or slightly below, so that the

sensitivity is maximum and weakly dependent of temperature. This criterium leads to a plasma frequency at switching in the range of 2 GHz$-$5 GHz, which corresponds to a $4-10$ GHz range at zero current. More precisely, Eq. 1.7 can be very well approximated (see p.53 of Ithier's thesis [17]) by a universal curve

$$P_S(\Delta s) = 1 - \exp\left[-|\ln 0.4|\ \exp\left(\frac{\alpha}{0.4|\ln 0.4|}\Delta s\right)\right], \tag{2.3}$$

where $s = I_p/I_0$ and $\Delta s = s - s_0$ with s_0 defined by $P_S(s_0) = 0.6$, where the slope of $P_S(s)$ is maximum and equal to

$$\alpha = 0.4|\ln 0.4|\frac{2\sqrt{2}\xi_J}{k_B T}\sqrt{1-s_0}. \tag{2.4}$$

The readout sensitivity is thus characterized by the width $\Delta I_p = I_0/\alpha$ of the interval of I_p over which $P_S(s)$ varies from almost 0 to almost 1 (sensitivity can be defined here as $1/\Delta I_p$), and one has

$$\Delta I_p = 1.2\left(\frac{k_B T}{\varphi_0}\right)^{2/3} \ln\left(\frac{\nu_p \tau}{|\ln 0.4|}\right) I_0^{1/3}. \tag{2.5}$$

Figure 2.8 shows iso-ΔI_p in the $\mathrm{i}_0 - C_r$ plane, as well as ν_p and Q, T=40 mK, $\tau = 10$ ns and taking $R_l = 50\Omega$ as the only element seen from the oscillator. The sensitivity increases slowly when I_0 is decreased. Moreover, resolving a small ΔI_p out of a small I_p is technically easier than out of a larger I_p, which also pushes to choose a low I_0 for the readout junction. However, I_0 needs to be larger than a few hundreds of nA in order to detect the switching fast enough in practise. Furthermore, reducing the critical current decreases Q, which can change the switching regime. Indeed, below a critical value $Q \simeq 1$, the escape out of the readout junction does not trigger the switching automatically since the junction can be retrapped in the next well. This noisy retrapping regime should definitively be avoided.

Besides, C_r has to be placed very close to the qubit, which imposes some restrictions on its shape and size. We have developed two techniques to fabricate multi-layer capacitors with high dielectric permittivity (see Annex D). The maximum capacitance available is about 3-4 fF/μm^2 and the size is limited to a few hundreds of μm^2 to avoid resonances below 20 GHz. C_r has thus to be definitely lower than 4 pF. Last but not least, the currents to be discriminated differ at best by 15 nA, as found in 2.1.1 (see Fig. 2.3). We are thus left with the white region of Fig. 2.8 for the possible values of (I_0, C_r).

Since a large C_r is also needed for reducing decoherence and a large difference between the plasma and qubit frequencies is desirable, we estimate that a critical current $I_0 \approx 0.65\mu$A and a capacitance $C_r \simeq 3$pF (dot in Fig. 2.8), which yield a bare plasma frequency $\nu_p \simeq 4$ GHz, provide a reasonable

trade-off between all requirements. The sensitivity is however barely sufficient.

A further issue to address is the possible crossing of the qubit and plasma frequencies during the readout ramp. Indeed, in the experiment, the qubit is ideally manipulated at $\delta = 0$ and then brought close to $\delta/2\pi \simeq 0.45$, where the difference between persistent currents is maximum. The qubit frequency ν_{01} drops down from 17 GHz to about 3 GHz (for $E_J = 0.97$ K, $E_C = 0.51$ K, and $d < 5\%$), while the plasma frequency ν_p decreases from 4 to 2 GHz. The crossing is thus avoided.

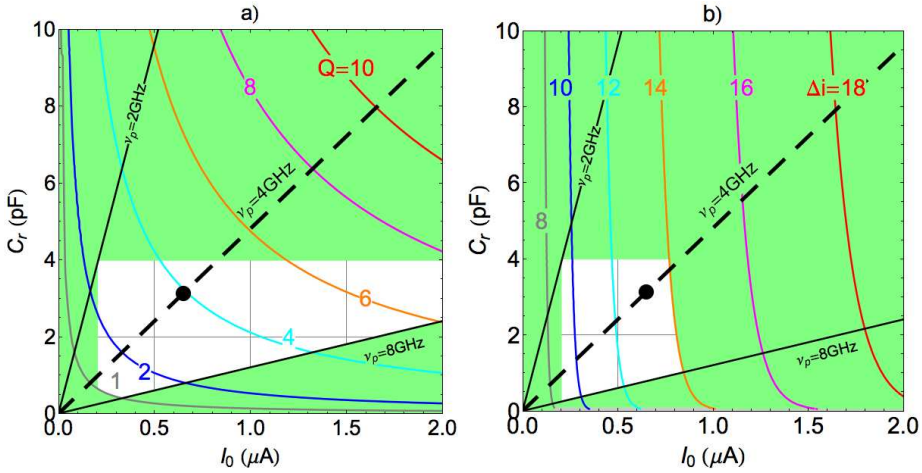

Fig. 2.8. Choice of readout oscillator parameters. a) Iso-Q curves (color lines) and iso-ν_p (black lines) in the $I_0 - C_r$ plane at zero bias current. b) Iso-Δi curves (color lines). The dash line indicates the chosen plasma frequency $\nu_p = 4$ GHz. Green areas are discarded to avoid retrapping, to get small enough capacitor, a sufficiently low ν_p, and a sufficient sensitivity. Black dot indicates our final target point

2.1.3.2 Minimization of the readout line induced decoherence

The relaxation rate $\Gamma_{rel}^{\delta/2\pi}$ due to the readout circuit is calculated from Eqs. (1.20)-(1.23)- (1.24) of section 1.1.8:

$$\Gamma_{rel}^{\delta/2\pi} = \frac{\pi}{2}\left|\frac{2\pi}{e}\langle 0|\,\widehat{I}\,|1\rangle\right|^2 \frac{1}{64\pi^4}\frac{h^2\nu_{01}}{2\pi\xi^2}2R_k\frac{Re[Y(\nu)]}{|1+i2\pi\mathcal{L}_J Y(\nu_{01})\nu_{01}|^2}. \quad (2.6)$$

As $\nu_{01} >> \nu_p$, the environment seen by the qubit reduces to C_r in parallel with R_l, and

$$\Gamma_{rel}^{\delta/2\pi} = \frac{2}{e^2}\left|\langle 0|\,\widehat{I}\,|1\rangle\right|^2 \frac{1}{2\pi^2 R_k R_l \nu_{01}^3}\frac{1}{C_r^2}, \tag{2.7}$$

where the matrix element $\langle 0|\,\widehat{I}\,|1\rangle$ depends on the asymmetry d The variations of the relaxation time $T_1 = 1/\Gamma_{rel}^{\delta/2\pi}$ through the readout circuit line with respect to I_0, C_r, and d are shown in Fig. 2.9. One deduces that C_r >2 pF in order to get $T_1 > 1$ μs, which is compatible with $C_r = 3$ pF, as chosen in the previous section.

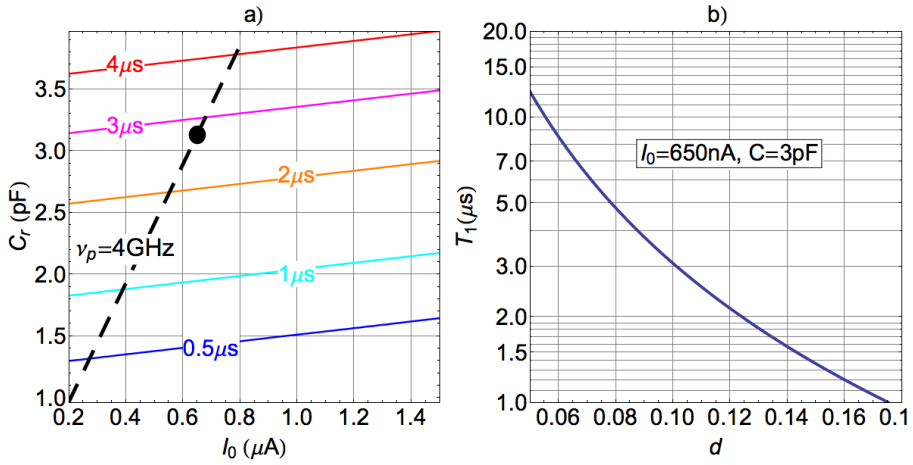

Fig. 2.9. Readout circuit induced relaxation. a) Iso-T_1 contours (colored lines) in the $I_0 - C_r$ plane at optimal point, and assuming a 50Ω impedance for the readout line. Dashed line corresponds to the target $\nu_p = 4$ GHz selected on Fig. 2.8. b) T_1 as a function of d for the selected parameters indicated by a dot in panel a.

We now check that the readout line circuit does not induce too much dephasing. The contribution to T_φ of the readout line admittance Y is calculated from Eq. (1.20), (1.23) and (1.27), to first order in δ:

$$\Gamma_{readout,\delta/2\pi}^{\varphi} = \frac{R_k}{32}|\langle 0|\,\widehat{I}\,|0\rangle - \langle 1|\,\widehat{I}\,|1\rangle)|^2 \frac{k_B T}{(\varphi_0 I_0)^2} Re[Y(\nu=0)]R_k. \tag{2.8}$$

with $R_k = h/e^2$ the quantum of resistance, $Re[Y(\nu=0)] = 1/(\mathrm{R}_l + \mathrm{R}_b + 50)$ (see Fig. 2.7) and $\mathrm{R}_b \simeq 500\Omega$ to develop a voltage $\mathrm{R}_b I_0$ at switching below the gap voltage ($\Delta/2e$). This expression gives $T_\varphi > 100\mu$s for $\delta \in [0, 0.1\times 2\pi]$. The readout line induced dephasing is thus not a limiting factor for the design.

Choice of readout oscillator parameters

As a summary, our selected trade-off is a bare plasma frequency $\nu_p \lesssim 4$ GHz with a quality factor $Q \simeq 4$ obtained with a critical current $I_0 = 650$ nA and a parallel capacitor $C_r = 3$ pF. As the critical current density has already been set to 1.1A/cm^2 (for fabrication of the CPB), one deduces an area $A = 1.1\mu$m^2 for the readout junction.

2.1.4 Choice of the coupling strength

Finally, the last parameter to determine is the coupling capacitance C_g between the two quantronium islands. From section 1.2.1 (Eq. (1.51)), the expression of the coupling frequency is
$\nu_{cc} = 4 \left| < 0|\widehat{N_a}|1 >< 1|\widehat{N_b}|0 > \right| E_{\Sigma a} E_{\Sigma b}/hE_{cc}$.
This coupling frequency is almost independent on δ, but strongly depends on the E_J/E_C ratio. For the selected values of E_J and E_C, one obtains ν_{cc} =2.45 MHz.aF$/C_c$. Ideally, we would like ν_{cc} ten times smaller than the maximum Rabi frequency (500 MHz), and ten times larger than the decoherence rate, which is expected in the range $1-10$ MHz. A convenient value is thus around 100MHz, which leads to $C_c = 80aF$.

We now discuss the consequences of moving one qubit away from its optimal point for the on-resonance coupling scheme. The required δ phase shift is smaller than $0.1 \times 2\pi$ rad provided the difference between the transition frequencies at the optimal points is smaller than 600 MHz. Such a δ shift away from the optimal point is in fact large, and induces a sizeable decrease of the dephasing time T_φ down to few tens of ns, as shown in Figs. 1.9-2.4.

However, the coherence time for coupled qubits is larger than the one for uncoupled qubits because each qubit behaves as a driving field for the other one. The coherence time $T_{\varphi,SWAP}$ within the subspace $\{|\Psi_1\rangle, |\Psi_2\rangle\}$ can be calculated following the method described in section 1.1.9 for a single quantronium subject to δ and N_g noises, but with $\{|\Psi_1\rangle, |\Psi_2\rangle\}$ playing now the role of $\{|0\rangle, |1\rangle\}$. This leads to

$$T_{\varphi,SWAP} = \frac{1}{\frac{2}{\nu_{cc}} \left(\frac{\partial \nu}{\partial(\Delta\nu/2\pi)} \right)^2 \frac{2}{7.2} A \ln(1/\omega_{ir} T_\varphi)}, \tag{2.9}$$

whose variations with δ are shown in Fig. 2.10. The $0.1 \times 2\pi$ rad phase excursion mentioned above yields $T_{\varphi,SWAP} \sim 500$ns, a value significantly longer than the duration of an ISWAP operation.

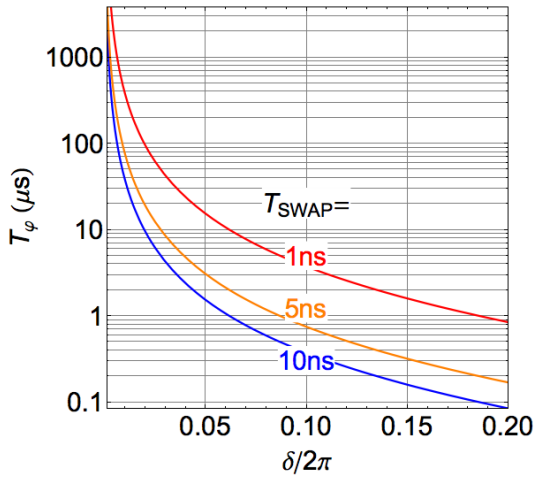

Fig. 2.10. Dephasing time $T_{\varphi,SWAP}$ of a superposition $\alpha\,|\Psi_1\rangle + \beta\,|\Psi_2\rangle$ with respect to the phase δ for different swapping time $T_{SWAP} = 1, 2, 10$ ns.

2.2 Quantroswap design and fabrication - Experimental Setup

Starting from the theoretical considerations developed in the previous section, we report here how a quantroswap experiment was prepared. The design of quantroswap chips is first presented, by discussing the gate and coupling capacitances, the readout resonator layout, as well as the techniques used for getting rid of out-of-equilibrium quasiparticles. Process steps involved in the fabrication of the chip are then described. Then, we show how the chip is connected to the electrical circuitry setup along the dilution fridge through a printed circuit board fitted with microwave connectors. Finally, we present the electronics and the software we have made for controlling the experiment.

2.2.1 Design of a quantroswap sample

2.2.1.1 Qubit-qubit coupling and gates

As already mentioned, the two quantronium islands have to be coupled by a fixed capacitance of the order of 80 aF (see section 2.1.4). Such a low capacitance is easily obtained by placing the islands next to one another, in a coplanar geometry. Furthermore, it allows making them small in order to maximize the output rate of out-of-equilibrium quasiparticles that could possibly reach them. Their exact shape (two rectangles supplemented with two lateral fingers with variable length) is shown on the design plot of the electrodes at the center of the device (see Fig. 2.11). A home-made 2D electrostatic solver (see Fig. 2.12) was used to determine the capacitance matrix of the circuit. As shown in the figure, the solver determines the charge distribution on all electrodes when one of them, say electrode i, is set at a finite potential (equal to 1 for convenience), with all the other ones being grounded. The solver operates by minimizing iteratively the electrostatic energy of the whole charge distribution. The total charge Q_j found on any electrode j then provides the capacitance $C_{ij} = (\epsilon_r + 1)/2Q_j$, where ϵ_r is the dielectric constant of the wafer. The ratio [electrode thickness/gap between electrodes] is in all cases small enough to warrant the validity of the 2D approximation. Note however that, for a Si wafer oxidized on a thickness d, the effective dielectric constant is an average over the Si and SiO_2 ϵ_r values, which depends on the ratio [gap between electrodes/d]. This correction is in practice relevant only for the two islands and their gate. The validity of the approximations was checked using the electromagnetic 2.5D simulator SONNET operated at low frequency. The conclusion is that our simple electrostatic solver provides good enough results for our purpose.

We have performed detailed capacitance calculations only within a small rectangular field for the sake of limiting the calculation time. We estimate that the long range contribution to the capacitance of an island is small. Indeed,

this long range contribution are completely screened, and long-distance electric fields are very weak. Consequently, the gate crosstalk ratio, i.e. the ratio $C_{g_A-island_A}/C_{g_B-island_A}$ with $C_{g_A-island_A}$ and $C_{g_B-island_A}$ the capacitances between gate A and island A and between gate B and island A respectively, is mainly determined by the local geometry of the electrodes in the vicinity of the islands. We have tried to minimize this crosstalk with the solver by increasing the size of the guard electrodes, and by decreasing the distance between each island and its gate. The best design leads to a 20% crosstalk. Minimizing it further would require a non coplanar technology for the gate capacitors. Finally, we were lead to design values for the gate capacitors and for the quantronium-quantronium coupling capacitance equal to 10-20 aF and 30-50 aF, respectively.

Gate lines on the chip were designed as superconducting (aluminum) coplanar waveguides (CPW) with one central wire and two lateral grounds, as shown in Fig. 2.11 and 2.14. They share one of their lateral grounds (central electrode in the figure) close to the islands. The impedance of the CPW is designed to be 50 Ω up to 20GHz and down to a distance of 100 μm (1% of the wavelength) from the islands. Closer to the islands, the lateral grounds get closer to the gates to minimize gate crosstalk. The gate lines were designed to be entirely fabricated either by electron beam lithography or by optical lithography.

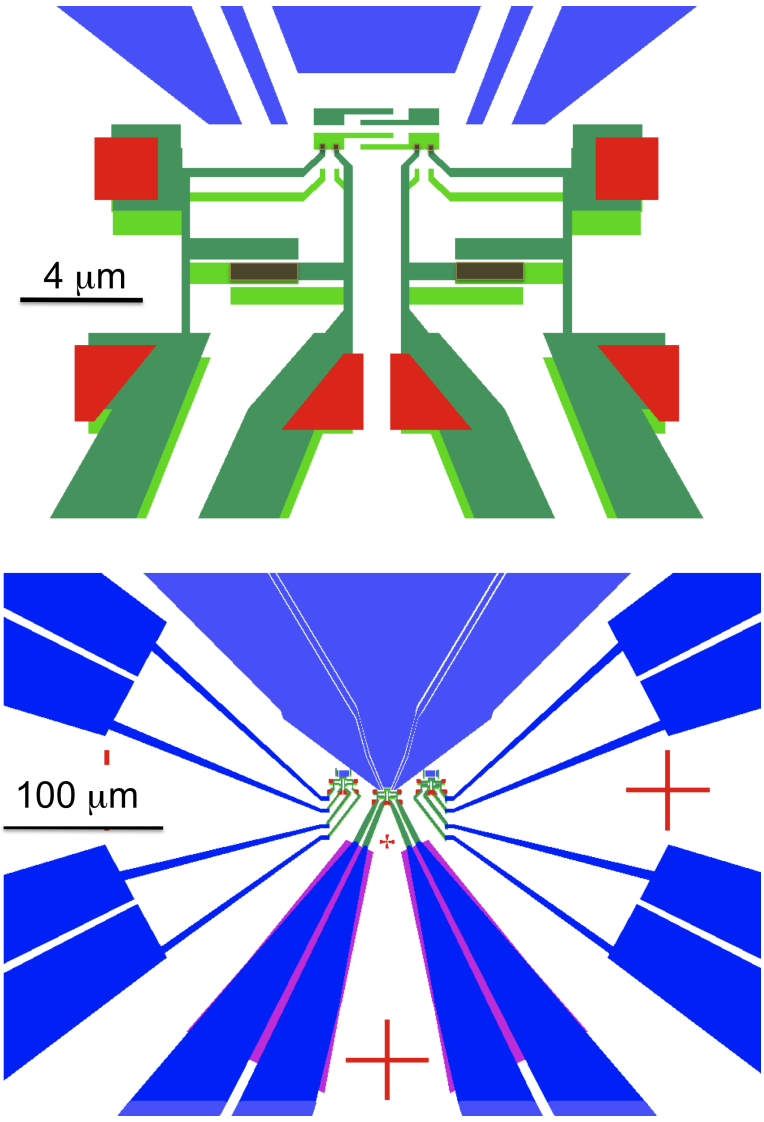

Fig. 2.11. Design pattern of a quantroswap sample. a) Central part of the device showing the two gates (blue) and the two quantroniums (green) as they can be obtained with a double-angle evaporation technique. The Josephson junctions between two overlapping aluminum layers are in brown. The four bottom electrodes lead to the readout capacitor. Red squares (partly overlapped) are gold pads aiming at quasiparticles. b) Larger view of the device showing the gates (top center) and the leads in blue, as well as the readout overlap capacitors in purple overlapped by blue leads (bottom center). Two quantroswap twins are also to be fabricated for characterization purpose.

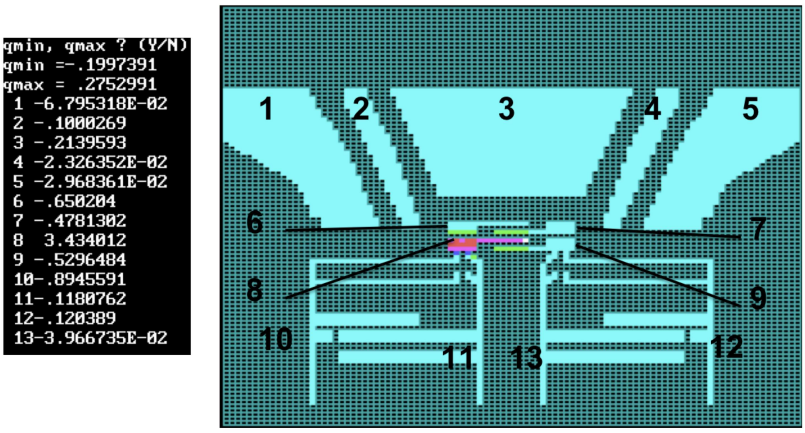

Fig. 2.12. Determination of the capacitance matrix of the quantroswap using a 2D electrostatics solver. Colors encode the charge density. Here the electric potential of one of the islands (8) is set to 1; all other electrodes are set to 0 potential, including the other island (9), the gate lines (2 and 4), the guards (1,3, 5) and the leads (10,11,12,13), as well as the islands images (6, 7) produced by the fabrication technique. The total charges of each electrode i displayed on the left encode the C_{i8} capacitances. After minimizing the electrostatic of the system, the solver finds $C_{28} = 6.7$ aF, $C_{48} = 1.55$ aF and $C_{98} = 35$ aF. A few runs lead to the relevant C_{ij} and allow to calculate the gate, coupling, and crosstalk capacitances.

2.2.1.2 Quantronium loops and readout resonator

The quantronium loop areas were made as small as possible in order to minimize the influence of flux noise. However, these areas have to be sufficiently large in order to be able to apply one or several flux quanta, given the coil setup in the fridge. The two loops are separated only by a fraction of a micron and we have checked that the inductive coupling between them is absolutely negligible even at readout when the current is maximum in the readout leads. Besides, the width of the superconducting wires is made small to avoid trapping magnetic vortices.

The design value of the critical current of the readout junctions is 650 nA, as determined in the previous section. These junctions are designed as rectangles with an aspect ratio as close of one as possible given the fabrica-

tion constraints, in order to avoid magnetic field penetration and associated diffraction effects.

The shunt capacitors of the readout resonators have a design value of the order of 3 pF (see section 2.1.3.2). They are fabricated as overlap capacitors in order to keep their size below a few hundreds of μm, which avoids resonances below 18 GHz. This small size also implies a large dielectric constant, ideally above 10. Furthermore, to simplify fabrication and avoid having to pierce vias in the structure, each readout capacitor consists in two capacitors in series, made up of to coplanar electrodes overlaping a third one. To place the capacitors not too far from the quantroniums and to avoid a too large series inductance that would decrease their effective capacitance, we choose an elongated shape with a width that increases with the distance to the qubits (see Fig. 2.11). As a result, the capacitors are placed at a distance of 80 μm from the quantronium loops, which introduces a series inductance of about 80 pH, i.e. 16% of the Josephson inductance of the readout junction. Two types of capacitors with two different dielectric materials ($Al0_x$ and Si_3N_4) have been fabricated and tested. Their fabrication and characterization are described in more details in Annex D.

The capacitor terminals have a coplanar stripline geometry with a wave impedance of about 50 Ω, which is connected through a two to three wire transition to a true 50 Ω coplanar waveguide going to one of chip edges (see top right panel of mask 1 in Fig. 2.14).

2.2.1.3 Getting rid of out-of equilibrium quasiparticles

In section 1.1, we have described the quantronium as an ideal device with perfect superconducting electrodes, in which all electrons are paired. In reality, out of equilibrium quasiparticles (QP) are commonly found in Josephson devices at low temperature. Furthermore, the switching readout method produces a large number of them in the quantronium leads, and recovering thermodynamical equilibrium takes a long time of about 1-10 ms. Now, from the quantronium point of view, a single QP entering its island corresponds to a state that does not belong to the Hilbert space considered in section 1.1.2, and has the effect of shifting N_g by $1/2$ and making the qubit dephase and also possibly relax. In order to minimize this QP poisonning of the island, we have used two well known technical tricks: gap engineering and quasiparticle trapping.

These two tricks are explained on Fig. 2.13, which shows the energy diagram of QPs in normal and superconducting aluminum electrodes with different thicknesses. First, the superconducting energy gap Δ of aluminum happens to increase for thinner films. A potential step $\Delta_{island} - \Delta_{lead}$ of a few microvolts, making the entrance of QPs in the island thermodynamically unfavorable, can thus be created by choosing island and lead thicknesses of about 12 nm and 45 nm, respectively (these are our target values).

Second, QP can be trapped in a non superconducting metallic electrode, which plays the role of a potential well with depth Δ_{lead}. When entering the well, the QPs thermalize with other conducting electrons, in thermal contact with the phonon bath [78]. Our design includes three such QP traps per quantronium (see Fig. 2.11). One is located as close to the island as possible, while the other two are located on both sides of the readout junction. These traps are in good contact with the quantronium leads. Consequently they weaken the superconductivity of these leads by inverse proximity effect. They are thus placed sufficiently far not to perturb the quantronium superconducting loop. They made of gold and appear as bright areas in Fig. 2.15.

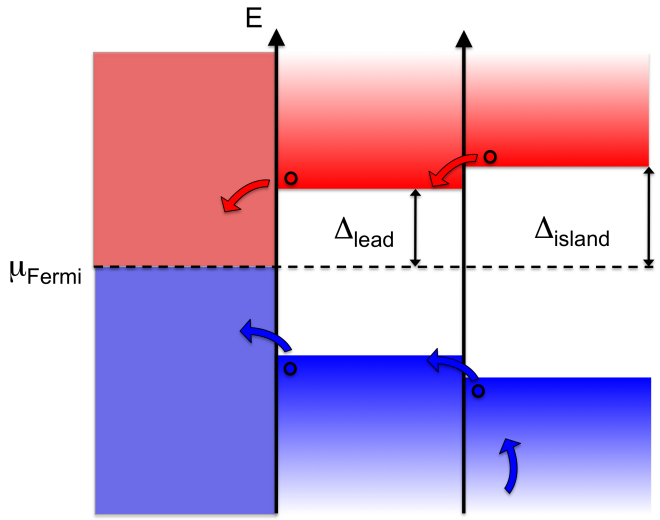

Fig. 2.13. Removing quasiparticles from the quantronium islands. The graph represents the quasiparticle density of state in a non-superconducting electrode (left), a thick superconducting Al lead (center), and thin Al island (right). Electron-like (red) and hole-like (blue) quasiparticles in the superconducting island (right) tend to tunnel to the lead and then to diffuse to the normal metal, where they get thermalized and trapped.

2.2.2 Fabrication of quantroswap samples

The samples were fabricated on oxidized silicon or saphire 2 inch wafers comprising 57 5×5mm^2 chips per wafer. The fabrication masks use optical lithog-

raphy at the scale of the whole wafer for the QP traps, for the readout capacitors, and for the leads. After the wafer has been cut with a dicing saw, e-beam lithography is used at the chip level for making the quantroniums, whose parameters have to be adjusted chip by chip.

2.2.2.1 Wafer process flow

The fabrication of a wafer involves three optical lithography steps, three metal depositions and one dielectric growth. Details on the optical process is given in Annex C. The three optical masks used are shown at different scales on Fig. 2.14.

The first step (see mask 1 in the figure) is the fabrication of the bottom electrode of the readout capacitors: a 40 nm thick aluminum layer is deposited by e-beam evaporation. The dielectric layer for the capacitors is then grown either by plasma oxidizing the aluminum at about 200°C (see Annex D) or by covering the whole wafer with a 15 nm thick layer of reactively sputtered silicon nitride (see Annex D).

The second step is the fabrication of the QP traps and of alignment marks for future e-beam lithography (see mask 2 in Fig. 2.14): a 30 nm thick gold layer is deposited by e-beam evaporation (see Annex C).

In a third step (mask 3), aluminum is deposited as in step 1 to form the top electrode of the capacitors, the quantronium gates, and the leads. A few things have to be noticed at this point: first, the gates have a sub-micron size and great care must be taken to perform a successful lithography. Second the alignment of this third mask (gates) with the second one (gold QP traps and alignment marks) is critical for future success of the e-beam lithography. Finally, notice that additional leads are available on the left and right sides of each chip for connecting quantroswap twins used for characterization purposes (see mask 1 in Fig. 2.14).

Then, the wafer is spin-coated with a 1 μm+0.1 μm thick bilayer of MAA/PMMA resists for subsequent e-beam lithography. In the case of a saphire wafer, the bilayer is covered with a 7 nm thick layer of evaporated aluminum to avoid charging effects during e-beam lithography. Finally, the wafer is cut with a dicing saw, and each chip is cleaned in propanol.

3)

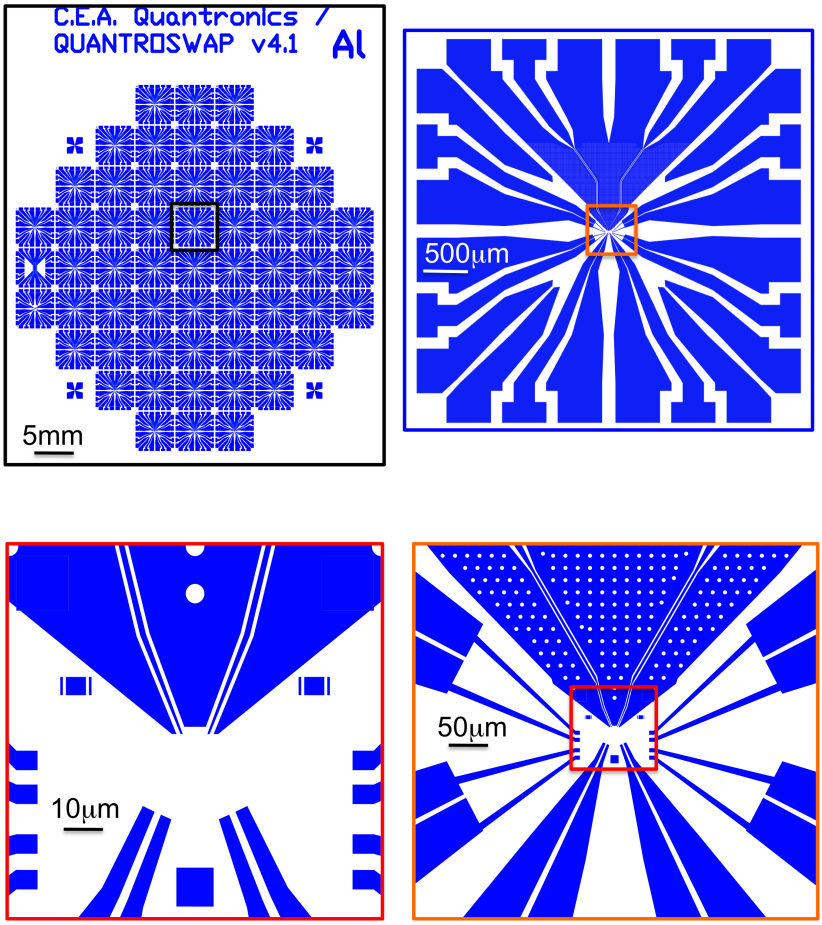

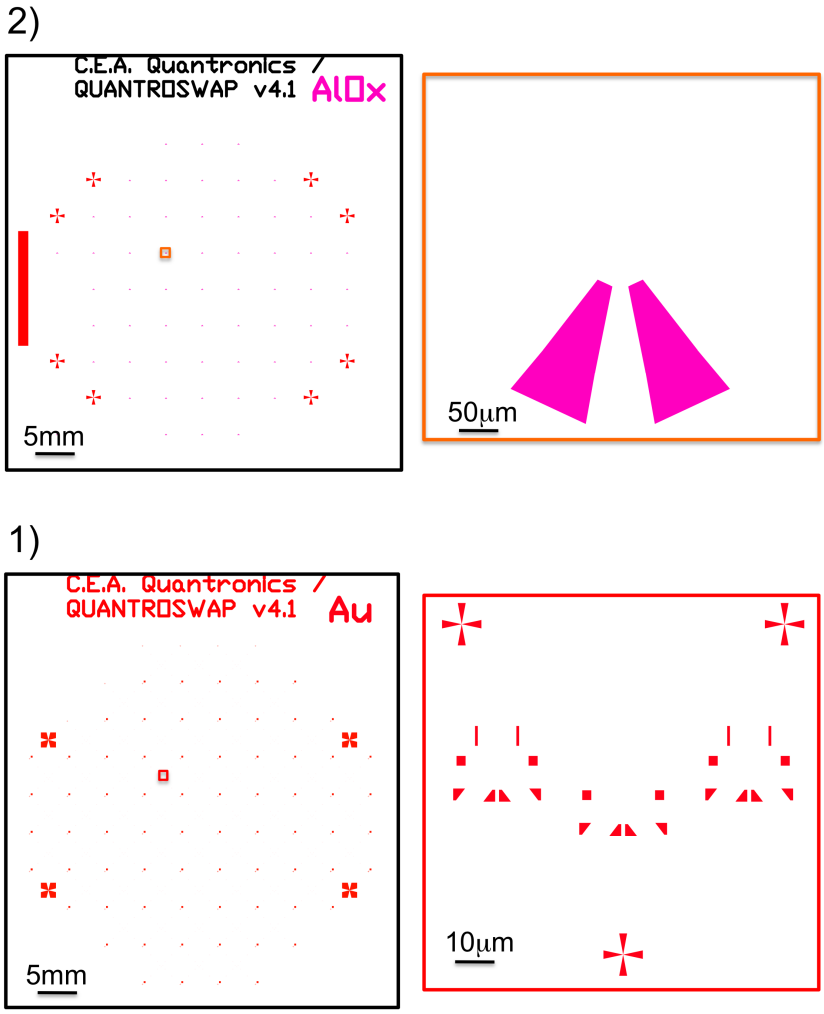

Fig. 2.14. Series of three optical masks used for fabricating quantroswap wafers (57 5×5mm^2 chips), shown at different scales. a) Third Mask used for the final Al deposition and lift-off of the top readout capacitor electrode, the gates, and the leads. The top panels show the mask the wafer (left) and chip (right) scale. Bottom panels show smaller scales. b) Second mask used for Au deposition and lift-off of the quasiparticles traps and alignment marks. c) First mask used for Al deposition and lift-off of the bottom electrodes of readout capacitors. Scales are indicated on each panels.

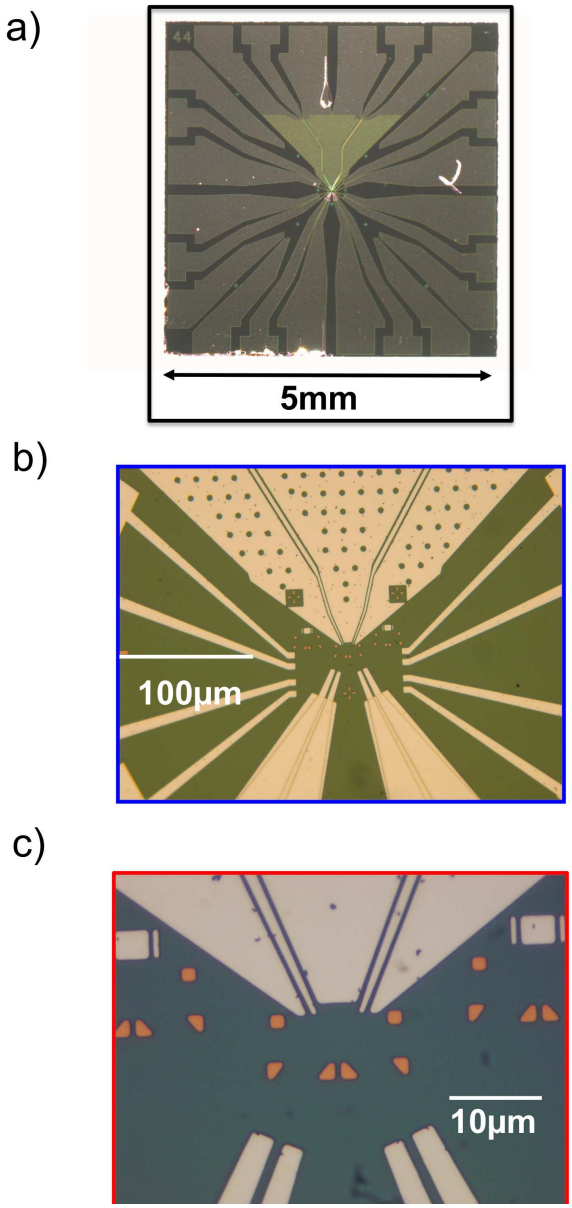

Fig. 2.15. Optical micrographies of a quantroswap chip before e-beam lithography. One can see the whole chip (a), the readout capacitor (bottom structure) and the $100\times100\mu\text{m}^2$ central area for e-beam lithography (b), as well as the central part with the gates (top electrodes), the readout leads (bottom electrodes), and the quasiparticles (small yellow pads)

2.2.2.2 Chip process flow

The quantroniums and the top electrodes of the readout capacitors are made chip by chip in a single pump-down by e-beam lithography and double angle shadow evaporation of aluminum (the principle of the technique is presented in Annex C). Figure 2.16 shows the e-beam lithography pattern designed for evaporating the two aluminum layers at opposite angles +/- 20° (angle between the axis perpendicular to the sample surface and the trajectory of evaporated Al atoms). Blue and green elements on the figure correspond to a nominal electron dose leading to openings in the mask, whereas orange elements correspond to a lower dose aiming at enlarging the undercut below the suspended mask (see Annex D). Note that the pattern includes an 100 μm^2 overlap (not shown) between each quantronium leg and its corresponding "optically pre-fabricated" lead. Note also that two additional pairs of quantroniums are included in the pattern (see Fig. 2.11) for characterization purposes and estimate of the parameter dispersion. These quantroswaps have the very same geometry and dose as those to be used in the experiment, except that one of the quantroniums of each pair has its readout junction open, whereas the other one has an open in the CPB arm.

E-beam exposure is performed in a XL30S FEI scanning electron microscope equipped with a Raith Elphy Quantum lithography system. A prealignment on optically made gold marks is performed with a 200 nm precision before exposure. Development of the exposed resist is done in a 1:3 MIBK/propanol mixture, at room temperature, during 1 minute. The sample is then dried and introduced in an e-gun evaporator with a base pressure of 10^{-7} mbar (resp. 10^{-6} mbar) at the level of the source (resp. sample). A gentle milling with few $10^{-16}\times$ 500eV Ar atoms/cm^2 is performed before depositing the first layer of aluminum, in order to warrant a good contact of the new pattern with the optically pre-fabricated leads and QP traps. Then, a 12 nm thick aluminum layer is deposited at 1nm/s and at angle -20°. It is oxidized at room temperature by introducing an 85%Ar-15%O_2 gas mixture in the vacuum chamber, during 10 minutes. After re-pumping, during a few minutes, a last 45 nm thick aluminum layer is deposited at the opposite angle. The resist is then removed by lift-off in acetone, and rinsed in propanol to obtain a circuit as that shown on Fig. 2.17. Finally, the tunnel resistances of the readout junction, of the CPB junctions in series, or of their parallel combination are measured at room temperature for the three quantroswaps on the chip.

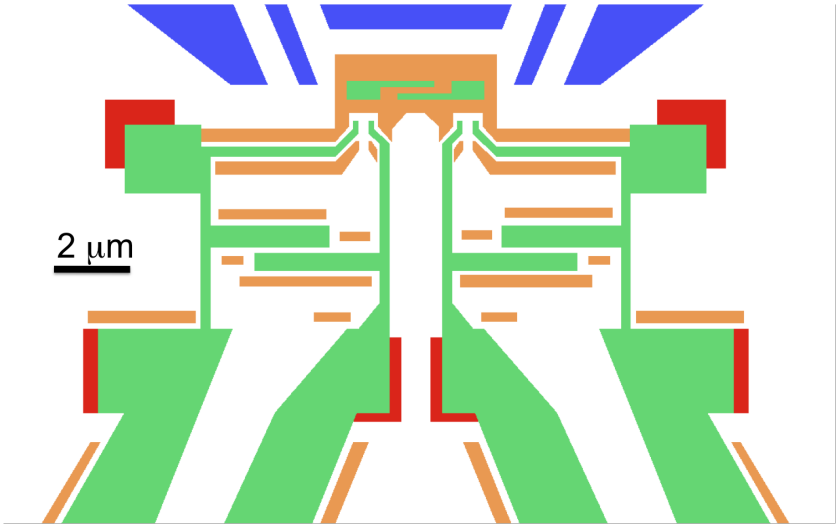

Fig. 2.16. E-beam exposure pattern of the central part of the quantroswap circuit. Green areas correspond to openings though the PMMA resist, that define the various quantroswap electrodes, whereas orange elements corresponds to lower exposure dose aiming at increasing the undercut below the suspended mask. Blue and red areas represent the optically pre-fabricated gates and quasiparticles traps.

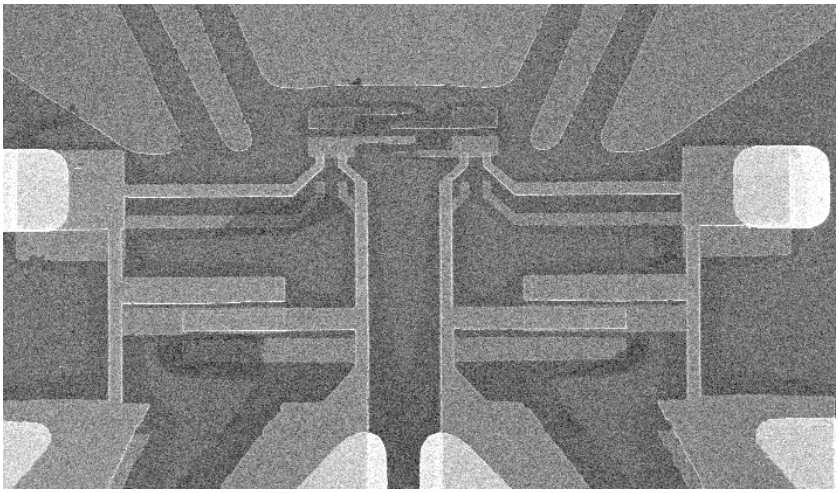

Fig. 2.17. Scanning electron micrography of the central part of the quantroswap obtained after double angle evaporation of aluminum through the mask defined in Fig. 2.16.

2.2.3 Connecting the chip to the rest of the circuit

After electrical characterization at room temperature, the chip is glued with a low melting temperature wax at the center of the printed circuit board (PCB) shown on Fig. 2.18. This PCB has a square lodging for the chip, so that its top surfaces and that of the chip are at the same level. It is made of a material (TMM10) with a relative dielectric constant (10) very close to that of silicon, and is designed to provide eight 50 Ω microwave CPW lines with the very same geometry as those on the chip. The gap between the chip and the lodging is of order 100 μm but could have been made smaller, taking into account the accuracy of the dicing saw that was used. The three stripes of a CPW line on the chip are wire-bonded to their corresponding stripes on the PCB, with two or three wires per strip. The lateral stripes of each CPW have vias through the PCB to a ground plane on the opposite side. The CPW lines on the PCB are terminated by a footprint optimized for soldered female microwave mini-SMP connectors. The typical reflection coefficient at the chip input is measured to be below -20 dB with such a setup. As already explained in section 2.1.3, our design includes a RC filter on each readout line to let fast readout pulses reach the readout junction, while preventing the qubit from seeing the electromagnetic environment behind the filter, at its transition frequency. These filters are implemented on the PCB with surface mounted microwave resistors and capacitors whose values undergo little variations when cooled at 20 mK. Each filter includes one R=50 Ω NiCr resistor inserted in the central strip of the CPW, and two 10 pF and two 1 pF SMC capacitors [69] between the central strip and the lateral grounds. Their transmission has been tested at 4K: their frequency cut-off at -3 dB is about 1 GHz and their attenuation is larger than 35 dB in the 6-20 GHz band. Characterization of the filters is documented in more details in Annex E.

The PCB with the chip, the filters, and the connectors is screwed in a copper case (see Fig. 2.18) with holes for male mini-SMP connectors. The cover of the case incorporates a small piece of microwave absorber for damping spurious microwave resonances in the box. It also incorporates a superconducting coil of inductance 0.12 H, located 3 mm above the chip, for flux biasing the quantronium loops. The outer surface of the case is plated with tin in order to avoid penetration of the external residual magnetic field. This case is anchored to the cold plate of a dilution refrigerator and the PCB is connected to the rest of the electrical circuit, as described now.

2.2.4 Electrical setup in the dilution refrigerator

The two quantroniums of the quantroswap pair are connected to separated and nominally identical circuits, although they share the same flux bias coil. Figure 2.19 gives an overview of this circuit along the dilution refrigerator, while Fig. 2.20 shows a picture of the setup between 600 mK and 20 mK. We describe now the gate and readout lines.

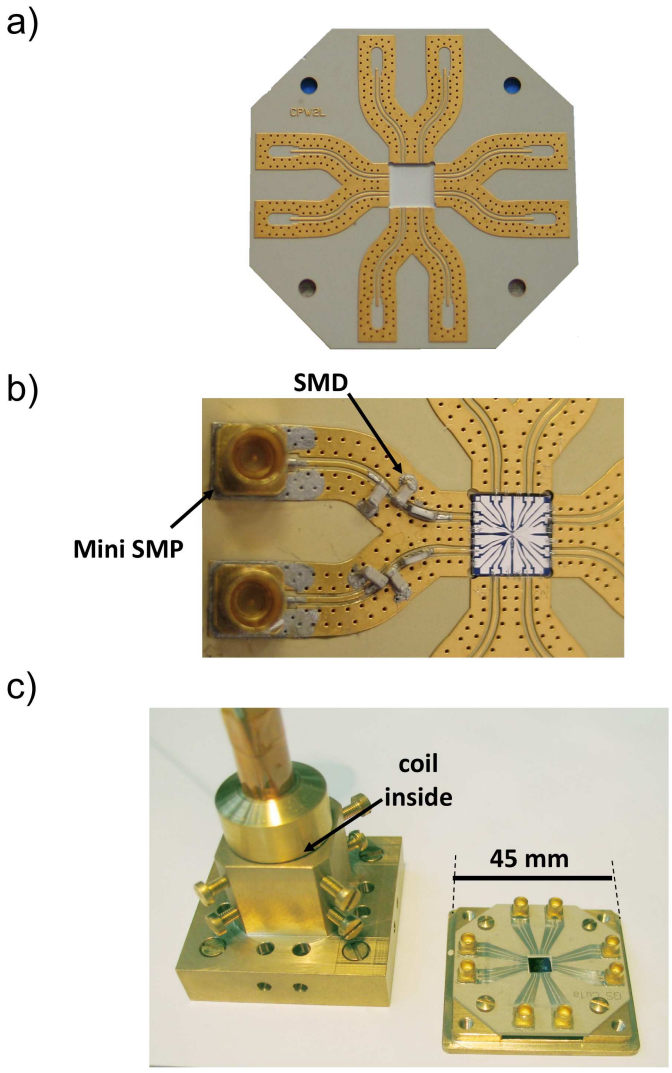

Fig. 2.18. Connecting the quantroswap chip to its electrical circuit. A Printed Circuit Board (a) with a central lodging for the chip is equipped with four mini-SMP microwave connectors (for gates and readout leads), and with Surface Mounted resistor and Capacitor for filtering the readout lines (b). The chip is glued in lodging (b)„ and wire-bonded. The PCB is inserted in a copper box with holes in front of the connectors, and which has a coil for flux biasing the quantroswap (c). The ensemble is anchored to the cold plate of a dilution refrigerator.

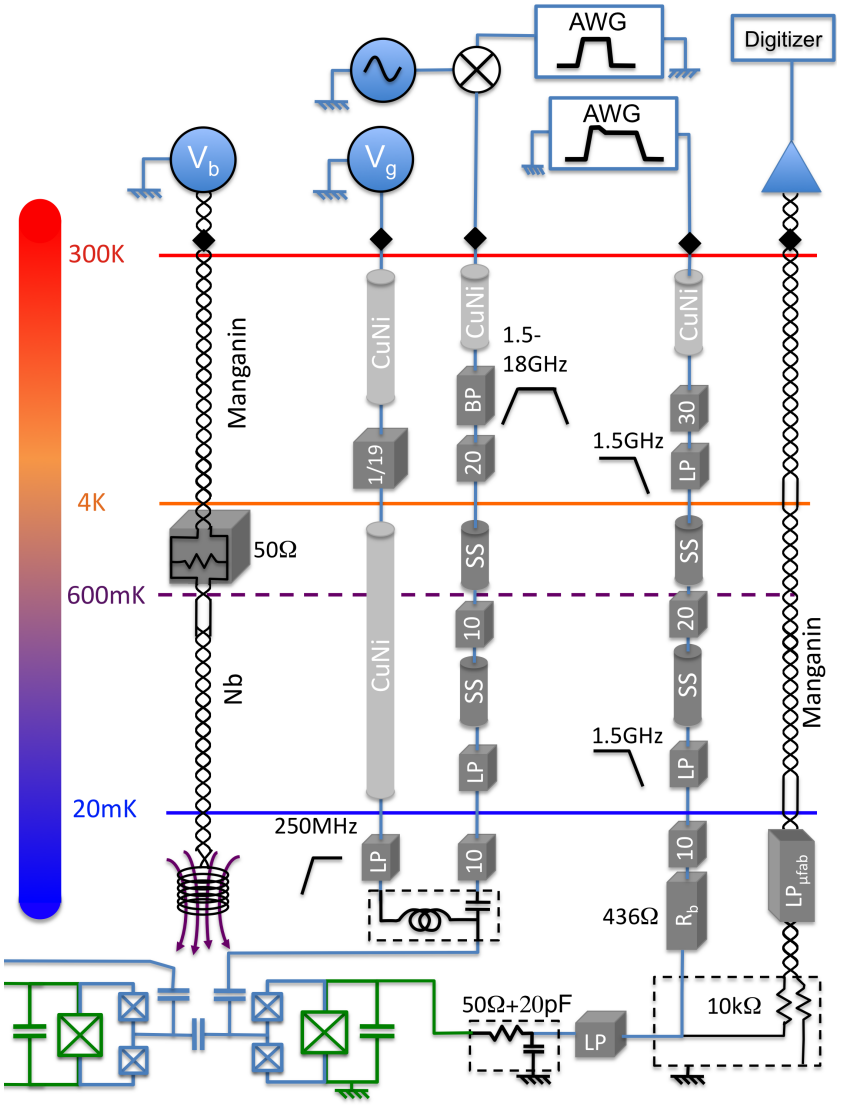
AWG
AWG
Digitizer
V_b
V_g
300K
4K
600mK
20mK
Manganin
CuNi
CuNi
CuNi
1.5-
18GHz
BP
20
1/19
1.5GHz
30
LP
SS
50Ω
10
SS
LP
Nb
CuNi
1.5GHz
SS
20
LP
Manganin
250MHz
LP
10
10
436Ω
R_b
$LP_{\mu fab}$
50Ω+20pF
LP
10kΩ

Fig. 2.19. Electrical wiring of the quantronium experiment. The two quantroniums share a common magnetic biasing line (left vertical line). Both of them being connected to nominally identical circuits, only the circuit of the right quantronium is shown here. This circuit comprises a DC gate line and microwave gate line (two vertical lines in the center) connected to the quantronium gate through an inductive bias tee, and a bias readout line and measurement readout line (two vertical lines on the right) connected to the sample through a special resistive tee. The gray boxes are NiCr microwave attenuators (attenuation indicated on the box). LP and BP boxes are low-pass and band-pass filters (cut-off frequencies indicated beside). Light gray cylinders are coaxial cables labeled according to the material of their inner conductor (CuBe-CuNi, CuNi-CuNi, StainlessSteel-StainlessSteel). The coil line and the measurement readout line are shielded twisted pairs whose inner wire material is indicated beside. The top part of the figure shows the room-temprature DC power supplies (V_b, V_g), the microwave and arbitrary waveform generator used for the different lines, as well as the amplifier and digitizer used for measurement. More details on this room temperature electronics is indicated on Fig. 2.22 . The color scale on the left indicates the temperature of the various elements.

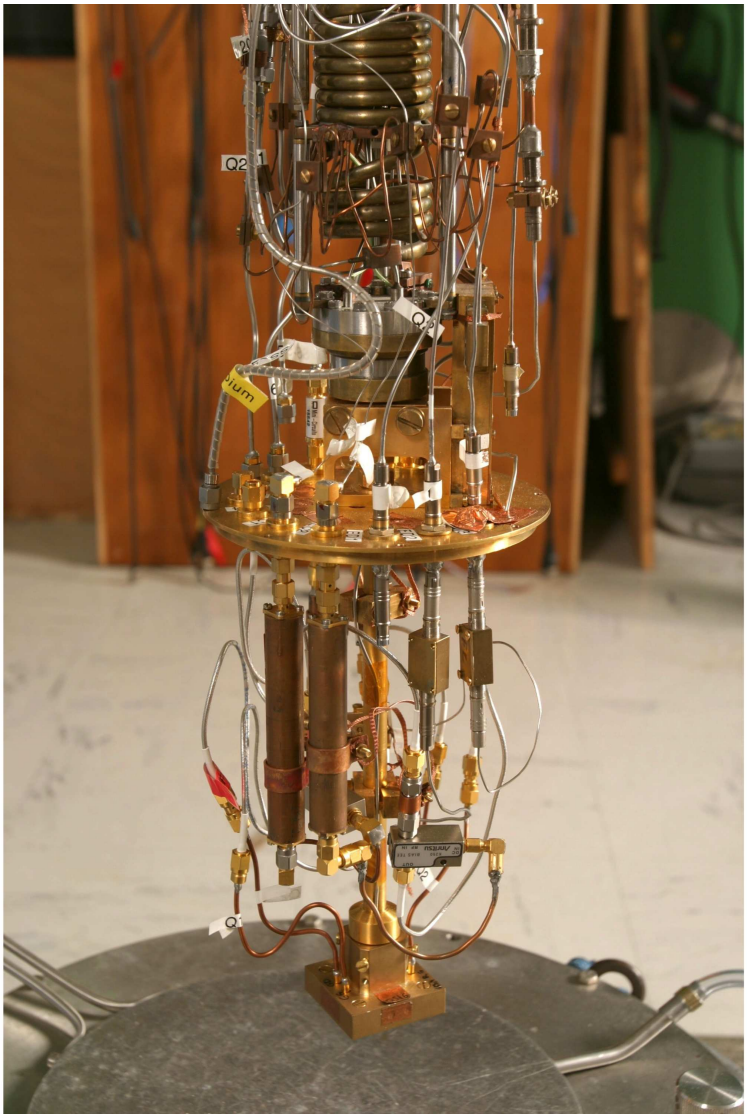

Fig. 2.20. Picture of the 20 mK to 600 mK stage of the experiment with the complete wiring.

2.2.4.1 Gate lines

Each quantronium gate is connected through an Anritsu bias tee placed at 20 mK to a DC and to a microwave gate line.

The DC line is heavily filtered with a copper powder filter at 20 mK and with lossy NiCr coaxes going from dilution temperature to room temperature. The total distributed resistance and capacitance of these coaxes are 480 Ω and 200 pF. A 10-180 kΩ resistance divider (factor 19) is inserted at 4K.

The microwave gate line is made of cryogenic (i.e. low thermal conductivity) 50 Ω microwave cables, in SS/SS (stainless steel) between 30 mK and 4 K, and in CuBe (inner wire)/ CuNi (external ground) between 4K and room temperature. This line has to have a transmission as smooth as possible in the microwave domain and a large attenuation so that the effective temperature T_{eff} of the 50 Ω impedance as seen from the qubit is below $h\nu_{01}/k_B$. For this purpose, several cryogenic (NiCr) 50 Ω matched SMA attenuators are inserted along the line. As already explained in section 2.1.2.1, the maximum allowed attenuation is given by the target value of the quantronium gate voltage and by the maximum available power. Besides, each element i placed at a given temperature T_i, if properly thermalized, plays the role of a 50 Ω thermal noise source. As long as $T_i > h\nu_{01}/k_B$, the game is thus to adequatly distribute the total attenuation so that the noise of every element i is attenuated by element $i+1$ with a factor larger than T_i/T_{i+1}. When $T_i \sim h\nu_{01}/k_B$, the attenuation has to be large enough in order to have an effective temperature lower than $h\nu_{01}/k_B$ after the penultimate elements. This problem can be solved graphically, as shown on Fig. 2.21, for the case of ν_{01}=17 GHz and -20 dB, -10 dB, and -10 dB attenuators placed respectively at 4K, 600 mK and 20 mK (taking into account the 3 dB additional attenuation by cryogenic coaxes). The figure shows that an effective temperature of $kT/h\nu_{01} \sim 0.2$ can be reached, which corresponds to an upper bound of 1% for the qubit excited state population.

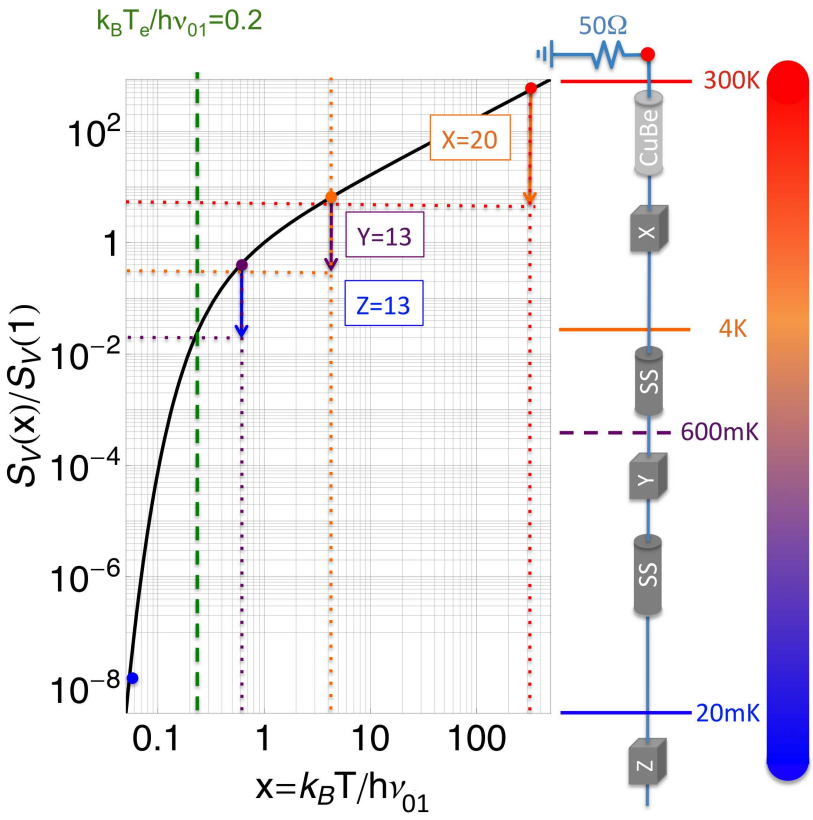

Fig. 2.21. Graphical determination of the attenuation at the qubit frequency ν_{01} along high-frequency lines. Left: Normalized voltage spectral density (black curve) at frequency ν_{01} as a function of the temperature T expressed in reduced unit $x = k_BT/(h\nu_{01})$. Colored dots show the noise of the 50 Ω impedances of the source and of the three attenuators X, Y, Z placed at 300K, 4K, 600mK and 20mK, respectively. Arrows show the attenuation applied to each of these noises by the attenuator placed immediately below (noise from 300K is attenuated by X, whose noise is attenuated by Y, whose noise is attenuated by Z). The goal is to have a spectral density of noise, such that the equivalent temperature is lower than $h\nu_{01}/k_B$ (green dashed line). The three attenuations X, Y, Z correspond to nominal attenuations of 20,10,and 10, respectively, supplemented by the coax losses (see text).

2.2.4.2 Readout lines

Starting from the PCB, a readout line is connected through a home made tee, placed at 20 mK, to a coaxial current bias line on one side and to a high impedance heavily filtered bifilar voltage measurement line on the other side (see Fig. 2.19). The tee is actually a through on the bias side; on the measurement side, it forms a bililar line from the qubit readout line and from its own ground. Two 10 kΩ resistors are inserted in the tee at the extremity of these two wires to provide a high impedance as seen from the bias side, and prevent any perturbation on the bias pulses.

The bias line includes a 436 Ω bias resistor placed at 20 mK, which is made big (several resistors in parallel and in series) for electron thermalization purposes. Although the spurious capacitance of this element was kept as low as possible, it limits the rise time of the bias at about I_0 (critical current of the readout junction) in 2-4 ns. The line is then made (see Fig. 2.19) of 50 Ω SS/SS and CuNi/SS coaxial cables, as well as of commercial 50 Ω attenuators and 1.3 GHz low pass filters (Mini-circuit VLFX-1350 and VLP-16) . The total attenuation of the line from DC to 1 GHz is about 60 dB.

The voltage measurement line is an RC distributed bifilar twisted pair made up of two Manganin wires in a SS capillary. In addition, a home made microfabricated distributed RC filter [79] is inserted in each wire at 20 mK. The effective RC time of the line is of order 1 μs, while its attenuation from 100 MHz to 20 GHz is larger than - dB.

2.2.5 Room temperature electronics

2.2.5.1 Qubit and readout control

The coil and each DC gate are biased with a commercial Yokogawa 7651 stabilized DC voltage source, further filtered above 1 Hz.

The microwave pulses for controlling the two quantroniums are generated by splitting the CW signal of an Anritsu 3692 microwave source and by mixing both outputs with DC pulses generated by an Agilent 81200 multichannel pulse generator, using Marki M8040 mixers, as described in Fig.2.22. Extra attenuators, filters and circulators are connected to these mixers in order to reduce the parasitic transmission of the mixers.

The current pulses used for tuning the quantroniums $\delta_{A,B}$ phases and for readout are made with a multichannel Tektronix 5014 arbitrary waveform generator having a DC-240MHz analog bandwidth. Since the noise temperature of the output signal is large, the output signal used is close to the maximum available voltage and is then attenuated by more than 20 dB before entering the fridge.

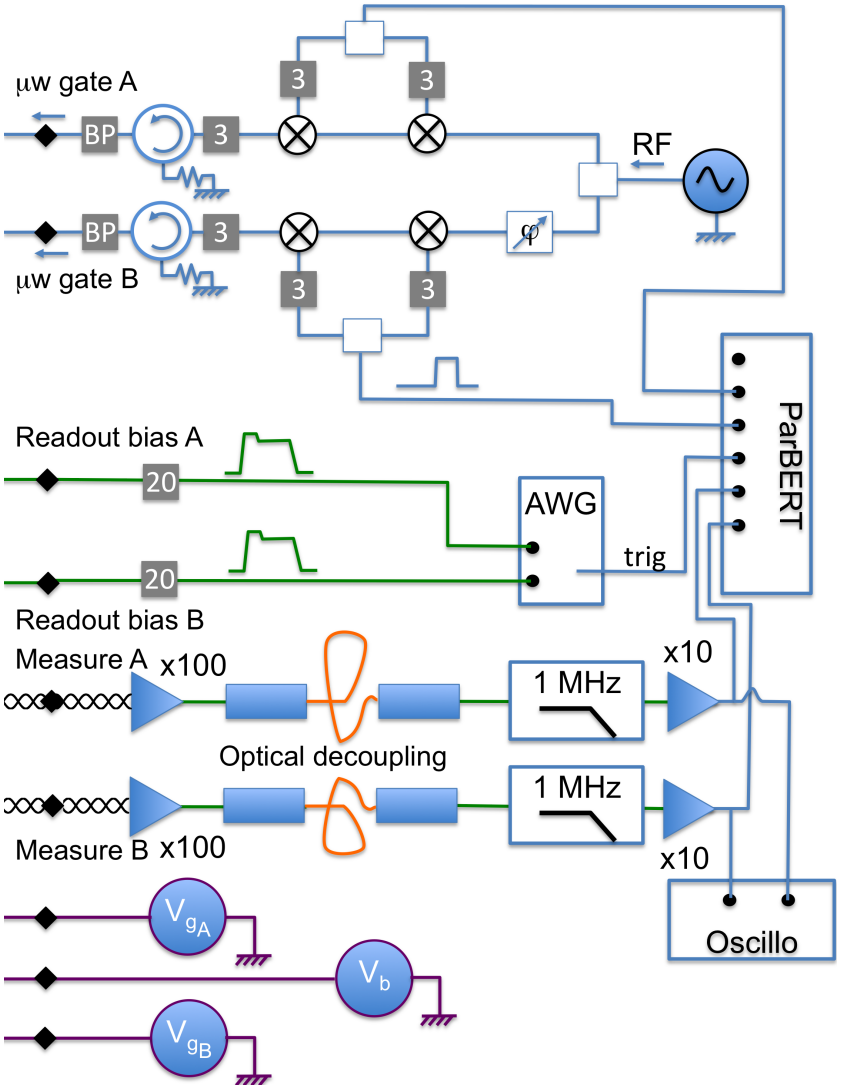

Fig. 2.22. Room temperature electronics for controlling the quantroswap experiments.

2.2.5.2 Readout signal measurement

The voltages that develop across the readout junctions at switching, and propagate along the bifilar measurement lines in about 1 μs, are measured with high impedance low noise amplifiers connected to a digitizer (see Fig. 2.22). To prevent the noise coming back from these devices from going through the amplifiers to the measuring lines, an optical decoupler is used: the output of each twisted pair is first connected to a battery-powered low noise amplifier NF LI75A [80], with a noise level of 1.2 nV/$\sqrt{Hz}$ in a 1MHz bandwidth. This amplifier and its batteries are placed in a shielded cabinet. Its output is amplified using an AC coupled preamplifier SA-220F5 [81], passing above 300Hz, and then sent to a battery-powered Ifotec optical transmitter, optically connected through the shielded box to a receiver. The receiver signal is finally connected to a SR560 Stanford amplifier [82] with a 1 MHz bandwidth.

The output voltages are finally analyzed using either a LeCroy LC 684DM oscilloscope or an Acqiris DC282 digitizer. As the output of interest is wether the readout junction has switched or not, one uses a voltage discriminator that compares the voltage at a precise time with a tunable threshold. Several counters as well as the inputs of the Agilent 81200 bit error rate tester (already used for generating the control pulses) have been used for that purpose.

2.2.6 Software control

All the apparatuses used for DC biasing the two quantroniums, for generating the control microwave pulses and arbitrary readout pulses, and for measuring the switching probabilities of the readout junctions are remotely controlled with a unique software developed in Testpoint, an event-driven object language for remote control. Figure 2.23 shows a few screenshots of the control interface with measured results.

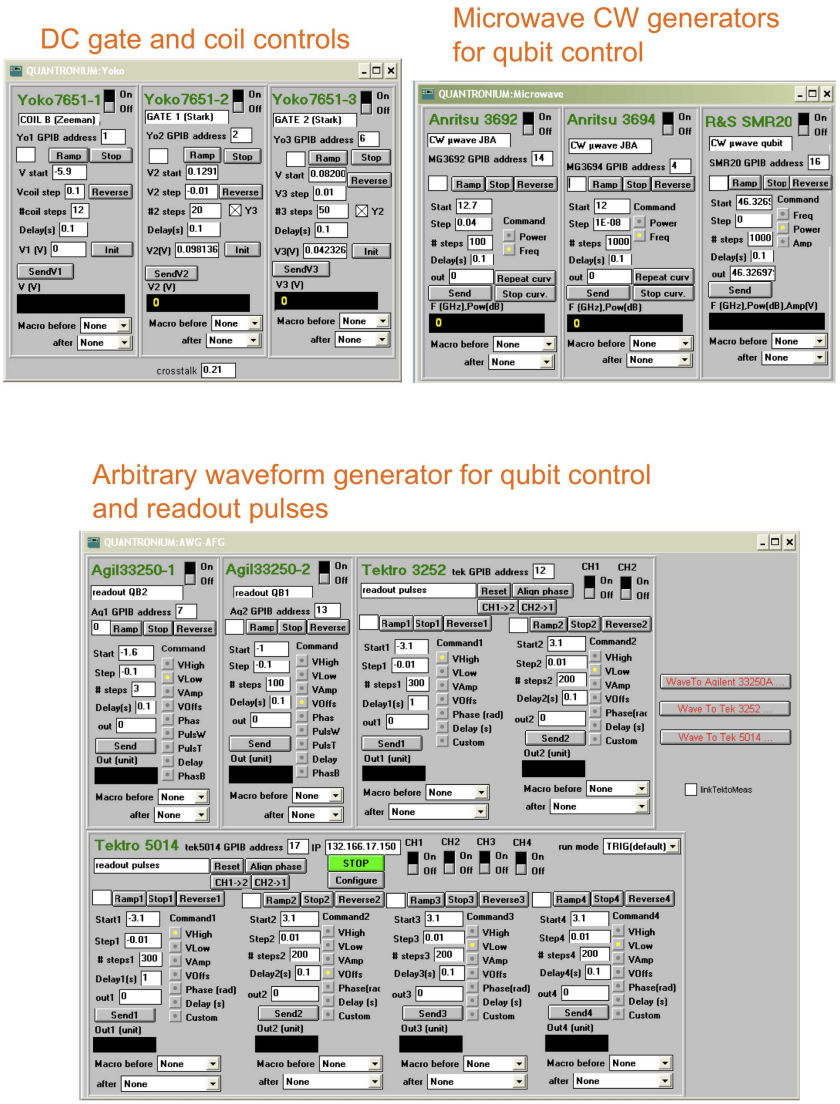

Fig. 2.23. Screen captures of the Testpoint software used for controlling the quantroswap experiment.

Timing of control and readout pulses using an Agilent 81200 Bit Error Rate Testor

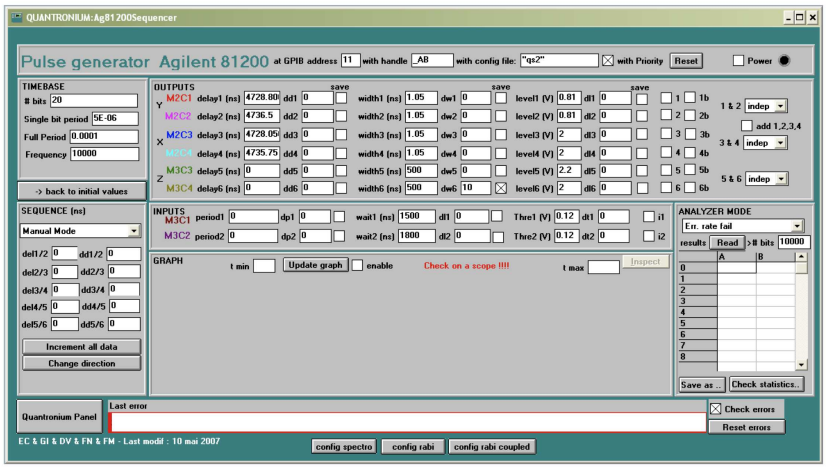

Switching probability measurement for the quantronium readouts

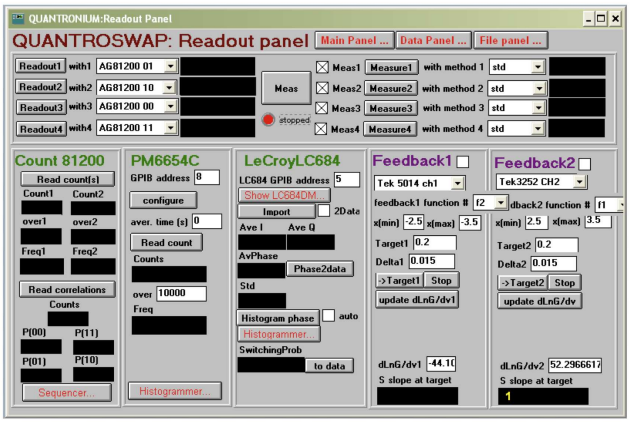

Chapter 3

The Quantroswap experiments

Contents

Preamble: drawing lessons from failing experiments

We report in this chapter the results obtained on different Quantroswap samples and for several cool-downs. Each experiment always started with the same protocol: characterizing the qubit parameters, the readout circuit, and the coherence properties. We soon found that the more complex quantronium qubits of our Quantroswap samples did not meet the performances already observed on simpler single Quantronium samples and those estimated in the previous design chapter. All the samples had a readout visibility lower than 25 %, most of them having a T_1 shorter than 100 ns; when one of the quantroniums of the quantroswap pair had a not too short T_1, the other quantronium with exactly the same fabrication parameters had a T_1 so short that finding its spectroscopic line was even impossible. In addition, spurious two level systems or charged TLS strongly coupled to the island were often observed, their effect being drastically detrimental to spectroscopic data. Due to these problems, we embarked in a series of sample and design variations. Let us say immediately that none of these variations resolved the critical problems encountered, and that we only tried to characterize them. We found that the quantronium samples fabricated in our laboratory and measured in our set-up suffer from problems so severe that they cannot be used for developing even a very elementary processor.
Despite these very negative results, we tried to operate the Swap gate. Although we could not probe it in depth, we could demonstrate the swapping phenomenon induced by the coupling between the two qubits.
All these experimental findings led us to re-think the quantum bit research project in depth.

3.1 Characterization methods of the different samples measured

We expose in this section the experimental methods used for characterizing all the samples measured. These samples could differ by:

- the presence of quasiparticle traps that help avoiding quasiparticles to enter the quantronium islands;
- the fabrication method of the shunt capacitance;
- the type of connecting lines;
- the nature of the wafer, whose dielectric constant controls the electrostatic couplings;
- the qubit parameters.

The main characteristics of the measured samples are summarized in Table 3.1.

Name	QS 1.1	QS 2.1	QS 3.1	QS 4.1	QS 4.2	QS 4.3
Fabrication characteristics						
Quasiparticle traps	yes	yes	yes	yes	yes	no
Dielectric	AlOx	AlOx	SiN	SiN	SiN	interdigitated
Leads metal	Au	Au	Al	Al	Al	Al
Wafer	Si	Si	Si	Si	Sapphire	Si
Bias resistance R_l (Ω)	4k	4k	240	436	436	436
JJ impedance (Ω)	350	560	550	380	436	
DC gate crosstalk	67%	24%		43% (66%)	36%	36%
Measured parameters						
E_J (k_BK)	0.81	0.76 (0.846)		1.35 (1.32)	0.97	0.76 (0.846)
E_C(k_BK)	0.58	0.55 (0.584)		0.59 (0.53)	0.5 (0.55)	0.55 (0.584)
T_1	$\leq$1ns	$\leq$ 100ns	$\leq$270ns	$\leq$50ns	$\leq$70ns	$\leq$300ns (Qubit2)
T_2						20-30ns
Max[$P_{S_{\|1>}}$-$P_{S_{\|0>}}$]		20%	10%	10%	14%	20%
Gate capacitance		29aF	30aF	17aF	22aF	14aF
Coupling frequency		230MHz			600MHz	

Table 3.1. Characteristics and parameters of the various measured samples when they could be measured or estimated.

Scanning Electron micrographies of sample QS 2.1

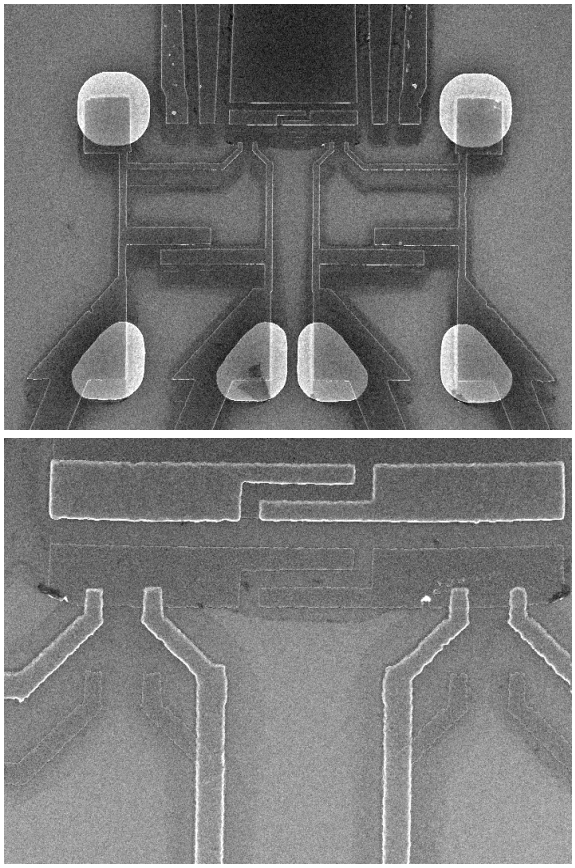

Fig. 3.1. Detailed Scanning Electron Micrography of the central part of sample QS 2.1.

3.1.1 Readout junction characterization

The first step in characterizing a quantroswap sample consists in measuring the superconducting gap of the aluminum, and the readout junction properties: the tunnel resistance, the critical current, and the electronic temperature that governs the sensitivity of the quantronium readout.

One first measures the I-V curve of the readout junction by applying a low frequency triangular voltage to the readout bias line, and by measuring the voltage V across the junction. Two branches can be distinguished in this curve: the supercurrent branch at $V = 0$ up to a maximum, the switching current, and the dissipative branch at voltages larger than the gap voltage. The switching current provides at low temperature an estimate of the junction's critical current with a 5 % accuracy. The precise shape of this I-V depends

on the biasing impedance R_l in series with the readout junction. The value of R_l was varied between the different samples (see Tab. 3.1):

- in experiment QS 1.1 and QS 2.1, this impedance was 10 times larger than the normal state resistance of the junction, and the voltage switched directly from the supercurrent branch to the gap voltage branch at about the same current.
- in the other experiments, R_l was of the same order as the junction's tunnel resistance, and the voltage switched to the end of sub-gap part of the $I-V$ characteristic, just before the gap voltage, as shown on Fig. 3.2. In this region the current is small, and the dissipated power is significantly smaller, which offers the advantage of generating fewer quasiparticles.

One also determines from the I-V curve shown in Fig. 3.2 that the superconducting gap voltage of the aluminum in our circuit is about 205 μeV, which is higher than the bulk value found for thick films ($\Delta_{bulk} = 180\mu$eV). Actually, as junctions are made of two layers of Aluminum with different thicknesses (12nm and 45nm), this value is an average of the superconducting gaps of the two electrodes. We estimate from refs. [83, 84, 85] that the superconducting gap is larger in the bottom thin layer by about $20-40$ μeV, a value compatible with our average gap.

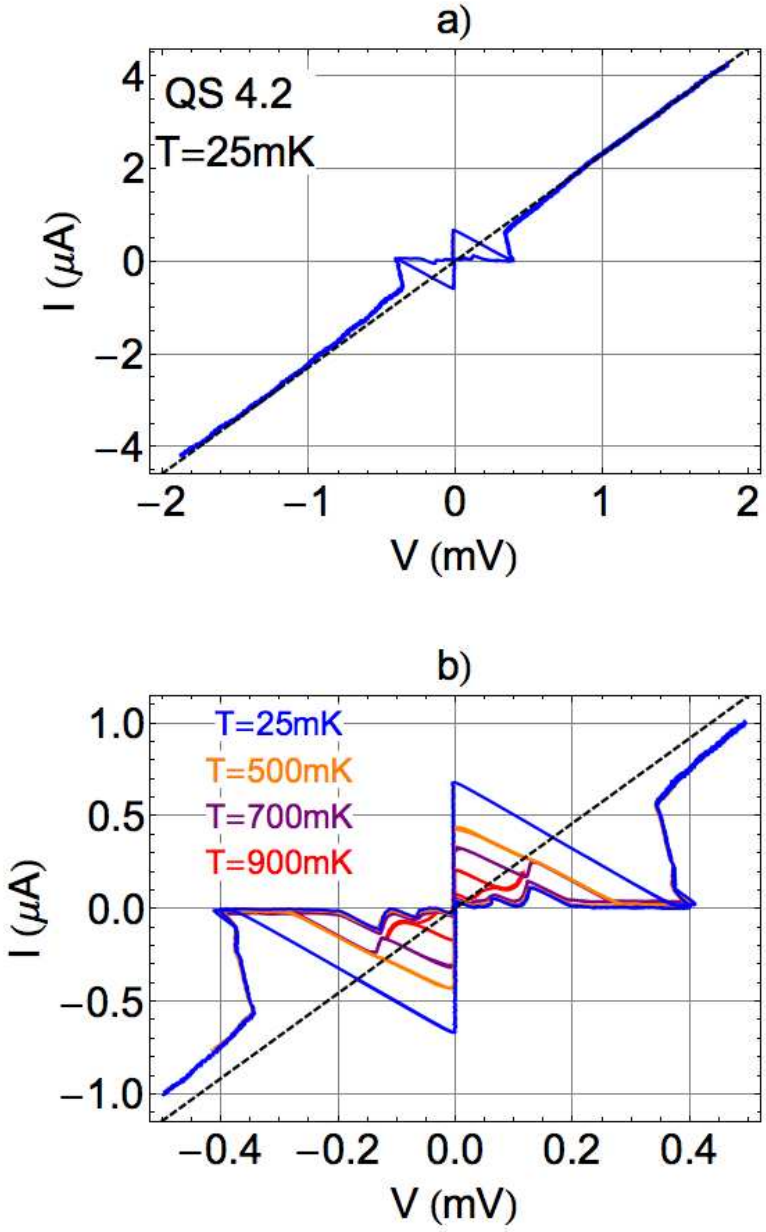

Fig. 3.2. I-V curves of sample QS 4.2 at different scales and different temperatures during cooling. a) Large scale IV curve whose slope gives a 436 Ω tunnel resistance. b) IV curves at a smaller scale and at different temperatures showing the superconducting gap as well as subgap structures attributed to dissipative resonances in the environment at high-frequency.

The critical current I_0 of the junction and the effective electronic temperature T_e are then determined precisely by applying trapezoidal bias current pulses and by measuring the switching probability as a function of the pulse height. The result of such a measurement is shown in Fig. 3.3. Using then Eq. 1.14 for the escape rate, one determines I_0 and T_e from the so called "$b^{2/3}$" plot (see Fig. 3.3). Although the fridge temprature was about 50 mK in the first experiments (QS 1.1, QS 2.1, and QS 3.1), it was 20 mK in the last ones (QS 4.1, QS 4.2 and QS 4.3). At this latter phonon temperature, one always found $T_e \leq 45$ mK, the difference being attributed to unperfect filtering. In principle, such a low effective T_e is supposed to lead to a sufficient resolution for discriminating the two quantronium persitent currents associated to the ground and excited states, as discussed in section 3.1.1.1. However, we always found an apparent sensitivity significantly lower, as we discuss below.

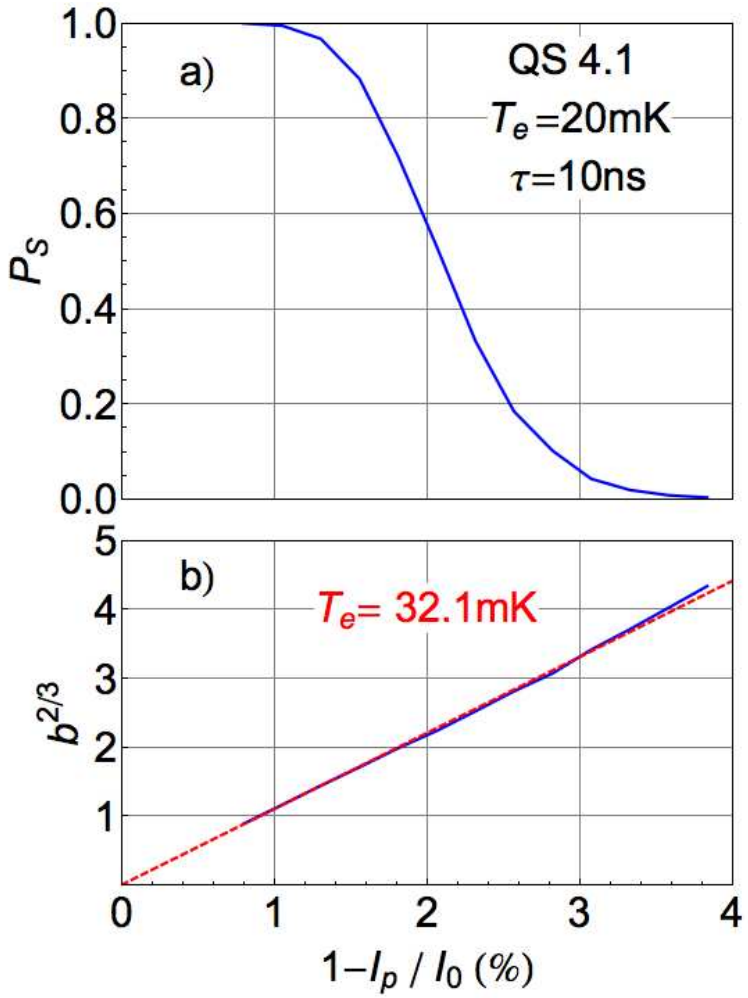

Fig. 3.3. Switching probability and electronic temperature on sample QS 4.1. a) Switching probability P_S as a function of the peak value I_p of the current readout pulse, for a readout-plateau duration $\tau = 10ns$. b) Plot of $b^{2/3} = \ln(\Gamma/\nu_{p_{\rm bias}})^{2/3} = (\frac{4\sqrt{2}}{3}\varphi_0 I_0/(k_B T_e))^{2/3}(1 - I_b/I_0)$ (blue line). The fit (red dotted line) yields an effective switching temperature equal to 32 mK and a critical current of about 830 nA. The shunting capacitance is about 2.8 pF, which yields a plasma frequency of 4.75 GHz at zero bias current, and of about 2.5 GHz at switching. The theoretical crossover temperature $T_{co} = 18$ mK is a bit lower than the temperature of the refrigerator and than the fitted escape temperature. Thus, the escape occurs at the beginning of the thermal regime.

3.1.2 Ground state characterization of the two quantroniums

In a second step, one characterizes the ground state of the quantroniums through the dependence of their persistent loop current on the gate voltage (or N_g) and on the magnetic flux (or δ). As the switching probability can easily saturate at 0 % or 100 % as δ is varied, it is convenient to operate in a so-called "feedback mode" that consists in adapting the peak height of the bias current pulse to keep the switching probability P_S at a constant value. Figure 3.4 shows such a mapping over N_g and δ of the ground state of one of the quantronium of the pair, for sample QS 2.1. One could think that this mapping provides a first estimate of the quantronium parameters E_J and E_C. Nevertheless, it is not the case due to a loss of signal reported below. E_J and E_C have thus to be determined spectroscopically.

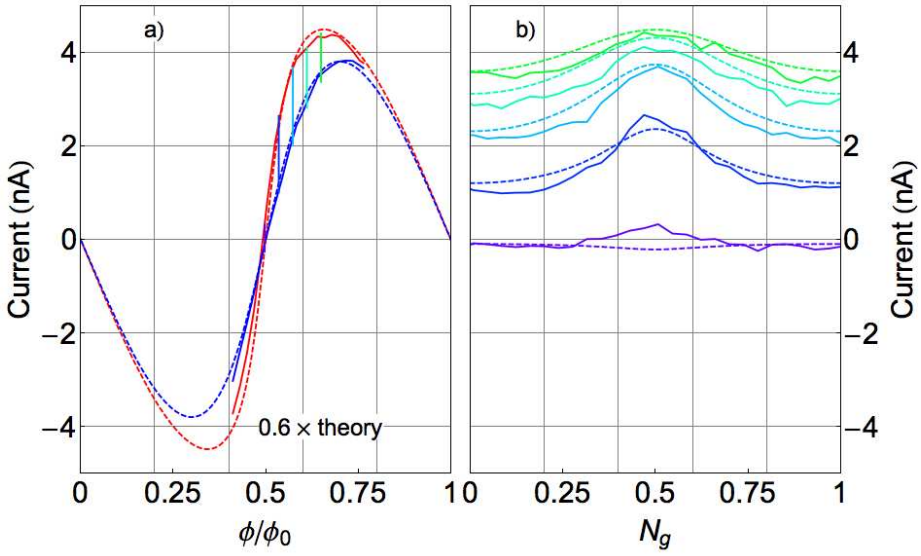

Fig. 3.4. Ground state mapping of one of the quantronium of sample QS 2.1. The two panels show the experimental apparent loop current modulation (solid lines), i.e. the switching current variations in feedback mode, as a function of $\delta/(2\pi) = \Phi/\Phi_0$ (a) for $N_g = 0$ (blue) and $N_g = 0.5$ (red), and as a function of N_g (b) for various Φ/Φ_0 represented by vertical segments in (a). Dashed lines correspond to 60% of the theoretical persistent loop current predicted from the parameters determined spectroscopically.

3.1.3 Spectroscopic characterization of each quantronium

The most important parameters E_J and E_C are determined by qubit spectroscopy. A spectroscopy experiment consists in applying on one of the two gates a microwave pulse long enough for saturating any transition it couples to, and in measuring the induced change in the switching probability of the readout junction when a readout bias pulse is applied immediately after. One expects a change in the switching probability whenever the applied frequency matches a transition of the quantroswap circuit initially prepared in its ground state by relaxation. Such a measurement is repeated while scanning the microwave frequency and either the flux Φ threading the quantronium loops or the gate charge N_g. One obtains 2D plots of the readout signal at fixed N_g (usually 1/2)or fixed δ (usually zero), as those shown on Fig. 3.9 for sample QS 4.2. These plots show the qubit resonance whose position is fitted with Eq. 1.9 to determine the qubit parameters. One finds $E_J = 0.97k_B$ K and $E_C = 0.5k_B$ K for this sample. The values for the other samples are indicated in Tab. 3.1. Note also that it was impossible to determine spectroscopically the asymmetry coefficient d since it has an effect only near $\delta = \pi$, where the resonance line of the qubit could never be observed.

3.1.4 Loss of signal in the persistent current of a quantronium loop

Once E_J and E_C are determined spectroscopically, one can directly compare the N_g and δ modulations of the switching current in feedback mode with the expected quantronium loop currents(see section 1.1.4). Figure 3.4 shows this comparison for sample QS 2.1 and shows that the experimental modulation is only 60 % of the expected one. This factor 0.6, observed on all our samples, was partly overlooked in previous experiments, and yields a reduction of the readout contrast compared to that expected (see Fig. 2.3). This effect can be interpreted either as a lowered effective sensitivity of our detector (when it converts a loop current into the bias current change keeping the switching probability P_S constant), or as a problem with the split Cooper pair box itself that would not be always in a state with the expected loop current.
Since the measurement of the supercurrent through a superconducting atomic size contact [86], performed with a very similar set-up, did not show such a discrepancy, we rather think that our problem is related to the CPB itself rather than to the detector. Another problem also identified and reported below is in favor this hypothesis.

3.1.5 Characterization of the gate lines

We then switch to the determination of the capacitances between the quantronium islands and the gate electrodes, and determine in particular the gate cross-talk. We address separately the DC and microwave gate signals aiming at tuning the working point and at resonantly controlling the qubit, respectively.

Low frequency crosstalk

The experimental gate capacitances are deduced from the gate voltage periods of the switching probalility in the ground state, at a magnetic flux where the gate modulation is maximum (see Fig. 3.4). Figure 3.5 shows this switching probability for the two quantroniums of sample QS 2.1, in their ground state, as a function of the gate voltage applied on gate A or on gate B. The capacitances between island B and gate B and between island B and gate A, are for instance estimated at about 29 aF and 6 aF, respectively. The low frequency gate crosstalk is thus 20%, close to the value expected from simulations (see section 2.2.1.1). Values of this DC crosstalk is indicated for the different samples in table 3.1.

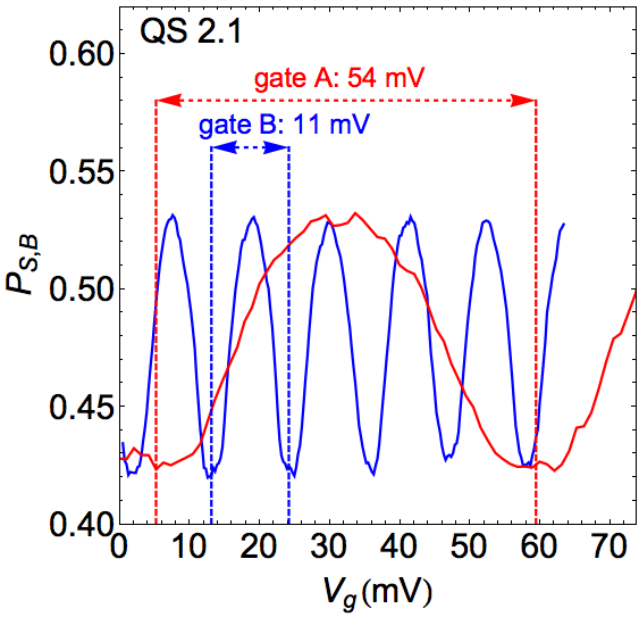

Fig. 3.5. Measurement of the DC gate capacitances in sample QS 2.1. The two curves show the modulation of the switching probability P_S of qubit B (in the ground state) as a function of the gate voltages V_{g_B} (red) and V_{g_A}(*blue*). From the voltage periodicity, one can determine the gate capacitances (29 aF and 6 aF), and the parasitic crosstalk (20%).

High frequency crosstalk and compensation

This second crosstalk regime is more complex and involves the non local microwave coupling between all the lines on the chip. It is deduced from the

measured Rabi periods of the two quantroniums driven from the same gate, as shown in Figure 3.6 for sample QS 2.1. In this experiment, the frequencies ν_A and then ν_B of the measured qubit are successively the same, the frequency of the non measured one being shifted away by applying a bias current pulse to its readout junction. The microwave gate crosstalks is found to be equal to about 50% in this sample, which is twice as large as the DC crosstalk.

Such a large microwave crosstalk raises the issue whether it is possible or not to manipulate the two qubits independently when they are close to or at resonance. Actually, one can do it using a compensation technique: two microwave signals are sent simultaneously to both gate lines, with opposite phases and well-adjusted amplitudes in order to cancel the driving signal for the qubit which should not be addressed. This method is demonstrated with sample QS 2.1 on Fig. 3.14. It was used to demonstrate swap oscillations between two quantroniums, as reported at the end of this chapter.

3.1.6 Characterizing the qubit coherence

Coherence times T_1 and T_2 were determined for each qubit when it was possible to do it, using standard manipulation techniques described in [16, 17] and in Annex 1. To summarize, T_1 is measured by applying a π gate pulse, then waiting for a time τ, and finally measuring the switching probability. The latter decreases exponentially with τ with the characteristic time T_1. The time T_2 is the decay time of the Ramsey oscillations produced by a sequence of two slightly out-of-resonance $\pi/2$ gate microwave pulses separated by a free evolution period of time. Table 3.1 indicates measured values of T_1 and T_2 for some of the sample, and estimated upper bound for other samples.

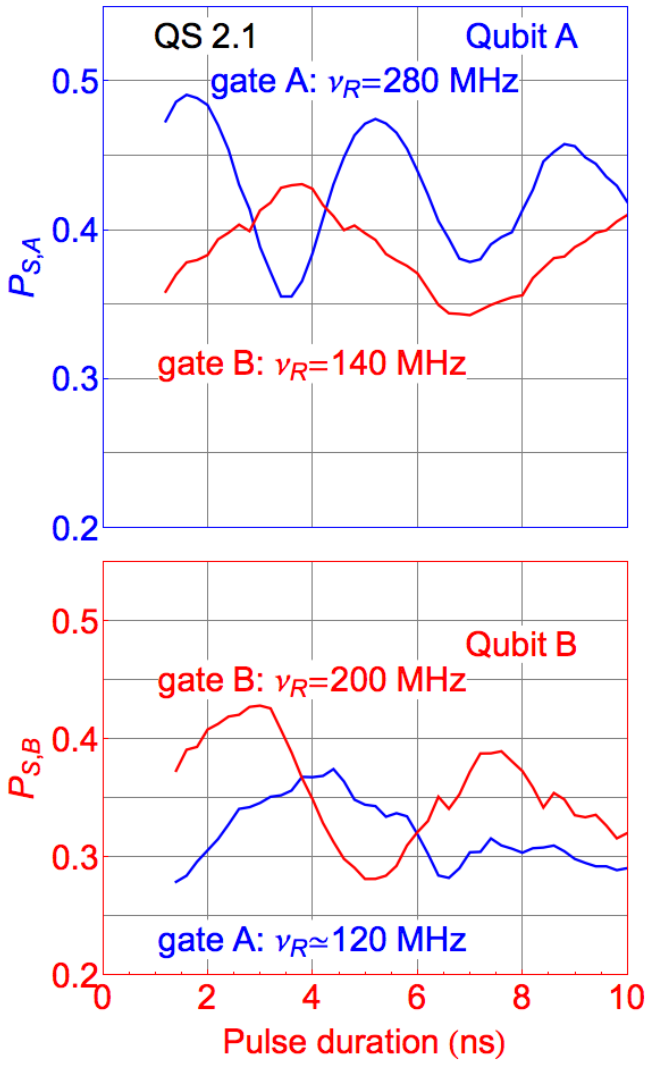

Fig. 3.6. Measurement of the microwave gate crosstalk in sample QS 2.1. The two panels show the switching probability variations induced by Rabi oscillations of qubit A (top) and B (bottom) when resonant microwave pulses at 12.17 GHz with identical nominal amplitudes are applied to gate A (blue) or to gate B (red). The frequency of the non measured qubit is shifted away. From the observed Rabi frequencies ν_R, one estimates a parasitic microwave crosstalks of about 50%

3.2 Spectroscopy of the coupled quantroniums

The coupling between the two quantroniums of a quantroswap pair can be first characterized by performing the spectroscopy of the coupled system, i.e. by finding the transition frequencies between the eigenstates of the two-qubit molecule, as explained in section 1.2.2.1.

3.2.1 Experimental protocol

The experimental protocol for a two quantronium spectroscopy consists in the following steps:

One first tunes the DC gate voltages so that $N_{g_A} = N_{g_B} = 1/2$, a condition that maximizes coherence and improves the visibility of spectroscopic lines.

Then, a delta phase shift $\delta_B - \delta_A$ between the two qubits is chosen for the whole experiment. As already mentioned, the two quantroniums share the same magnetic flux, and

$$\delta_A = \Phi/\varphi_0 + \gamma_A$$
$$\delta_B = -\Phi/\varphi_0 + \gamma_B.$$

Since the qubit eigenenergies are even functions of δ, we have always applied readout pulses with opposite signs, so that the qubit frequencies evolve in the same direction when the flux is varied, which facilitates the analysis. The effective δ shift is thus equal to $\gamma_B + \gamma_A$, and is imposed by the values of the readout currents at the footing of the readout pulses (the so-called prepulse currents introduced in section 1.1.6).

The magnetic flux ϕ is then swept step by step. For each flux value, one goes over the following sub-steps:

a) The gate voltages are fine tuned to $N_{gA} = N_{gB} = 1/2$ in order to compensate for any gate charge drift due to 1/f charge noise.
b) The peak value of the readout pulse is chosen, so that the switching probability of each active readout is set to $P_{S,0} = 20\%$ in the absence of microwave.
c) The microwave frequency ν_{rf} is then switched on and swept step by step. The same excitation-readout sequence is repeated a few thousands of time:

- The bias currents in the readout junctions are set to zero to let the electron reach the thermal equilibrium.
- Then, the prepulse currents are established during about one microsecond, a time longer than the qubit relaxation times T_1.
- During this step, a microwave gate pulse is applied to one of the gates. When the microwave frequency matches a molecular transition $|\Psi_0\rangle \rightarrow |\Psi_1\rangle$, $|\Psi_0\rangle \rightarrow |\Psi_2\rangle$ or $|\Psi_0\rangle \rightarrow |\Psi_3\rangle$ (two-photon transition), the corresponding level gets populated.

Since the microwave pulse is long with a small amplitude, it is expected to saturate the transition and populate the corresponding upper molecular level with a weight of about 50%.
- At the end of the microwave gate pulse, the readout current is established in the active readouts. One can use either one readout, or two readouts. In the latter case, one can switch them on simultaneously, or with a short delay of a few tens of nanoseconds between one another. The repetition of the sequence leads to a single switching probability $P_S(\Phi, \nu_{rf})$

The double sweep over the frequency and the flux produces a 2D plot of $P_S(\Phi, \nu_{rf})$ or of $P_S(\Phi, \nu_{rf}) - P_{S,0}$, which contains the spectroscopic lines. One finally fits the positions of these lines to determines the qubit parameters E_J and E_C, and the coupling frequency ν_{cc} when the qubits undergo a level crossing in the explored flux range.

A discussion of what is measured is needed at the present point. Indeed, the switching probability of readout X (X stands for A or B) gives the weight of the excited state of qubit X in the two-qubit system state, at the readout plateau, i.e. at the end of the readout pulse rise. Ideally, when the state populated by the microwave pulse is $|\Psi_i\rangle = \alpha\,|10\rangle + \beta\,|01\rangle$, the switching probabilities of readout A and B should vary as the weights α^2 and β^2, respectively. But as explained in section 1.1.9, these weights can be modified along the readout pulse rise, especially when the two qubit frequencies are equal at the beginning of the rise or cross each other during the rise. Indeed, as shown in Fig. 3.7, when the coupling frequency is large enough to make the Landau-Zener transition rate small at the level crossing between the two qubits (see section 1.2.3), the level crossing occurs adiabatically and the quantum states are swapped during the readout ramp.
This means that the increase in the switching probability of readout A, for example, is either due to an excitation of qubit A by the microwave pulse, or due to an excitation of qubit B (or both of them) and to a swapping between qubit B and qubit A during the readout pulse rise.
In our experiments, the rise time of the current readout pulse is in the range 4-6 ns, whereas the coupling frequency is in the range of $[100\text{ MHz}, 600\text{ MHz}]$ depending on the sample. Since the Landau-Zener transition probability strongly depends on ν_{cc}, as shown in Figure 1.15, we estimate that the only sample in which swapping occurs at readout with a large probability is sample QS 4.2 for which $\nu_{cc} = 600$ MHz is the largest. For the other samples, the evolution at readout is more diabatic and swapping is estimated not to exceed 40 %. Figure 3.7 shows the influence of the readout pulse rise on the eigenenergies and on the qubit eigenstate populations for different initial states and for the parameters of sample QS 4.2. This issue will be considered in more details when comparing the experimental spectra to numerical simulations later in this section.

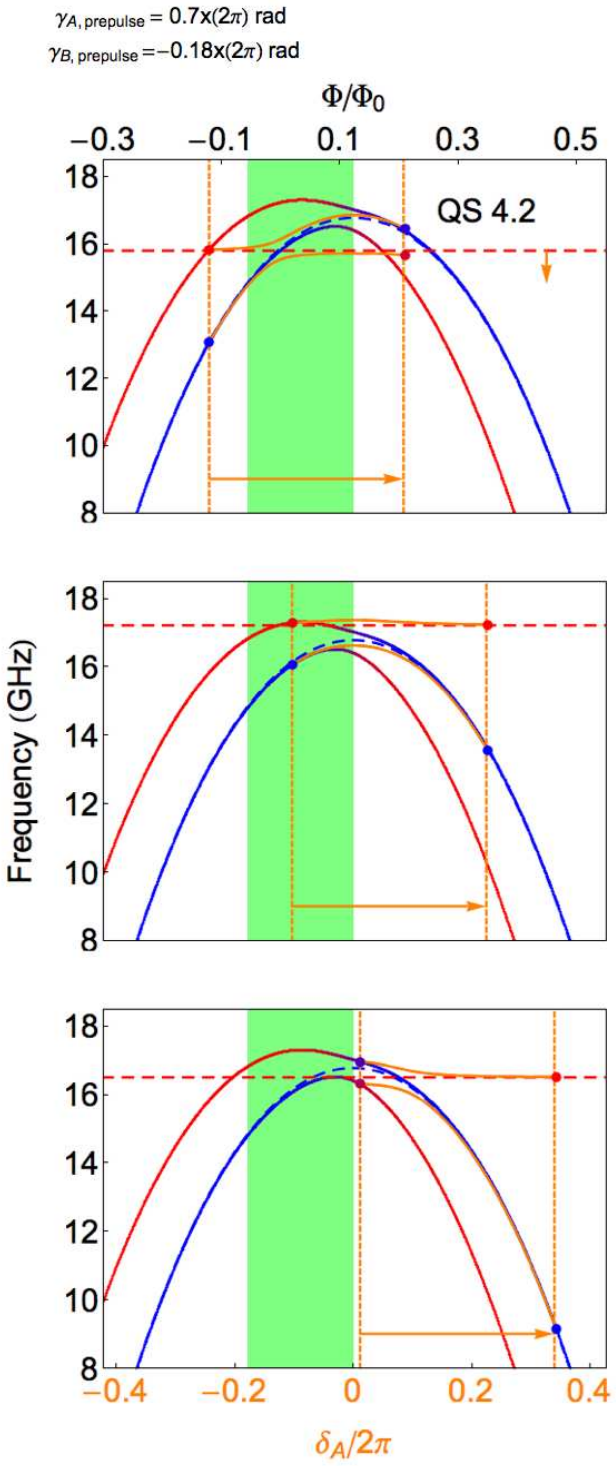
$\gamma_{A,\,\mathrm{prepulse}} = 0.7\mathrm{x}(2\pi)$ rad
$\gamma_{B,\,\mathrm{prepulse}} = -0.18\mathrm{x}(2\pi)$ rad
Φ/Φ_0
−0.3
−0.1
0.1
0.3
0.5
QS 4.2
Frequency (GHz)
18
16
14
12
10
8
−0.4
−0.2
0
0.2
0.4
$\delta_A/2\pi$

Fig. 3.7. Effect of readout pulse A on the state populations of qubit A and B, for the parameters of sample QS 4.2, for $N_g = 1/2$, and for $\gamma_A/(2\pi) = 0.7$ and $\gamma_A/(2\pi) = -0.18$ before readout. Blue and red colors code for the weights of qubit A and B in a particular state, respectively. All panels show the eigenenergies $|\Psi_1\rangle$ and $|\Psi_2\rangle$ of the system (solid lines) as a function of flux Φ (top scale), as well as the uncoupled qubits eigenenergies (dashed lines)as a function of δ_A (bottom scale). During the readout pulse rise, δ_A evolves between the two vertical orange lines in the direction of the orange arrow. Correspondingly, the eigenenergies $|\Psi_1\rangle$ and $|\Psi_2\rangle$ evolves along the solid orange lines. The initial and final energies are also indicated with dots. The green Φ interval is where the two qubit frequencies do not cross during the readout ramp, so that the qubits do not swap. Panels a), b), and c) correspond to initial working points, on the left, in, and on the right of this green interval.

3.2.2 Spectroscopic data on two samples

We present in this section two sets of spectroscopic measurements performed on samples QS 2.1 and QS 4.2, which have the minimal and maximal coupling frequencies ν_{cc} that we have explored.

3.2.2.1 Spectroscopic measurement of sample QS 2.1

We have first characterized each qubit separately by performing its spectroscopy while displacing the frequency of the other qubit with a large bias current pulse (around 0.7 I_0). Results are shown in Fig.3.8a. This data were also completed by performing the spectroscopy in N_g in the vicinity of $N_g = 1/2$. Despite a very low visibility, the peak positions could be fitted to determine E_J and E_C for each qubit (see. Table 3.1).

We have then performed the spectroscopy of the coupled system, in the vicinity of the point where the two qubit frequencies cross one another, by measuring both switching probabilities at the same time and by following the method described above. Figure 3.8 shows the result. When the two qubits are in resonance (here at $\delta/(2\pi) \simeq 0.07$), one observes somehow (see Fig. 3.8b) the superposition of an avoided level crossing induced by the coupling and of a crossing of the levels (this point will become clearer with sample QS 4.2). By fitting with the eye the anticrossing (see Fig. 3.8c), one determines the order of magnitude of the coupling frequency, i.e. $\nu_{cc} = 230 + / - 20MHz$.

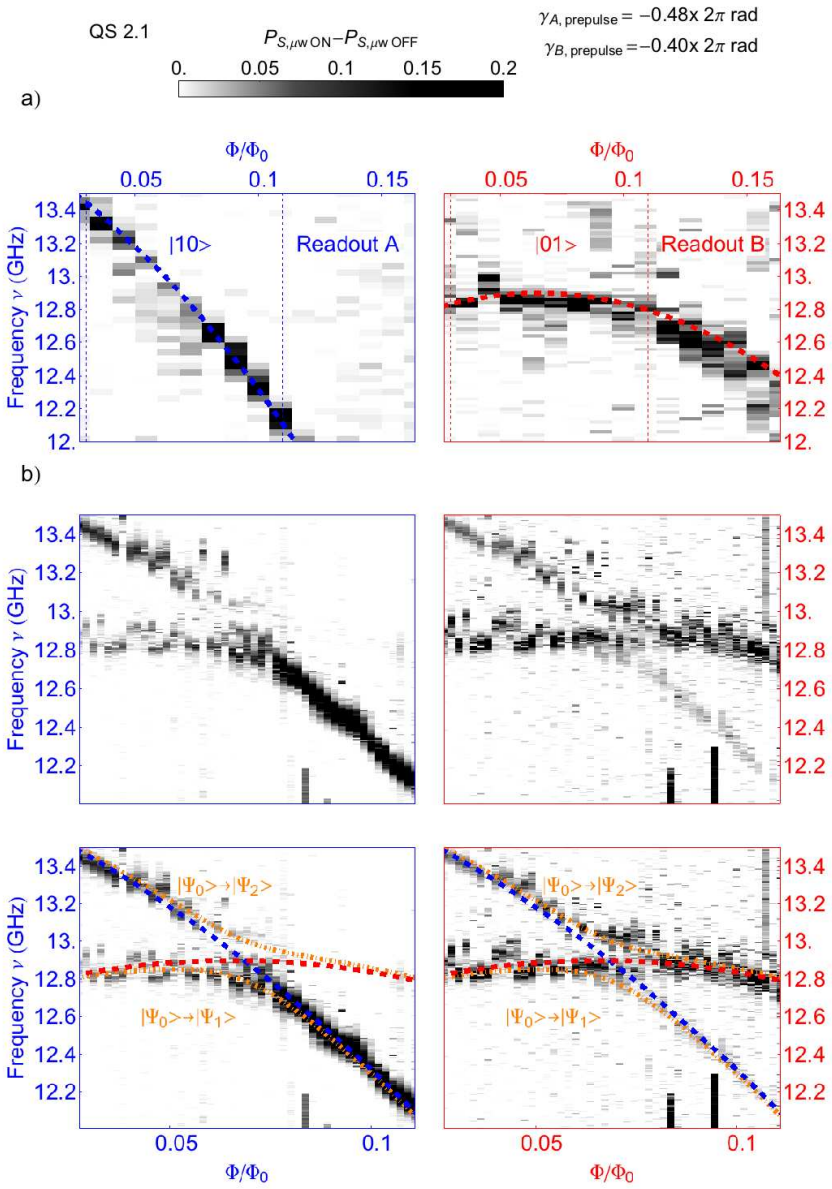
QS 2.1
$P_{S,\mu w\,ON} - P_{S,\mu w\,OFF}$
0. 0.05 0.1 0.15 0.2
$\gamma_{A,\,prepulse} = -0.48 \times 2\pi$ rad
$\gamma_{B,\,prepulse} = -0.40 \times 2\pi$ rad
a)
Φ/Φ_0
0.05 0.1 0.15
Frequency ν (GHz)
13.4 13.2 13. 12.8 12.6 12.4 12.2 12.
|10>
Readout A
|01>
Readout B
b)
$|\Psi_0> \rightarrow |\Psi_2>$
$|\Psi_0> \rightarrow |\Psi_1>$
0.05 0.1

Fig. 3.8. Independent switching probabilities of readout A (top) and of readout B (bottom) with respect to the microwave frequency applied to both qubits, and to the reduced flux Φ/Φ_0 during excitation, for sample 2.1 . The prepulse bias currents are adjusted to displace the resonance frequency of the qubit not being measured. The excitation microwave pulse has a duration of 200 ns, and its on-resonance Rabi frequency is 30 MHz. Black and white color scale codes for the switching probability: black meaning high and white low. The switching probability are measured over 40000 samples.
Simultaneous readout of qubit A (top) and qubit B (bottom) with respect to the excitation frequency and to the reduced flux Φ/Φ_0 during excitation. The prepulse bias currents are 0.48 I_0 (qubit A) and 0.4 I_0 (qubit B). The excitation microwave pulse has a duration of 200ns, and its on-resonance Rabi frequency is 30 MHz.

3.2.2.2 Evidence for a major problem on sample QS 4.2

We have performed a similar spectroscopy experiment on sample QS 4.2, fabricated on a Sapphire wafer. Due to the high-dielectric constant of sapphire, the coupling frequency ν_{cc} of this sample is increased by a factor 2.5 compared to similar ones fabricated on silicon wafers. The effect of the coupling on the energy levels is thus larger, which makes them more clearly visible even when the linewidth is large due to strong decoherence. Figure 3.9 shows the spectroscopy of this sample, with qubit B measured 30 ns after qubit A.

This figure displays clearly a surprising, and let us say here extremely worrying, phenomenon: transition lines are observed at positions predicted for the coupled qubit system, AND at positions predicted for the qubit A and B decoupled from the other one. In other words, each qubit seems to disappear part of the time, leaving the other one alone! This dramatic problem was already guessed from other samples (i.e. see Fig. 3.8) fabricated on silicon, but a clear proof could be obtained only from this sample with a large coupling frequency ν_{cc}.

Several hypothesis can now be made for explaining such a strange behavior:

a) The capacitive coupling itself is unstable and randomly vanishes with a sizeable probability.

b) The frequency of each qubit is unstable, and varies between its expected value and other ones that are not detected. Such an instability could for instance be explained by strongly coupled charged two level fluctuators inducing a large ΔN_g and a large frequency shift to a point where decoherence is so large that no spectroscopic line is detected;

c) The quantronium qubit does not even longer exist as a "two-level-atom". Poisonning of the island by quasiparticles introduces for instance a third level whose dynamics is not necessary coherent.

Since the coupling capacitance is obtained from the electrostatic coupling between the islands, hypothesis a) is hard to believe. We rather attribute the observed effect to hypotheses b) or c), although a more precise diagnosis could not be performed. Indeed, quantroniums could not be controlled and measured away from $N_g = 1/2$ since decoherence drastically increases away from the degeneracy point. A pairing instability in the qubit islands (hypothesis c), is plausible since the variations of the persistent current in each qubit ground-state provide some evidence for depairing effects close to $N_g \simeq 1/2$, as often observed in single Cooper pair transistors.

Besides, it is also possible that this problem of qubit dissapearence also explains the 40% apparent effective loss of persistent current presented in previous section 3.1.4.

To evaluate more quantitatively this disappearance effect, we show on Fig. 3.11 the spectroscopic lines obtained from readout A when the two quantroniums are in resonance. The central peak in this spectroscopy corresponds to the excitation of the transition $|0\rangle \rightarrow |1\rangle$ of qubit A uncoupled from qubit B, whereas

the two other peaks corresponds to the expected transitions $|\Psi_0\rangle \rightarrow |\Psi_1\rangle$ (left) and $|\Psi_0\rangle \rightarrow |\Psi_2\rangle$ (right) of the coupled system. As the two qubits are in resonance, the weights of qubit A and B in $|\Psi_1\rangle$ and $|\Psi_2\rangle$ are equal to 0.5, and qubit A is in principle to be found in state $|1\rangle$ at readout with the very same probability for both states $|\Psi_1\rangle$ and $|\Psi_2\rangle$. The experimental dissymmetry between the amplitudes $A_{|\Psi_0\rangle\rightarrow|\Psi_1\rangle}$ and $A_{|\Psi_0\rangle\rightarrow|\Psi_2\rangle}$ of the lateral peaks is due to the non-adiabaticity of the readout process (see section 1.2.3 and next section), which induces a swap of energy between the two qubits. Nevertheless this effect only transfers weights from the right-hand peak to the left-hand one, and does not change the total weight of the two lines. The probability p for the two qubits to be normally coupled can thus be calculated from the ratio between the sum amplitude of the two lateral peaks and the total sum over the three peaks [1]: one finds

$$p = \frac{A_{|\Psi_0\rangle\rightarrow|\Psi_1\rangle} + A_{|\Psi_0\rangle\rightarrow|\Psi_2\rangle}}{A_{|\Psi_0\rangle\rightarrow|\Psi_1\rangle} + A_{|\Psi_0\rangle\rightarrow|\Psi_2\rangle} + A_{|10\rangle}}. \tag{3.1}$$

From the fit of Fig. 3.11, we obtain a probability $1 - p \sim 30\%$ of disappearance of qubit B, to be compared to the 40% apparent effective loss already mentioned.

3.2.2.3 Experimental evidence for swapping at readout

Do the spectroscopic data of Fig. 3.9 provide any evidence for a swapping at readout, as expected from the discussion of section 1.2.3, when the working point during excitation (before readout) is not in the green interval of Fig. 3.7? Sample QS 4.2 has indeed a large coupling frequency that yields a small Landau-Zener probability when the qubit A (in the excited or ground state) crosses qubit B (in its ground or excited state, respectively) during a fast readout ramp. Taking into account the prepulse currents in the junctions, the region where swapping is supposed to occur corresponds to $\delta/(2\pi) \in [-0.2, -0.08] \bigcup [0.17, 0.4]$. Note that intermediate situations can also occur, in which the readout of qubit A transfers some weight from $|10\rangle$ to $|01\rangle$ (and vise and versa).

In order to demonstrate more precisely this swap effect at readout, we have performed a simulation of the whole spectroscopy experiment including readout by time-integrating the master equation of the system (next section). The result of this simulation is shown on Fig. 3.10 and is to be compared with the experimental data of Fig. 3.9. Both the experiment and the simulation show the large signal on readout A at $\Phi/\Phi_0 < -0.08$; this can be understood only because the two qubits swap at readout.

Note that a similar effect was also observed when one of the two qubits is

[1] As spectroscopic lines have a low visibility, a large excitation power was used to perform the spectrscopy, so that all lines are saturated. The weight of a line is consequently given by its amplitude rather than by its area.

coupled to a Two Level System in the environment (see Annex G).

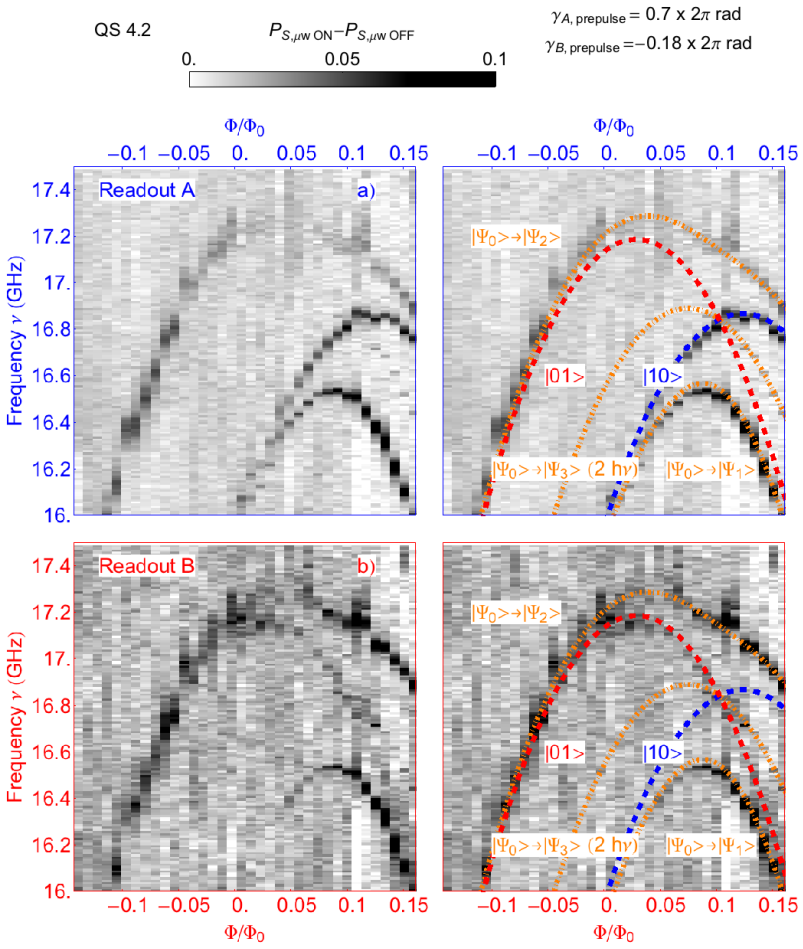

Fig. 3.9. Experimental spectroscopy of the coupled quantroniums in sample QS 4.2. The current prepulses in the readout A and B are 0.7 I_0 and -0.18 I_0, respectively, which corresponds to γ values indicated on the figure. The microwave pulse duration is 500 ns and the amplitude corresponds to a Rabi frequency of 150MHz. The current pulse on readout B is delayed by 30ns with respect to readout A. Top and bottom panels shows the measured changes in switching probabilities (see scale at the top) of readout A (top) and B (bottom) as a function of the excitation frequency and of the magnetic flux Φ. The probability is calculated by averaging over 40000 samples. Left panels contains only recorded data, whereas theoretical curves are superposed on right panels. Dashed curves are the energies of qubit A (blue) and qubit B (red) calculated from the parameters deduced from the spectroscopy of uncoupled qubits. The dashed orange lines are fits leading to a coupling frequency $\nu_{cc} = 600$ MHz.

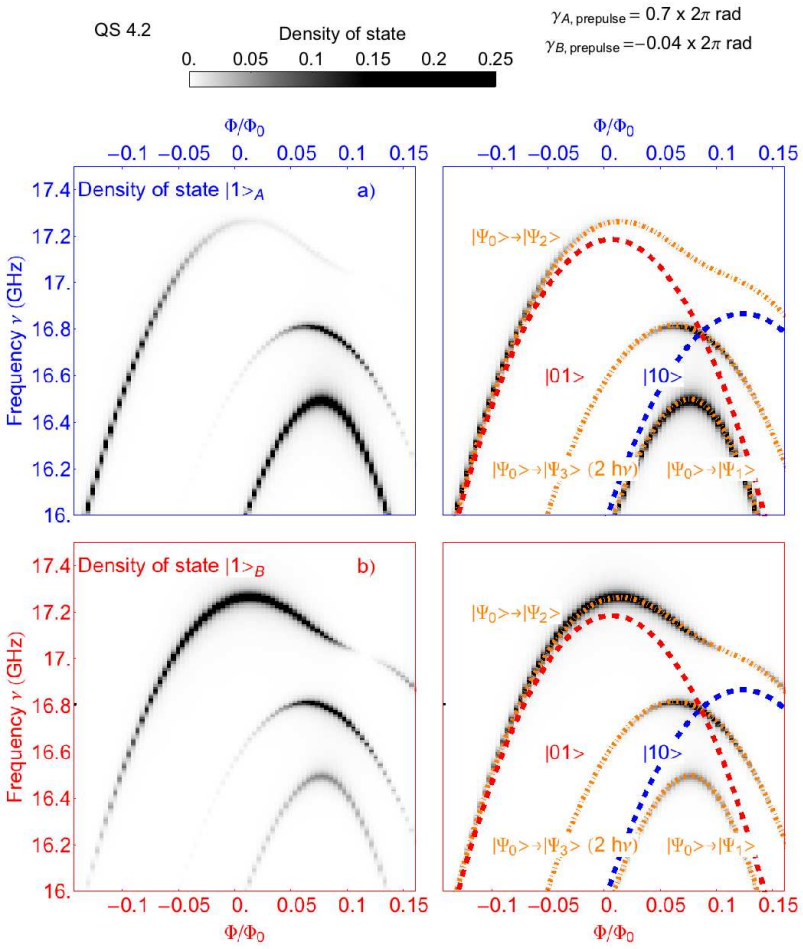

Fig. 3.10. Theoretical spectroscopy of the coupled quantroniums of sample QS 4.2 obtained by numerical integration of a master equation (see text). The parameters of the simulation are those used or determined independently in the experiment of Fig. 3.9: the energies of the sCPB, the coupling frequency $\nu_{cc} = 600MHz$, the prepulse currents, the 50% microwave crosstalk between the two gates, and the readout risetime of 6 ns. The panels show the simulated weights of state $|1\rangle$ for qubit A (top) and qubit B (bottom) as a function of the excitation frequency and of the magnetic flux Φ. The theoretical spectroscopic lines are shown in the right panels as in Fig. 3.9. One observes weight transfers in the phase regions indicated in Fig. 3.7.

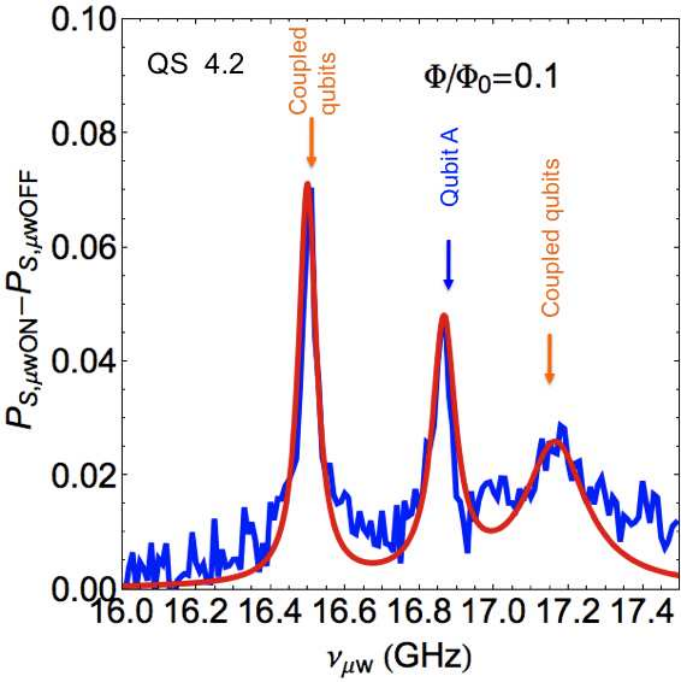

Fig. 3.11. Spectroscopic lines of sample QS 4.2 when the two quantroniums are in resonance, i.e. at $\Phi/\Phi_0 = 0.1$ on Fig. 3.9. The central peak corresponds to the excitation of the transition $|0\rangle \rightarrow |1\rangle$ of qubit A uncoupled to qubit B, whereas the two other peaks corresponds to the transition $|\Psi_0\rangle \rightarrow |\Psi_1\rangle$ (left) and $|\Psi_0\rangle \rightarrow |\Psi_2\rangle$ (right). The blue lines corresponds to the measured switching probability variations, whereas the red lines is a fit with three lorenztian lines of amplitude x, y, and z (from left to right).

3.2.3 Comparison with numerical simulation

The simulation of a complete spectroscopy experiment was performed by integrating the Lindblad equation for the driven two-qubit system in presence of decoherence. In the simple case of a unitary Hamiltonian evolution, the density matrix ρ of a quantum system obeys the equation

$$\frac{\partial \rho}{\partial t} = -\frac{i}{\hbar}\left[\mathbf{H}, \rho\right]. \tag{3.2}$$

In presence of Markovian decoherence sources, this equation can be generalized to non-unitary evolution, and the density matrix obeys a master equation that can be put in the so-called Lindblad form:

$$\frac{\partial \rho}{\partial t} = -\frac{i}{\hbar}\left[\mathbf{H}, \rho\right] + \sum_k \mathbf{C}_k \rho \mathbf{C}_k \dagger - \frac{1}{2}\left(\mathbf{C}_k^\dagger \mathbf{C}_k \rho + \rho \mathbf{C}_k^\dagger \mathbf{C}_k\right), \tag{3.3}$$

where the operators $\mathbf{C}_k$ and $\mathbf{C}_k^\dagger$ are the collapse operators. For the quantroswap system, $\mathbf{H}$ is given by Eq. (1.51), and the operators $\mathbf{C}$ correspond to the relaxation operator $\sqrt{\gamma_r}\sigma_-$ with γ_r the relaxation rate and the dephasing operator $\sqrt{\gamma_\varphi}\sigma_z$ with γ_φ the dephasing rate.

The simulation uses the same parameters as in the experiment described in the previous section. The two qubits are initialised in state $|0\rangle$, and their phases are shifted with the same amount as for the spectroscopy experiment shown on Fig. 3.9. Then a microwave field is applied on both gates during 200 ns (i.e. 10 times longer than the relaxation time used in the simulation) with an amplitude corresponding to a Rabi frequency $\nu_{r0} = 100$ MHz, taken into account the 50% microwave crosstalk. Finally, a ramp in δ with a duration τ is applied to qubit A, such that it simulates the readout ramp. At the end of the ramp, the probabilities of being in state $|00\rangle$, $|01\rangle$, $|10\rangle$, and $|11\rangle$ are obtained from the density matrix.

The results obtained are shown on Fig. 3.10 for a ramp with duration $\tau = 6$ ns. They qualitatively reproduce important features of the spectroscopic data shown in Fig. 3.9:

- First, the comparison between the amplitude of $|\Psi_0\rangle \rightarrow |\Psi_2\rangle$ observed with readout A and B shows that no or little energy transfer from qubit B to qubit A occurs during readout A, when $\nu_B = 16.8$ GHz $> \nu_A$ (region green in Fig. 3.7).
- Second, in presence of a level crossing during the readout ramp, one does find that the Landau-Zener transition probability is very small, and that an adiabatic energy transfer takes place from one qubit to the other one, as expected from Fig. 1.72 for such values of ν_{cc} and τ. The presence of the spectroscopic lines $|00\rangle \rightarrow |01\rangle$ on readout A (in experiment and in simulation) indeed clearly shows the effect.

- Finally, note that the microwave excitation power was sufficiently large to populate the state $|11\rangle$ (transition $|\Psi_0\rangle \rightarrow |\Psi_3\rangle$ in Fig. 3.10), as also observed in the experimental spectra (see middle orange dashed curves in top right panel of Fig. 3.7).

3.2.4 A necessary discussion: are our quantronium samples suitable for gate experiments?

We have determined the coupling between two quantronium qubits by fitting spectroscopic data in the vicinity of their avoided level crossing. During these investigations, we have characterised a dramatic problem found in our quantroswap samples: their transition frequency is unstable and undergoes sudden changes, which we attribute to large changes of the gate charge. We have not been able to determine the characteristic time of these changes: how long and how often do they occur? We can only affirm that the time spent away from the tuned operating point is not small, which severely hinders qubit operation. Moreover, these frequency changes cannot be analyzed using standard coherence time measurement technique, like Ramsey sequence, as it requires first to prepare the qubit in a superposition of state $|0\rangle$ and $|1\rangle$.

Two consequences can be directly seen. First, it implies that in quantronium experiments (single or two qubit experiment), part of the time we do not address the qubit at the correct frequency, which decreases the contrast on all experiments, including the observation of Rabi oscillations. Secondly, it also implies that the amplitude of the swap oscillations between the coupled quantroniums will be severely reduced. Note that a similar problem was also found for a charge qubit coupled to a phase qubit (see Aurelien Fay's thesis [87]).

3.3 Demonstration of swapping oscillations between two coupled quantroniums

Despite the problems encountered in our samples, we have been able to observe experimental evidence for swapping oscillations in Quantroswap samples. We present here the results obtained on sample QS 2.1.

3.3.1 Calibration of microwave pulses

In experiment QS 2.1, the short relaxation time (see Table 3.1) prevented us from preparing the system in state $|01\rangle$ with the qubits at different frequencies, and to displace then their working points to achieve the resonance condition necessary for performing swapping oscillations.
We have thus prepared the state $|01\rangle$ with the two qubits already on resonance, but using a very short π pulse on qubit B. As explained in section 1.2.2, the π pulse duration has to be much shorter in this case than the swapping time $1/\nu_{cc}$. In experiment QS 2.1, $\nu_{cc} = 230$MHz, and the π pulse duration was set to 1.5 ns. Besides, the 50% microwave gate crosstalk was compensated using the technique presented in section 3.1.5: two microwave pulses with a phase shift and an amplitude properly adjusted to compensate the crosstalk were applied to both gates. The two microwave pulses then interfere destructively on island A, which enables to maintain qubit A in the ground state.
To implement this strategy, we have first calibrated the delay between the microwave gate lines in order to cancel it.

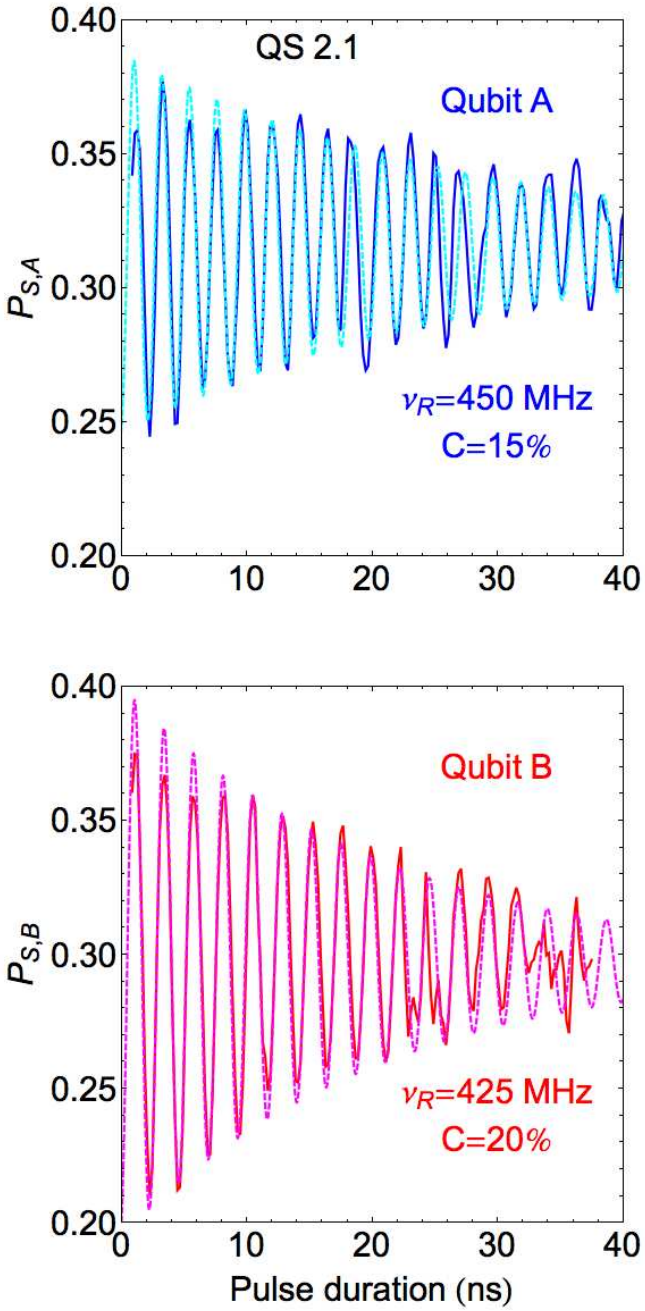

Fig. 3.12. Determination of the readout sensitivity using Rabi oscillations for both qubits. The lines are fit curves. The measured contrast and switching probabilities are used to calculated the expected switching probabilities in Fig. 3.16.

3.3.1.1 Delay compensation

The time calibration of the readout pulses was achieved by measuring the switching probability for both readout lines when varying the delay between the readout pulses and a 1ns resonant microwave pulse applied to gate A (or B), as shown on Fig. 3.13. These delays are then compensated by applying the microwave pulses at different times as needed.

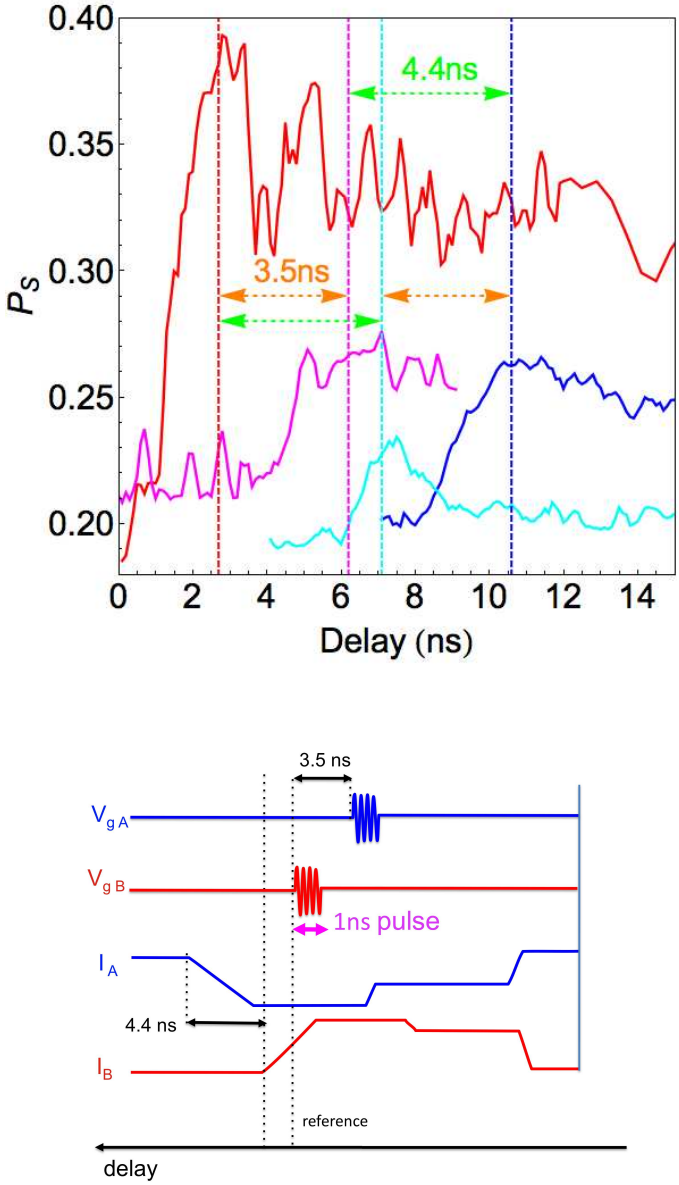

Fig. 3.13. Time calibration of the microwave excitation pulses and readout pulses. Measured switching probabilities of readout A (blue and cyan) and readout B (red and magenta) with respect to the delay between a π pulse on gate A (blue and magenta) or a π pulse on gate B (cyan and red) for nominal 0 delays on all sources. When the excitation pulse lays just before the readout pulse, the switching probability P_S is maximum. The arrows show the 3.5 ns long delay between the two microwave lines (orange) and the 4.4 ns long delay between the two readout lines (green). These measured delays are then canceled by programing proper delays on each source.

3.3.1.2 Microwave crosstalk compensation

In order to cancel the 50% microwave crosstalk already discussed in section 3.1.5, we have applied two similar microwave pulses on gate A and B, but with an amplitude twice as small on gate A as on gate B and an adequate phase shift (see Fig. 3.14) in order to have destructive interferences on island A. Using this technique, we were able to reduce spurious Rabi precession of the qubit A by a factor better than 5 as shown on Fig. 3.14, and to induce a π pulse on qubit B with a spurious excitation of qubit A of only 2%.

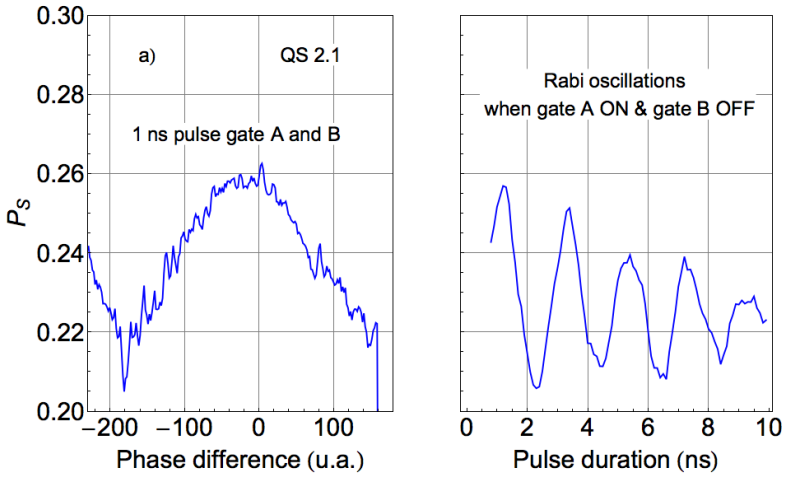

Fig. 3.14. Calibration of the phase shift between the two gate lines. a) Switching probability as a function of the dephasing due to the phase shifter when a microwave pulse is applied on both gates. b) Reference contrast (Rabi oscillations) on the same qubit with only one microwave applied.

3.3.2 Experimental demonstration of SWAP oscillations

For observing SWAP oscillations, we have first tuned the two qubits in resonance by adjusting the magnetic flux through the loops and the bias currents of the prepulses (see section 1.1) applied to the readout junctions, as shown on Fig. 3.15. The spectrocopy experiment shown in Fig. 3.8 shows that, when the reduced flux $\Phi/(2\pi)$ is set to 0.065 and the phases $\gamma_{A,B}/(2\pi)$ adjusted by the prepulses respectively equal to -0.065 and 0.08, the qubits are on resonance, with a transition frequency equal to 12.87 GHz.

In order to improve the contrast on the readout A (see section 1.1), we have used better parameters, i.e. $\Phi/(2\pi)$ to 0.081, $\gamma_A/(2\pi)$ to 0.07 and $\gamma_B/(2\pi)$ to

0.11. Then two microwave pulses at 12.83 GHz with duration 1.2 ns are applied using the techniques described above. The switching probability of the two readout junctions are finally measured with respect to the delay between them and the microwave pulses. Between preparation in state $|01\rangle$ and readout, the system evolves under the effect of the coupling, as explained in section 1.2.2.2, and swapping between the two qubits is expected. The data obtained are shown in Fig. 3.16.

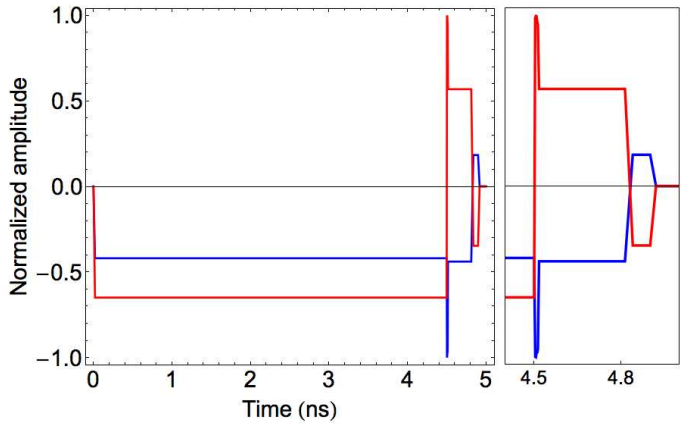

Fig. 3.15. Time dependence of the bias signals (unscaled) applied to readout A (blue) and readout B (red) for achieving the resonance condition, and for performing the readout.

3.3.2.1 Data analysis

The dashed curves on Fig. 3.16 show the predicted switching probabilities calculated from the model described below using the readout contrast $C_A = 15\%$ and $C_B = 20\%$ measured from the Rabi oscillations of the uncoupled qubits (see Fig. 3.12), and a relaxation time $T_1 = 40$ ns. The goal of this model is to include the qubit disappearance already discuss in section 3.2. For that purpose we make the following assumption:

- first, we assume that the frequency of each qubit is fixed during one measurement sample, and is equal to the excitation frequency ν with a probability p;
- second, when the qubit "disappears", we assume that the switching probability of its readout junction is P^*.
- third, we use the switching probabilities $P_{|0\rangle_{A,B}}$, $P_{|1\rangle_{A,B}}$ measured from Rabi oscillations on each qubit A and B, when they are in state

$|0\rangle$ and $|1\rangle$ (see in Fig. 3.12).
The two switching probabilities, when qubit is prepared in state $|0\rangle$ and $|1\rangle$, are thus

$$P_{0_{A,B}} = pP_{|0\rangle_{A,B}} + (1-p)P^*,$$
$$P_{\pi_{A,B}} = pP_{|1\rangle_{A,B}} + (1-p)P^*,$$

respectively, and the contrast $C_{A,B}$ is equal to $P_{\pi_{A,B}} - P_{0_{A,B}} = p(P_{|1\rangle_{A,B}} - P_{|0\rangle_{A,B}})$.
- finally, we suppose that any excited state relaxes in state $|00\rangle$ with a characteristics time T_1.

As explained in section 1.2.2.3, when qubit B is prepared in state $|1\rangle$ (or equivalently the system is prepared in state $|01\rangle$), the two qubits being in resonance, the probabilities for being left in state $|01\rangle$ and $|10\rangle$ at the end of the free evolution are given by $\cos(\nu_{cc}t)^2$, and $\sin(\nu_{cc}t)^2$, respectively. Thus, taking into account relaxation, these probabilities are actually $\cos(\nu_{cc}t)^2 e^{-t/T_1}$ and $\sin(\nu_{cc}t)^2 e^{-t/T_1}$, whereas the probability for being in state $|00\rangle$ is $1 - e^{-t/T_1}$. Using all these expressions, one obtains the switching probability of readout B during a SWAP experiment:

$$\begin{aligned}
P_B = {} & p^2\left[\cos(\nu_{cc}t)^2 e^{-t/T_1} P_{|1\rangle_B} + \sin(\nu_{cc}t)^2 e^{-t/T_1} P_{|0\rangle_B} + (1-e^{-t/T_1})P_{|0\rangle_B}\right] \\
& + p(1-p)\left[e^{-t/T_1} P_{|0\rangle_B} + (1-e^{-t/T_1})P_{|0\rangle_B}\right] \\
& + (1-p)pP^* \\
& + (1-p)^2 P^*,
\end{aligned}$$

where the first, second, third, and fourth lines correspond to case where $\nu_A = \nu = \nu_B$, $\nu_A = \nu \neq \nu_B$, $\nu_A \neq \nu = \nu_B$, and $\nu_A \neq \nu \neq \nu_B$, respectively. One simplifies this expression in

$$\begin{aligned}
P_B = {} & p(P_{|1\rangle_B} - P_{|0\rangle_B})e^{-t/T_1}\left[p\cos(\nu_{cc}t)^2 + (1-p)\right] \\
& + pP_{|0\rangle} + (1-p)P^* \\
P_B = {} & C_B e^{-t/T_1}\left[p\cos(\nu_{cc}t)^2 + (1-p)\right] + P_{0_B}.
\end{aligned}$$

The switching probability of readout A is

$$P_A = C_A e^{-t/T_1} p\sin(\nu_{cc}t)^2 + P_{0_A}.$$

The dashed curves on Fig. 3.16 corresponds to these probabilities with $p = 0.4$, a value is similar to the reduction coefficient used for fitting the loop current modulation shown in Fig. 3.4.

This model is actually based on the assumption that qubit disappearance has a slow dynamics. More precisely, once qubit B is excited at its nominal frequency, no frequency change occurs during the later 50 ns.

Moreover, this model does not take into account possible reduction of the swap oscillations due to the adiabaticity of the readout pulse (see section 1.2.3 for theory, section 3.2.2 for simulations). Indeed, when starting from two resonant qubits, measuring state $|01\rangle$ and $|10\rangle$ requires to move qubit frequencies faster than $0.01 \times \nu_{cc}^2$ (see Fig. 1.15 in section 1.2.3). Considering readout ramp about 4-6 ns, and the experimental working points of each qubits, we estimate that $\nu_{cc}^2 \times (\partial\Delta\nu/\partial t)^{-1} \simeq 0.07 \pm 0.02$, which gives an error due to readout of about $25\% \pm 10\%$.
To prevent the contrast from being reduced, we have applied an other π pulse on qubit B just before the measurement. This pulse transforms states $|10\rangle$ and $|01\rangle$ into states $|11\rangle$ respectively $|00\rangle$, which are uncoupled eigenstates of the system. Figure 3.16b shows that amplitudes of the SWAP oscillations on both readout are indeed increased compared to experiment in 3.16a.

Finally, this model does not take into account eventual spurious correlations between the switchings of the two readout junctions. More precisely, we have observed an increase of about 20% the switching probability on one readout when the second one switches with 100% probability, and this change follows the switching probability of the second one. Unfortunately, we have not been able to investigate this problem, and to determine the origin of this effect: electron heating in the wires, electromagnetic coupling, ...

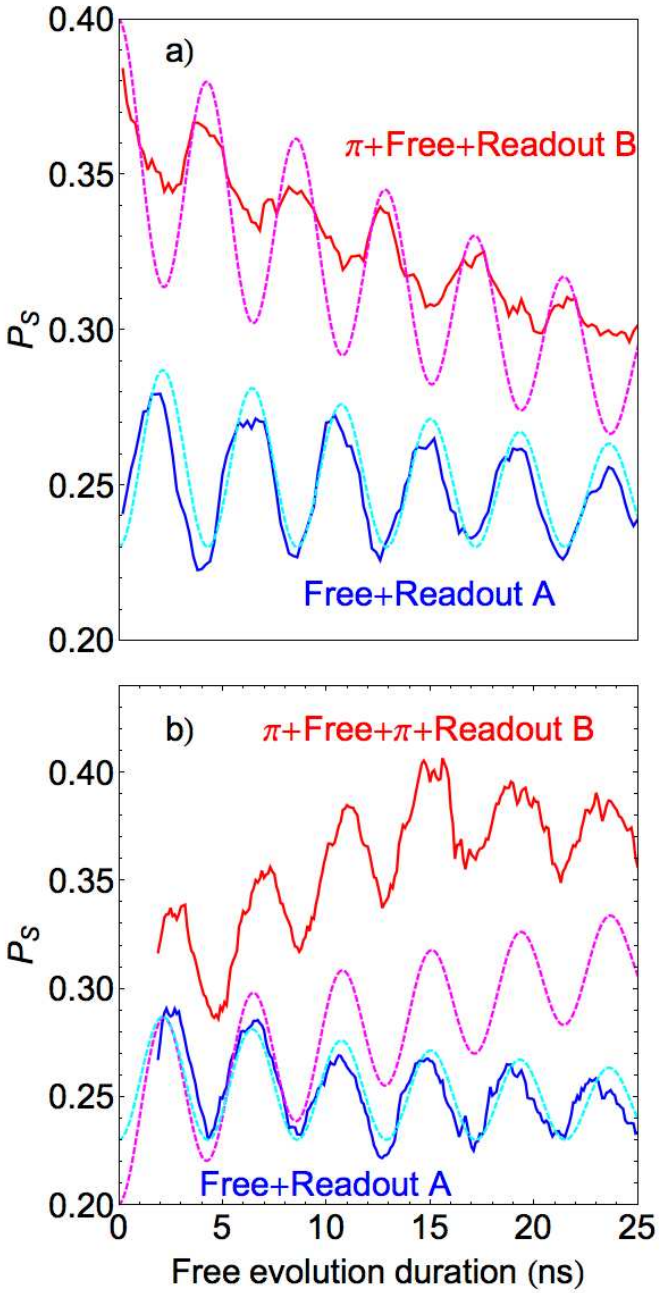

Fig. 3.16. Oscillations of switching probabilities corresponding to the swapping of the quantum of energy between the two qubits. Plain curves correspond to measured switching probabilities of readout A (blue) and B (red). Dashed curves are plots of the two functions $P_{\text{readout A,B}}(t)$. a) the system is prepared in state $|01\rangle$ with a 1.2 ns pulse, and is measured after a time t. b) the system is also prepared in state $|01\rangle$, then evolves freely during a time t, and is finally submitted to the same π pulse just before measurement. For an unknown reason prediction (magenta) and experiment (red) differ.

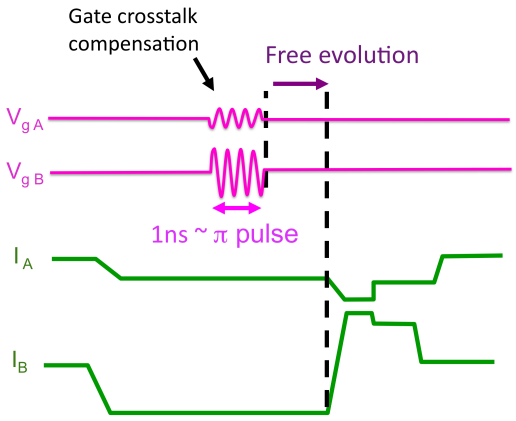
Gate crosstalk
compensation
Free evolution
$V_{g\,A}$
$V_{g\,B}$
1ns ~ π pulse
I_A
I_B

3.4 Conclusion

In conclusion, despite huge problems with our samples, we have demonstrated swapping oscillations between two coupled quantroniums. However, due to the low T_1 and readout visibility, we have been able neither to measure correlations between qubit readouts, nor to perform the full tomography of the $\sqrt{iSWAP}$ gate. In the course of the experiments, we have provided evidence for a very serious problem encountered in our quantronium qubits. They stay only part of the time at their nominal working point. Their transition frequency is thus not stable, which reduces the amplitude of any measurement performed. We attribute this instability problem to charge noise, possibly due to quasiparticle poisoning. The characteristic time of this instability is not known. We know from the observation of Rabi, Ramsey and swapping oscillations that it is longer than 100 ns. The reduced amplitude of all experimental signals involving an averaging time longer than a fraction of ms indicates that jumps already occur on this time scale.
Whatever the explanation, the conclusion is that the lack of coherence and of readout visibility in our Quantroswap samples does not make our quantroniums suitable for multiqubit experiments. We need more robust qubits, with better coherence properties, and with better readout fidelity. In this aim, in a subsequent chapter, we propose to use an other type of qubit circuits that was developed by R. Scholkopf's group at Yale combining at the same time another readout method developed by M. Devoret in order to achieve at the same time the two long sought-after goals of coherence and readout fidelity. We will present the first results obtained.

Chapter 4

Towards long coherence time qubits and single-shot high-fidelity readout

The quantroswap experiments have put in evidence many problems of quantronium qubits : "'blinking"' of the qubit (see chapter 3), irreproducibility of the decoherence time from sample to sample, and low readout fidelity.
The first problem seems to be related to the quantronium sensitivity to microscopic charge fluctuators and quasiparticle poisoning. The second problem might be related to the complexity of the quantroswap circuit compared to the first quantronium, leading to an imperfect control of the microwave impedance seen by the qubits (in particular through the readout circuit) despite our efforts. This opens unforeseen channels of relaxation and decoherence. The low readout fidelity might be due to the qubit blinking problem. Realizing multi-qubit experiments requires to solve all these issues.

Reducing the qubit sensitivity to charge noise can be achived by increasing the E_J/E_C ratio in order to have a qubit frequency almost insensitive to variation of N_g as shown on Fig. 1.2. Rob Schoelkopf group at Yale proposed and demonstrated a modification of the Cooper Pair box design : shunting the Cooper Pair box by a large interdigitated capacitor lowers E_C while maintaining E_J to a value comparable to the quantronium circuit. This circuit has been nicknamed "'the transmon"' [47] and has shown good coherence times [46]. In the Yale experiments, the transmon is driven and measured through a high-Q resonator, detuned from the qubit frequency, which filters out the electromagnetic noise at the qubit frequency. This setup offers a good control over the environment impedance seen by the qubit. The dispersive coupling between the qubit and the cavity provides an interesting readout method,

which perturbs only weakly the qubit during readout. However, this readout is not single-shot due to insufficient signal-to-noise ratio. We propose here to improve the dispersive readout method by using the bifurcation of a non-linear oscillator.

In order to discuss the dispersive readout of a qubit through a resonator, we will start with a brief introduction on the coupling of a qubit to a simple harmonic resonator. We will then explain the basic principles of dispersive coupling, starting with the simple linear dispersive method used in previous experiments. We will finally explain how the bifurcation of a non-linear resonator can improve this readout, and present first experimental results already demonstrating high-fidelity single-shot qubit state readout of a transmon qubit.

4.1 Theory and design

4.1.1 Dispersive coupling of a Cooper Pair box with a harmonic oscillator

4.1.1.1 A Cooper-pair box coupled to a harmonic oscillator

Our readout system is based on the dispersive interaction between a qubit and a harmonic oscillator. The system considered is shown in Fig. 4.1. A split Cooper Pair Box (assumed perfectly symmetric) of total Josephson energy E_J and charging energy E_C is capacitively coupled to a LC harmonic oscillator of resonance frequency ω_{cav} with a gate capacitor C_g. As explained in section 1.2, the sCPB is described by the Hamiltonian (1.8)

$$\widehat{H}_{CPB} = E_C \left(\widehat{N} - N_g\right)^2 - E_J \left[\cos\left(\frac{\delta}{2}\right)\cos\left(\widehat{\theta}\right)\right] \tag{4.1}$$

where $\delta = 2\pi\Phi/\Phi_0$ is the total phase imposed on the SQUID loop by the external flux Φ.

The resonator Hamiltonian is

$$\widehat{H}_{cav} = \hbar\omega_{cav}(a^+a + \frac{1}{2}). \tag{4.2}$$

The resonator voltage and current operators are

$$\widehat{V}_{cav} = \sqrt{\frac{\hbar\omega_k}{2C}}(\widehat{a}_k^+ + \widehat{a}_k)$$
$$\widehat{I}_{cav} = i\sqrt{\frac{\hbar\omega_k}{2L}}(\widehat{a}_k^+ - \widehat{a}_k).$$

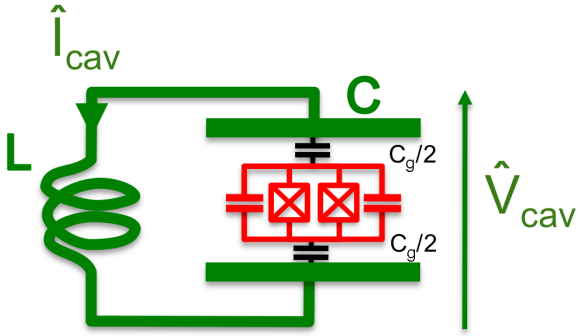

Fig. 4.1. Schematic representation of a transmon embedded in an microwave resonator.

We treat the qubit-resonator capacitive coupling in the same way as we did in Annex B for the inductive coupling. The reduced charge N_g is replaced in hamiltonian (4.1) by the operator

$$\frac{C_g}{2e}(V_{g_{\mathrm{DC}}} + \widehat{V}_{cav}), \tag{4.3}$$

and the Hamiltonian $\widehat{H}_{sCPB}$ is

$$\begin{aligned}\widehat{H}_{sCPB} = E_C\left(\widehat{N} - N_{g_{\mathrm{DC}}}\right)^2 - E_J\left[\cos\left(\frac{\delta}{2}\right)\cos\left(\widehat{\theta}\right)\right] \\ -2E_C\frac{C_g}{2e}\widehat{N}\widehat{V}_{cav} \\ +E_C\frac{C_g}{2e}\widehat{V}_{cav}^2 - 2E_C\frac{C_g}{2e}N_{g_{\mathrm{DC}}}\widehat{V}_{cav}\end{aligned} \tag{4.4}$$

The second line corresponds to the coupling Hamiltonian H_i between the sCPB and the resonator, whereas the third line can be seen as a renormalization term for the resonator capacitance. The Hamiltonian $\widehat{H}_i$ is

$$\begin{aligned}\widehat{H}_i &= -2E_C\frac{C_g}{2e}\widehat{N}\widehat{V}_{cav} \\ &= -2\frac{(2e)^2}{2C_\Sigma}\frac{C_g}{2e}\sqrt{\frac{\hbar\omega_k}{2C}}\widehat{N}(\widehat{a}+\widehat{a}^+) \\ &= -2e\frac{C_g}{C_\Sigma}\sqrt{\frac{\hbar\omega_k}{2C}}\widehat{N}(\widehat{a}+\widehat{a}^+) \\ &= -\hbar g_0\widehat{N}(\widehat{a}+\widehat{a}^+)\end{aligned} \tag{4.5}$$

with $g_0 = 2e\frac{C_g}{C_\Sigma}\sqrt{\frac{\hbar\omega_k}{2C}}$. The Hamiltonian of the whole system is thus

$$\widehat{H} = \widehat{H}_{sCPB} + \hbar\omega_{cav}(\widehat{a}^{+}\widehat{a} + \frac{1}{2}) - \hbar g_0 \widehat{N}(\widehat{a} + \widehat{a}^{+}). \tag{4.6}$$

This Hamiltonian can be simplified by considering only the first two energy levels $\{g, e\}$ of the CPB, and removing fast oscillating terms (rotating wave approximation) yielding

$$\begin{aligned}\frac{\widehat{H}}{\hbar} = & \frac{\omega_{ge}}{2}\widehat{\sigma}_z \\ & + g(\widehat{\sigma}^{+}\widehat{a} + \widehat{\sigma}^{-}\widehat{a}^{+}) \\ & + \omega_{cav}(\widehat{a}^{+}\widehat{a} + \frac{1}{2})\end{aligned}$$

where ω_{ge} (see Fig. 1.2) is the transition frequency between ground state and first excited state, $g = g_0 \langle g| \widehat{N} |e\rangle$. This is the well-known Jaynes-Cummings Hamiltonian on which relies all cavity Quantum Electrodynamics (cavity QED) experiments. In particular, when the $g - e$ transition is resonant with the resonator frequency ($\omega_{ge} = \omega_{cav}$), the coupled system energy eigenstates are coherent superpositions of qubit and photonic wavefunctions. This leads to the opening of an anticrossing in the system's energy spectrum, the vacuum Rabi splitting $2g$. A numerical calculation of the system's first two energy states as a function of the phase δ is shown in Fig. 4.2 top, for a situation where the maximum CPB frequency $\omega_{ge}(\delta)$ is above ω_{cav} (so that it crosses the cavity frequency for a certain value of δ) and for typical sample parameters. The anticrossing is clearly visible. The first experimental observation of this anticrossing with superconducting circuits by the Yale group [18] has opened the way to the realization of cavity QED experiments with circuits, a promising new field nicknamed circuit QED.

4.1.1.2 The dispersive approximation

In this chapter we will be mainly concerned by the possibilities of performing qubit state readout using circuit QED setups. For readout purposes, the most interesting regime is the so-called dispersive regime, in which $|\omega_{ge} - \omega_{cav}| >> g$ so that there can be no energy exchange between the qubit and the resonator. One can then derive an effective Hamiltonian [88] that reads

$$\frac{\widehat{H}}{\hbar} = \frac{\omega_{ge} + \chi}{2}\widehat{\sigma}_z + \underbrace{[\omega_{cav} + \chi\widehat{\sigma}_z]}_{\omega'_{cav}}(\widehat{n} + \frac{1}{2})$$

with

$$\chi = \frac{g^2}{\omega_{ge} - \omega_{cav}} \tag{4.7}$$

This Hamiltonian shows that the cavity resonance frequency $\omega'_{cav} = \omega_{cav} + \chi\widehat{\sigma}_z$ is shifted by $\pm\chi$ depending on the qubit state (an effect called "'cavity pull"' by the qubit). This constitutes the basis of all dispersive readout methods that we are going to analyze in the following. The value of the parameter χ fully determines the amount of cavity pull ; the larger it is, the easier the measurement. In Fig. 4.2 bottom, the value of χ is shown as a function of δ (blue dashed line), together with a non perturbative calculation of $\chi_{non-pert}$ (red dashed line). The domain of non-validity of the dispersive approximation is the region where red and blue lines are far from each other. It is shown in green in Fig. 4.2. Note the strong dependence of χ with the detuning from the cavity resonance frequency $|\omega_{ge} - \omega_{cav}|$. This means that the fidelity of dispersive readout methods based on this Hamiltonian depends on the specific bias point at which the experiment is done. The best situation is when $|\omega_{ge} - \omega_{cav}|$ is just large enough to be in the dispersive limit while small enough so that χ still has significant value (for instance, $|\omega_{ge} - \omega_{cav}| \approx 5g$ is typically a good compromise).

A slight complication arises when the CPB is of the transmon type. Indeed, transmons are less anharmonic than CPBs with a smaller E_J/E_C ratio. As a result, the resonance frequency between first and second excited state ω_{ef} is relatively close to ω_{ge} [1]. This does not change the form of the dispersive Hamiltonian describing a transmon coupled to a resonator, but just the value of $\chi = g_{ge}^2/(\omega_{ge}-\omega_{cav}) - g_{ef}^2/2(\omega_{ef}-\omega_{cav})$ where g_{ge} (resp. g_{ef}) is the coupling constant between the $g-e$ (resp. $e-f$) transition and the resonator mode. [88].

Note also that the validity of the dispersive approximation is limited to low photon number occupation of the resonator. Indeed, if the cavity contains N photons, the coupling constant on the $g-e$ transition becomes $g_{ge}\sqrt{N}$, which should always stay smaller than the detuning $|\omega_{ge} - \omega_{cav}|$. This leads to the definition of a *critical photon number* below which the dispersive approximation is valid $n_{crit} = |\omega_{ge} - \omega_{cav}|^2/4g_{ge}^2$. This important caveat means that all dispersive readout experiments should be performed at low measurement powers.

Before going on with the description of the principles of dispersive readout, we need to discuss a small technical detail which has to do with the experimental implementation of the resonator. Lumped element LC resonators working at GHz frequencies are in fact difficult to realize properly using microfabrication techniques. Distributed resonators allow to obtain larger quality factors and give a better control of the impedance seen by the qubit at microwave frequencies. We will now briefly describe distributed resonators and show under what conditions the coupling hamiltonian is still valid.

[1] To be more specific, $\omega_{ef} \approx \omega_{ge} - E_C/4\hbar$

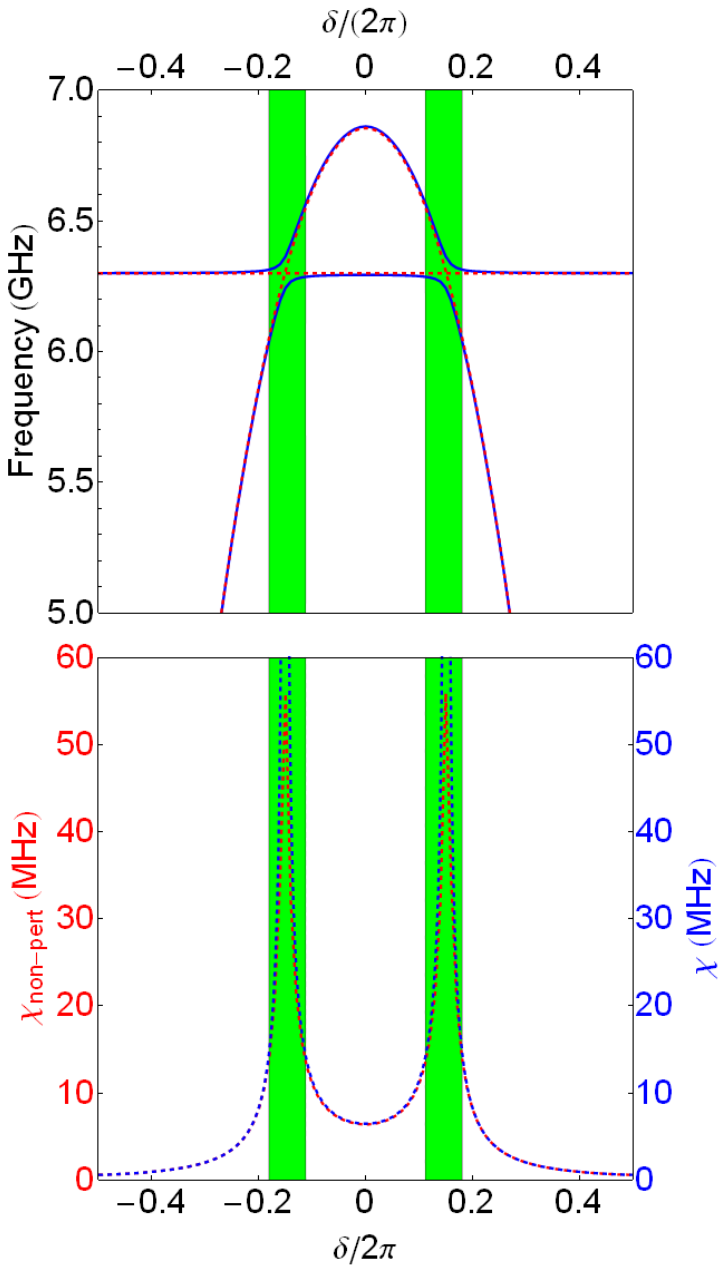

Fig. 4.2. (top) First two energy levels of a two-level Cooper-pair box coupled to a resonator for $E_J = 400\text{mK}$, $E_C = 200\text{mK}$, $\omega_{cav} = 2\pi \times 6.3\text{GHz}$ and $g = 2\pi \times 60\text{MHz}$ as a function of $\delta/(2\pi)$(top). The dashed lines show the uncoupled energy states, the blue solid line shows the coupled system energy spectrum. (bottom) (dashed blue line) Dispersive coupling constant χ as a function of $\delta/(2\pi)$. (dashed red line) Non-perturbative cavity frequency shift. The non-validity domain of the dispersive approximation is the shaded green region.

4.1.1.3 Distributed resonator

We consider the system shown in Fig. 4.3 : a transmission line of length L, of inductance and capacitance by unit length $\mathcal{L}$ and $\mathcal{C}$, of characteristic impedance $Z_0 = \sqrt{\mathcal{L}/\mathcal{C}}$, is interrupted at its two ends at $x = -L/2$ and $x = L/2$. The voltage at point x and time t can be decomposed on the resonator's eigenmodes at frequencies $\omega_k = k\pi\bar{c}/L$, where $\bar{c} = 1/\sqrt{\mathcal{L}\mathcal{C}}$ is the wave phase velocity. More precisely [89], one can show that the voltage operator at point x and time t can be written

$$\widehat{V}(x,t) = -\sum_{k=1}^{\infty} \sqrt{\frac{\hbar\omega_{2k-1}}{L\mathcal{C}}} \sin\left(\frac{(2k-1)\pi x}{L}\right)[a_{2k-1}(t)+a_{2k-1}^{+}(t)]+\sqrt{\frac{\hbar\omega_{2k}}{L\mathcal{C}}}\cos\left(\frac{2k\pi x}{L}\right)[a_{2k}(t)+a_{2k}^{+}(t)] \tag{4.8}$$

Here we restrict ourselves to the fundamental mode $k = 1$ so that $\omega_{cav} = \pi\bar{c}/L$. The voltage at $x = -L/2$ is $V(t) = \sqrt{\frac{\hbar\omega_{cav}}{L\mathcal{C}}}[a(t) + a^{+}(t)]$.

The equivalent lc circuit can be found by satisfying two conditions : the resonant frequency of the lc oscillator should be ω_{cav}, and the voltage operator across the capacitor c should be equal to $V(t)$. This leads to the conditions $1/\sqrt{lc} = \omega_{cav}$ and $\sqrt{\frac{\hbar\omega_{cav}}{L\mathcal{C}}} = \sqrt{\frac{\hbar\omega_{cav}}{2c}}$. This yields $c = \frac{L\mathcal{C}}{2}$ and $l = 2L\mathcal{L}/\pi^2$. This can be reexpressed by noting that $\mathcal{L} = \pi Z_0/(L\omega_{cav})$ and $\mathcal{C} = \pi/(LZ_0\omega_{cav})$, yielding $c = \frac{\pi}{2\omega_{cav}Z_0}$ and $l = \frac{2Z_0}{\pi\omega_{cav}}$. Under these conditions, the Hamiltonian of the coupled qubit-distributed resonator shown in Fig. 4.3 is the same as the coupled qubit-lumped element lc resonator.

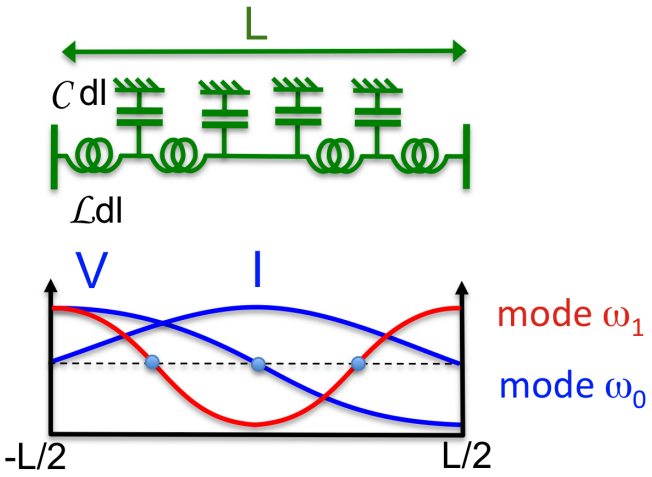

Fig. 4.3. Schematic representation of a distributed microwave resonator of length L.

4.1.2 Dispersive readout with a Josephson Bifurcation Amplifier

4.1.2.1 Linear dispersive readout

The basic principle of the linear dispersive readout method is shown in Fig. 4.4a. The qubit-cavity system is coupled to a 50Ω transmission line through a capacitor C_g. An input microwave signal V_{in} at the bare cavity resonance frequency ω_{cav} is reflected on the cavity. Measuring the phase of the reflected signal V_{out} should ideally yield φ_e or φ_g depending on the qubit state.

Unfortunately, for technical reasons, in present-day setups the signal-to-noise ratio (SNR) is not enough to discriminate between φ_g and φ_e in one single experimental sequence (so-called single-shot regime). This is due to two distinct constraints limiting the efficiency of the linear dispersive readout method. First of all, the integration time during which the phase is measured after each experimental sequence can not be longer than the excited state relaxation time T_1. In addition to that, the measurement power should always stay below the critical photon number inside the cavity. This means that we are bound to measure the phase of a weak signal, in a limited time. The bottleneck is then the noise of our first amplifier. Although it is one of the best commercially available HEMT amplifier with a noise temperature of 3K, the final signal-to-noise is not sufficient to properly discriminate between φ_g and φ_e.

Nevertheless, the average value of the phase computed over many identical experimental sequences still gives the average qubit excited state population. This method has been successfully applied by the Yale group to perform a number of interesting experiments : high fidelity single-qubit operations [90], two-qubit coherent exchange of energy [30], ... but the lack of single-shot resolution is a serious limitation of this linear dispersive readout method.

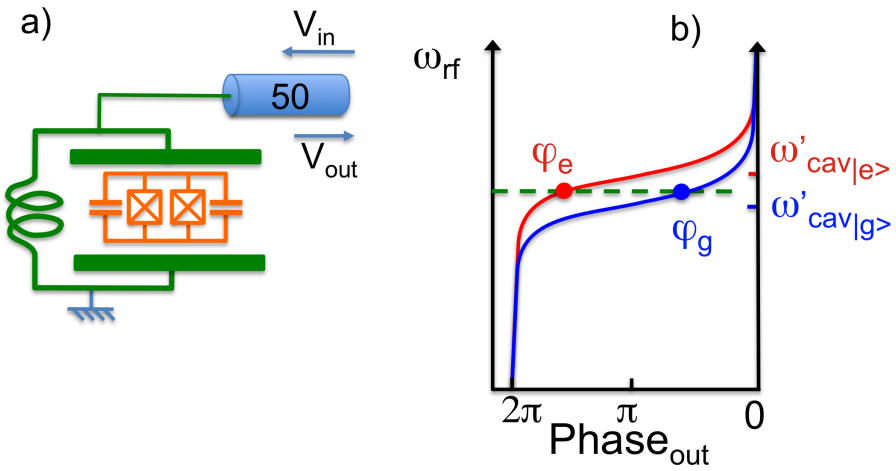

Fig. 4.4. (a) Principle of the dispersive readout, and (b) qubit-state dependent phase of the reflected signal

4.1.2.2 Cavity Josephson Bifurcation Amplifier based dispersive readout

In order to increase the signal to noise ratio, and thus to achieve single-shot measurement, with a dispersive readout, we have decided to build an active device, on-chip, cooled at 20 mK, which should thus have a much lower noise temperature than our HEMT amplifier. A natural choice is to use a Josephson-junction based amplifier, which can be very naturally integrated with qubit circuits. We have decided to use a device called "'Josephson Bifurcation Amplifier"' (JBA) developed at Yale University by M. Devoret's group [19]. We will first explain the basic principle of Josephson Bifurcation Amplifiers.

Principle of the Josephson Bifurcation Amplifier

The Josephson Bifurcation Amplifier (JBA) is based on the existence of several dynamical states of oscillations for a non-linear oscillator submitted to

a radio-frequency excitation. As an example, we can first consider the case of a Josephson oscillator made of a Josephson junction (of superconducting phase γ) in parallel with a capacitance C, and connected to a 50 Ω line. When driven at a frequency νrf close to the resonance frequency ν_p, the phase γ develops oscillations, which obey the following equation of motion (see Annex F)

$$\ddot{\gamma} + \frac{\omega_p}{Q}\dot{\gamma} + \omega_p^2 \sin(\gamma) = \eta\omega_p^2 \cos(\omega_{rf} t) \tag{4.9}$$

with $\eta = V/(ZI_0)$, $Q = 50C2\pi\nu_p$ the quality factor of the resonator and $\omega_p^2 = I_0/(\varphi_0 C)$. With a drive frequency sufficiently detuned from ν_p ($1 - \nu_{rf}/\nu_p > \sqrt{3}/(2Q)$), the amplitude $|\gamma|$ of oscillations can be multi-valuated. Indeed, considering only stationary solutions for this equation, and thus looking for solutions for γ under the form $|\gamma|\cos(2\pi\nu_{rf}t + \varphi)$, this equation is simplified in

$$-\Omega^2|\gamma|\cos(\omega_{rf}t+\varphi) - \frac{\Omega}{Q}|\gamma|\sin(\omega_{rf}t+\varphi) + 2J_1(|\gamma|)\cos(\omega_{rf}t) = \eta\cos(\omega_{rf}t)\,, \tag{4.10}$$

where $\Omega = \omega_{rf}/\omega_p$ and the Bessel function J_1 comes from the Jacobi-Anger relation (see Annex F). By multiplying this expression by $\cos(\omega_{rf}t)$ and integrating over one period of oscillation, one obtains

$$(2J_1(|\gamma|) - \Omega^2|\gamma|)^2 + \left(\frac{\Omega}{Q}\right)^2 |\gamma|^2 = \eta^2, \tag{4.11}$$

By expanding the Bessel function around 0 at the third order, one obtains a polynomial, whose roots are the solutions of the simplified equation:

$$((1-\Omega^2) - \frac{x}{8})^2 x + \left(\frac{\Omega}{Q}\right)^2 x = \eta^2, x \in \mathbb{R}^+. \tag{4.12}$$

Depending on the driving parameters ω_{rf}, and η, this equation has one, two or three solutions. Points $\{\omega_{rf}, \eta\}$ where only two solutions exists are called bifurcation points B, as they corresponds to borders between region where one solution exists, and region where three exist. These two regions are noted I and II, respectively, in Fig. 4.5 and 4.7. These bifurcation points are gathered into two categories $B_\uparrow$ and $B_\downarrow$, which correspond to bifurcation from region of low-amplitude oscillations to large-amplitude ones, and from large ones to low ones, respectively. These two categories have one common point, called the critical point, where the three solutions are degenerated.

As explained in [91, 17], in region II only the low and large amplitude mode of oscillations are stable. Moreover, the existence of multiple solutions induces an hysteric behavior of the oscillator. More precisely, for a given frequency when increasing the amplitude η, the oscillations switches at point $B_\uparrow$ from low to large amplitude oscillations; while, when coming backward, the oscillations switches at point $B_\downarrow$ from large to small amplitude oscillations [91, 17].

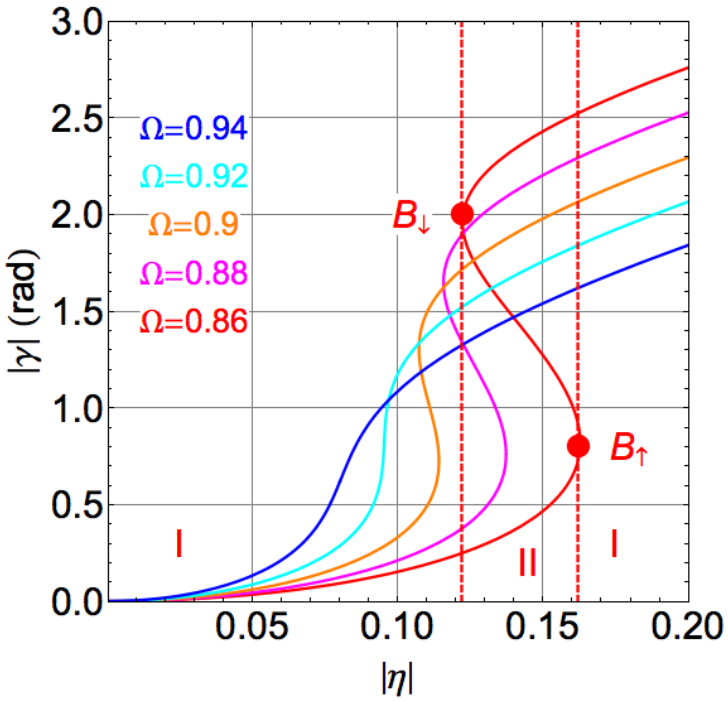

Fig. 4.5. Amplitude $|\gamma|$ of the oscillations as a function of the reduced driving amplitude η for different value of Ω. The two bifurcation points $B_\uparrow$ and $B_\downarrow$ at $\Omega = 0.86$ are indicated by dots, they define the two regions I and II for this value of Ω.

Switching occurs by activation above an energy barrier. At high temperatures, the activation is thermal and switching is a stochastic process characterized by a transition rate Γ that depends on temperature and on the distance between the working point and the nearest bifurcation point. In the case of the Duffing oscillator, M. Dykman has proposed a method to calculate the switching probability P_s [92, 93]. At low temperature ($T < \hbar\omega_{cav}/k_B$), the switching becomes activated by quantum fluctuations [94] with equivalent temperature $T_q = \hbar\omega_{cav}/(2k_B)$.

In this paragraph we discussed so far a lumped element version of the bifurcation amplifier, consisting of a Josephson junction in parallel with a capacitor. It is also possible to realize a JBA with a non-linear distributed resonator, consisting of a transmission line resonator with a Josephson junction in its center (an anti-node for the current) as shown in Fig. 4.6. Such device is called a Cavity Josephson Bifurcation Amplifier (CJBA) and has

been studied shown in [19].

Cavity Josephson Bifurcation Amplifier based readout

Our readout circuit design is shown in Fig. 4.6. It consists in a CJBA capacitively coupled to a Cooper Pair Box of the transmon type. As in the linear dispersive readout method, this circuit relies on the shift of the cavity frequency experienced by the cavity when the qubit changes state due to the dispersive qubit-cavity Hamiltonian ; but we now probe this frequency shift using the CJBA.

The experimental sequence allowing to measure the qubit state with a CJBA is shown in Fig. 4.7. The envelope of the readout microwave pulse is shown on top of the figure. The microwave amplitude is first increased at a value V_p and kept constant during a time interval called "'plateau"'. One choses V_p such that $B_{\uparrow e} < V_p < B_{\uparrow g}$, so that the CJBA bifurcates if the qubit is in state e and does not if the qubit is in state g. The qubit state measurement is performed during this plateau. After the plateau, the microwave amplitude is decreased to a value V_l such that $B_{\downarrow e} < V_l$ during a time interval called "latching". This second part of the measurement pulse has nothing to do with qubit readout ; it simply maintains the CJBA in its final oscillation mode reached at the end of the plateau. The duration of this latching step can be as long as needed to properly distinguish between the two oscillator states, without limitation. This allows to discriminate with 100% efficiency the two oscillator states by measuring the phase of the reflected signal. Provided the two switching curves associated with the two qubit states are separated enough, one should obtain a single-shot discrimination of the two qubit states. As for DC switching measurement, we define the fidelity of the readout as the difference of switching probabilities when the qubit is in state $|g\rangle$, and $|e\rangle$.

Comparison with existing dispersive readout methods

Our readout method is based on the coupling of a qubit to a resonator whose frequency slightly depends on the qubit state. In order to understand properly the specific interest of our circuit design, it is useful to compare it to other existing dispersive readout methods based on the same principle. As we will see, various coupling types have been investigated. We will more specifically discuss 3 experiments and compare them to our setup : (1) dispersive readout of a Cooper-pair box by linear capacitive coupling to a linear resonator [18, 90] (2) dispersive readout of a Cooper-pair box coupled to a non-linear resonator via the inductance of a Josephson junction [28, 37, 42, 48] and (3) dispersive readout of a flux qubit inductively coupled to a DC SQUID based non-linear resonator [43, 44]. Our circuit design consists in (4) the dispersive readout of a Cooper-pair box capcitively coupled to a non-linear resonator. All these readout circuits are summarized in Fig. 4.8.

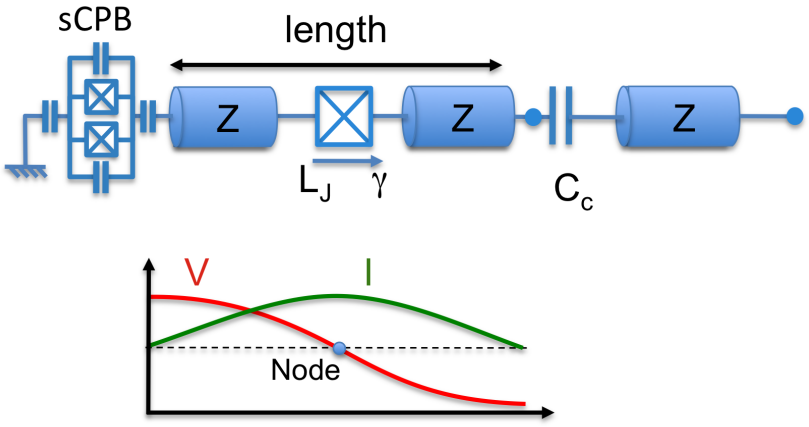

Fig. 4.6. Cavity Josephson Bifurcation Amplifier based dispersive readout scheme. A transmon is capacitively coupled to a microwave cavity resonator. A Josephson junction is inserted at the antinode of the magnetic field (and current), making the resonator non-linear.

Let us remind that an ideal readout method would take at its input an unknown qubit state $\alpha|e\rangle + \beta|g\rangle$ and measure 0 with a probability $|\alpha|^2$ and 1 with probability $|\beta|^2$. Readout errors occur 1) if the mapping between the quantum state of the qubit $|i\rangle$ $(i = e, g)$ and the result of the readout j $(j = 0, 1)$ is not perfect 2) if the readout takes so much time that the qubit has time to relax before being measured (this results in an asymmetric readout error, present only if the qubit is in $|e\rangle$), or 3) if the readout process by itself induces some transition between the two qubit states. For instance, the readout process may lower the qubit excited state lifetime, or even induce some excitation from ground to excited state. It is therefore important to properly understand, for each readout method, what limits its speed, and what backaction it will exert on the qubit. We would like to stress that the only relevant backaction here is the backaction that induces some mixing between states $|g\rangle$ and $|e\rangle$; a measurement backaction that leads to dephasing is not a problem at all ; in fact, the best readout apparatus has to induce a complete dephasing of the qubit state once readout is completed. Although a detailed comparison of all qubit-resonator coupling schemes is out of the scope of this paragraph, we would like to point out in this paragraph a few differences between these circuits in order to understand better the interest of our design. These differences consist in the type of backaction seen by the qubit during the measurement.

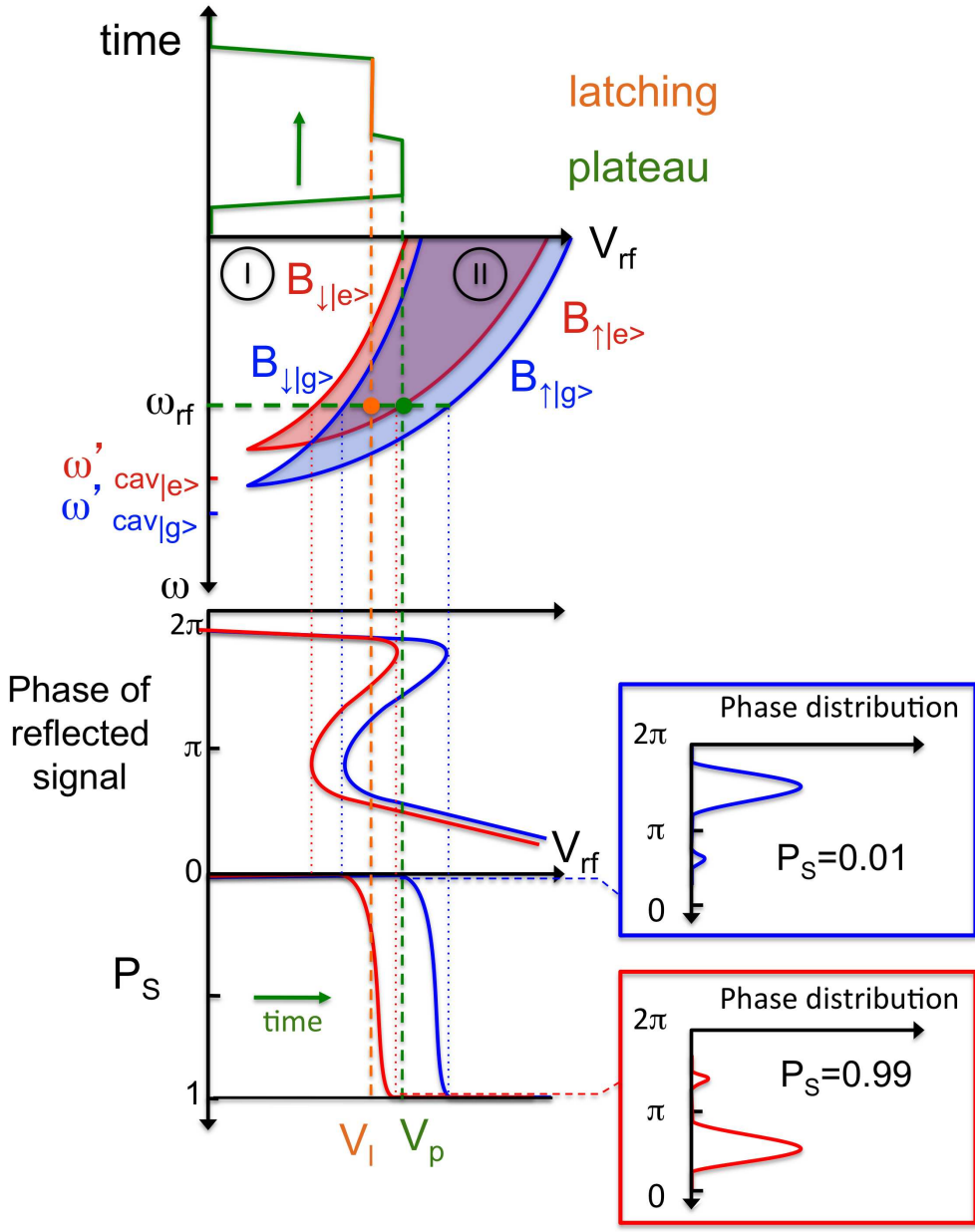

Fig. 4.7. Principle of the dispersive qubit state readout with a CJBA. The microwave pulse envelope (top) includes a measurement plateau at a value V_p and a latching part at a value V_l. The plateau maps the qubit state on the resonator dynamical state, and the latching part keeps the oscillator in the same state as at the end of the plateau. Depending on the qubit state, the switching probebilities are very different and allow to discriminate between the two qubit states in a single measurement.

	Description	Backaction	Visibility	Ref
	CPB capacitively coupled to a linear resonator	Photon number (AC Stark Shift)	not single -shot	[18, 89]
	CPB coupled to non-linear Resonator via Josephson junction	Photon number (AC Zeeman shift) + current through junction	60%	[28, 37, 42, 48]
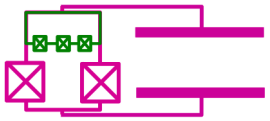	Flux-qubit inductively coupled to non-linear SQUID resonator	Photon number (AC Zeeman shift) + current through SQUID	87%	[43, 44]
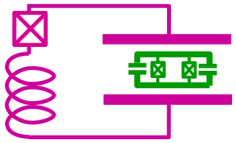	CPB capacitively coupled to a non-linear resonator	Photon number (AC Stark Shift)	89%	

Fig. 4.8. Comparison between four different dispersive qubit state readout methods: 1) Cooper pair box capacitively coupled to a linear resonator, 2) Cooper pair box inductively coupled to a non-linear resonator through a Josephson junction, 3) flux qubit inductively coupled to a non-linear SQUID based resonator, and 4) Cooper pair box capacitively coupled to a non-linear resonator.

Given the basic principle of dispersive readout detection, it seems natural to think that the ideal system Hamiltonian would be $H = H_q + H_{cav} + H_I$ with $H_q = -\hbar\omega_q/2\sigma_z$, $H_{cav} = \hbar\omega_{cav}a^\dagger a$, and $H_I = \chi a^+ a\sigma_z$, so that the resonator frequency is shifted by a quantity $\chi\sigma_z$ that bears some information on the qubit state. All the experiments considered in this paragraph do contain such interaction term, that describes a coupling between the qubit energy (σ_z operator) and the photon number stored in the resonator (term $a^\dagger a$). This interaction leads to a measurement-induced dephasing by ac-Stark (or Zeeman) shift [95] that is nearly unavoidable in any dispersive readout scheme, and which should not induce any energy relaxation. However, in circuits (2) and (3) other terms are also present. For instance, in circuit (2), the qubit energy depends not only on the photon number stored in the resonator, but also on the current that flows through the readout junction. In order to perform readout, one needs to excite the resonator at its resonance frequency ω_{cav}, so that the qubit frequency is then modulated at ω_{cav} during readout, on a frequency range that may be relatively important (typically a few 100 MHz).

This is also valid for circuit (3), and may cause spurious relaxation from state $|e\rangle$ to state $|g\rangle$ as has indeed been observed [96]. To the contrary, in circuits (1) and (4), the transmon resonance frequency does not depend at all on a DC electric field because of its large E_J/E_C ratio, so that the qubit frequency is not modulated at ω_{cav} during readout (purely transverse coupling term) ; it is only shifted due to measurement-induced ac-Stark shift. Preliminary measurements seem to indicate that the qubit relaxation rate is indeed hardly affected by the readout in our design, in contrast with other readout schemes [96].

To summarize, our goal with this circuit design (4) was to combine the minimum backaction during readout that had been achieved with circuit (1) together with the large signal-to-noise ratio provided by the bifurcation amplifier as demonstrated in circuits (2) and (3) allowing single-shot discrimination between the two qubit states.

4.2 Implementation

4.2.1 Fabrication

We briefly present in this section the various techniques used to fabricate our samples. Fig. 4.9 shows the main parts of the circuit.

The center photograph is a view of the distributed resonator. It consists of a Niobium coplanar waveguide (CPW) deposited on a Si-SiO_2 wafer, interrupted on the right by a coupling capacitor towards the 50Ω line, and on the left by an open end with a gap in which the qubit is fabricated. The inner conductor has a width of 10 μm and the gap between it and the ground is 5 μm, so that the impedance of the CPW is 50 Ω ($\epsilon_{r_{Si}} \simeq 12$). The resonator length was chosen such that the resonance frequency of the fundamental mode is close to 7 GHz (for a resonator without junction). In the middle of the resonator, the inner conductor is interrupted in order to place a Josephson junction.
The CPW is fabricated by first sputtering Niobium on top of a wafer, which is then reactive-ion etched through a resist mask patterned by optical lithography (see Annex C). The central Josephson junction and the sCPB are fabricated by e-beam lithography and double-angle evaporation of Aluminum (see Annex C).

4.2.2 Measurement Setup

A schematic drawing of our measurement setup is shown in Fig. 4.10. Once the circuit is fabricated, it is glued with wax on a microwave printed circuit board and connected to copper gold-plated coplanar waveguides using wirebonding. The PCB is placed in a copper box, and thermally anchored at 20 mK.
Microwave signals are generated by mixing continuous wave signals with DC

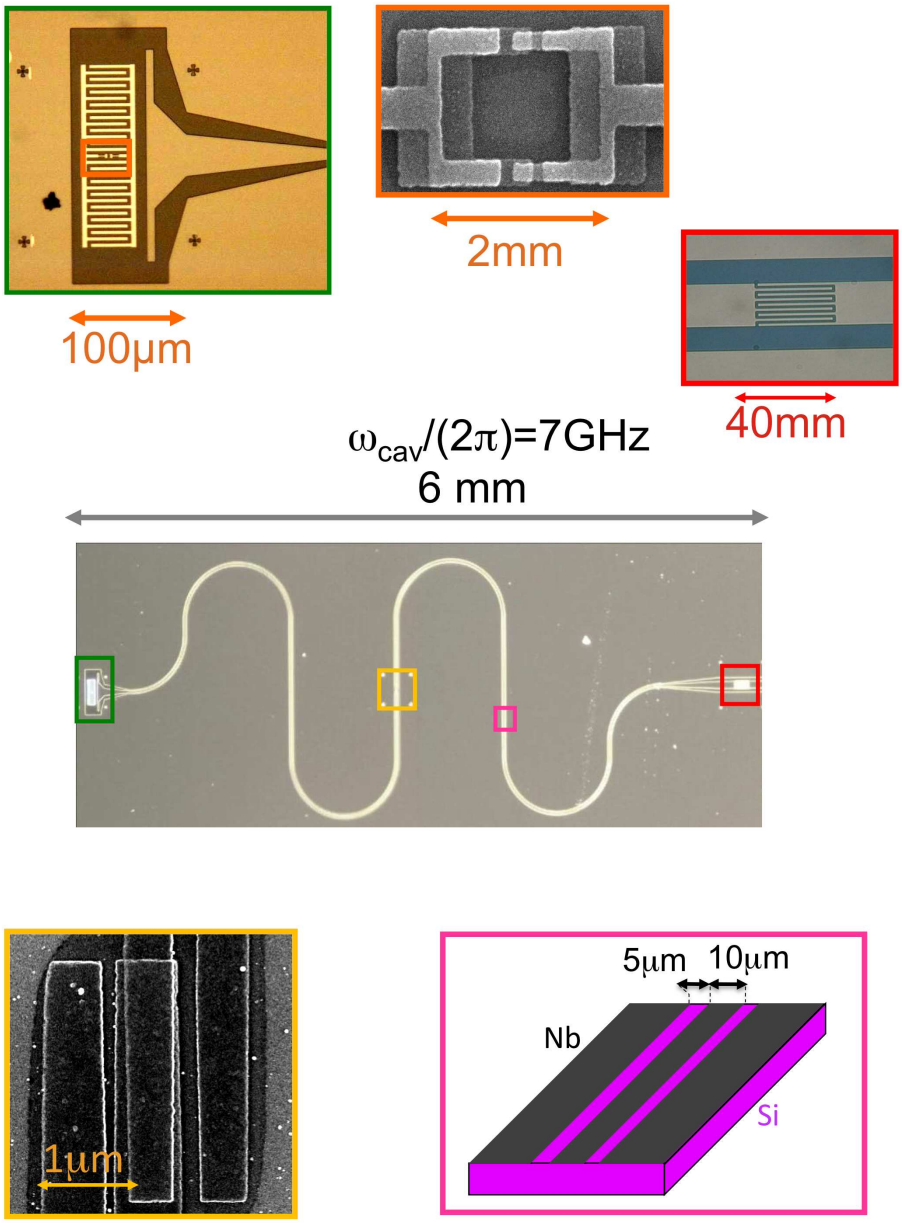

Fig. 4.9. Pictures of the main circuit elements. In the center, the Coplanar Waveguide resonator. At its left side (green) is placed the transmon (top left), while at its right side, it is connected to 50 Ω line through an interdigitated capacitor (red) (top right). In the middle of the resonator (yellow), a Josephson junction is inserted in the inner conductor.

pulses generated by an Arbitrary Waveform Generator [2]. Two distinct sources are used, one tuned in resonance with the qubit resonance frequency ω_{ge} to coherently drive it, and another one at the frequency ω_{rf} required by the bifurcation readout scheme (note that each source is associated with a separate set of mixers and envelope pulses). The two pulses are then combined and sent down the cryostat through the input line, which includes heavy attenuation and filtering at low temperatures in order to suppress thermal radiation at the resonator input. After reaching circulator C_1, the microwave pulses reach the sample input, are reflected and channeled by C_1 towards the output line. The pulses are amplified by a cryogenic amplifier cooled at 4 K, after passing through a low-loss superconducting coaxial cable and 2 isolators which protect the qubit from thermal and amplifier noise. The pulses are then further amplifier at room-temperature. Homodyne detection is performed on the readout pulse by mixing it with a local oscillator originated from the same microwave readout source. The mixed-down I and Q quadratures are finally sampled by a fast digitizer.

[2] We use IQ mixer, and send DC pulse on both quadrature in order to compensate defaults of mixers, and increase the ratio on/off.

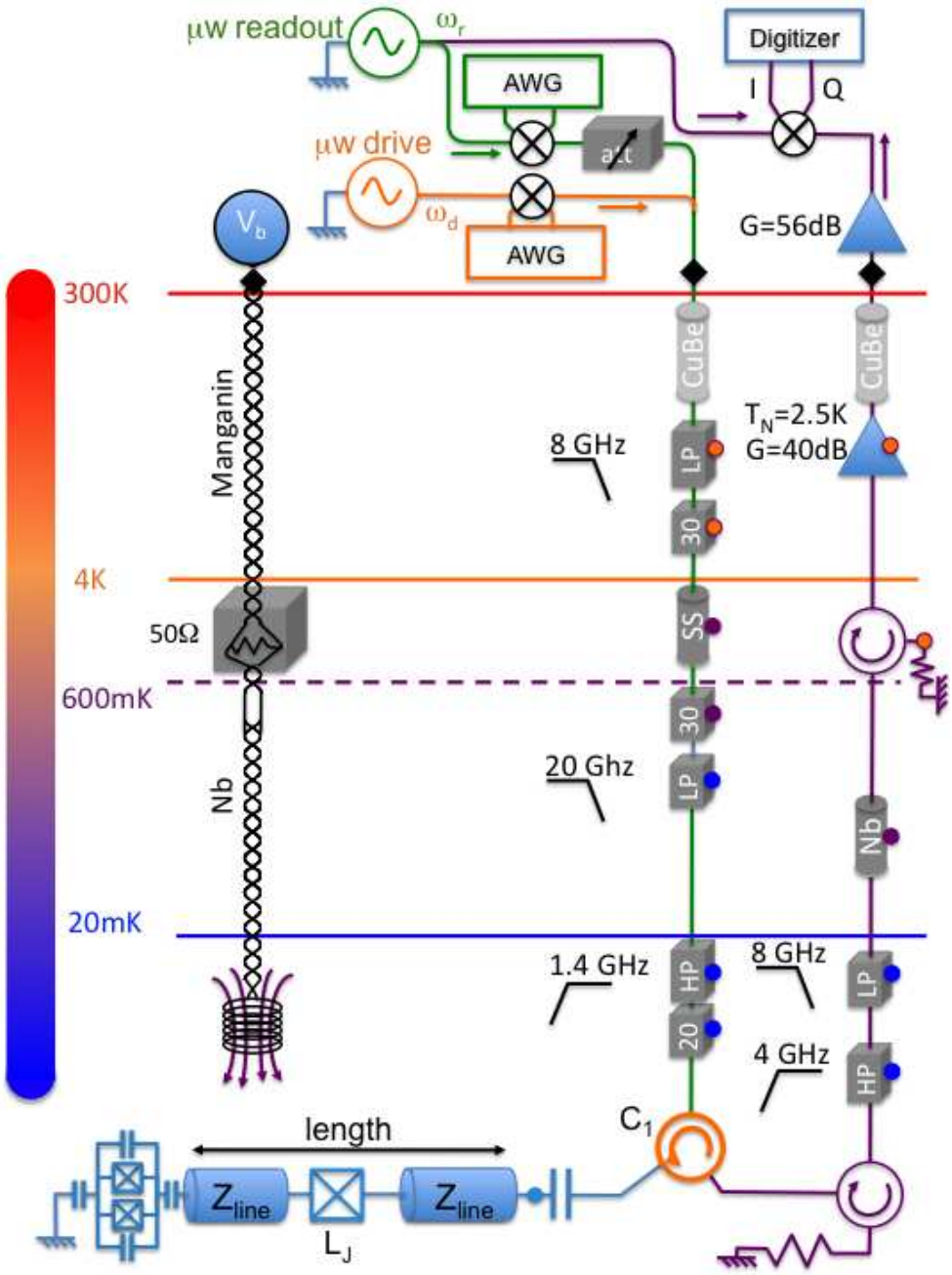

Fig. 4.10. Electrical wiring of the experiment. The flux applied through the transmon loop is changed using the coil (left). The drive and readout microwave pulses are generated by mixing continuous wave with DC pulses generated by Arbitrary Waveform Generator. They pass from room temperature to 20 mK through the input microwave line (green), which is attenuated and filtered. At 20 mK, they are sent towards the microwave resonator by a cryogenic circulator C1. The reflected signal is sent via C1 to the output line (purple), which includes a niobium microwave line, filters and isolators. At 4K the signal is amplified by a cryogenic amplifier with a noise temperature $T_N = 3K$. After being amplified at room temperature, the reflected signal is sent to a digitizer.

4.3 Experimental results

In this section are summarized preliminary results obtained on the first sample fabricated and tested.

4.3.1 Characterization of the sample

4.3.1.1 Characterization of the non-linear cavity

We first characterize the resonator by sending a continuous microwave signal of adjustable frequency and power, and measuring the phase of the reflected signal using a Vector Network Analyser. The results are shown in Fig. 4.11. At low signal powers, the phase of the reflected wave displays the characteristic behavior of a linear resonator, allowing us to fit the resonance frequency and quality factor (see Fig. 4.12): here, $\omega_{cav} = 2\pi \times 6.332$ GHz and $Q = 600$, close to the design values. At higher powers, the resonance curve shifts towards low frequency and sharpens, until for even larger powers the phase presents a discontinuity indicating the bifurcation phenomenon.

4.3.1.2 Characterization of the bifurcation phenomenon

The bifurcation phenomenon can be further characterized by applying a slow triangular ramp, and monitoring the reflected phase as a function of the triangle amplitude. Results are shown in Fig. 4.13. Figure 4.13a (top graph) shows the reflected phase when the triangle is rising ; figure 4.13b (middle graph) when the amplitude is decreased. The difference between the two graphs (fig. 4.13c, bottom graph), reveals the hysteresic nature of the bifurcation process. We compare these measurements to the theory of the CJBA given in Annex F, with all the parameters determined from the experiment. Indeed, we know $Q = 600$, $\omega_{cav} = 2\pi \times 6.332$ GHz (see previous paragraph). From additional measurements on identical resonators without a Josephson junction, we also know $\omega_{cav,b} = 2\pi \times 7.35$ GHz yielding $\omega_{cav}/\omega_{cav,b} = 0.86$. This allows us to compute the switching $B_{\uparrow}(\omega_{rf})$ and retrapping $B_{\downarrow}(\omega_{rf})$ curves. They are shown in Fig. 4.13 as red and blue solid lines. The agreement with the retrapping curve is excellent ; however there is a discrepancy for the switching curve which may be due to an experimental artifact in these preliminary data.

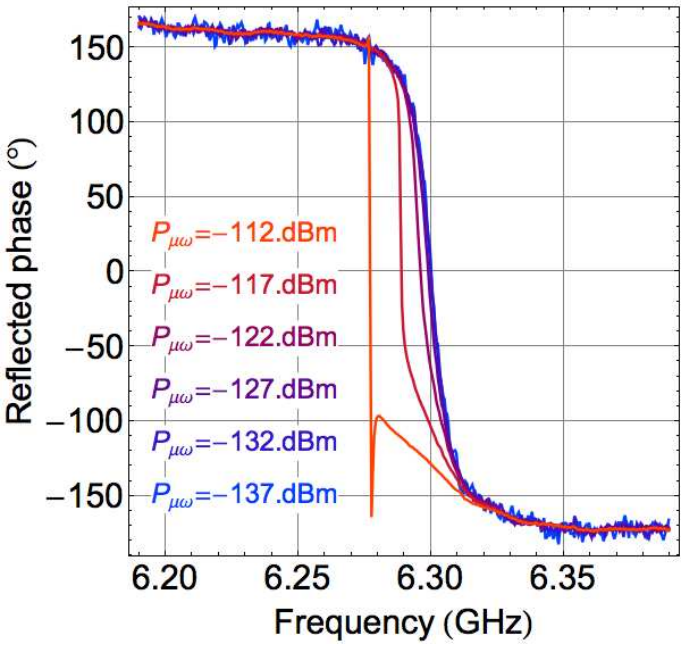

Fig. 4.11. Resonator measurements with a Vector Network Analyzer. Phase of the reflected signal as a function of the microwave frequency ω_{rf} for various input powers. At high power, the resonance curve shifts towards low frequency and sharpens, indicating the bifurcation phenomenon.

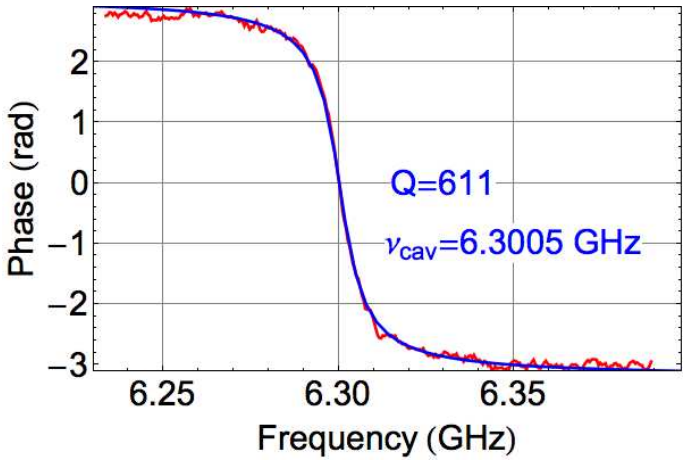

Fig. 4.12. Determination of the resonance frequency ν_{cav} and quality factor Q of the resonator. Note that the resonance frequency is changed by about 2.5 MHz compared to fig. 4.13 due to the change of the working point of the qubit. Here $\omega_{ge} << \omega_{cav}$.

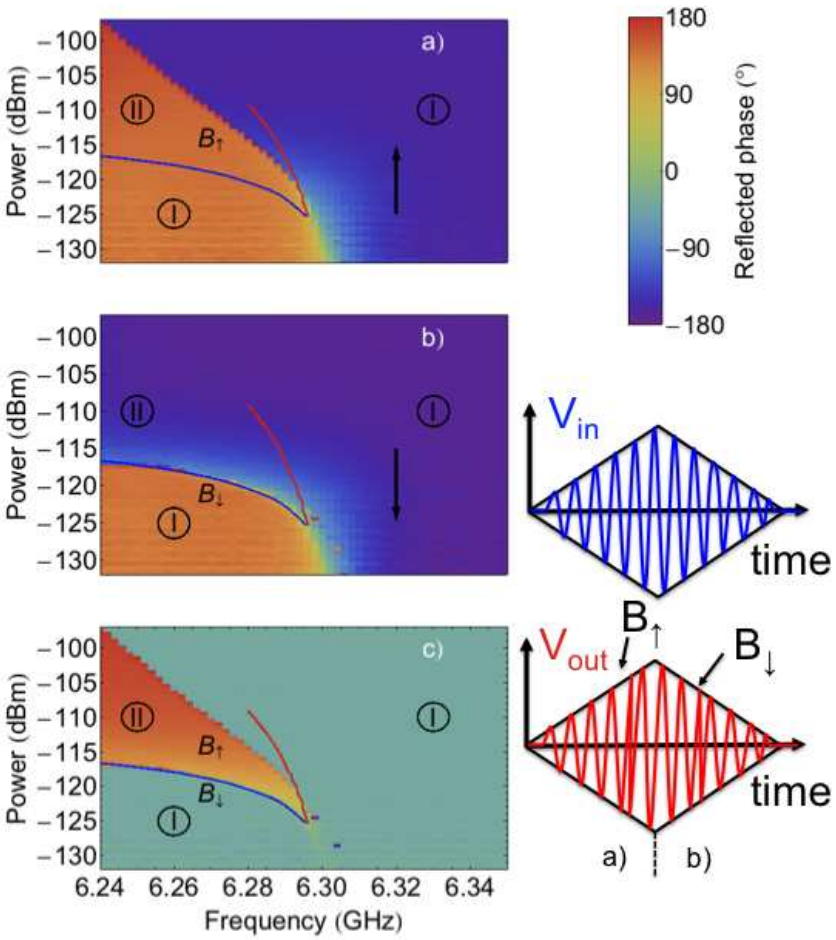

Fig. 4.13. Bifurcation and hysteresic behavior of a non-linear cavity. Phase of the reflected signal as a function of microwave power for various frequenceis, measured with a triangular envelope microwave pulse for (a) increasing microwave power (b) decreasing microwave power (retrapping). The switching (retrapping) is shown as a sharp transition between red and blue regions. The theoretical curves for switching $B_\uparrow(\omega_{rf})$ and retrapping $B_\downarrow(\omega_{rf})$ are shown as red and blue lines. In region (I), the system has only one metastable oscillating state. In region (II), two metastable dynamical states are possible and the system is hysteretic. (c) Difference between the two curves (a) and (b) displaying clearly the hysteretical region (II).

In order to measure the qubit state, we need much faster pulses than this triangular ramp. Pulse envelopes such as shown in Fig. 4.7, including a measurement pulse and a latching plateau, with a total duration of typically 600 ns, are used (see Fig. 4.14). The same microwave pulse is sent many times, and the quadratures of the reflected pulse are measured for each pulse. Typical time traces of one quadrature are shown in Fig. 4.14 for V_{rf} close to the bifurcation threshold. Two different families of traces are clearly observed, revealing the two metastable states of the oscillator. A histogram of the measured values of one quadrature is shown in Fig. 4.14. It is possible to define a threshold value V_{th} allowing to perfectly discriminate between the two dynamical states of the oscillator by comparing the measured quadrature value to V_{th} *in one single shot*. This allows us to measure the switching probability at a value V_{th} by counting the number of events during which the resonator switched. By varying V_{rf}, we obtain switching curves (s-curves) analogous to the ones obtained with DC switching. If we manage to have a good mapping of the qubit state on the resonator state, we should therefore obtain a high-fidelity single-shot qubit state readout.

Readout sensitivity

To characterize the readout sensitivity of our system, we should compare s-curves obtained at a given readout frequency ν_{rf} for two different cavity frequencies $\nu_{cav} - \chi$ and $\nu_{cav} + \chi$, since a change in the qubit state modifies the resonator frequency by 2χ. It is easier instead, and equivalent, to keep ν_{cav} fixed and measure s-curves for various readout frequencies ν_{rf}. Such a measurement is shown in Fig. 4.15 for various frequencies with a step of 5 MHz. At the temperatures at which we work ($T = 20$ mK), M. Dykman's theory [94] predicts that the width of the switching curves is due to quantum noise, and that it amounts to a thermal noise corresponding to half an energy quantum, i.e. $T_{eff} = \hbar\omega_{cav}/2k_B = 150$ mK. We performed some simulations to compute the s-curves at $T = 150$ mK, and obtained curves that are somewhat less steep than the ones measured in Fig. 4.15. More detailed and systematic measurements and analyses are needed to understand this discrepancy. Putting this problem aside, we note that given our experimental s-curves we should have an excellent single-shot qubit readout fidelity provided $2\chi \geq 5$ MHz.

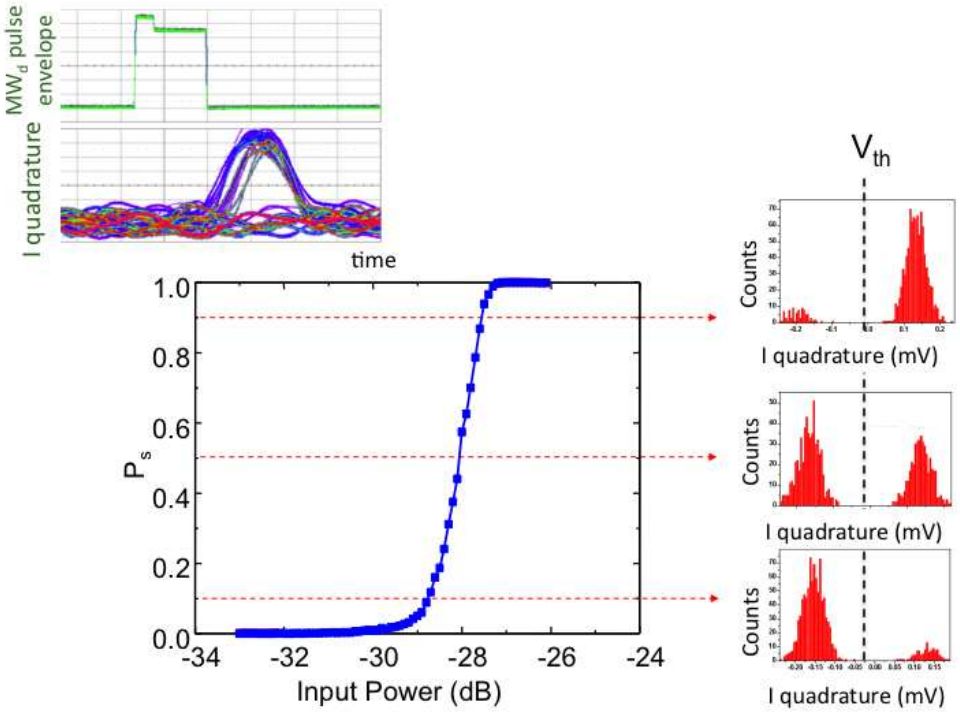

Fig. 4.14. Switching probabilities P_S as a function of the microwave signal power and distribution of the quadrature amplitude of the reflected signal for three different values of P_S 10%, 50%, and 90%. Top right : oscillograms of the microwave pulse envelope (green) and of on of the quadratures of the reflected signal.

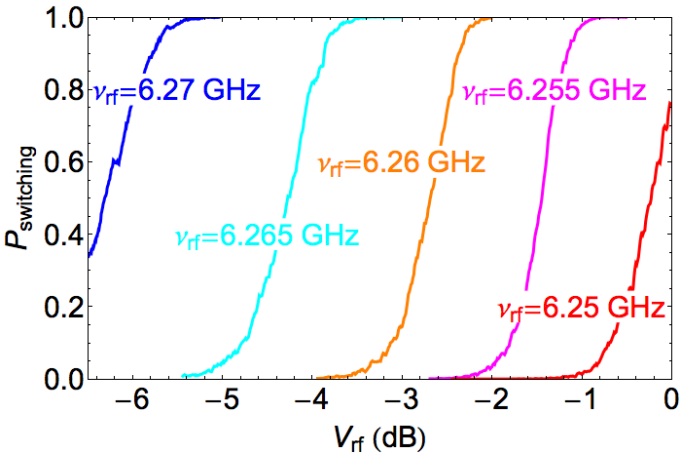

Fig. 4.15. Switching probabilities P_S as a function of the microwave signal power for different values of the microwave frequency ω_{rf}. The microwave pulse has a plateau duration of 150 ns, and a latching duration of 400 ns.

4.3.1.3 Characterization of the transmon

Spectroscopy

We first determine the split Cooper Pair box characteristics (E_J and E_C) by performing the spectroscopy of the qubit using the exact same technique as for the quantronium experiments. By convenience, we performed these experiments using the readout in the linear regime, without bifurcation (which is still possible at very low measurement powers). More precisely, a microwave pulse is applied with a frequency ω_d, and a duration of 2 to 5 μs. The readout microwave signal is then applied with an amplitude corresponding to one photon in the cavity, and the phase of the reflected signal is measured as a function of the flux Φ (proportional to the coil voltage) and ω_d. Experimental data are shown in Fig. 4.16As explained in previous sections, this phase changes when ω_d matches the qubit frequency ω_{eg}, and it is thus possible to measure the qubit frequency as a function of $\delta = \Phi/\varphi_0$.
To determine both energy E_J and E_C of the sCPB, one also needs to measure, for example at $\delta = 0$, the transition frequency ω_{ef}. In this purpose, a third microwave pulse at frequency ω_{aux} is inserted in the pulse sequence between the first pulse at frequency ω_{ge}, and the readout pulse. As for the first excited state $|e\rangle$, the phase of the reflected signal changes when ω_{aux} matches ω_{ef}. In the regime of large E_J/E_C ratio, the difference of frequency between the two transition is equal to $E_C/(4h)$. The measured values, $E_J = 0.698$K and $E_C = 0.05$K, demonstrate that the CPB is indeed in the large E_J/E_C regime. However, E_J was in this sample 20% lower than expected, causing the maximum qubit frequency ω_{ge} to stay always below the cavity resonance ω_{cav}. The smallest detuning is thus obtained when $\delta = 0$. It is equal to 700 MHz.

Coherence times

We have characterized the qubit coherence times by applying the same method than for quantronium experiments, and explained in Annex A.

The characterization was first performed at $\delta = 0$, where the qubit-cavity detuning is minimal, and thus the readout sensitivity is the largest. We first measured Rabi oscillations using the CJBA readout, as shown in Fig. 4.17. This allowed us to determine the pulse duration necessary to perform a π rotation of the qubit state.
Figure 4.17c shows a measurement of the relaxation time T_1. A π pulse is first applied in order to populate the qubit in state $|e\rangle$, then the readout pulse is applied after a delay time Δt. The switching probability decreases exponentially with a characteristic time T_1 following the relaxation of the quantum of energy. In this sample, we measure $T1 = 750$ns. This relaxation time is longer than the ones obtained in the Quantroswap experiment (see chapter 3), which confirms the interest of protecting a qubit by measuring it through a resonator that filters out the electromagnetic quantum noise at its resoannce frequency. Over three different samples, the relaxation time was found to be

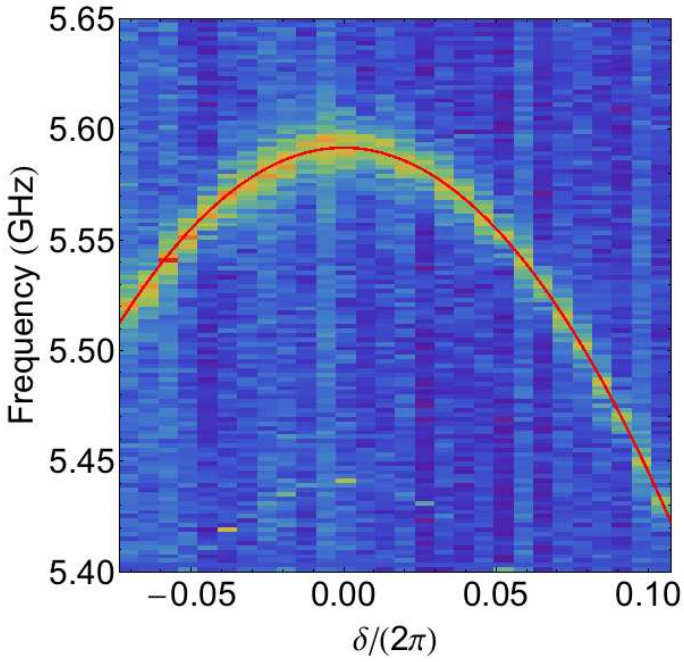

Fig. 4.16. Spectroscopy of the transition $|g\rangle - |e\rangle$. The spectroscopy of the transition $|e\rangle - |f\rangle$ gave a difference $\omega_{ge} - \omega_{ef} = 300$ MHz, yielding $E_C = 0.05$K. One can thus fit (red) the spectroscopy with $E_J = 0.698$K. The two photon transition $|g\rangle \rightarrow |f\rangle$ is visible in the bottom of the figure.

sensibly the same in similar biasing conditions. In addition, this relaxation time is actually close to the one obtained taking into account the relaxation through the resonator in the 50Ω line [47, 46].
We also measured the decoherence time T_2 (see Fig. 4.17d) with a Ramsey fringe experiment. The amplitude of the Ramsey oscillations decays exponentially with a characteristic time $T_2 = 1.44\mu$ s. This is much longer than the coherence times measured with the Quantronium design (see chapter 3), even at the doubly optimal point. In addition, since the measured $T2$ is extremely close to $2T1$, dephasing is completely limited by relaxation. The pure dephasing time is not even measurable, and is at least larger than 10μs. This clearly demonstrates that working in the $E_J >> E_C$ regime gives much better coherence times. Note also that only the magnetic flux needs to be tuned in this circuit, the dc gate voltage being not relevant for the qubit operation. This results in much simpler and robust operation than with previous Cooper pair box designs.

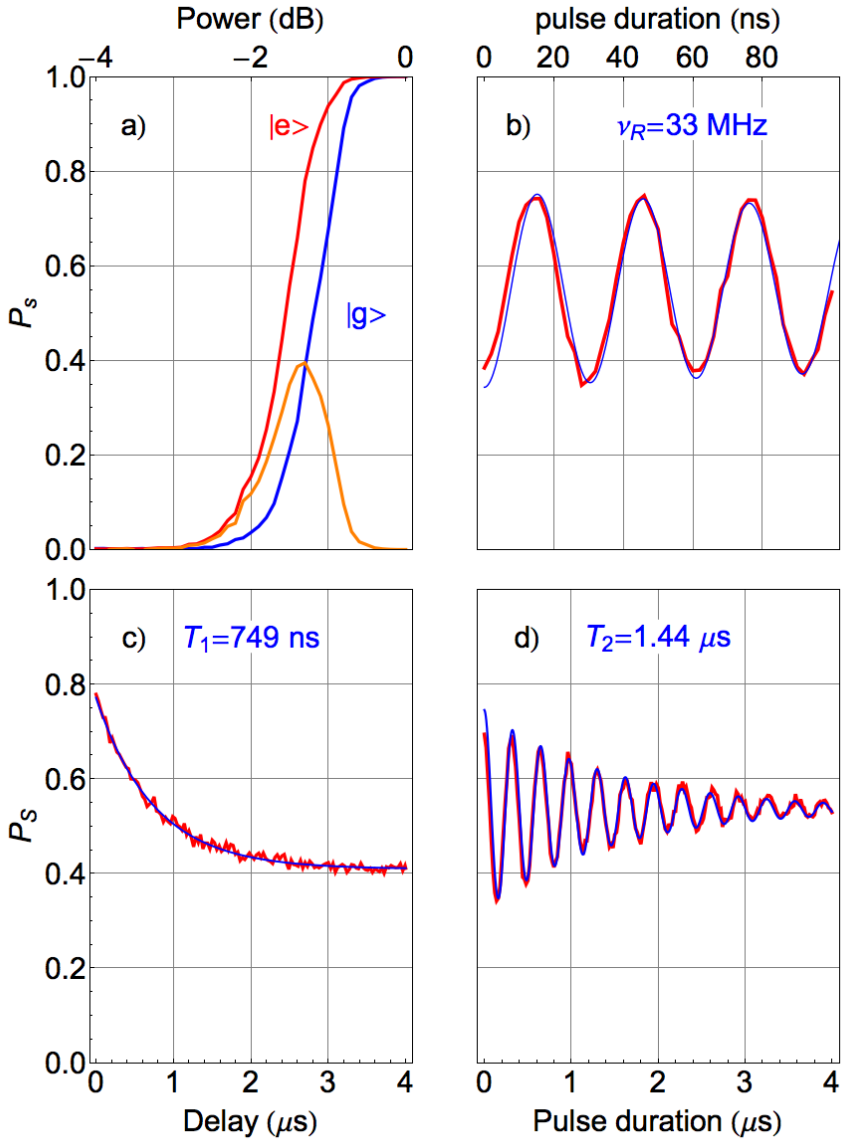

Fig. 4.17. Coherence times measurement at $\delta = 0$ when $\nu_{ge} = 5.553$ GHz. a) Switching probabilities P_S as a function of the readout plateau amplitude V_p for the two qubit states $|g\rangle$ and $|e\rangle$. b) Rabi oscillations with a frequency $\nu_R = 33$ MHz. The contrast (amplitude of oscillations) is about 40%. c) T1 measurement. Experimental curve (red) corresponds the exponential decay of the quantum of energy. The fit (blue curve) gives $T_1 = 749ns$. d) Ramsey fringes obtained with two $\pi/2$ pulses 8 MHz detuned from the qubit resonance and of duration 15 ns. The fit (blue line) gives $T_2 = 1.44$ μs, very close to $2T_1$.

4.3.2 Single-shot readout for a sCPB

We present in this section the characterization of the Cavity Josephson Bifurcation readout method of a transmon qubit.

4.3.2.1 Readout fidelity

In order to characterize the readout fidelity, we measured an s-curve without and with a π pulse. Results are shown in Fig. 4.17a, together with a curve showing the difference between the two curves. The maximum fidelity obtained is 40%. Additional measurements have shown that this fidelity did not seem to strongly depend on the value of ω_{rf} used for the readout. This can be qualitatively explained looking at 4.15. One observes that the s-curves measured with ω_{rf} being close to ω_{cav} are more separated, but also wider, than the s-curves measured further from ω_{cav}. In total, the readout sensitivity is roughly unchanged. Further theoretical and experimental studies are however needed to address this question more precisely. Note however that it is in principle better to work with ω_{rf} as close as possible to ω_{cav} because switching occurs at lower power, so that the dispersive approximation will have a greater validity making the readout potentially less destructive for the qubit state. The limited fidelity of 40% in that sample is simply due to the excessive qubit-cavity detuning, which yields $2\chi = 1.4$MHz, not enough to properly separate the switching curves when the qubit is in state $|g\rangle$ and $|e\rangle$. A later sample corrected this error, giving a much larger fidelity.

4.3.2.2 Is this readout method QND ?

Finally, we have also characterized eventual qubit relaxation and excitation during readout. For this purpose, we have applied two readout microwave pulses successively, and measured the switching probabilities and their correlations, similar to previous experiments [42, 97]. The plateau duration was set to 150 ns and the latching duration to 320 ns. The two pulses were separated by 150 ns so that the field inside the resonator has enough time to relax in-between. The measurements are shown in Fig. 4.18.
In Fig. 4.18a we show the switching probability measured with the second pulse in presence of a first measurement pulse (but irrespective of what the first pulse measured), in red, and the switching probability measured with one single readout pulse sent after the exact same delay as the other, in blue. The two curves are practically identical. This is a strong indication that the readout essentially does not affect at all the qubit state.

In order to obtain more quantitative results, we have measured the joint probabilities Pij where $i, j = 0, 1$ indicate the result of the first (i) and the second (j) result. The data are shown in Fig. 4.18b. To account for these data, we use a model similar to the one explained in [42] to determine the

measurement error rates and the non-destructive character of the readout. The principle is shown in Fig. 4.19 : the readout gives result 0 when the qubit is in $|g\rangle$ with an error rate α, and 1 when the qubit is in $|e\rangle$ with an error rate $1-\beta$; and the qubit stays in state g after a measurement with a rate $1-s$, and $1-r$ for e. Assuming that the Rabi oscillation is in fact perfectly accomplished (the qubit oscillates with 100% contrast between states $|g\rangle$ and $|e\rangle$), we can fit the data in Fig. 4.18b (dashed lines). We obtain $\alpha = 0.23 \pm 2$, $\beta = 0.72 \pm 2$, $r = 0.58 \pm 4$, $s = 0.05 \pm 4$. As already mentioned, the readout error rates are due to the insufficient separation between the s-curve obtained when the qubit is in $|g\rangle$ and the one obtained after a π pulse when the qubit is in $|e\rangle$ (see Fig. 4.17a). As for the non-destructive character, we have a relatively large rate r, but it is completely explained by the qubit relaxation time even in absence of the measurement pulse. The excitation rate s is negligible within the error bars. We therefore conclude that a readout pulse seems to have a negligible effect on the qubit state ; unfortunately, the duration of a measurement pulse is too long (of order $T1$) and the measurement error rate too large to obtain large correlations between the two measurement results as has been measured with flux-qubits [97].

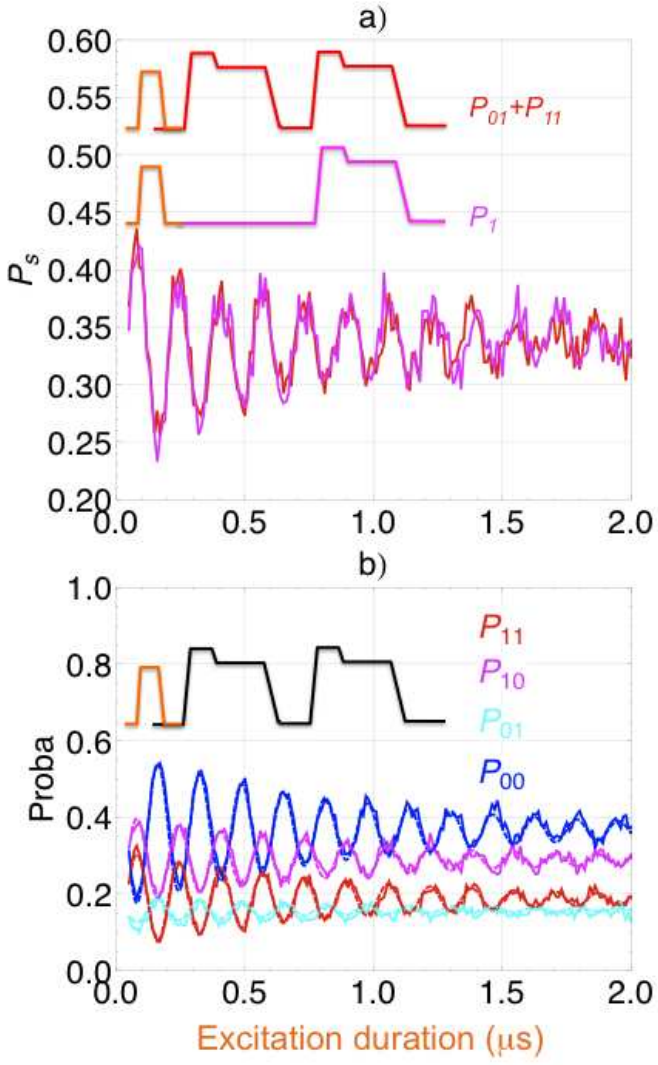

Fig. 4.18. Switching probabilities of two successive readout measured for $\nu_{rf} = 6.26$ GHz and $\nu_{ge} = 5.59$ GHz, and comparison with theory using parameters shown on Fig. 4.19. a) Comparison of the probabilities of switching of the second readout pulse with the probabilities of switching of the same readout pulse when first readout pulse is absent. In this case the change in amplitude of oscillations is only due to the relaxation decay. b) Probabilities P_{11} (red), P_{10} (magenta), P_{01} (cyan), and P_{00} (blue) of two successive readout pulse (0 and 1 code for non-switching and switching respectively). Dashed lines corresponds to fitted curves with model described in text.

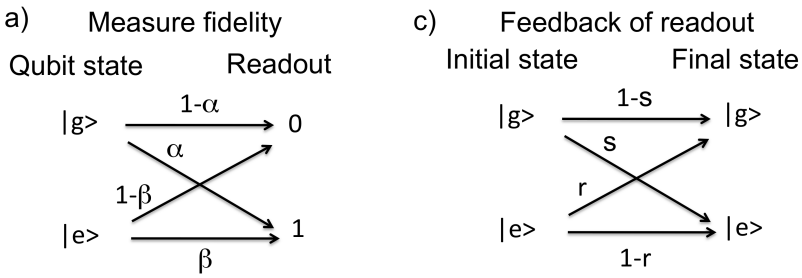

b)

α=0.23 β=0.72

|g>		|e>	
00	0.59	00	0.08
01	0.18	01	0.2
10	0.18	10	0.2
11	0.05	11	0.52

d)

r=0.58 s=0.05

	|g> (2π)		|e> (π)	
	Th	Exp	Th	Exp
00	0.57	0.54	0.16	0.21
01	0.20	0.18	0.12	0.11
10	0.17	0.2	0.41	0.37
11	0.06	0.07	0.31	0.31

Fig. 4.19. Schematic representations of the parameters characterizing the measurements errors. a) Schematic representation of the probabilities of non-switching (0) and switching (1) as a function of the state $|g\rangle$ and $|e\rangle$. From Fig. 4.18b (calculating the switching probability during the first readout), one determines that $\alpha = 0.77$ and $\beta = 0.28$ (contrast is equal to 49%). b) The corresponding probabilities of switching for the two qubit states. c) The measurement can also induce changes in the qubit state in addition to the projection of the qubit state into a pure state: excitation (s) or relaxation (r). The relaxation probabilities in absence of readout is fitted from Fig. 4.18c, and is equal to 0.58. d) The corresponding probabilities of switching for the two qubit states.

4.3.2.3 Conclusion

In this first sample, the readout fidelity was about 40%. This value was clearly limited by a too small value of χ, due to a too large qubit-resonator detuning, about 730 MHz at $\delta = 0$, larger than was actually designed.
Since this experiment we have fabricated a new sample, whose qubit frequency at $\delta = 0$ is higher than ω_{cav}, and thus enables to have a frequency detuning as small as desired. Preliminary results have shown that when the qubit is closer to the cavity the fidelity is increased (see Fig. 4.20) up to 90%, even slightly better than the highest single-shot fidelity reported so far [44]. However, bringing ω_{ge} to close to ω_{cav} also slightly increases the relaxation rate [47]. A further optimization of the sample parameters is thus still needed, in order to have a large readout fidelity together with long relaxation and coherence times at the same bias point. In conclusion, this readout scheme

associated to a sCPB with large E_J/E_C ratio embedded in a cavity seems to be very promising to create robust multi qubit circuit. We have demonstrated the first single-shot high-fidelity qubit state readout for a transmon. Further optimization of the sample parameters should lead to high-fidelity measurements of quantum correlations in multi-qubit experiments.

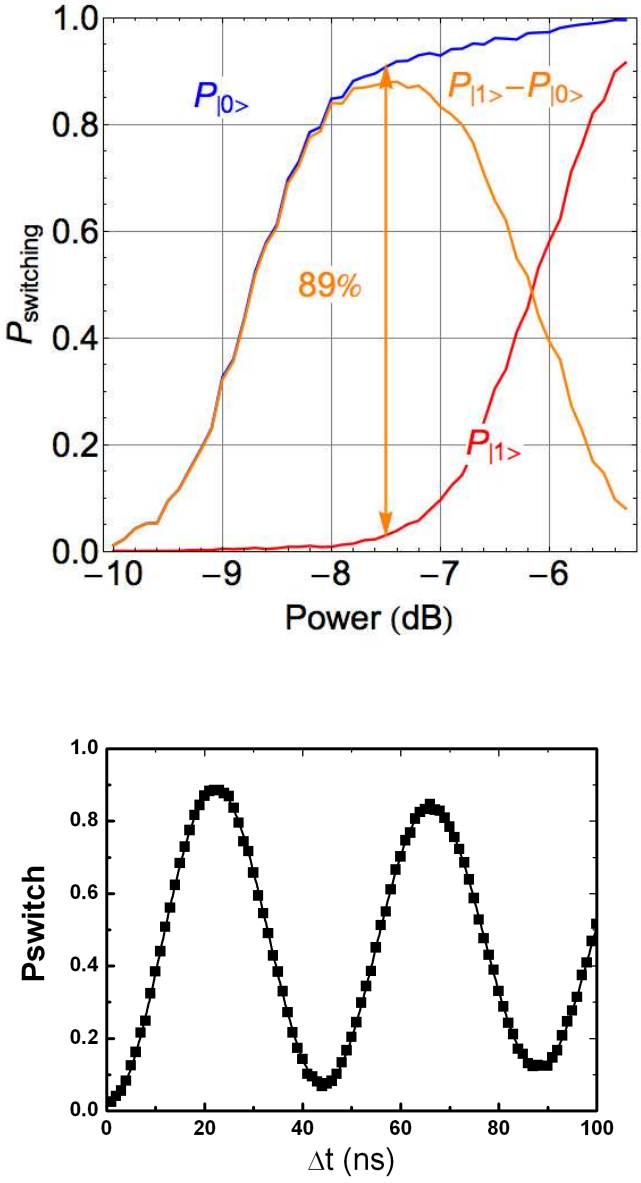

Fig. 4.20. Contrast and Rabi oscillations. Top) Switching probabilities qubit being in state $|0\rangle$ (blue) and $|1\rangle$ (red) and their difference (orange). Bottom) Corresponding Rabi oscillations.

Chapter 5

Current to frequency conversion in a Josephson circuit

Contents

We report in this chapter the results obtained with a quantronium device for converting a current i into a frequency $f = i/2e$. The experiment performed aims at demonstrating Bloch oscillations in a split Cooper Pair Box probed by microwave reflectometry. This work is related to the effort aiming at redefining electrical units a explained below.

5.1 Towards a new metrology of electrical units

The present status of the electrical units in the SI system, like the volt and the ampere, is presently profoundly unsatisfactory. Their definitions, which relate them to mechanical units, are the following:

- the ampere is the current passing through two parallel wires, distant by 1 m, that produces a force of 2.10^{-7} N per unit length.
- the volt is the electrical potential drop across a wire dissipating one watt when the current is 1 A.

One easily understands that these definitions cannot lead to accurate representations. Since January 1st 1990, the recommendation of the CIPM (Comité International des Poids et Mesures) is to redefine the volt by using the AC Josephson effect, which relates the AC voltage U across the junction to the frequency f of its Josephson oscillations through the relation $U = h/(2e)f = f/K_{J-90}$, with $K_{J-90} = 483597.9GHz/V$ [98]. A similar recommendation is to redefine the ampere by using the Quantum Hall Effect, which relates the current I through a Hall bar to the transverse Hall voltage V through the relation $V = h/e^2 I = R_{K-90}I$, with $R_{K-90} = 25812.807557\ \Omega$ the von Klitzing resistance [9].

5.1.1 The triangle of quantum metrology

According to the present knowledge of physics, the above physical constants R_{K-90} and K_{J-90} are related to fundamental constants h and e through the relations:

$$K_{J-90} = 2e/h, \qquad (5.1)$$
$$R_{J-90} = h/e^2$$

One notices the relation $1/(K_{J-90}R_{J-90}) = e/2$. The consistency of the two above relations could thus be checked by relating a current to a frequency through a third relation of the type $I = ef$. Establishing the consistency of the three relations, which form the triangle of quantum metrology shown in Fig. 5.1 would then provide a solid basis for changing the SI system, and basing the electrical units on physical phenomena involving fundamental physical constants. In a second step, one could relate the mass unit to the electrical units with the watt balance experiment [99] that equates a mechanical power mgv to an electrical power IV. The success of this experiment would then free the SI system from any artefact subject to unavoidable hopefully small drifts.

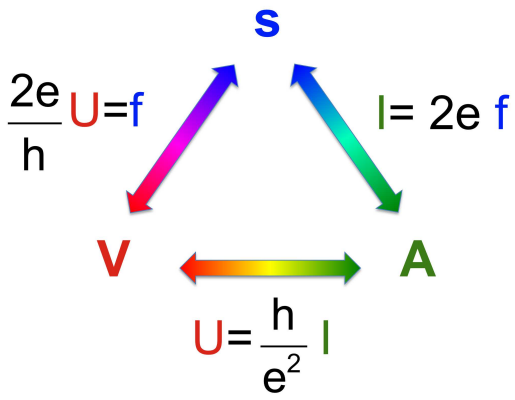

Fig. 5.1. Quantum metrological triangle relating the second s to the volt V through the AC Josephson effect (left branch, U is the voltage and f the frequency), the volt to the Ampere A through the quantum Hall effect (bottom branch, I is the current), and the Ampere to the second through an experiment to be defined.

5.1.2 $I = 2ef$

5.1.2.1 Experimental requirements for closing the triangle of quantum metrology

Closing the triangle of quantum metrology is demanding because the operation of a Quantum Hall Device requires a rather large current in the μA range when the searched accuracy is in the 10^{-8} range. With the help of a superconducting transformer with a topologically defined transformation ratio [100], it is possible to bring this current range down to the sub nA range, which is still a large current compared to what can current produced by electron pump, which are in the tens of pA. We briefly review here existing devices for relating a current to a frequency.

5.1.2.2 Single electron pumps

The most advanced device is presently the single electron pump first operated in the Quantronics group [101]. In this Coulomb blockade device, a single electron charge is transferred during each operation cycle by forcing its passage across a series of tunnel junctions by applying suitable gate voltages to the islands between the junctions. Single electron pumps have already been used for the metrology of the electrical charge [102, 103, 104], and present day single electron pumps can deliver currents up to a few tens of pA with metrological accuracy (10^{-8}), which is still too small for closing the triangle of quantum metrology.

5.1.2.3 A new hybrid turnstile

Different types of pumps now exist, but the only device able to reach the needed current range is the hybrid SNS device recently developed in the group of J. Pekola [105]. This device is a turnstile [106], which makes use of the gap energy to stabilize a charge configuration. This device has the potential to deliver 0.1 nA, and is simple to parallelize (its accuracy is currently analyzed and in rapid progress).

5.2 Current to frequency conversion from Bloch oscillations in a Josephson device

A rather different approach had been proposed earlier to relate a current to a frequency: the Bloch oscillations of a current biased Josephson junction [107, 20]. Indeed, Likharev and Zorin have predicted that the voltage across a Josephson junction, which is perfectly current-biased by a current I oscillates periodically at a frequency $f_B = I/(2e)$. A simple way to understand

this phenomenon is to consider the mechanical analogue of the current biased junction: the phase difference φ across the junction is equivalent to the position of a particle moving in the Josephson potential $-E_J \cos\varphi$, the voltage across the junction to the particle velocity, and the bias current I to a constant applied force. The dynamics of the particle is well-explained within the framework of the Bloch energy bands $\epsilon_i(q)$ formed by the eigenstates of the particle, with q its quasimomentum having the dimension of an electric charge. The particle velocity oscillates at the Bloch frequency f_B due to the reflection of the Bloch waves at the edge of the Brillouin zone.
Provided a perfect current bias can be applied to a junction, a direct observation of the voltage oscillations should be possible. It was also suggested to detect these Bloch oscillations by inducing quantized current plateaus in presence of an applied microwave frequency. These current plateaus would be the dual of the voltage Shapiro steps of the AC Josephson effect.

5.2.1 First observation of Bloch oscillations in a current-biased Josephson junction

The indirect observation of Bloch oscillation in a Josephson junction was first reported in [108, 109]. This experiment consisted in measuring the $I(V)$ characteristic of a small Josephson junction embedded in a resistive environment made of thin Chromium resistors, and subject to microwave irradiation. An effect of the microwaves on the $I(V)$ characteristic was convincingly observed at currents close to that predicted by theory, but the expected current plateaus were not observed. The authors found that current-biasing was not perfect enough in this experiment for obtaining narrow Bloch lines at a given current. The estimated frequency width for the Bloch oscillations produced is about 1 GHz [109], which is too large for locking Bloch oscillations in the explored frequency range 3-10 GHz. The experiment clearly demonstrated that current-biasing a Josephson junction is extremely difficult, and furthermore prone to effects difficult to control, such as electron heating.

5.2.2 A new experiment for demonstrating Bloch oscillations

In order to circumvent the difficulty to current-bias a Josephson junction, one can use a Cooper pair box (CPB) circuit in which the junction is charge-biased by applying a voltage to a small gate capacitance. Increasing linearly the gate voltage mimics a perfect current bias, and produces oscillations of the box island potential, i.e. Bloch-like oscillations of the voltage across the box junction. We now show that embedding this CPB in a quantronium like sample leads to an easy detection of these Bloch oscillations.

5.2.2.1 The split Cooper Pair Box as a 2D lattice for observing Bloch-like oscillations

More precisely, the proposed experiment consists in using a split Cooper Pair Box (sCPB) in a quantronium geometry for detecting the Bloch oscillations by microwave reflectometry. The Hamiltonian of the sCPB is

$$\widehat{H} = E_C(\widehat{N} - N_g)^2 - E_J\left[\cos\left(\frac{\delta}{2}\right)\cos\widehat{\theta} + d\sin\left(\frac{\delta}{2}\right)\sin\left(\widehat{\theta}\right)\right], \qquad (5.2)$$

with N_g the reduced gate charge, δ the phase across the two small junctions of the box, and $\widehat{N}$ and $\widehat{\theta}$ the two conjugated observables forming the degree of freedom of the Cooper pair box. This Hamiltonian is 1-periodic in N_g, and 2π-periodic in δ. Thus, if N_g is varied in time at a constant rate $\dot{N}_g = I/(2e)$, a constant displacement current I flows through the gate capacitance C_g, and if the sCPB stays in its ground state, the system is forced to evolve at a constant speed along the periodic ground state energy band (see Fig. 5.2).As explained above, the sCPB undergoes periodic oscillations of its island voltage. Correlatively, all the physical quantities such as the island charge $< N >$, the persistent current, or all the derivatives of the Hamiltonian with respect to the control parameters N_g and δ vary periodically at the Bloch frequency $\nu_B = I/(2e)$. We use one of these derivatives, the inverse inductance $L^{-1}(N_g, \delta) = \varphi_0^{-2}\partial^2 E/\partial\delta^2$ (see Fig. 5.2) to detect Bloch oscillations.

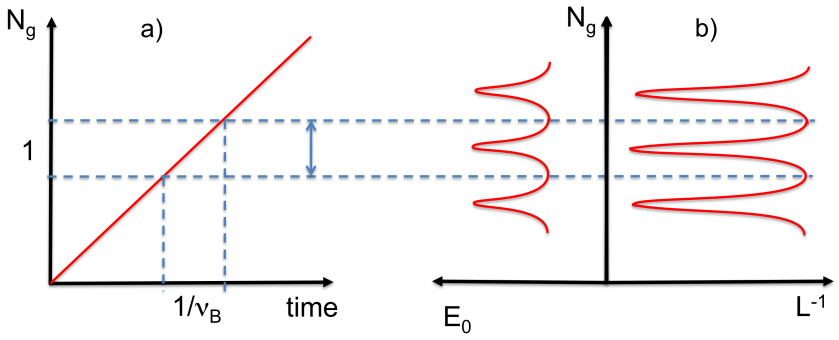

Fig. 5.2. Principle of the current to frequency conversion with a Cooper pair box. a) Linear evolution of $N_g(t)$. b) Ground state energy band (left) and its second derivative L^{-1} with respect to δ (right) as a function of N_g.

5.2.2.2 The Blochonium oscillator

As explained in section 1.1.4, different techniques have been developed for the purpose of qubit readout, and in particular microwave methods. For the

detection of Bloch oscillations, we exploit the periodic modulation of the resonance frequency of a quantronium-like sample with the gate charge N_g, which we call Blochonium in this context. More precisely, we apply a microwave CW signal to a quantronium and monitor the spectrum of the reflected signal.
As explained in section 1.2, the whole quantronium circuit forms a resonator with resonance frequency

$$\nu_p = \frac{1}{2\pi}\sqrt{\frac{1}{C_r}\left(\frac{1}{L(N_g,\delta)} + \frac{1}{L_J(\gamma)}\right)}, \tag{5.3}$$

where $\gamma = \delta - \Phi/\varphi_0$ is the phase across the "readout" junction, Φ is the flux in the quantronium loop, and C_r is the total capacitance in parallel with the readout Josephson of inductance $L_J(\gamma)$. The iso-inverse inductance curves $L^{-1}(N_g,\delta)$ are shown in Fig. 5.3. These curves show the periodicity in N_g and δ. They also show that the maximum modulation in N_g, is obtained for $\delta = \pi$, which makes this point optimal for probing the variations of the resonator frequency ν_p.

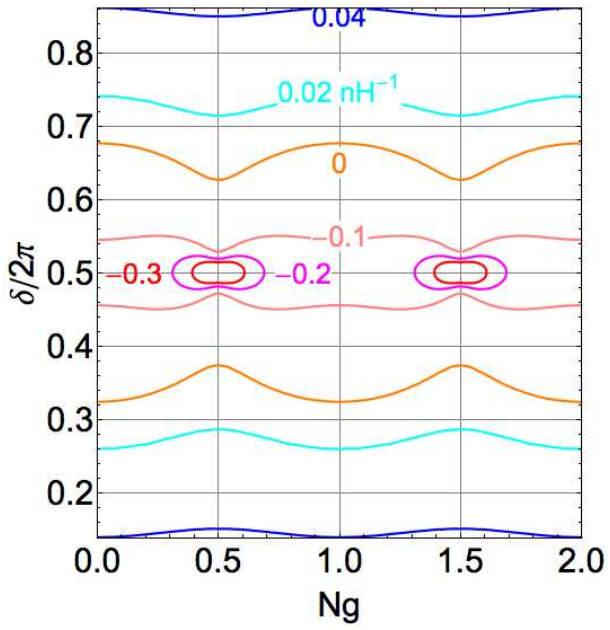

Fig. 5.3. Iso-inverse inductance of the split CPB as a function of its working point (N_g,δ) for $E_J = 2k_BK$, $E_C = 1k_BK$ and $d = 0.05$. This inductance is 1-periodic in N_g, and its maximal modulation in N_g occurs at $\delta = \pi$.

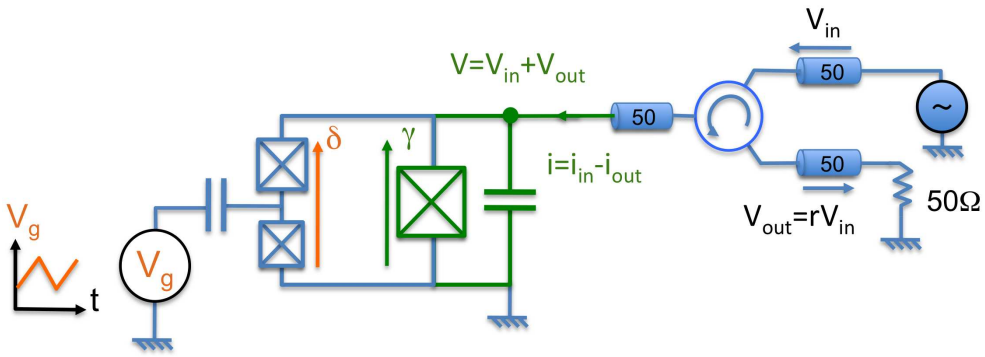

Fig. 5.4. Electrical scheme of the Blochonium circuit. A 50 Ω source applies an incoming wave of amplitude $V_{\rm in}$ to a quantronium-like sample. This wave is reflected on the Blochonium oscillator and propagates through a circulator to a 50 Ω amplifier (50 Ω resistor on the figure).

5.2.2.3 Dynamics of the driven Blochonium oscillator

Here we focus only on the dynamics of the Blochonium oscillator submitted to a continuous incoming microwave signal of amplitude $V_{\rm in}$ and frequency ν_{rf} (see Fig. 5.4). Using the constitutive relations of the Josephson junction, the dynamics of γ is :

$$\frac{\partial^2\gamma}{\partial(\omega_p t)^2}+\frac{1}{Q}\frac{\partial\gamma}{\partial(\omega_p t)}+\sin(\gamma)=\eta\cos(2\pi\nu_{rf}t)\,, \tag{5.4}$$

where $\eta=2V_{in}/(RI_0)$, $Q=RC_r\omega_p$ is the quality factor of the resonator, and $R=50\ \Omega$ is the load impedance of the 50 Ω matched microwave lines (see Fig. 5.4). This equation describes the dynamics of a fictitious unit mass particle with position γ in a cosine potential, subject to friction, and harmonically driven.
Two regimes can be distinguished: a linear regime, where the restoring force $-\sin(\gamma)\simeq-\gamma$, and a non-linear regime, where the third-order term $-\gamma^3/6$ in the expansion of $\sin(\gamma)$ has to be taken into account. Both regimes are described in [110].

In our experiment, we do not monitor directly the oscillations of γ, but the microwave signal which is reflected by the Josephson oscillator. In an adiabatic ($\nu_g << \nu_p/Q$) and linear approach, assuming the oscillations γ are

small, we define the coefficient of reflection $r = V_{\rm out}/V_{\rm in}$ (the outgoing and incoming signal), and the admittance of the Blochonium oscillator

$$Y(\omega, \gamma, N_g(t), \delta) = iC_r\omega + \frac{R}{iL_J(\gamma)\omega}\left[1 + \frac{L_J(\gamma)}{L(N_g(t), \delta)}\right]. \tag{5.5}$$

One has

$$V_{\rm in} = 50 i_{\rm in}\ ,\ V_{\rm out} = 50 i_{\rm out},$$

$$(i_{\rm in} - i_{\rm out}) = \frac{1}{50}(V_{\rm in} - V_{\rm out}) = Y(\omega, \gamma, N_g, \delta)(V_{\rm in} + V_{\rm out}),$$

leading to

$$r(t) = \frac{2}{1 + RY(\omega, \gamma, N_g(t), \delta)} - 1. \tag{5.6}$$

Since the Blochonium oscillator is dissipation-less $|r| = 1$and the information on $N_g(t)$ is carried by the phase $\varphi(N_g) = Arg(r(N_g))$. Figure 5.8 shows an example of resonance curves $\varphi(N_g = 0)$ and $\varphi(N_g = 1/2)$ for this linear regime and parameters determined in the next sections. Nevertheless, we will see that the maximization of the signal requires using large drive amplitude $V_{\rm in}$ for which the linear approximation is no longer valid. More general calculations of the reflected signal will be presented later.

5.2.2.4 An experimental trick for performing an impossible experiment

In a real experiment, it is impossible to increase linearly and indefinitely N_g, which would lead at some point to a break-down of the capacitor C_g. Instead, one can apply a triangular gate voltage with frequency ν_g, amplitude ΔN_g, and offset N_{g_0} (see Fig. 5.5) covering the range $[N_{g_0} - \frac{\Delta N_g}{2}, N_{g_0} + \frac{\Delta N_g}{2}]$. If the extremal values of this range coincide with symmetry points of the Blochonium inductance modulation pattern, i.e. ΔN_g and N_{g_0} are half-integers, this inductance is the same as for an infinite linear increase of N_g (see Fig. 5.5). This trick thus allows to perform the proposed experiment, although it can not demonstrate Bloch oscillations with a true DC current.

5.2.2.5 Calculation of the reflected signal for triangular gate voltage

We now calculate the reflected signal for a triangular gate voltage with arbitrary N_{g_0} and ΔN_g by looking for steady state solutions for $\gamma(t)$ involving only the frequency ν_{rf}, and ν_g and its harmonics:

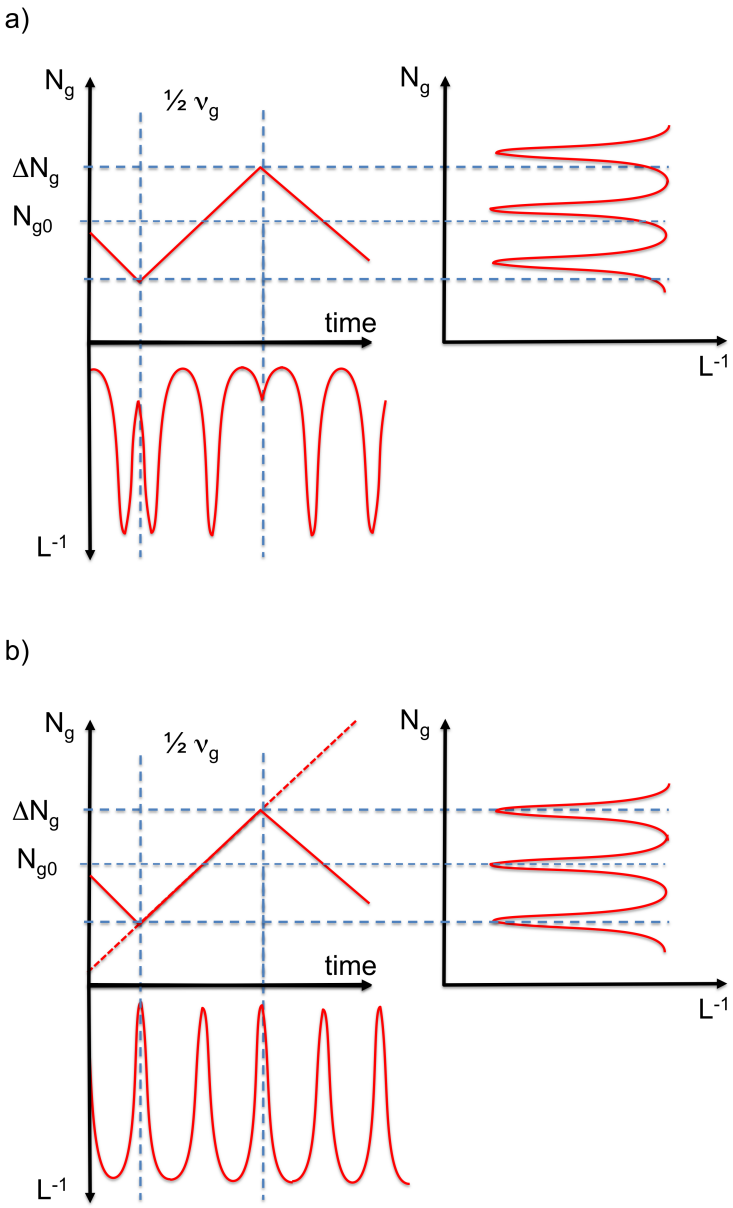

Fig. 5.5. Mimicking a linear N_g ramp with a triangular $N_g(t)$. Both panels show a triangular time evolution of N_g with amplitude ΔN_g and offset N_{g_0} (top left), the corresponding $L(N_g)^{-1}$ dependance (top right), and the corresponding $L(t)^{-1}$ (bottom left). a) When N_{g_0} or ΔN_g is not half-integer, $L(t)^{-1}$ is different from what it would be with a linear ramp. b) When N_{g_0} and ΔN_g are half-integers, $L(t)^{-1}$ mimics what it would be with a linear ramp.

$$\begin{aligned} V_{\text{in}}(t) &= v_{\text{in}} e^{i2\pi\nu_{rf}t} \\ V_{\text{out}}(t) &= \sum_{n\in\mathbb{Z}} \alpha_n v_{\text{in}} e^{i2\pi(\nu_{rf}+n\nu_g)t}, \end{aligned} \tag{5.7}$$

with α_n are complex number. This form assume implicitly that the dynamics is not chaotic and monochromatic in the sense that it does not involve oscillating terms at frequencies multiple of ν_{rf}. But it does not assume an adiabatic behavior of the reflection coefficient as in section 5.2.2.3. In this formalism, Eq. (5.6) takes the form

$$\begin{aligned} v_{\text{in}} e^{i2\pi\nu_{rf}t} + \textstyle\sum_{n\in\mathbb{Z}} \alpha_n v_{\text{in}} e^{i2\pi(\nu_{rf}+n\nu_g)t} = \\ RY(2\pi\nu_{rf},\gamma,N_g,\delta) v_{\text{in}} e^{i2\pi\nu_{rf}t} - \textstyle\sum_{n\in\mathbb{Z}} RY[2\pi(\nu_{rf}+n\nu_g),\gamma,N_g,\delta]\alpha_n v_{\text{in}} e^{i2\pi(\nu_{rf}+n\nu_g)t}. \end{aligned} \tag{5.8}$$

By multiplying this expression by $e^{-i2\pi\nu_{rf}t}$, one simplifies it in

$$\begin{aligned} 1 + \textstyle\sum_{n\in\mathbb{Z}} \alpha_n e^{i2\pi n\nu_g t} = \\ RY(2\pi\nu_{rf},\gamma,N_g,\delta) - \textstyle\sum_{n\in\mathbb{Z}} RY[2\pi(\nu_{rf}+n\nu_g),\gamma,N_g,\delta]\alpha_n e^{i2\pi n\nu_g t}. \end{aligned} \tag{5.9}$$

It is then convenient to rewrite Y as a series of $e^{ik\nu_g t}$ (with $k \in \mathbb{Z}$). For this purpose, Y is first rewritten as the Fourier series in N_g

$$RY(\omega,\gamma,N_g,\delta) = \sum_{k\in\mathbb{Z}} \beta_k(\omega) e^{i2\pi k N_g}, \tag{5.10}$$

where

$$\begin{aligned} \beta_k(\omega) = \beta_{-k}(\omega) = \delta_{k0}\left[iRC_r\omega + \frac{R}{iL_J(\gamma)\omega} - \frac{R}{i\omega}\int_{N_g=-0.5}^{0.5} \frac{1}{L(Ng,\delta)} dNg \right] \\ + \frac{2R}{i\omega}\int_{N_g=-0.5}^{0.5} \frac{1}{L(N_g,\delta)} \cos(2\pi k N_g)\, dN_g. \end{aligned}$$

Note that we limit the expansion of Y to cosine functions due to the parity of $L(N_g)$. A small number of harmonics $k \in [-10, 10]$ is sufficient to provide an accurate description of the gate modulation of the inductance.
In a second time, each cosine functions of $N_g(t)$ is also expanded as the Fourier series

$$\cos[2\pi k N_g(t)] = \sum_{p\in\mathbb{Z}} s_p^k \cos(2\pi p\nu_g t), \tag{5.11}$$

where the Fourier coefficients are

$$s_p^k = s_{-p}^k = 2(2-\delta_{k0})\nu_g \int_{t=0}^{1/2\nu_g} \cos[2\pi k N_g(t)] \cos(2\pi p\nu_g t)\, dt.$$

Note that for a proper tuning of ΔN_g N_{g_0} simulating an infinite N_g ramp, $s_p^k = \delta_{p\ 2k}$. One reduces Eq. 5.9 to

$$2 + \sum_{n\in\mathbb{Z}} \alpha'_n e^{i2\pi n\nu_g t} = -\sum_{n\in\mathbb{Z}}\sum_{k\in\mathbb{Z}} \beta_k^n \alpha'_n e^{i2\pi kN_g} e^{i2\pi n\nu_g t} \tag{5.12}$$

with $\alpha'_n = \alpha_n - \delta_{n0}$ and $\beta_k^n = \beta_k 2\pi(\nu_{rf} + n\nu_g)$. Using Eq. 5.11, one finally obtains

$$2 + \sum_{n\in\mathbb{Z}} \alpha'_n e^{i2\pi n\nu_b t} = -\sum_{n\in\mathbb{Z}}\sum_{k\in\mathbb{Z}} \beta_k^n \alpha'_n \sum_{k\in\mathbb{Z}} s_p^k e^{i2\pi k\nu_g t} e^{i2\pi n\nu_g t}. \tag{5.13}$$

By identifying the terms oscillating at the same frequency, one obtains a linear system of equations in α_n:

$$\sum_{l\in\mathbb{Z}} (\sum_{k\in\mathbb{Z}} \beta_k^l s_{n-l}^k + \delta_{nl})\alpha'_l = -2\delta_{n0}, n \in \mathbb{Z}. \tag{5.14}$$

Solving this system gives the amplitude $\{\alpha_n\}_{n\in\mathbb{Z}}$ of all the sidebands present in the reflected signal.

5.2.3 Circuit design

This section explains how we have designed the Blochonium circuit in order to observe Bloch oscillations.
We have first maximized the signal by increasing the amplitude of modulation of $1/L$ with N_g. Then, in order to avoid excitation of the CPB in its upper energy bands, we have chosen its parameters in order to have a sufficiently large energy gap between the ground state and the first excited state. Finally, we have determined the parameters of the Josephson oscillator and of the microwave probe signal in order to maximize the modulation of the reflected signal with a drive frequency ν_{rf} falling in the [1.1 GHz, 1.7 GHz] bandwidth of our cryogenic low-noise amplifier.

5.2.3.1 Avoiding quasiparticle poisoning of the Blochonium island

As explained in the previous section, the Bloch oscillations and their frequency are determined by the time-variation of N_g. This implies to reduce any fluctuations of N_g due to electronic noise or to quasiparticles entering the island and shifting suddenly N_g by 1/2. To make this quasiparticle poisoning energetically unfavorable even when out-of-equilibrium quasiparticles are already present in the leads, the superconducting gap of the island was made larger than that of the leads. To estimate the poisoning rate in our experiment, we use the model proposed by J. Aumentado et *al.* [111] for single Cooper pair transistors. Given a rate $\gamma_{0,l}$ (resp. $\gamma_{l,0}$) for the creation (resp. annihilation) of a quasiparticle in the leads, the ratio α between the probabilities of having one quasiparticles in the lead or in the island is given by

$$\alpha = \alpha_{0,l} e^{-\frac{E_0(Ng+0.5)-E_0(Ng)+\Delta_v}{k_B T}} \tag{5.15}$$

with $\alpha_{0,l} = (1 + \gamma_{l,0}/\gamma_{0,l})$ and Δ_v the difference of superconducting gap between leads and island. α is maximum at $N_g = 1/2$ and depends essentially on the ratio $(E_C)/(4\Delta_v)$. In practice, the variation of the gap is obtained by varying the thickness of the aluminum. Indeed, the typical superconducting gap of bulk Al is about 180 eV; when reducing the thickness down to 12 nm, the gap increases up to 220 eV. Thinner layers would have a larger superconducting gap, but their fabrication requires depositing aluminum at low temperature in order to obtain a "continuous" film rather than isolated grains. We thus chose this 12 nm thickness of the island, which leads to E_C smaller than 2 K to get $\alpha/\alpha_{0,l} < 0.04$ at 50mK.

5.2.3.2 Maximizing the modulation of $1/L(N_g)$ over N_g

As explained in the previous section, the goal of the experiment is to impose a linear variation of N_g and to measure the change in the sCPB inductance by reflectometry on the Josephson oscillator. As already shown in Fig. 5.3, the maximum amplitude of variation, which is actually the difference of $1/L$ between $N_g = 0$ and $1/2$, is obtained at $\delta = \pi$. Figure 5.6 shows that this maximum difference increases with both E_J and E_C. At the maximum allowed E_C (2 K), this increase is almost linear in the [1 K, 4 K] E_J range, and saturates above 5 K. We can not choose a too high E_J value that would lead to very transparent junctions, which are unstable and fragile; this is why we choose $E_J \simeq 4$ K.
This yields a size for the two junctions of about $(150\ \text{nm})^2$ assuming a specific capacitance $C_{Ju} \simeq 100\ \text{fF}/\mu\text{m}^2$, and a critical current density of about 6 $\mu\text{A}/\mu\text{m}^2$.

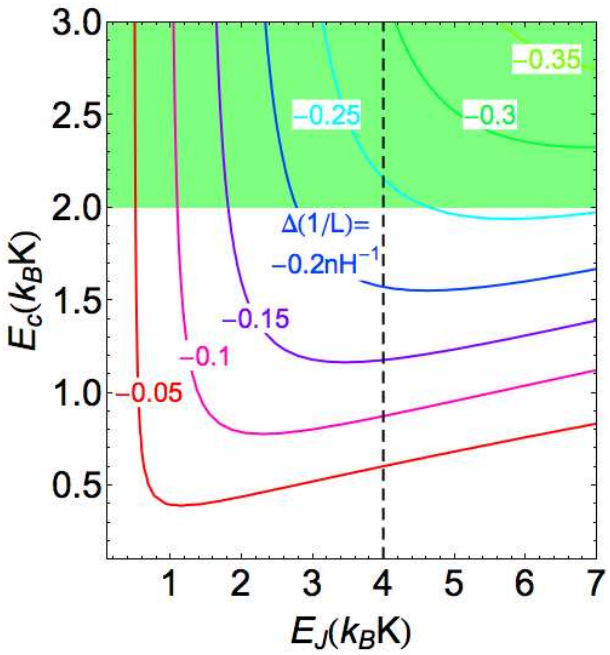

Fig. 5.6. Iso-amplitude of variation of $1/L(N_g, \delta = \pi)$ as a function of E_J and E_C for $d = 0.15$. The green region indicates forbidden values of E_J and E_C in order to avoid poisoning. Our target design values are at the intersection of the dashed line and of the green border.

5.2.3.3 Adiabaticity of the evolution

Whatever the choice of the sCPB parameters, this experiment requires first that the sCPB stays in its ground state. One has thus to avoid a Landau-Zener transition to the first excited state, while ramping N_g. The probability of such a transition is

$$P_{LZ} = e^{-\frac{[h\nu_{01}(N_g=0.5,\delta=\pi)]^2}{\hbar E_C f_B}}, \tag{5.16}$$

where $h\nu_{01}(N_g = 0.5, \delta = \pi) \simeq dE_J$ for $E_J/E_C \lesssim 5$ and $d \lesssim 0.2$. As already explained in section 2.1.3 for the Quantroswap experiments, lowering this probability requires either to evolve at low enough speed or to increase the energy difference $h\nu_{01}$ between the two levels. In the case $f_B = 1$ GHz for the already given value of E_J and E_C, P_{LZ} is equal to 1%4 for $d = 0.065$.

Besides, one has also to avoid the multi-photon excitation of the sCPB due to δ oscillations at the plasma frequency ν_p, when $\nu_{01} = k\nu_p$, $k \in \mathbb{N}$. It requires $k > 8$ at $\delta = \pi$ and $N_g = 1/2$, which yields an asymmetry $d \geq 15\%$ for the value of E_J and E_C already given.

5.2.3.4 Design of the Blochonium oscillator

Finally one has to determine the parameters of the readout oscillator. Ideally, its resonance frequency ν_p should be in the middle of our cryogenic amplifier bandwidth [1.1 GHz, 1.8 GHz], i.e. at about 1.5 GHz. Its quality factor Q should be low enough so that the Bloch sideband falls within the resonance bandwidth even if $\nu_B > 100$ MHz, and so that the response time of the oscillator is not too large compared to the Bloch period $1/\nu_B$. On the other hand, a large Q yields larger signals as the reflected signal response is sharper when passing through resonance. We estimate that a quality factor $Q \approx 10$ is a reasonable trade-off (see Fig. 5.8) as the variation of the Blochonium frequency is about 70 MHz for the given values of E_J and E_C.

This low-enough quality factor also ensures that the phase difference γ is a classical variable as well as $\delta = \pi + \gamma$.
The bare plasma frequency (without the CPB) and the associated quality factor being

$$\nu_p = \frac{1}{2\pi}\sqrt{\frac{I_0}{\varphi_0 C_r}}$$

and

$$Q = R\sqrt{\frac{I_0 C_r}{\varphi_0}},$$

the choices made above lead to $C_r = 20pF$ and $I_0 = 620$ nA.

Finally, one has also to choose the frequency ν_{rf} and the amplitude V_{rf} of the microwave probe. For this purpose, one maximizes the phase modulation of the reflected signal given by Eq. (5.6).

$$iRC_r\omega + \frac{R}{iL_J\omega} + \frac{R}{iL(N_g,\delta)\omega} = \frac{1 - r(N_g,\pi)}{1 + r(N_g,\pi)}, \tag{5.17}$$

where

$$\begin{aligned}\delta &= \pi + \gamma,\\ \gamma &= \gamma_a e^{-i\frac{\pi}{2}} e^{i2\pi\nu_{rf}t} = \frac{V}{i\varphi_0 2\pi\nu_{rf}},\end{aligned}$$

and $V = (1 + r)V_{\text{in}} = e^{i2\pi\nu_{rf}t}$ (For a sake of simplification, we have changed the phase reference compared to previous sections).
This equation is normally valid for small oscillations of γ. Nevertheless it is possible to extend its validity to large γ_a by replacing L_J by an effective inductance $L_{J,eff}(\gamma_a)$ (see Annex F). Indeed, using Jacobi-Anger relation and limiting the expansion of the dynamics to oscillating terms at frequency ν_{rf} (monochromatic approximation), one obtains

$$L_{J,eff}(\gamma_a) = \frac{\gamma_a}{2J_1(\gamma_a)} L_J$$

with J_1 the Bessel function of the first kind.
The very same expansion in δ is also performed for the sCPB inductance $L(N_g, \delta)$ in order to take into account the AC-Stark shift effect induced by the γ oscillations. For this purpose, $1/L(N_g, \delta = \pi + \gamma)$ is first expanded as a Fourier series

$$\frac{1}{L(N_g, \pi + \gamma)_{\text{eff}}} = \sum_{n \in \mathbb{Z}} \alpha_k(N_g) \cos(k\gamma) \tag{5.18}$$

where

$$\alpha_k = (2 - \delta_{k,0}) \int \frac{1}{L(N_g, \pi + \gamma)} \cos(\gamma)\, d\gamma. \tag{5.19}$$

Then, replacing γ by $-i\gamma_a e^{i2\pi\nu_{rf}t}$, using the the same Jacobi-Anger relation, and eliminating fast oscillating terms, one obtains

$$\frac{1}{L(N_g, \delta = \pi)_{\text{eff}}} = \sum_{n \in \mathbb{Z}} \alpha_k [J_0(k\gamma_a) + J_2(k\gamma_a)], \tag{5.20}$$

with J_0 and J_2 the Bessel functions of the first kind. The reduction ratio of the inverse effective inductance, $L(N_g, \delta = \pi)/L(N_g, \delta = \pi)_{\text{eff}}$, depends essentially on the asymmetry d. As an example for the already chosen parameters of the sCPB ($E_J = 4$ K and $E_C = 2$ K), this ratio is equal to 0.96 for $\gamma_a = 0.1$ rad and to 0.7 for $\gamma_a = 0.4$ rad.

Using the above expressions, one calculates the reflexion coefficient r. Figure 5.7 shows its 2π phase shift when passing through the resonance. One notices that, when increasing V_{in}, the oscillator becomes non linear, its resonance frequency decreases, and the phase shift becomes more abrupt. Thus, the small N_g modulation of the resonance frequency (much smaller than the bandwidth $\Delta\nu = \nu_p/Q$) can be enhanced by increasing γ_a as shown on Fig. 5.8. However, γ_a can not be increased too much, taking into account the reduction of $1/L$ due to the AC-Stark shift mentioned above.

As a conclusion, it is convenient to work at maximum power but still below $|\gamma_a| = 0.1$ rad, with a probe frequency ν_{rf} between $\nu_p(Ng = 0)$ and $\nu_p(Ng = 1/2)$ (see Fig. 5.8), where the amplitude of the phase modulation of the reflected signal is maximum for the chosen values of E_J, E_C, and d.

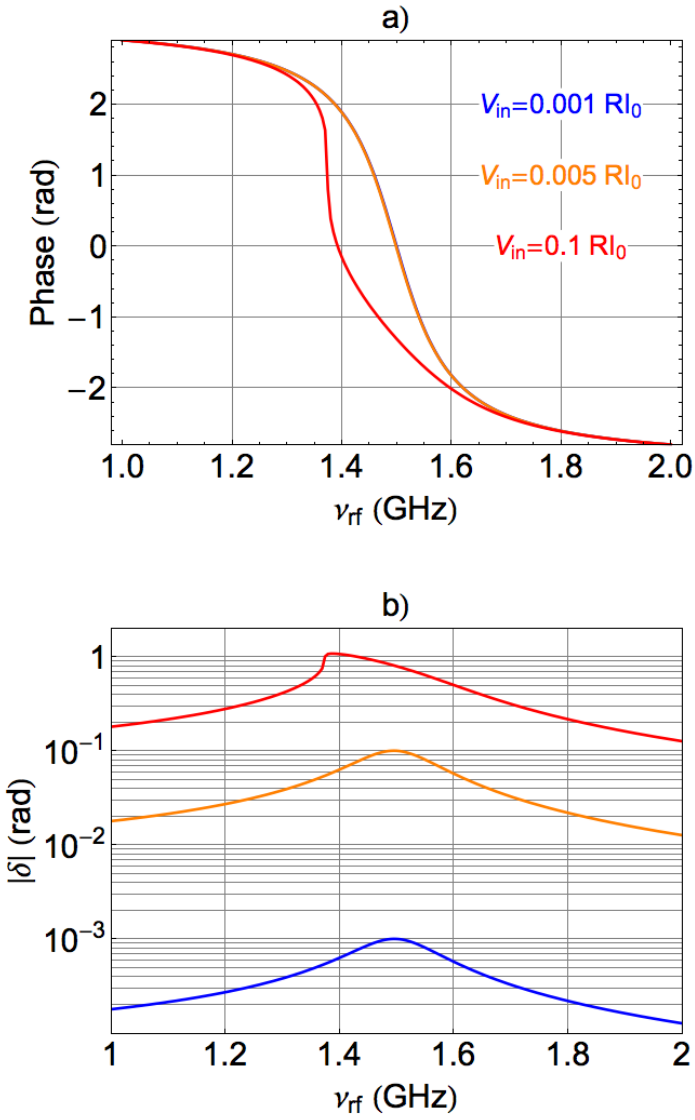

Fig. 5.7. Response of the Blochonium oscillator to microwave excitation as a function of the probe signal frequency for three drive amplitudes $|2V_{in}/(RI_0)| = 0.001$ (blue), 0.01 (orange) and 0.1 (red): phase of the reflected signal (a) and amplitude γ_a of oscillations (b) for $\nu_p = 1.5$ GHz and $Q = 10$.

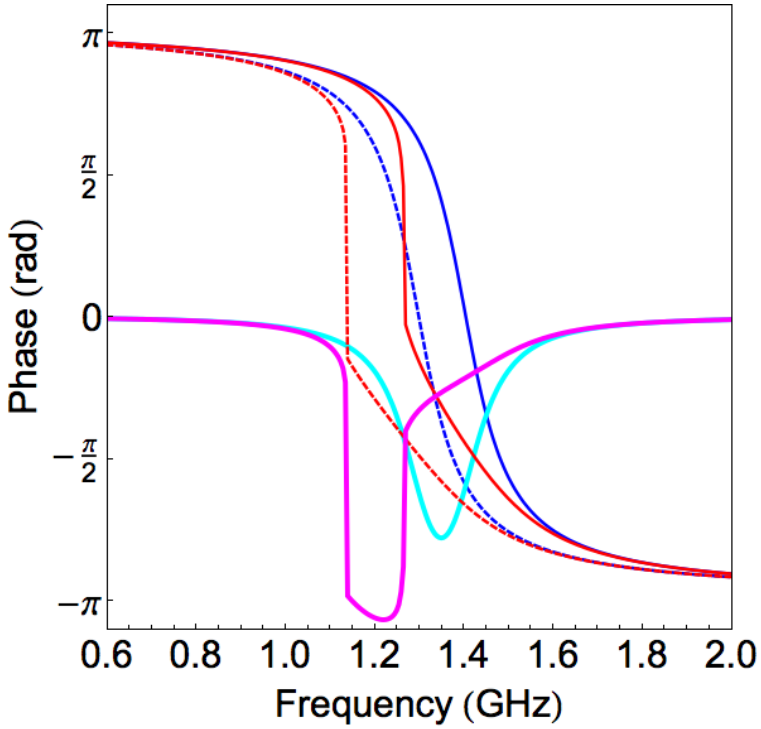

Fig. 5.8. Gate charge induced phase modulation of the Blochonium for $\nu_p = 1.5$ GHz, $Q = 10$, $E_J = 4$ K, $E_C = 2$ K, and $d = 0.15$. Thin lines are absolute phases of the reflected signal as a function of the probe signal frequency for two amplitudes $|2V_{\rm in}/(RI_0)|= 0.001$ (blue) and 0.1 (red), and for $N_g = 0$ (solid) and 1/2 (dashed). Bold lines are the corresponding differences between $N_g = 0$ and 1/2 for $|2V_{\rm in}/(RI_0)|= 0.001$ (cyan) and 0.1 (magenta).

5.2.4 Fabrication and experimental setup

5.2.4.1 Sample fabrication

The sample was fabricated using techniques similar to those used for the quantronium. In a first step, large leads (width larger than 100 μm) and quasiparticle traps are fabricated by optical lithography and Au deposition. Then, the Al bottom layer of the capacitance C_r is deposited and plasma-oxidized in a reactive Ion Etching machine following the process described in Annex 3. Finally, the sCPB, the readout junction, and the top layer of the capacitance are fabricated by e-beam lithography and double-angle shadow evaporation of Aluminum. In order to avoid quasiparticle poisoning, the island is made thinner than the leads (13 nm and 42 nm respectively). Pictures of the sample are shown ion Fig. 5.9.

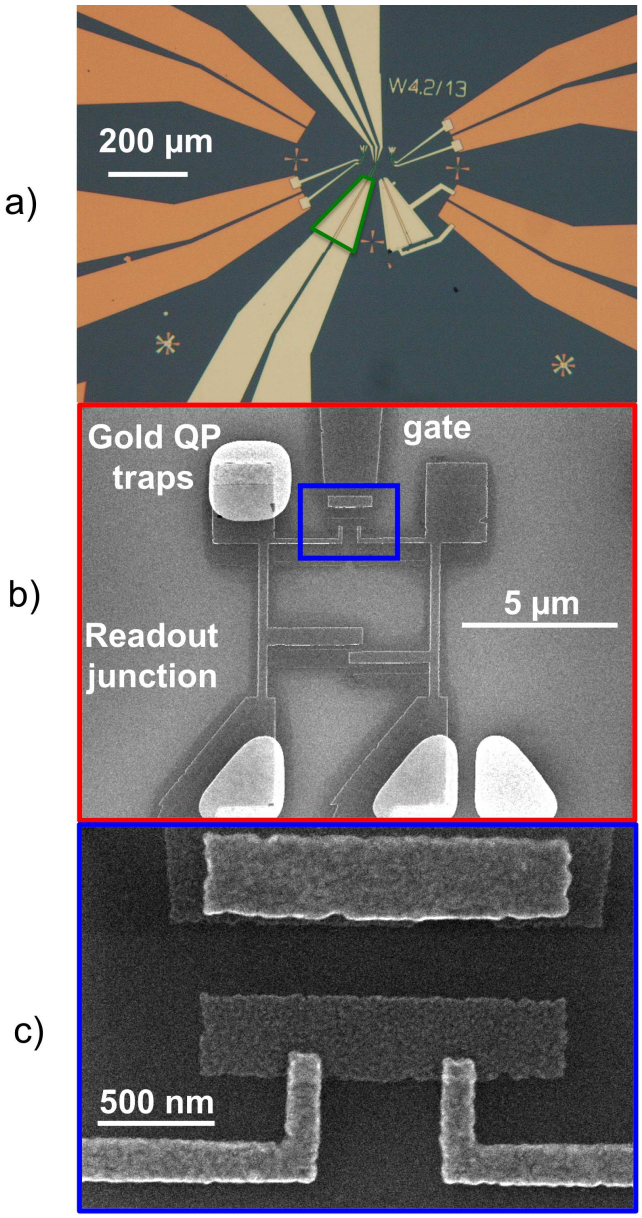

Fig. 5.9. Optical and scanning electron micrographs of the central part of the Blochonium from large (top) to small (bottom) scale. a) Large scale view showing the C_r capacitors (green box) and gate (top electrodes). b) SEM picture showing the split Cooper Pair Box in parallel with its "readout" Josephson junction, and gold quasiparticle traps (bright structures). c) Detailed view of the gate (top structure), of the island (middle rectangle), and of the two asymmetric Josephson junctions with $d = 15\%$ (bottom structure).

5.2.4.2 Microwave reflectometry measurements on the Blochonium

The circuit is glued with wax on a Printed Circuit Board, and is wire-bonded to two coplanar Waveguide lines made of gold-platted copper. Mini-SMP connectors are soldered at the end of each CPW line.
The PCB is then placed in a tin-lead platted copper box anchored to the cold plate bottom of a dilution fridge with base temperature 25 mK. It is connected to the gate and to measuring lines, as shown in Fig. 5.10. The gate line is attenuated and filtered above 250 MHz in order to prevent electromagnetic noise to affect Bloch oscillations. The measuring line is actually made of two lines: one for the microwave injection, and one for measuring the reflected signal.
For generating and demodulating the microwave signal, the output of a microwave generator (Anritsu MG3692) is split in two channels. One of them is used as a reference local oscillator for the demodulation of the reflected signal. The other one is sent to the excitation line, which is strongly attenuated, and passed through a bandpass filter [1.2 GHz-1.8 GHz]. At 25 mK, the injected signal goes through a circulator, then is phase modulated and reflected on the Blochonium oscillator. The reflected signal goes through the same circulator to the measuring line. The signal is then transmitted through a superconducting line to a cryogenic amplifier (Quinstar L-1.5-30H) with a noise temperature of 2.4K at 1.5 GHz. To prevent outside noise to pass through this line, three circulators are inserted at different temperatures. At room temperature, the signal is amplified again. The output signal is finally sent to the input of a spectrum analyzer for spectral measurement, or to the input of mixer for time-domain measurement.

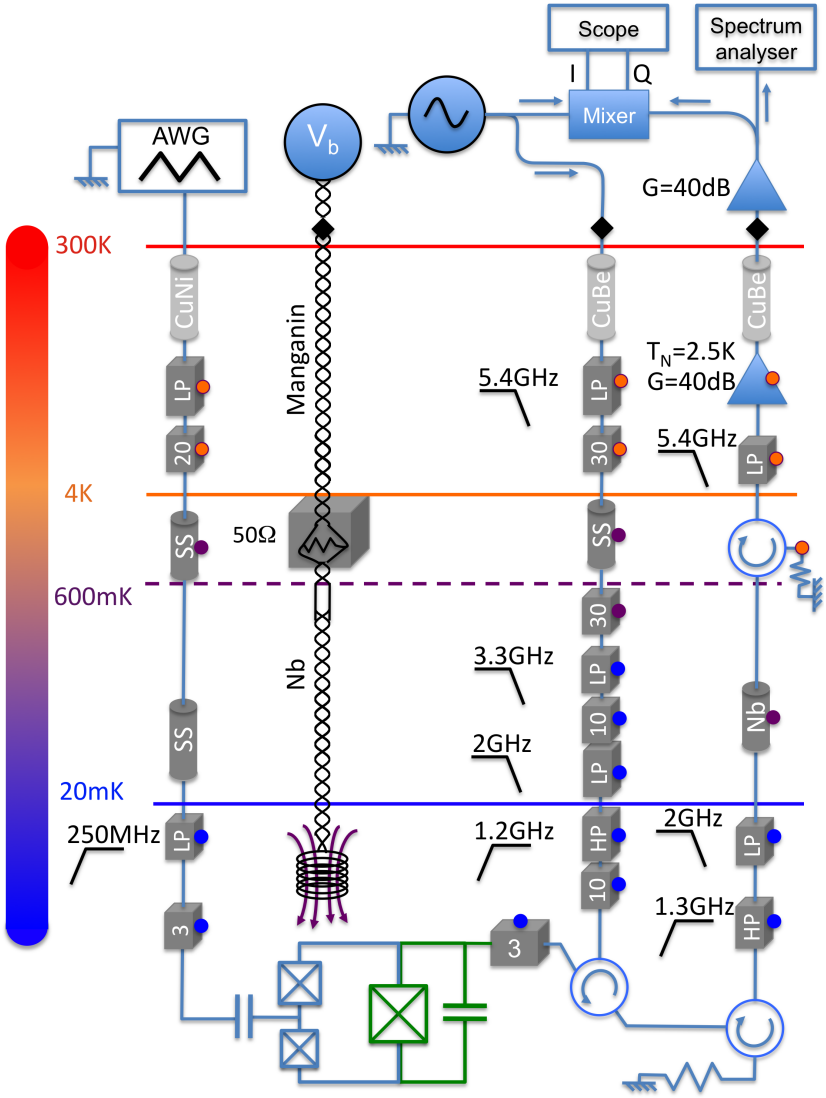

Fig. 5.10. Electrical wiring of the experiment. The triangular gate voltage is applied through a filtered attenuated line (left vertical line). The flux is tuned using the central vertical line. The microwave signal generated by a microwave source passes through a attenuated and filtered line. At 20 mK, it goes through a first circulator, goes to the probe junction on which it is reflected. Then it goes back through the same circulator, and two other ones, before being amplified at 4 °K by a cryogenic amplifier with noise temprature $T_N = 2.2$°K. At room temperature, the signal is either sent to a spectrum analyzer or demodulated by homodyne detection.

5.3 Experiments

5.3.1 Sample characterization

We have first characterized the sample by measuring the resonance frequency of the sCPB in parallel with the Josephson oscillator. Using a vector network analyser, one applies a microwave continuous wave, and measures the reflected signal φ. By sweeping the frequency, the phase φ changes by about π when passing across the resonance at ν_p. This allows to follow ν_p as a function of N_g and δ. As the values of the critical current I_0 and the parallel capacitor C_r are known from room temperature measurements of the resistance and capacitance, one can use the expression (5.3) to determine the sample parameters E_J, E_C, and d (see Fig. 5.11). In this sample $I_0 = 870nA$, $C_r = 47pF$, $E_J = 2.879k_BK$, $E_C = 1.416k_BK$, and $d = 0.139$. Note that this measurement requires low power injection in order to induce oscillations of γ small enough for staying in the linear regime and for inducing small renormalisation of $1/L$ by the AC-Stark shift.

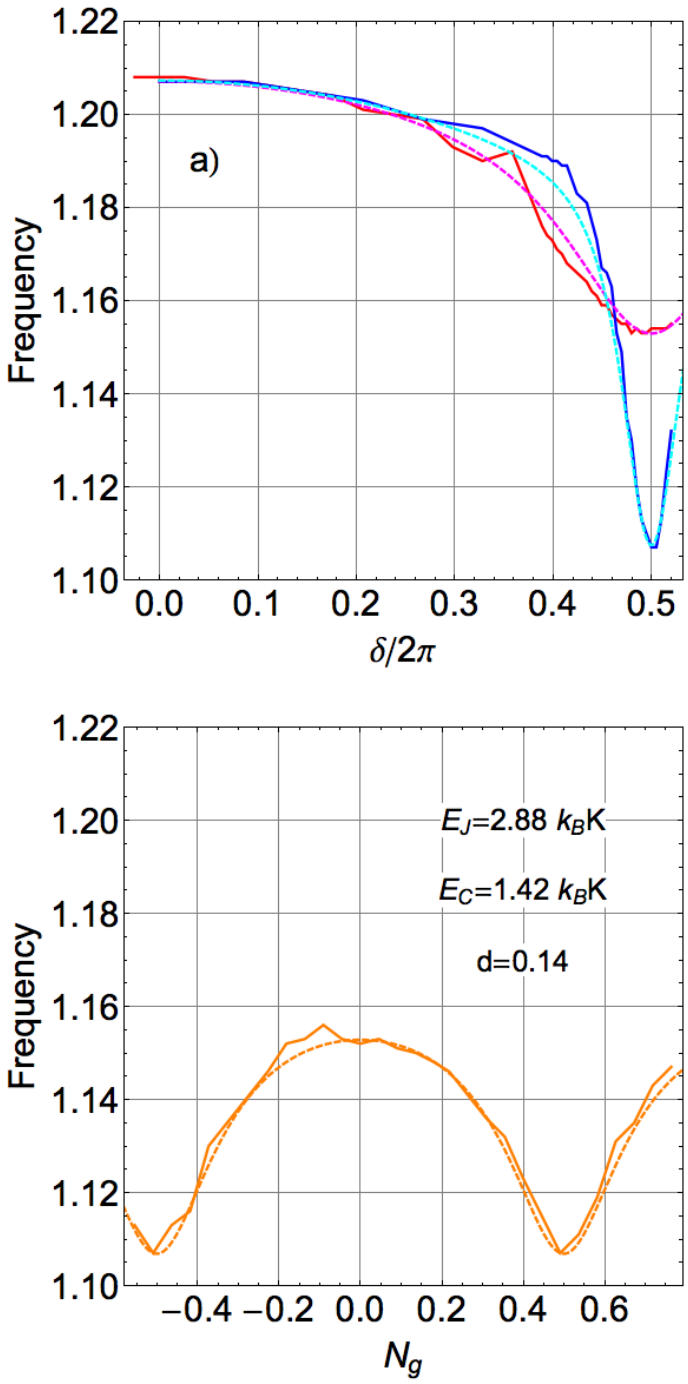

Fig. 5.11. Modulation of the resonance frequency of the Josephson oscillator in parallel with the sCPB as a function of δ (a) and N_g (b). a) The curves at $N_g = 0$ (red) and $N_g = 0.5$ can be fitted (dashed lines) in order to determine the sample parameters: $E_J = 2.88 k_B K$, $E_C = 1.42 k_B K$, and $d = 0.14$. These resonance frequencies were determined by fitting the phase of the reflected signal as a function of the microwave frequency for all the values of δ and N_g plotted here. For these experiments, the amplitude of the induced oscillations of γ was about 0.1 rad.

5.3.2 Direct observation of Bloch oscillations in the time domain

The Bloch oscillations of the Blochonium were first directly probed in the time domain by applying a low frequency triangular modulation to the gate, and by measuring one quadrature of the reflected signal with a demodulator (AD8347 from Analog Devices). Figure 5.12 shows this quadrature for a Bloch frequency of 8 kHz. The limiting factor for this experiment is the noise temperature of the cryogenic amplifier, which imposed to reduce the measurement bandwidth, and thus the Bloch frequency. When monitoring the signal during 2 s, we have not observed any spurious change of N_g, which indicates the absence of stable quasiparticle poisoning.

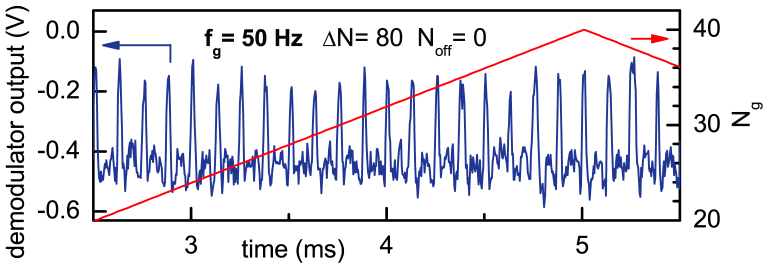

Fig. 5.12. Quadrature of the demodulated reflected signal (blue trace) when the gate charge is varied at low frequency (red trace). The periodic oscillations of the reflection coefficient result from the Bloch oscillations of the current-biased split cooper Pair Box during the linear ramps. Each period corresponds to a single Cooper pair injected in the box island.

5.3.3 Bloch oscillation spectrum

The oscillations of the sCPB inductance have been more quantitatively measured from the power spectrum of the reflected signal.
A microwave signal, which induces γ oscillations with an amplitude of about 0.1 rad, is applied to the Josephson oscillator at a frequency ν_{rf}. At the same time, a gate charge triangular modulation pattern is applied to the gate line with reduced voltage offset N_{g_0}, amplitude ΔN_g, and frequency ν_g. The spectral power of all the i^{th} harmonics at frequency $\nu_{rf} + \mathrm{i}\nu_g$ is measured using a power spectrum analyzer with a 1 Hz bandwidth. Figure 5.13 shows the harmonic amplitudes for different sets of N_{g_0} and ΔN_g. Starting from a modulation pattern that does not fulfil the criteria for observing only Bloch

sidebands, one progressively clean the spectrum by adjusting the amplitude and the offset till the spectrum contains only Bloch lines, as in the case of a perfectly current-biased Josephson junction.

Figure 5.14 shows the comparison between similar data and the theoretical predictions using the model given in section 4.2.1.2, and using the measured transmission of our microwave lines. One can notice that the plasma frequency of the Josephson oscillator was smaller than expected, which imposed to work on the lower side of the circulator frequency bandwidth, which yielded some spurious leakage and interferences between incident and reflected signals.
It was possible to increase the amplitude ΔN_g and the frequency ν_g, and to reach ν_B values of a few hundreds of MHz, as shown on Fig. 5.15. At this frequency, the sideband amplitudes were nevertheless significantly reduced due to the finite oscillator bandwidth. Moreover, the finite bandwidth of the pulse generator AG 3252 used to produce the triangular modulation patterns yields an appreciable rounding at the turning points, which results in spurious peaks in the spectrum.

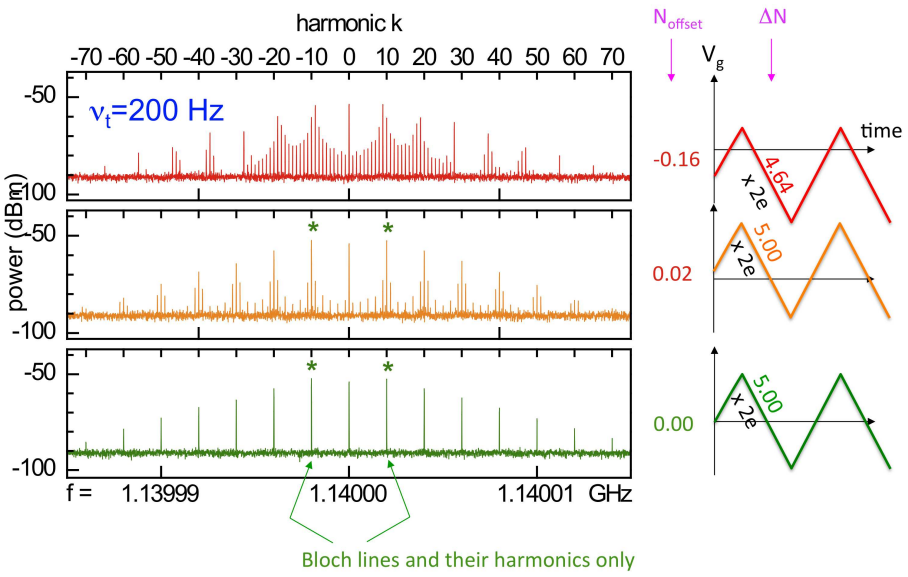

Fig. 5.13. Spectra of a reflected signal at 1.14 GHz for different triangular gate voltages (see pictograms on the right) at frequency ν_g=200 Hz. These spectra consist in peaks at the different harmonics at frequency i$\times\nu_g$. When N_{g_0} and ΔN_g are tuned to integer values only peaks at the Bloch frequency and its multiple $\nu_B = 2\Delta N_g \nu_g$ remain (see bottom panel).

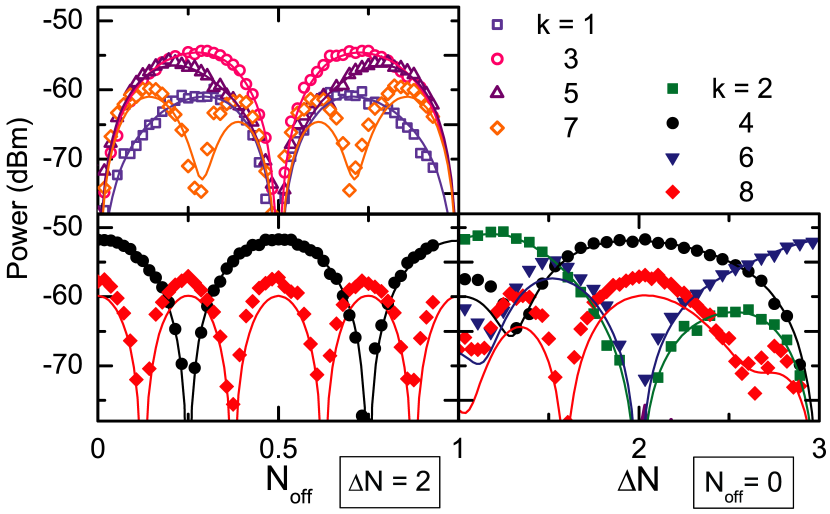

Fig. 5.14. Comparaison of the measured and calculated harmonics amplitudes as a function of N_{g_0} and ΔN_g, for $\nu_g = 1$ kHz. Calculated curves were shifted by 45dB (estimated value was 44dB) to best match the experimental Bloch line of order 1. Left: Offset dependance for $\Delta N_g = 2$; the observed harmonics correspond to odd multiples of ν_g (top), and to the Bloch line k=4 and its harmonics k=4n, with period $1/(2n)$ in N_{g_0} (bottom). Right: amplitude dependance for $N_{g_0} = 0$. The Bloch lines correspond to k=2 for $\Delta N_g = 1$, k=4 for $\Delta N_g = 2$, and k=6 for $\Delta N_g = 3$.

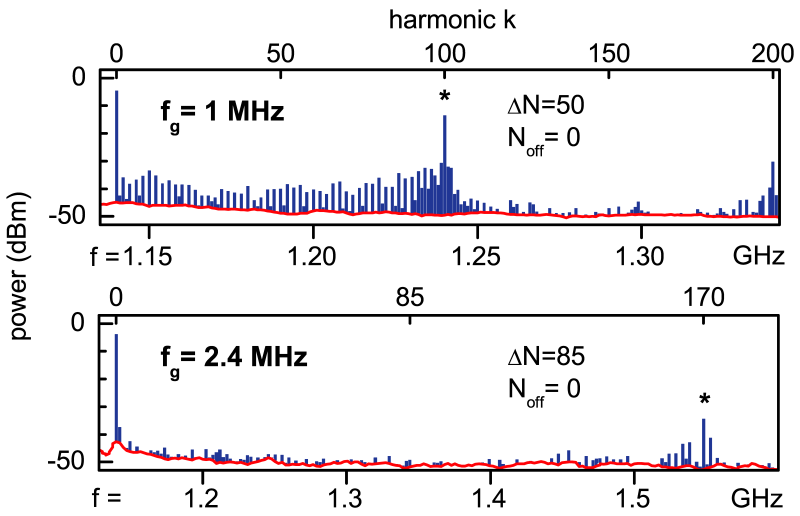

Fig. 5.15. Amplitudes of the harmonics of ν_B. Top: $N_{g_0} = 0$, $\Delta N_g = 50$, and $\nu_g = 1$ MHz. Bottom: $N_{g_0} = 0$, $\Delta N_g = 85$, and $\nu_g = 2.4$ MHz. The Bloch lines of order 1 are marked with an asterisk and correspond to Bloch frequency of 100 MHz = 32 pA and 408 MHz = 130 pA.

5.3.4 Conclusion

Using microwave reflectometry techniques, we have demonstrated Bloch-like oscillations in a charge-biased Cooper pair box, a circuit equivalent to a current-biased Josephson junction. Bloch oscillations were observed up to 400 MHz, which corresponds to a current of about 130 pA.
This experiment demonstrates that current to frequency conversion in the sub-nA range requested for closing the triangle of quantum metrology can in principle be performed using Bloch oscillations in a current-biased Josephson junction.
As discussed in [107, 109], this requires to invent and fabricate a current source with specific characteristics:

- a high impedance to ensure that the split junction is in the Coulomb blockade regime
- a very low noise in order to maintain the fluctuations of the injected charge well below a single Cooper pair, so that Bloch lines are sufficiently narrow for current metrology.

This is undoubtedly a difficult goal that goes beyond the reach of this thesis, which just demonstrates the validity of current to the frequency conversion with Bloch oscillations.

Annex A

Manipulation of the qubit state: a few protocols

In this annex we present the different pulse sequences used in qubit experiments, in particular to characterize the decoherence.

- π pulse: resonant microwave pulse whose duration is $1/2\nu_{Rabi}$. It induces a rotation of π around the x-axis, and transforms $|0>$ into $|1\rangle$.

- $\pi/2$ pulse: resonant or nearly resonant microwave pulse whose duration is about $1/4\nu_{Rabi}$ in order to transform $|0\rangle$ into $(|0\rangle + e^{i\varphi}|1\rangle)/\sqrt{2}$, where φ depends on the phase of the microwave pulse (with respect to a reference) and on the possible frequency detuning.

- Ramsey sequence n°: this sequence is used to measure the precession around the z-axis at the qubit frequency during a free evolution. A first nearly resonant $\pi/2$ pulse with a zero phase and a detuning $\Delta\nu = \nu_{rf} - \nu_{01}$ prepares a equal-weight superposition of state $|0\rangle$ and $|1\rangle$; then the qubit evolves freely in the equatorial plane during a time Δt, precessing around z at frequency $\Delta\nu$; finally a second $\pi/2$ pulse with a possible different phase χ is applied. The probability of being in state $|1>$ is $\cos(\chi)^2$.

- Echo sequence : it is based on the Ramsey sequence n° 2, where a π pulse is applied at $\Delta t/2$. This enables to measure z-axis precession being sensitive only to high-frequency (higher than $1/\Delta t$) noise.

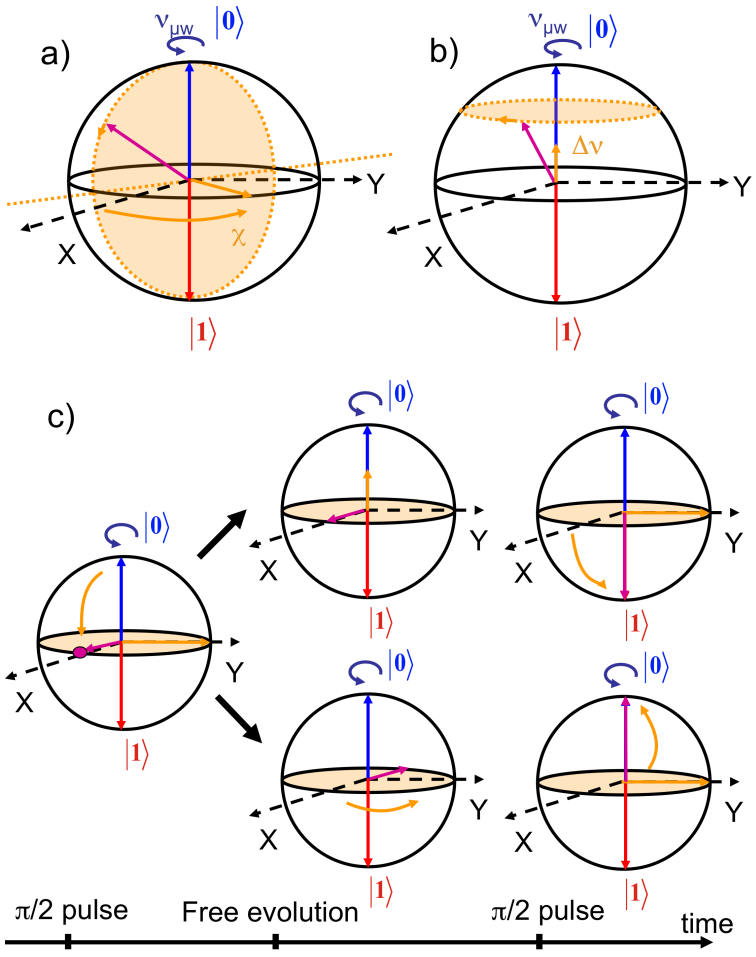

Fig. A.1. a) is the Bloch sphere in a rotating frame with a microwave field in resonance. b) is the free evolution of the qubit. c) is a typical Ramsey sequence for two different values Δt 0 and $1/2\delta\nu$

Annex B

How the quantronium can be simplified as a basic Cooper Pair Box

We explain here why it is possible to simplify the quantronium circuit made of a split CPB in parallel with a current biased and capacitively shunted Josephson junction as an equivalent basic CPB (see Fig. B).

The Hamiltonian of the quantronium circuit can be calculated following the method proposed by M. Devoret [68] and B.Yurke [67], which is summarized at the beginning of section 1.2.1.

Figure B shows the spanning tree that we choose for the circuit, and its three nodes A, B, and C. All these nodes X are connected to ground by only one branch, so that $\phi_X = \Phi_{XGround}$.
The three Kirchoff's current laws at nodes A, B, C are

$$0 = i_{bias} - I_{0_r}\sin(\gamma) - I_{0_1}\sin(\theta_1) + C_r\ddot{\phi}_A + C_{J_1}(\ddot{\phi}_A - \ddot{\phi}_B),$$
$$0 = -I_{0_1}\sin(\theta_1) - I_{0_2}\sin(\theta_2) + C_{J_1}(\ddot{\phi}_B + C_{J_1}(\ddot{\phi}_B - \ddot{\phi}_A) + C_g(\ddot{\phi}_B - \ddot{\phi}_C),$$
$$0 = C_S\ddot{\phi}_C + C_g(\ddot{\phi}_C - \ddot{\phi}_B),$$

where $\theta_1 = \phi_A - \phi_B$, $\theta_2 = \phi_B$ and $\gamma = \theta_1 + \theta_2 + \Phi/\varphi_0$.

These equations of motion are the Euler-Lagrange equations

$$\frac{\partial \mathcal{L}}{\partial \phi} = \frac{\partial}{\partial t}\frac{\partial \mathcal{L}}{\partial \dot{\phi}} \text{ and } \dot{\phi} = \frac{\partial \phi}{\partial t} \tag{B.1}$$

associated with a lagrangian $\mathcal{L}$ defined as the kinetic energy (energy of the capacitive elements) minus the potential energy (energy of the inductive el-

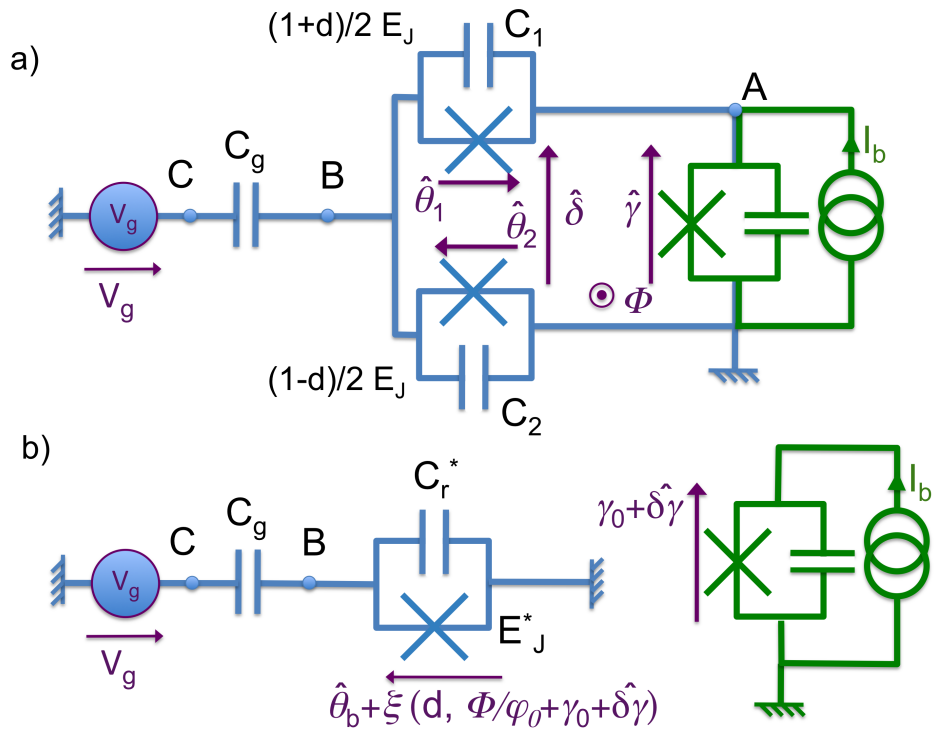

Fig. B.1. Transforming the quantronium in an equivalent circuit with a basic CPB. a): Electrical schematic of the whole quantronium circuit with its three biases V_g, Φ, and i_b. The different parameters and quantum variables. b): Equivalent circuit involving a basic CPB instead of split one. The coupling between the two sub-circuits occurs the $\hat{\gamma}$ observable. For low enough bias current i_b, quantum fluctuations of γ can be neglected and $\hat{\gamma}$ replaced $\gamma_0 = \langle\gamma\rangle$.

ements). Then, by integrating Eq. (B.1) from $t = -\infty$ (one has to integrate carefully the infinite terms coming from sources), one obtains

$$\begin{aligned}
\mathcal{L} = & \frac{C_\Sigma}{2}\dot{\phi}_B^2 + E_{J_1}[\cos(\theta_1) - 1] + E_{J_2}[\cos(\theta_2) - 1] - \frac{C_g}{2}\dot{\phi}_C^2 \\
& - C_{J_1}\dot{\phi}_B\dot{\phi}_A - C_g\dot{\phi}_B\dot{\phi}_C \\
& + \frac{C_{J_1} + C_r}{2}\dot{\phi}_A^2 + E_{J_r}(\cos(\gamma) - 1) + \varphi_0\gamma i_{bias} \\
= & \frac{C_\Sigma}{2}\left(\dot{\phi}_B - \frac{C_{J_1}}{C_\Sigma}\dot{\phi}_A\right)^2 + E_{J_1}\cos(\theta_1) + E_{J_2}\cos(\theta_2) - C_g\dot{\phi}_B\dot{\phi}_C \\
& + \frac{1}{2}\left[C_r + C_{J_1}\left(1 - \frac{C_{J_1}}{C_\Sigma}\right)\right]\dot{\phi}_A^2 + E_{J_r}\cos(\gamma) + \varphi_0\gamma i_b + cst. \qquad \text{(B.2)}
\end{aligned}$$

Here $C_\Sigma = C_{J_1} + C_{J_2} + C_g \simeq 2C_J$ with $C_{J_{1,2}} = (1 \pm d)C_{J_{1,2}}/2$.
It is convenient to rewrite this Lagrangian using the two conjugate variables $\{q_B = 2eN, \phi_B\}$ of node B with

$$q_B = \frac{\partial \mathcal{L}}{\partial \dot{\phi}_B} = C_\Sigma \left(\dot{\phi}_B - \frac{C_{J_1}}{C_\Sigma} \dot{\phi}_A \right) - C_g V_g$$

and $V_g = \dot{\phi}_C$.
Finally, one then deduces the Hamiltonian from the Lagrangian:

$$\begin{aligned} H &= \sum_{i=\{A,B\}} \frac{\partial \mathcal{L}}{\partial \dot{\phi}_i} \dot{\phi}_i - \mathcal{L} \\ &= \left[C_r + C_{J_1} \left(1 - \frac{C_{J_1}}{C_\Sigma} \right) \right] \dot{\phi}_A^2 - C_{J_1} \left(\dot{\phi}_B - \frac{C_{J_1}}{C_\Sigma} \dot{\phi}_A \right) \dot{\phi}_A \\ &\quad + C_\Sigma \left(\dot{\phi}_B - \frac{C_{J_1}}{C_\Sigma} \dot{\phi}_A \right) \dot{\phi}_B - C_g V_g \dot{\phi}_B - \mathcal{L}. \end{aligned}$$

One finds

$$\begin{aligned} H = {} & E_C (N - N_g)^2 - E_{J_1} \cos(\theta_1) - E_{J_2} \cos(\theta_2) \\ & + \frac{1}{2} \left[C_r + C_{J_1} \left(1 - \frac{C_{J_1}}{C_\Sigma} \right) \right] \dot{\gamma}^2 - E_{J_r} \cos(\gamma) \\ & - \varphi_0 \gamma i_b \end{aligned} \tag{B.3}$$

with $\dot{\phi}_A = \varphi_0 \dot{\gamma}$, $E_C = (2e)^2/C_\Sigma$. Hamiltonian (B.3) can be regarded as the sum of the split Cooper Pair Box Hamiltonian (line 1), of the readout Josephson oscillator Hamiltonian (line 2), and of the current source Hamiltonian (line 3). The readout contribution contains a Josephson term analogue to a potential energy and a $\dot{\gamma}^2$ term analogue to a kinetic energy, with the "mass" C_r slightly renormalized by the CPB (term in C_{J_1}). This renormalization comes from the asymmetric grounding of the circuit (only one CPB junction is directly connected to ground). It is nevertheless negligible as $C_r >> C_{J_1}$.

Using the definitions $E_{J_{1,2}} = E_J \frac{1 \pm d}{2}$, $\theta = \frac{\theta_1 - \theta_2}{2}$ and $\delta = \theta_1 + \theta_2$, and considering the degrees of freedom as quantum observables, one obtains

$$\widehat{H} = \widehat{H}_{sCPB} + \widehat{H}_{readout}$$

$$\widehat{H}_{sCPB} = E_C (\widehat{N} - N_g)^2 - E_J \left[\cos\left(\frac{\widehat{\delta}}{2} \right) \cos\widehat{\theta} + d \sin\left(\frac{\widehat{\delta}}{2} \right) \sin\left(\widehat{\theta} \right) \right] \tag{B.4}$$

$$\widehat{H}_{readout} = \frac{C_r^*}{2} \varphi_0^2 \widehat{\dot{\gamma}}^2 - E_{J_r} \cos(\widehat{\gamma}) - \varphi_0 \widehat{\gamma} i_b \tag{B.5}$$

with $C_r^* = C_r + C_{J_1}(1 - C_{J_1}/C_\Sigma) \simeq C_r$. Considering quantum fluctuations of the phase $\widehat{\gamma}$ as small, $\widehat{H}_{sCPB}$ in Eq. (B.4) is mathematically equivalent to [16]

$$\widehat{H}_{sCPB} = E_C \left(\widehat{N} - N_g\right)^2 - E_J^*(d,\delta)\cos\left(\widehat{\theta}^*\right) \tag{B.6}$$

with

$$\begin{aligned} E_J^*(d,\delta) &= E_J\sqrt{(1+d^2+(1-d^2)\cos(\delta)/2} \\ \widehat{\theta}^* &= \widehat{\theta} + \zeta(d,\delta) \end{aligned} \tag{B.7}$$

with $\tan[\zeta(d,\delta)] = -d\tan(\delta/2)$ and $\delta = \gamma - \Phi/\varphi_0$. As a conlusion, the quantronium circuit can be regarded as two separate (but dependent) circuits: a basic CPB with effective Josephson energy E_J^* and island phase $\widehat{\theta}^*$, and the readout circuit. This equivalence will be used to calculate Lagrangian and Hamiltonian of the quantroswap circuit in section 1.2.1.

$\widehat{H}_{readout}$ can be furthermore simplified to enlight the coupling between the split CPB and the readout circuit: it can be expanded in fluctuations $\widehat{\delta\gamma}$ near the value γ_0 that minimizes the potential energy of the readout junction (in presence of the sCPB):

$$\widehat{H}_{readout} = \frac{C_r}{2}\varphi_0^2\widehat{\dot{\delta\gamma}}^2 - \frac{\varphi_0^2}{2L_{J_r}}\widehat{\delta\gamma}^2$$

with $L_{J_r}(\gamma_0) = \varphi_0/(I_0\sin(\gamma_0))$. Switching to second quantification, one has

$$\widehat{H}_{readout} = h\nu_p\left(\widehat{a}^+\widehat{a} + 1/2\right)$$

with $\nu_p(\gamma_0) = 1/2\pi\sqrt{L_{J_r}C_r}$ the resonance frequency of biased junction, $\widehat{a}^+$ $\widehat{a}$ the creation annihilation operators, $\widehat{\delta\gamma} = \delta\gamma_0(\widehat{a}^+ + \widehat{a})$, and $\delta\gamma_0^2 = h\nu_p L_{J_r}/\varphi_0^2$. The Hamiltonian of the whole systems finally

$$\begin{aligned} \widehat{H} = \widehat{H}_{sCPB}&(N_g, \delta = \gamma_0 + \Phi/\varphi_0) \\ &+\widehat{I}\Big|_{N_g,\delta=\gamma_0-\widetilde{\Phi}/\varphi_0}(\delta\gamma_0\varphi_0)(\widehat{a}^+ + \widehat{a}) + \widehat{\frac{1}{L}}\Big|_{N_g,\delta=\gamma_0-\widetilde{\Phi}/\varphi_0}\frac{(\delta\gamma_0\varphi_0)^2}{2}(\widehat{a}^+ + \widehat{a})^2 \\ &+h\nu_p\left(\widehat{a}^+\widehat{a} + 1/2\right) \end{aligned}$$

with

$$\widehat{I} = \frac{\partial\widehat{H}_{sCPB}}{\partial\delta} \text{ and } \widehat{1/L} = \frac{\partial^2\widehat{H}_{sCPB}}{\partial\delta^2}. \tag{B.8}$$

This expression can be used to evaluate relaxation rate of the CPB due to the exchange of one and two photons (terms in $\widehat{I}$ and $\widehat{1/L}$) with the environment.

Annex C

Lithography

We present in this Annex the optical and electron-beam lithography processes used for fabricating the quantroswap and blochonium circuits.

C.1 Sub-micron UV lithography

We have developed a sub-micron UV lithography process on two-inch wafer (Si or Sapphire) using an MJB4 mask aligner equipped with a 365 nm monochromatic UV source (i-line).
Three-inch squared Chromium-quartz masks were designed using the AutoCad software and were ordered to the Toppan Photomask company. The first step is to draw the circuit and fabricate a Cr coated mask using AutoCad. Since all the masks were used for lift-off, a bilayer of resists (LOL1000+Shipley S1805) was always used to obtain a large undercut facilitating the final dissolution of the resist mask.This procees led to pattern with minimal size down to $600nm$, which is close to the UV wavelength.

Sub-micron UV lithography recipe

- Wafer dehydration at 155°C × 2 min (hotplate). Cooling back to room temperature.
- Spin of Shipley primer (adhesion promoter): 3000 rpm × 60s.
- Spin of filtered LOL 1000 (ballast resist): 6000 rpm × 60 s. Thickness of about 150 nm
- Softbake at 155°C × 5 min (hotplate). Cooling back to room temperature.
- Spin of Shipley S1805 (optically active resist): 6000 rpm × 60 s (2 s acceleration).
- Softbake at 115°C × 60s. Cooling back to room temperature.
- UV Exposure in "vacuum contact": 15 s × 5.7 mW/cm2 on MJB3 (broadband lamp), or 1.2 s × 30.5 mW/cm2 on MJB4 (i-line).
- Pure MF319 development at room temperature.

  The developing time is a critical parameter if your goal is a submicron resolution. It has to be measured each time, using a test wafer for instance. It can depend strongly on the storing time at air of the MF319 and on the amount of resist already dissolved during previous developments. It can be determined by observing the red cloud formed by the resist dissolved close to the edges of big pattern elements, while moving the wafer back and forth in the developer. The correct time corresponds to the disappearance of the cloud + 5-10 seconds depending on the targeted undercut. Typical time is between 30+5 and 60+10 s.
- Rinse in water and dry at 60°C × 2 min
- Metal evaporation below 150 nm.
- Lift-off in an ultrasonic bath of Remover 1165 at 50 ąC × 10 min.

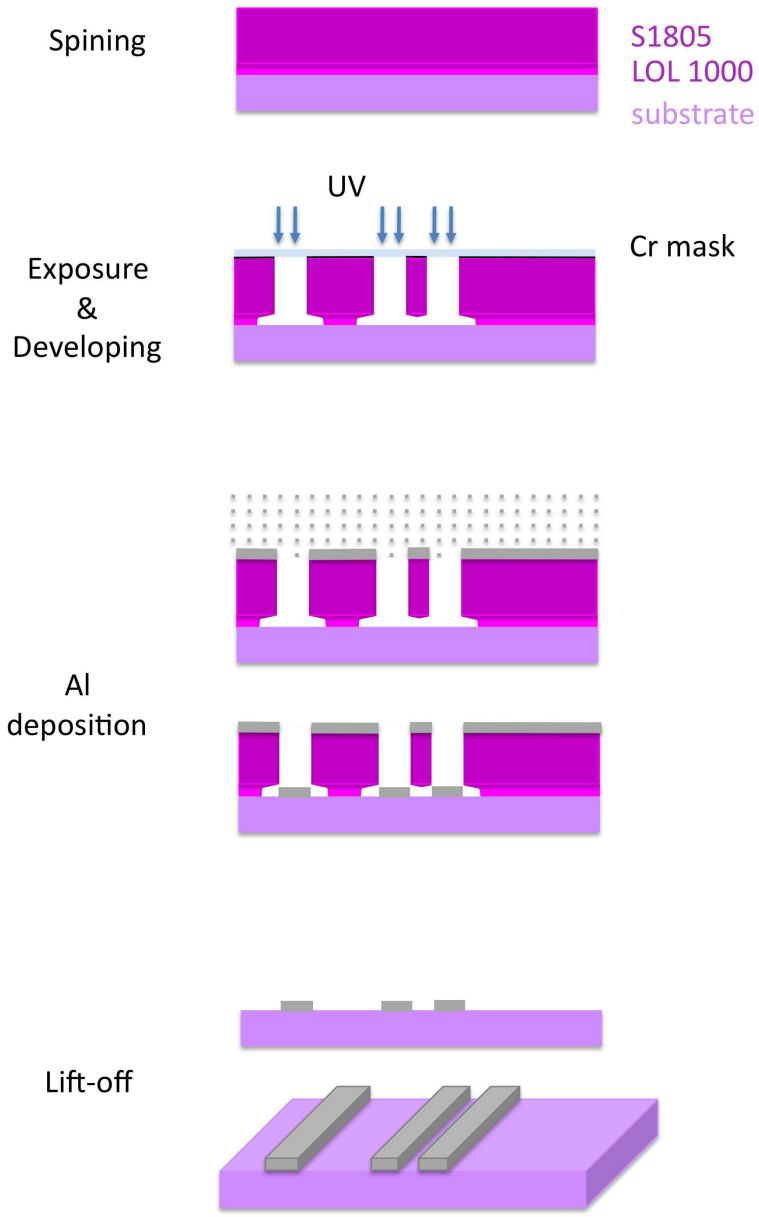

Fig. C.1. Illustration of the submicron optical lithography process developed during this thesis work. LOL1000 and S1805 resist (pink) are first spun on a Si-$Si0_2$ or sapphire 2-inch wafer. In a second step, the wafer is exposed to a monochromatic UV light (i line) trough a Cr-quartz 3-inch mask. The exposed resist is developed by immersion in MF319. Then metal is evaporated in an electron gun evaporator. Finally the mask is lifted off.

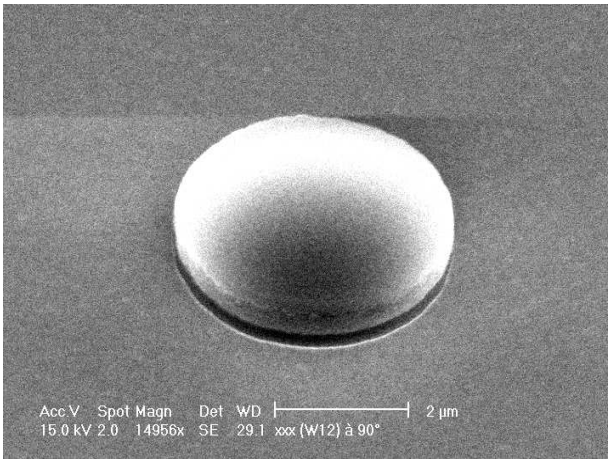

Fig. C.2. Detailed Scanning Electron Micrography showing the role of the buffer layer (LOL 1000) in our lift-off process. The image is taken just before lift off and shows that the resist dot will be easily dissolved thanks to the gap (dark region) between the metallic layer deposited on the substrate and the resist dot (undercut).

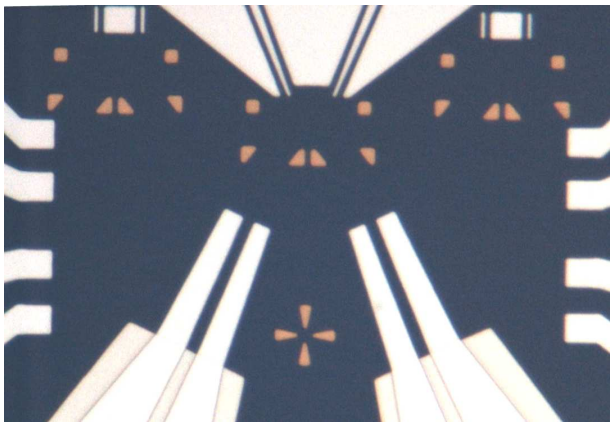

Fig. C.3. Micrographies of the central part of the quantroswap chip after three optical lithography steps. a) Optical micrography. Bottom aluminum electrodes (bottom of the Figure), then gold pads (yellow), and finally top aluminum layer were deposited successively. Gold crosses are used for further alignment in e-beam lithography. b) SEM micrography showing both the optical and e-beam fabricated electrodes. The lateral size of the optically made quantronium gates is indicated.

C.2 Electron-beam lithography

E-beam lithography was used for fabricating our Josephson devices by double angle evaporation of Aluminum. This technique consists in making a mask suspended well-above the surface of the substrate so that two successive depositions through the mask at different angles can lead to an overlap between different electrodes (see Fig. C.5). An oxidation step between the two deposition steps leads to Superconductor-Insulator-Superconductor structure at the overlaps, thus defining Josephson junctions.
The suspended mask is obtained from a resist bilayer: a less sensitive thin resist layer on top of a more sensitive bottom layer. The openings of the mask are obtained by exposing the corresponding areas to an electron beam that cracks the resist molecules. The exposed area are then dissolved in a solvent. Whereas openings are precisely defined in the top layer, the higher sensitivity of the bottom one leads to large cavities or undercut in their vicinities, hence the suspended mask. The depth of these undercuts can be enlarged by exposing additional areas on the edges of the openings (undercut boxes) at sufficiently lower dose so that the top layer is not impacted. The bilayer resist for all the sample made during this thesis work is made of an about 100 nm thick PMMA (PolyMethylMetaAcrylate) layer on top of an about 1 μm thick PMMA/MAA (PolyMethylMetaAcrylate/MethylAcrylate acid) layer. The developer is a mixture of 25% MethylIsoButyl Ketone (MIBK)- 75%IsoPropanol (in volume).

Electron-beam lithography recipe

- Bilayer 1 μm MAA - 100 nm PMMA
  - Spin filtered PMMA/MAA 8.5K EL10 (8.5 kg/mol in EthylLactate solvent) at 2000 rpm $\times$ 60s
  - Dry at 170 °C $\times$ 60 s. Cool down to room temperature.
  - Spin again filtered PMMA/MAA 8.5K EL10 at 2000 rpm $\times$ 60 s.
  - Dry at 170 °C $\times$ 60 s. Cool down to room temperature.
  - Spin filtered PMMA 950K A3 (950 kg/mol in Anisole solvent) at 4000 rpm $\times$ 60s.
  - Dry at 170 °C $\times$ 20 min.
- Expose the pattern with a dose of 260 μC/cm^2, and undercut boxes below 50 μC/cm^2 if necessary.

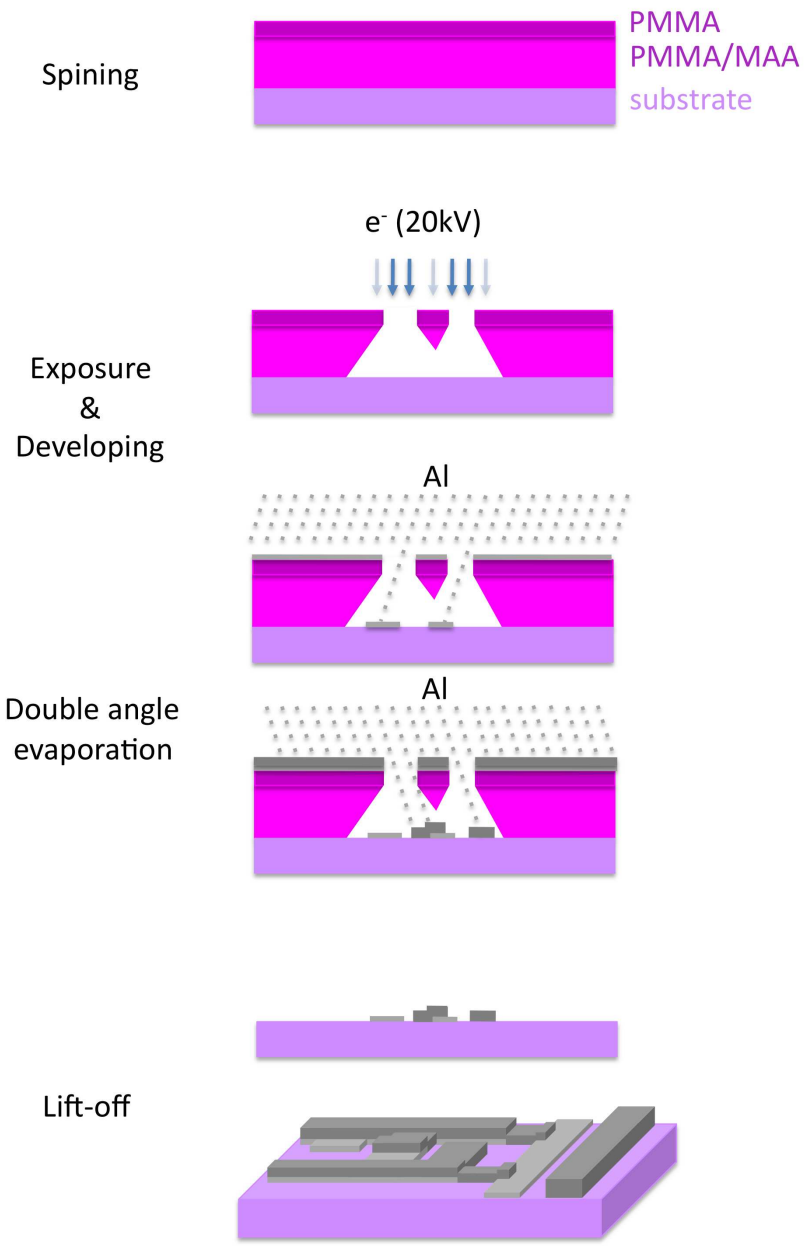

Fig. C.4. Electronic lithography process. PMMA-MMA and PMMA-MAA resist (pink) are spinned. Then specific part are exposed by steering on the desired pattern electrons. Aluminum is then evaporated a first time at a first angle, then aluminum is oxidized to form a thin layer of insulator, and a second layer of aluminum is deposited at a different angle. Finally the resist is removed. Overlapping layers form the Josephson junctions.

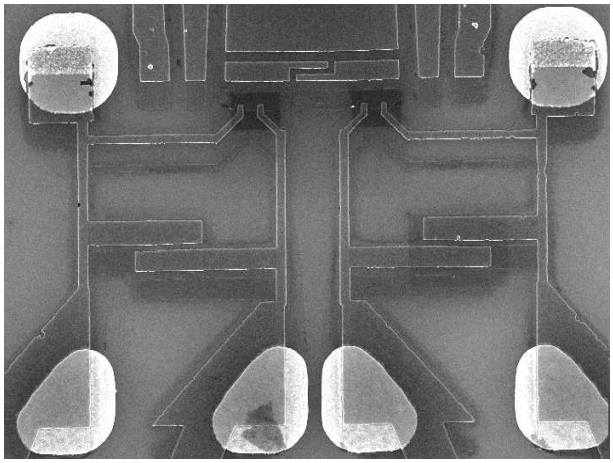

Fig. C.5. SEM image of central part of quantroswap circuit.

Josephson junctions fabrication

During the metal evaporation process, an oxidation step can be added in order to create a very thin (few Amgstrons) insulator layer between two overlapped layers. More precisely, the already deposited layer of Aluminum is oxidized at room temperature in the main chamber of the electron gun evaporator with a 15% O_2-85% Ar mixture at a pressure of about 20 mbar (static) during 20 min.

Alignment of e-beam lithography on the already deposited pattern

As our device fabrication processes imply several step of optical and electronic lithography. All the mask contain alignment cross. The precision of realignment between two optical lithography step, and between optical and electronic lithography is about 100-200 nm.

Annex D

Microfabricated microwave capacitance

We explain in this annex the two processes we have developed to fabricate microwave capacitors with high-dielectric constant materials. These capacitors are made of a floating Aluminum electrode either thermally and plasma oxidized, or covered with a sputtered Si3N4 layer, then overlapped by two other electrodes. The ensemble forms two capacitors in series.

D.1 Al/AlOx/Al capacitors fabrication

D.1.1 Al/AlOx/Al recipe

- 1st optical lithography according to C.1
- E-beam evaporation of a 40 nm thick aluminum layer at a rate of 1nm/s.
- Oxidation in the e-beam evaporator chamber: 15% O_2-85% Ar mixture at a pressure 20 mbar $\times$ 2 min at room temperature.
- Lift off in an ultrasonic bath of acetone during a few minutes.
- Rinse the wafer in ethanol.

- Plasma oxidation in a plasma cleaner.
  - Heat the wafer at 150 °C in vacuum $\times$ 4 min at an O_2 pressure of 12×10^{-3} mbar.
  - Transfer to the plasma chamber in about 15 s (the wafer is still hot).
  - Oxidize in an O_2 plasma at 0.2 mbar and a power of 50 W on about 75 cm^2 (self bias voltage = -540 V)

or

- Plasma oxidation in a Reactive Ion Etcher
  - Heat a massive sample holder between 170 and 200 °C in an oven.
  - Transfer this sample holder in a RIE, put the wafer on it, and pump down the chamber.
  - Oxidize in an O_2 plasma at 0.0112 mbar and a power of 260W on about 75 cm^2 (self bias voltage = -500V). Oxygen mass flow is 50 cm^3/min. The duration was varied between 10 s and 5 min.
- 2nd optical lithography according to C.1
- E-beam evaporation of a 40 nm thick aluminum layer at a rate of 1nm/s.
- Lift off in an ultrasonic bath of acetone during a few minutes.

D.1.2 Capacitor characteristics

Capacitance per unit area, DC leakage resistance, breakdown voltages, and fabrication yield were measured on large area test capacitors of about 1 mm^2 as a function of several process parameters.
Capacitance per unit area was measured using a RLC-meter (ISO-TECH 819) and a probe station at room temperature. When the substrate was semiconducting (for example Si), samples were also measured at 4K, in order to get rid of any contribution from the substrate. DC leakage resistance, and breakdown voltages were measured by ramping slowly a voltage source and measuring the current. The results are summarized in the table below.

Process	1	2	3	4
Size	1.1 mm^2	0.36 mm^2	0.36 mm^2	0.21 mm^2
Temperature	200°C	200°C	200°C	200°C
Duration	45 s	40 s	25 s	10 s
Capacitance	3 nF/mm^2	10 nF/mm^2	12 nF/mm^2	15 nF/mm^2
DC leakage	3 GΩ	1 GΩ	1 GΩ	few MΩ
Yield	>90%			50%

Unexpected problem with plasma oxidized capacitors

This fabrication process is based on the implantation of oxygen ions in the aluminum. As the process requires to heat the substrate at 200°C, it is difficult to protect the metal-free part of wafer with resist. Thus, the whole wafer is submitted to the oxygen plasma, and in the case of Si wafers, oxygen ions are implanted in the Silicon oxide (see Fig. D.1). Charge defects are created

and induce an electric field at the semiconductor-insulator border. A conductive region below $Si0_2$ is thus created. The scenario was first suggested to us by anomalous microwave losses in our quantroswap devices (experiment 4.1 in chapter 3). We have then validated it by fabricating test structures with two large non-overlapping electrodes whose coplanar capacitance was negligible. The measured capacitance between these electrodes could be interpreted only by a conducting layer below $Si0_2$ with conductance as high as about x mS/square at 4 °K.

D.2 SiN capacitor

An other way to create a capacitor is to deposit an insulator (Al0x, $Si0_2$ or Si_3N_4) on top of the first floating layer of Aluminum. In this project we have deposited Si_3N_4 with a reactive magnetron sputtering machine using the following recipe.

D.2.1 Magnetron sputtering recipe

- Si3N4 sputtering
  - Clean the wafer: alcohol + nitrogen
  - Pump down the chamber and heat the sample to 250 °C during 2 min.
  - Stabilize partial pressures of N_2 and Ar at 0.210^{-3} mbar and 0.810^{-3} mbar, respectively (mass flows are unknown in this process, and these pressures have been optimized empirically).
  - Set the plasma power to $450W$ (the area of the target is about x cm^2), and a pre-deposition during x s (the sample is behind a shutter during this step).
  - Make the deposition during 30 s. Self-bias voltage is equal to $-520V$, and deposition rate to 30 nm/min.
- Cool down the sample in nitrogen gas.

D.2.2 Capacitor characteristics

This process leads to a capacitance of 2.5nF/mm^2, which corresponds to a Si_3N_4 thickness of about 15nm calculated from the Si_3N_4 dielectric constant. This thickness was confirmed by a measurement with a spectral reflectometer (Filmetrics F20 [112]). The DC leakage resistance is about $10G\Omega$ up to $10V$ (for an overlapping area of about xx mm^2), and the breakdown voltage is more than $15V$.
We have also checked qualitatively that the dielectric losses in Si_3N_4 were not too large by sputtering it on top of an high quality-factor resonator ($Q = 10^5$), and by measuring that Q did not change.

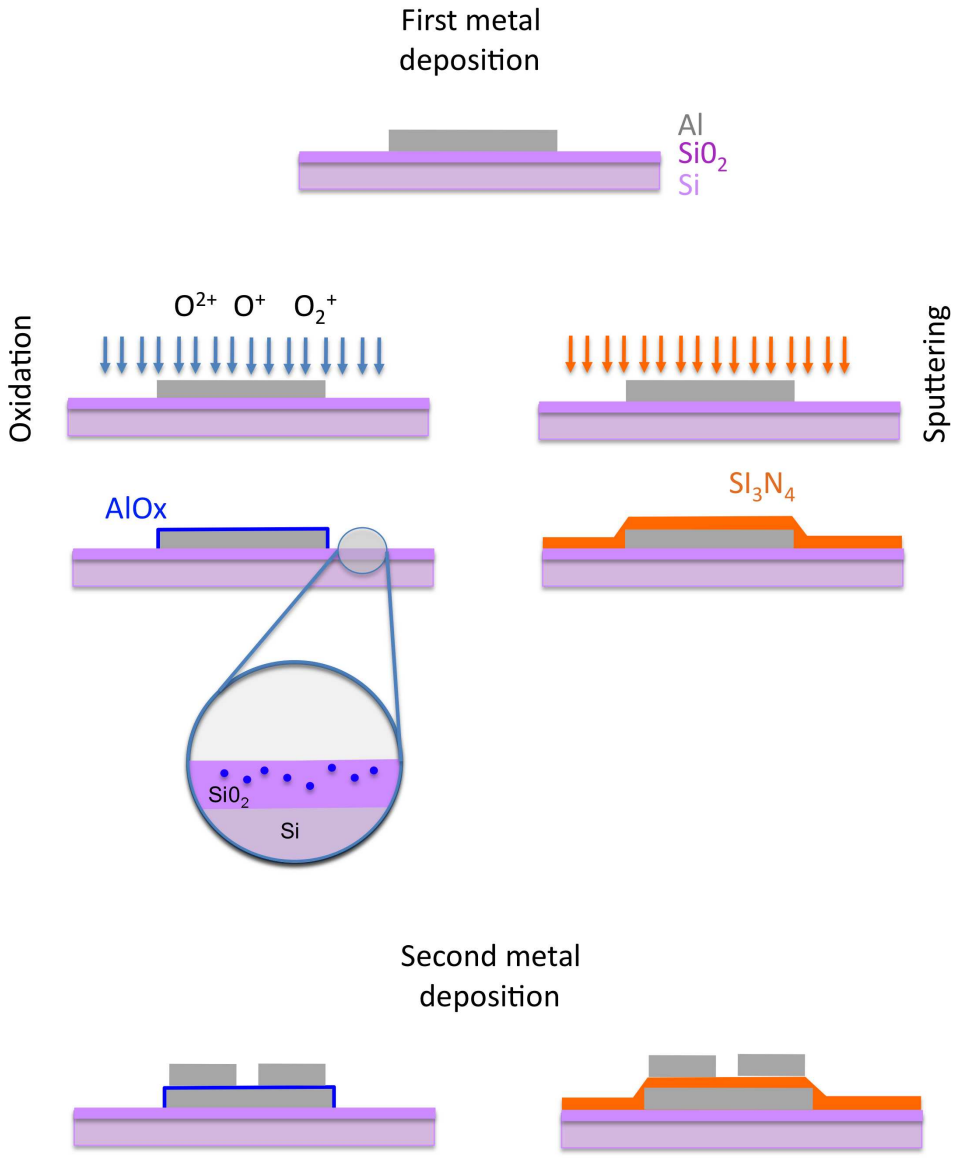

Fig. D.1. Fabrication steps of microwave capacitors made of a first floating electrode, either plasma oxidized (left) or covered with sputtered Si_3N_4 layer (right), and then covered by two overlapping electrodes. Process steps, materials, and chemicals species involved are indicated in the drawings. The circular inset on the left points out an unexpected technical problem encountered during fabrication (see text).

Annex E

Printed Circuit Board test

We explain in this annex how we have tested the printed circuit board (PCB) used for the quantroswap experiment of chapter 3.

Different tests have been made:

- Characterization of the spurious coupling between lines by measurement of the S parameters of a special PCB with no chip in the center.
- Characterization of the microwave lines of the normal PCB with a special chip with simple coplanar waveguides going through it (see Fig. E.2a).
- Test of the readout lines with their on-PCB surface mounted filters (see Fig. E.2b).

All the tests were done at 4 K. The last two were performed with a chip having two niobium coplanar waveguides, whose shapes are very similar to that of the gate lines (see Fig. E.1). However, these two waveguides are never closer than 200μm in the center of the chip (which is more than 10 times higher than the waveguide width).
Figure E.2 shows that spurious cross-transmission exists between these two lines. By comparing this transmission on PCBs having a ground plane or not, we were able to attribute this effect to resonances due to an imperfect impedance matching between the chip and the PCB.

without filters (blue),

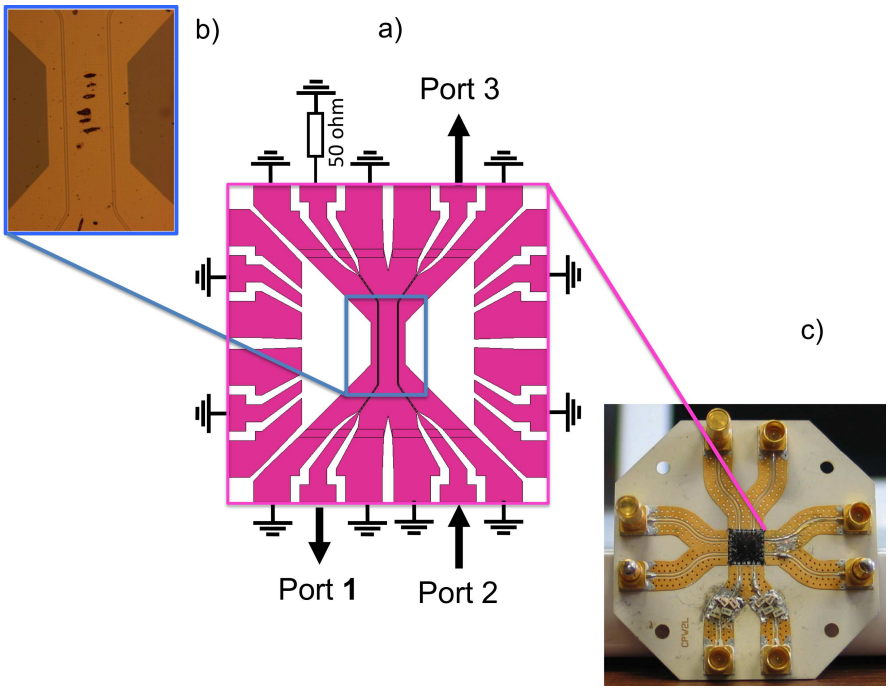

Fig. E.1. Geometry of the special chip used in the PCB characterization (quantroswap experiment). a) Drawing of the chip with its two 50Ω niobium microwave coplanar waveguides. Arrows indicates the different ports for the S parameters. b) Detailed optical micrograph of the central part. c) Overall view of the PCB with the surface mounted filters of the readout lines.

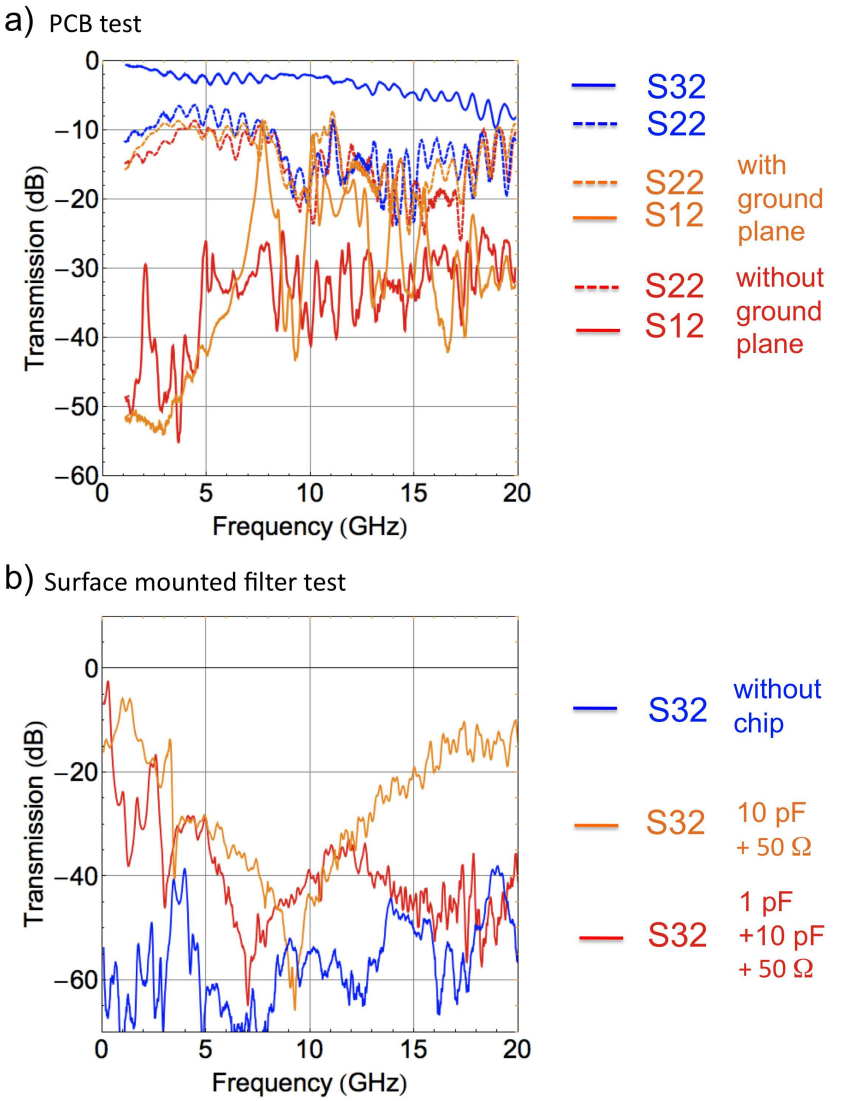

Fig. E.2. Microwave characterization at 4 K of the PCB used for the quantroswap experiment, using the special chip shown of Fig. E.1. The two panels show S_{ij} parameters, where ij refers to the port numbers defined in Fig. E.1. a) S parameters of the unfiltered microwave lines with and without a ground plane below the PCB. b) S parameters of the microwave lines supplied with the filters used for readout lines. Filter 1: 50 Ω in series + 10 pF to ground (orange); filter 2: 50 Ω in series + 1 pF + 10 pF to ground(red); no filtering as a reference (blue). Note that these results correspond to those expected from the datasheets of the Surface Mounted Capacitor.

Annex F

Microwave reflectometry

We present in this section a general method to calculate the coefficient of reflection of a linear or a non-linear oscillator submitted to a resonant or nearly resonant microwave excitation. The method is very similar to the one in [91].

F.1 Introduction to scattering matrix representation of electrical circuit

Let first introduce the notations and relations for describing the scattering matrix representation applied to electrical circuits.

F.1.1 Transmission line

Two points M and N are connected through a transmission line MN of length l_{MN} and characteristic impedance [1] Z equal to the impedances Z_{M} and Z_{N} of the two lines on the M and N sides (see Fig. F.1c). The potentials $V_{\mathrm{M,N}}$ and currents $i_{\mathrm{M,N}}$ at M and N obey the relation

$$\begin{aligned} V_{\mathrm{M}} &= (1 + r_{\mathrm{M}})V_{\mathrm{M}}^{+} \\ I_{\mathrm{M}} &= (1 - r_{\mathrm{M}})\frac{V_{\mathrm{M}}^{+}}{Z_{\mathrm{M}}} \end{aligned} \tag{F.1}$$

where $V_{\mathrm{M,N}}^{+,-}$ are the incoming and outgoing signal voltages, $r_{\mathrm{M,N}} = V_{\mathrm{M,N}}^{+}/V_{\mathrm{M,N}}^{-}$ are the reflexion coefficients, and

[1] The characteristic impedance is defined as the ratio $\sqrt{\mathcal{L}/\mathcal{C}}$, where $\mathcal{L}$ and $\mathcal{C}$ are the inductance and capacitance per unit length.

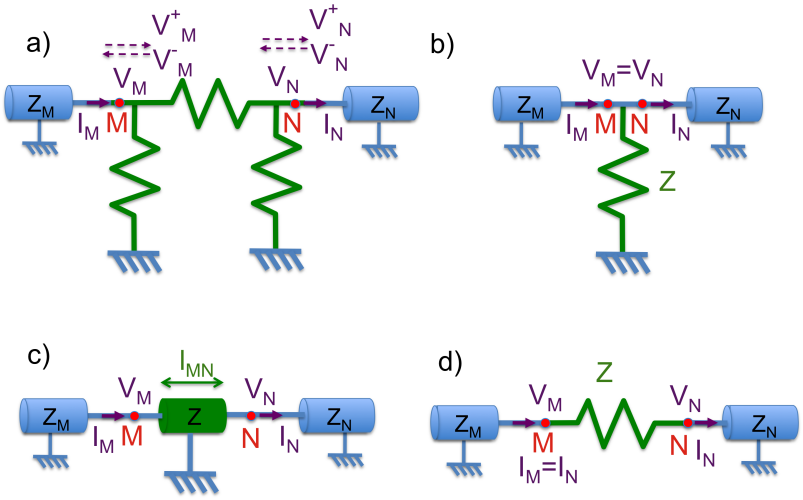

Fig. F.1. Schematic representation of circuits a) General representation of a electrical component (green) connected to two points M and N, and the associated voltages and currents. b) Case where the component is a discrete impedance Z connected to ground. c) Case where the element is transmission line of impedance Z and length l. d) Case where M and N are connected through a discrete impedance Z.

$$V_{\rm N} = (1 + r_{\rm N})V_{\rm N}^{+} = (e^{ikl_{\rm MN}} + r_{\rm M}e^{-ikl_{\rm MN}})V_{\rm M}^{+}$$
$$Z_{\rm MN}i_{\rm N} = (1 - r_{\rm N})V_{\rm N}^{+} = (e^{ikl_{\rm MN}} - r_{\rm M}e^{-ikl_{\rm MN}})V_{\rm M}^{+},$$

with k the wave vector. This gives a general relation between voltage and current at points M and N

$$\begin{bmatrix} V_{\rm N} \\ Z_{\rm N}i_{\rm N} \end{bmatrix} = \begin{bmatrix} \cos(kl_{\rm MN}) & i\ \sin(kl_{\rm MN}) \\ i\ \sin(kl_{\rm MN}) & \cos(kl_{\rm MN}) \end{bmatrix} \begin{bmatrix} V_{\rm M} \\ Z_{\rm M}i_{\rm M} \end{bmatrix}. \tag{F.2}$$

F.1.2 Discrete series impedance

The same relation can be determined when a discrete element of impedance $Z_{\rm MN}$ (capacitor or inductor) is inserted between M and N (see Fig. F.1d). One has

$$\begin{bmatrix} V_{\rm N} \\ Z_{\rm N}i_{\rm N} \end{bmatrix} = \begin{bmatrix} 1 & -Z/Z_{\rm M} \\ 0 & Z_{\rm N}/Z_{\rm M} \end{bmatrix} \begin{bmatrix} V_{\rm M} \\ Z_{\rm M}i_{\rm M} \end{bmatrix}. \tag{F.3}$$

In the case where the element is a Josephson junction, one has

$$\begin{aligned} V_{MN} &= V_J = \varphi_0 \dot{\gamma} \\ I_M &= I_N = i_J = I_0 \sin(\gamma) \end{aligned}$$

with I_0 the critical current and γ the superconducting phase between M and N. Considering a junction undergoing to microwave oscillations

$$\gamma = \gamma_a \cos(\omega_{rf} t),$$

the Jacobi-Anger relation gives

$$\sin(\gamma) = -2 \sum_{n \in \mathbb{N}^*} (-1)^n J_{2n-1}(\gamma_a) \cos[(2n-1)\omega_{rf} t]. \tag{F.4}$$

Thus, keeping only terms oscillating at frequency ω_{rf} (single frequency approximation),

$$\begin{aligned} i_J &= 2 I_0 J_1(\gamma_a) \cos(\omega_{rf} t) \\ &= \frac{2 J_1(\gamma_a)}{\gamma_a} \frac{1}{L_J} \varphi_0 \gamma \end{aligned}$$

with $L_J = \varphi_0 / I_0$. The derivative of the above expression gives

$$V_J = \frac{\gamma_a L_J}{2 J_1(\gamma_a)} \dot{i}_J \tag{F.5}$$

and thus an effective inductance for the Josephson junction

$$L_{J,eff}(\gamma_a) = \gamma_a L_J / (2 J_1(\gamma_a)). \tag{F.6}$$

F.1.3 Discrete impedance to ground

When the points M and N are equal and are connected to ground through a discrete element of impedance Z (see Fig. F.1b), one has

$$\begin{bmatrix} V_{\mathrm{N}} \\ Z_{\mathrm{N}} i_{\mathrm{N}} \end{bmatrix} = \begin{bmatrix} 1 & 0 \\ -Z_{\mathrm{N}}/Z & Z_{\mathrm{N}}/Z_{\mathrm{M}} \end{bmatrix} \begin{bmatrix} V_{\mathrm{M}} \\ Z_{\mathrm{M}}\ i_{\mathrm{M}} \end{bmatrix}. \tag{F.7}$$

F.1.4 Voltage source with internal impedance Z

When a voltage source with internal voltage V_0 is connected at one side of the previous circuit, and when its internal impedance Z matches the wave impedance of the line that connects it, one has, as shown on Fig. F.2, $V_0 = 2V_{\mathrm{in}}$, and

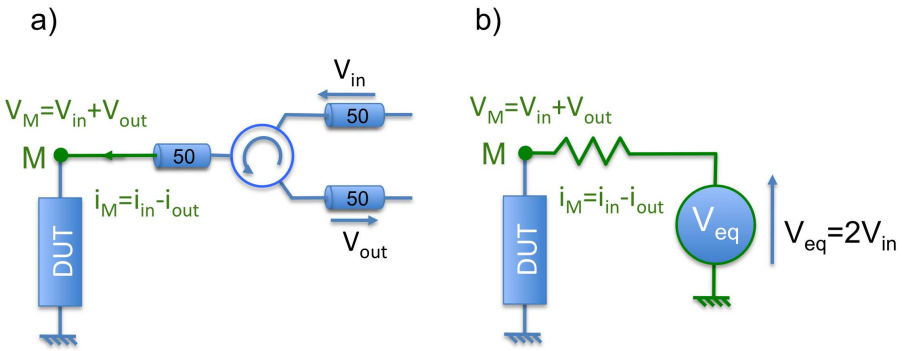

Fig. F.2. Schematic representation of circuit for microwave reflectometry measurement.

$$\begin{bmatrix} V_{\mathrm{M}} \\ Z i_{\mathrm{M}} \end{bmatrix} = \begin{bmatrix} V_{\mathrm{in}} + V_{\mathrm{out}} \\ V_{\mathrm{in}} - V_{\mathrm{out}} \end{bmatrix}, \tag{F.8}$$

where V_{in} and V_{out} are incident and reflected voltage at point M. One can then calculate the reflexion coefficient $r = V_{\mathrm{out}}/V_{\mathrm{in}}$.

F.2 Coefficient of reflexion of a Josephson oscillator

Using the expressions above within the single frequency approximation, one can calculate the reflexion coefficient of a Josephson oscillator (as the one used in the Blochonium experiment of chapter 5) made of a Josephson junction with inductance L_J in parallel with a capacitance C_r, both connected to ground (see Fig. F.3a). Equation (F.7) gives

$$\begin{bmatrix} 1+r \\ 0 \end{bmatrix} V_{\text{in}} = \begin{bmatrix} 1 & 0 \\ -Z_{\text{line}}/Z & 1 \end{bmatrix} \begin{bmatrix} 1+r \\ 1-r \end{bmatrix} V_{\text{in}}. \tag{F.9}$$

where $Z_{\text{line}} = 50$ and

$$\frac{1}{Z} = iC_r\omega_{rf} + \frac{1}{iL_{J,eff}(\gamma_a)\omega_{rf}}. \tag{F.10}$$

Using Eq. (F.5), one obtains

$$\frac{1-r}{1+r} = iRC_r\omega_{rf} + \frac{R}{iL_{J,eff}(\gamma_a)\omega_{rf}} = \frac{2}{1+r} - 1. \tag{F.11}$$

As the non-linearity is a function of $\gamma_a \propto (1+r)V_{\text{in}}$, it is convenient to rewrite this equation as a function of $1+r$, and more precisely as a function of $|1+r|$ by taking the moduli of left and right terms of the Eq. (F.11). This gives

$$\frac{4}{|1+r|^2} = 1 + \left[RC_r\omega_{rf} - R\frac{2J_1(\gamma_a)}{\gamma_a L_J \omega_{rf}} \right]^2 \tag{F.12}$$

or in reduced units,

$$\eta^2 = \frac{\Omega^2\gamma_a^2}{Q^2} + \left[\Omega^2\gamma_a - 2J_1(\gamma_a)\right]^2, \tag{F.13}$$

where $\Omega = \omega_{rf}/\omega_p$ is the reduced frequency, $\omega_p = 1/\sqrt{L_J C_r}$ is the plasma frequency, $Q = RC_r\omega_p$ is the quality factor, and $\eta = 2V_{\text{in}}/(RI_0)$ is the reduced drive amplitude. This expression is similar to the one in [17, p140]. Once, this equation is solved, one uses the solutions for γ_a in Eq. (F.11), and obtain the solutions for r.

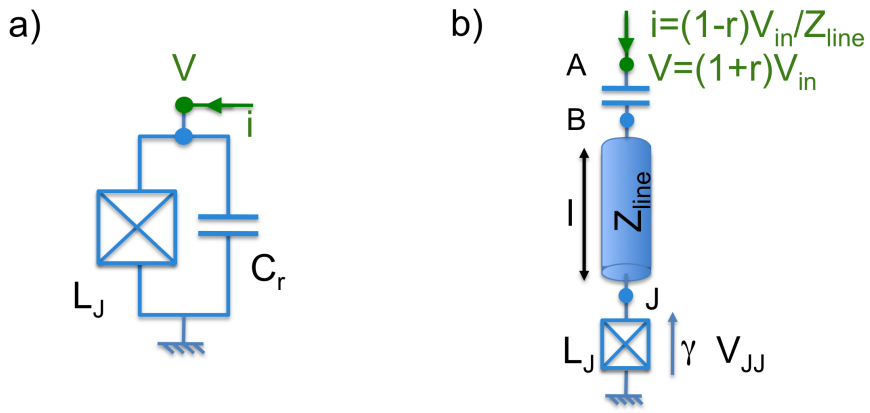

Fig. F.3. Schematic representation of a discrete Josephson oscillator (a) or of a non-linear distributed resonator (b) measured by microwave reflectometry.

F.3 Coefficient of reflexion of a non-linear distributed resonator

The same method can be applied to calculate the reflexion coefficient of a resonator of length l and characteristic impedance Z, whose one of the two sides is connected to a microwave line of impedance $Z_{\rm line}$ through a capacitance C_c and the other one is connected to ground through a josephson junction of critical current I_0 (see Fig. F.3 b).
Equation (F.7) gives

$$\begin{bmatrix} V_{JJ} \\ 0 \end{bmatrix} = \begin{bmatrix} 1 & 0 \\ -Z/(i\omega_{rf} L_{J,eff}(\gamma_a)) & 1 \end{bmatrix} \begin{bmatrix} V_J \\ Z i_J \end{bmatrix} \tag{F.14}$$

with $V_{\rm J}$ and i_J the voltage and current across and through the junction.
Equation (F.2) gives

$$\begin{bmatrix} V_J \\ Z i_J \end{bmatrix} = \begin{bmatrix} \cos(kl) & i\ \sin(kl) \\ i\ \sin(kl) & \cos(kl) \end{bmatrix} \begin{bmatrix} V_{\rm B} \\ Z i_{\rm B} \end{bmatrix}. \tag{F.15}$$

Equation (F.3) yields

$$\begin{bmatrix} V_{\rm B} \\ Z i_{\rm B} \end{bmatrix} = \begin{bmatrix} 1 & -1/(iZ_{\rm line} C_c \omega_{rf}) \\ 0 & Z/Z_{\rm line} \end{bmatrix} \begin{bmatrix} V_{\rm A} \\ Z_{\rm line} i_{\rm A} \end{bmatrix} \tag{F.16}$$

with

$$\begin{bmatrix} V_{\mathrm{A}} \\ Z_{\mathrm{line}} i_{\mathrm{A}} \end{bmatrix} = \begin{bmatrix} 1+r \\ 1-r \end{bmatrix} V_{in}. \tag{F.17}$$

Combining the last three equations, one obtains a set of two equations that can be solved as a function of the two external parameter V_{in} and ω_{rf}:

$$\begin{bmatrix} 1 & 1 \\ 1 & -1 \end{bmatrix} \begin{bmatrix} 1 & 1/(iZ_{\mathrm{line}}C_c\omega_{rf}) \\ 0 & Z/Z_{\mathrm{line}} \end{bmatrix} \begin{bmatrix} \cos(kl) & -i\ \sin(kl) \\ -i\ \sin(kl) & \cos(kl) \end{bmatrix} \begin{bmatrix} V_J \\ Zi_J \end{bmatrix} = \begin{bmatrix} 1 \\ r \end{bmatrix} 2V_{in}.$$

By expanding this equation and replacing i_J by $V_J/(iL_{J,eff}(\gamma_a)\omega_{rf})$, one obtains the system

$$\left[Q + i\Omega + \alpha(i\Omega)^2\right]\cos(x) - i\left[(1+Q\alpha)i\Omega + (i\Omega)^2\right]\sin(x) = \frac{i\alpha\Omega 2V_{\mathrm{in}}}{V_J}$$
$$\left[Q - i\Omega + \alpha(i\Omega)^2\right]\cos(x) + i\left[(1+Q\alpha)(-i\Omega) + (i\Omega)^2\right]\sin(x) = r\frac{i\alpha\Omega 2V_{\mathrm{in}}}{V_J},$$

where $Z = Z_{\mathrm{line}}$, $\alpha(\gamma_a) = L_{J,eff}(\gamma_a)\omega_0/Z$, $Q = 1/(ZC_c\omega_0)$, $\Omega = \omega_{rf}/\omega_0$ and $x = kl = -\pi\Omega/2$.
Using notation $L_{\mathrm{eff}} = Z/\omega_0$ and $C_{\mathrm{eff}} = 1/Z\omega_0$, $\alpha(\gamma_a) = L_{J,eff}(\gamma_a)/L_{\mathrm{eff}}$ is the ratio between effective Josephson junction inductance and the effective inductance of the resonator. Note that the left terms of these equations are complex conjuguates, which means $|r| = 1$.
As $L_{J,eff}(\gamma_a) = \gamma_a L_J/(2J_1(\gamma_a)$ and $\omega_{rf}\varphi_0\gamma_a = |V_J|$, solving the first equation leads to V_J. In a second step, one can use these solutions in the second equation to calculate r.

F.4 Coefficient of reflexion of the non-linear cavity used in the transmon experiment

The same procedure can be applied to the non-linear cavity used for the transmon experiment of chapter 4. It consists in a cavity of length $l = \lambda_0/2 = c/(2\nu_0)$ (with ν_0 the resonance frequency of the first harmonic). One side of this cavity is connected to an external microwave line through a capacitance C_c. The impedance of the line is 50 Ω. A Josephson junction of critical current I_0 is inserted in the center of the cavity, i.e. at a distance $l/2$ of both cavity "walls".

Following the very same procedure as in the previous section, one obtains

$$\begin{bmatrix} 1 & 1 \\ 1 & -1 \end{bmatrix} \begin{bmatrix} 1 & Q/(i\Omega) \\ 0 & Z/Z_{\mathrm{line}} \end{bmatrix} \begin{bmatrix} \cos(kl) & -i\ \sin(kl) \\ -i\ \sin(kl) & \cos(kl) \end{bmatrix} \begin{bmatrix} i(\alpha\Omega + \tan(kl)^{-1}) \\ 1 \end{bmatrix} \frac{\varphi_0}{I_0 L_{J,eff}(\gamma_a)}\gamma = \begin{bmatrix} 1 \\ r \end{bmatrix} \eta$$

with $\eta = 2V_{\mathrm{in}}/(ZI_0)$. From this system of equations, one can calculate the amplitude γ_a of the oscillations (see Fig. F.5) and the phase Arg(r) of the

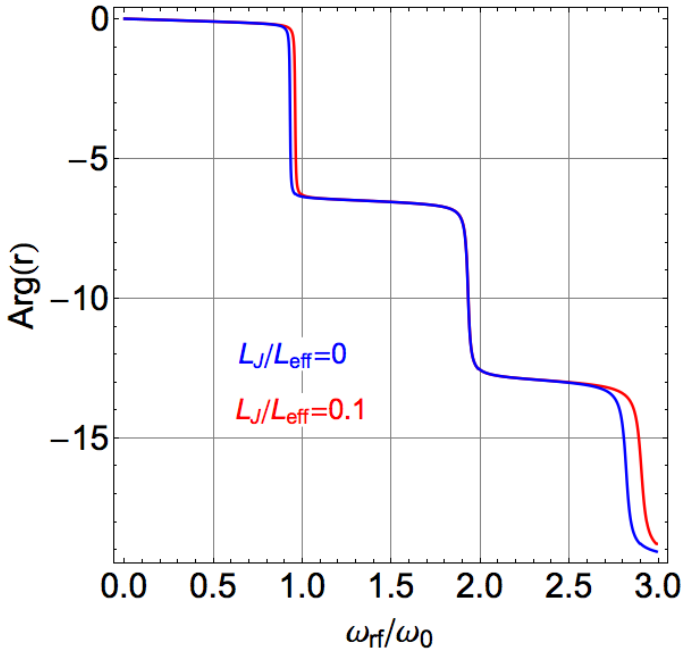

Fig. F.4. Calculated phases of the reflected signal in the linear regime as a function the drive frequency ω_{rf} for two value of the Josephson inductance inserted at the center of a $\lambda/2$ resonator. The resonance frequency of the second harmonic ($\omega_{rf} = 2\omega_0$) is not modified by the presence of the Josephson junction at the center of the resonator as this point corresponds to a node of the current for even harmonics of ω_0.

reflected signal in both the linear (see Fig. F.4) and the nonlinear regimes (see Fig. F.6).

valued

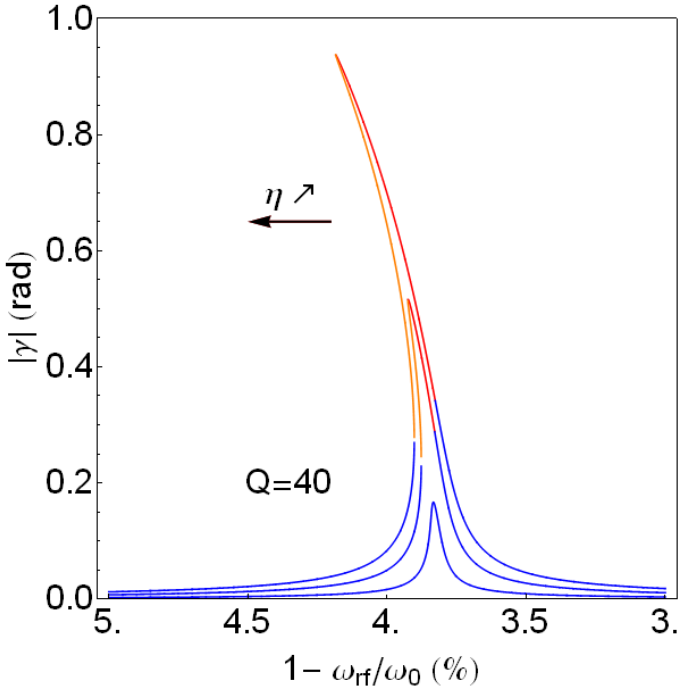

Fig. F.5. Calculated amplitudes γ_a, the superconducting phase across the junction inserted at the center of a $\lambda/2$ resonator as a function of the drive frequency ω_{rf} and for different drive amplitudes η. At low drive amplitude the resonance peak is lorentzian, whereas at large drive amplitude, multiples solutions appears corresponding to multistability regime of the oscillations. Orange curves are unstable solutions, whereas red and blue ones are stable. The curves join each others at points called bifurcation points (see chapter 4).

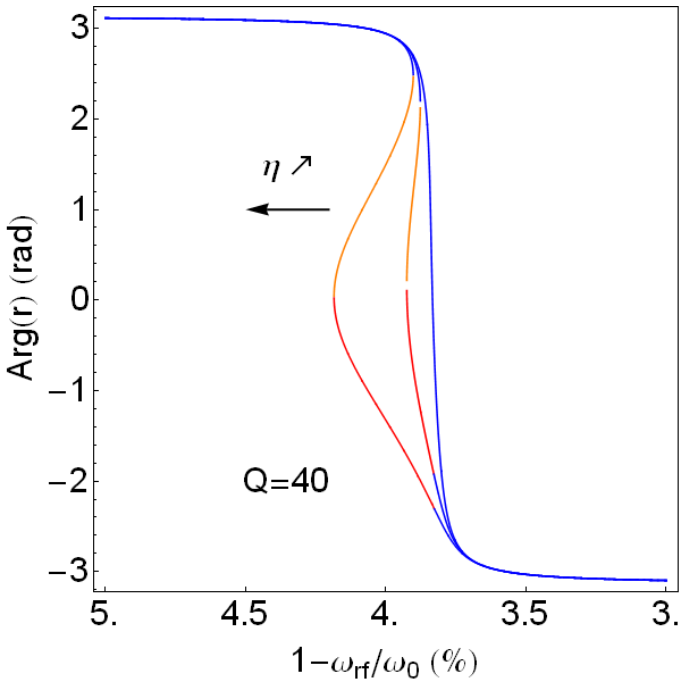

Fig. F.6. Calculated phase of the reflection coefficient r in the linear and non-linear regimes from the solutions γ_a plotted in Fig. F.5. The phase are multi-valued for certain values η and ω_{rf}.

Annex G

Quantronium qubits coupled to Two Level Systems

We present, in this section, complementary results obtained while measuring quantroswap samples.
We focus here on the coupling between qubits and spurious two level systems of unknown origin. The data presented here were obtained while performing spectroscopic measurements on sample QS 4.1.

Figure G.1 shows the switching probabilities of readout A and B as a function of the flux and of the microwave excitation frequency.
As in spectroscopic measurements presented in chapter 3, dark lines correspond to transition frequencies of the system made of the two qubits.
One notices first the avoided level crossings at different frequencies: 21.7 GHz and 19.5 GHz on qubit A (top), and 18.5 GHz and 17.5 GHz on qubit B (bottom). We attribute them to the coupling between the qubits and two level systems in their environment. The shape of the avoided crossings, and in particular the horizontal black lines, indicates that the resonance frequency of the TLSs does not depend on the flux. Moreover, the TLSs coupled to qubit A and to qubit B have different resonance frequencies ν_{TLS} and different coupling frequency $\nu_{cc,TLS}$, which indicates that the qubits are probably coupled to microscopic degrees of freedom. We have calculated the transition frequencies of the system using a model consisting in two coupled qubits and two TLSs, each of them being coupled to one qubit (see Fig. G.1). The fact that qubits are not coupled to the same TLS and the large values of the coupling frequencies between qubit and TLS (about 600 MHz - 800 MHz) indicate that the TLSs are localized in the vicinity of the qubit and are strongly coupled to the qubit. As a coupling frequency between two qubits in the 100 MHz range requires to have large island (few μm^2) and small gap between them (100 nm-

200 nm), we attribute the TLSs to defects localized in the oxide barrier of the Josephson junction, where the electric field is maximum. These observations are similar to the one obtained in phase qubit experiment [53, 113].

As in the case of coupling between two qubits, coupling between qubit and TLS induces a drastic reduction of the measurement signal. Indeed, for example in the case of $\mathrm{TLS}_{21.5\mathrm{GHz}}$, the readout ramp induces a energy swap between qubit and TLS, and makes spectroscopic peaks disappear (contrast is smaller) above 21.5 GHz. Below this frequency, the readout phase ramp amplitude ($+\ 0.3\ \Phi_0$) is large enough to induce two crossings during ramp : a first swap of the energy from qubit to TLS at $\delta/(2\pi) = -0.12$ and a second one from TLS to qubit at $\delta/(2\pi) = 0.08$, which makes the spectroscopic peaks reappears below 21.5 Ghz. For the other TLSs, the swap effect at readout is less important as the TLS-qubit coupling frequency is smaller.

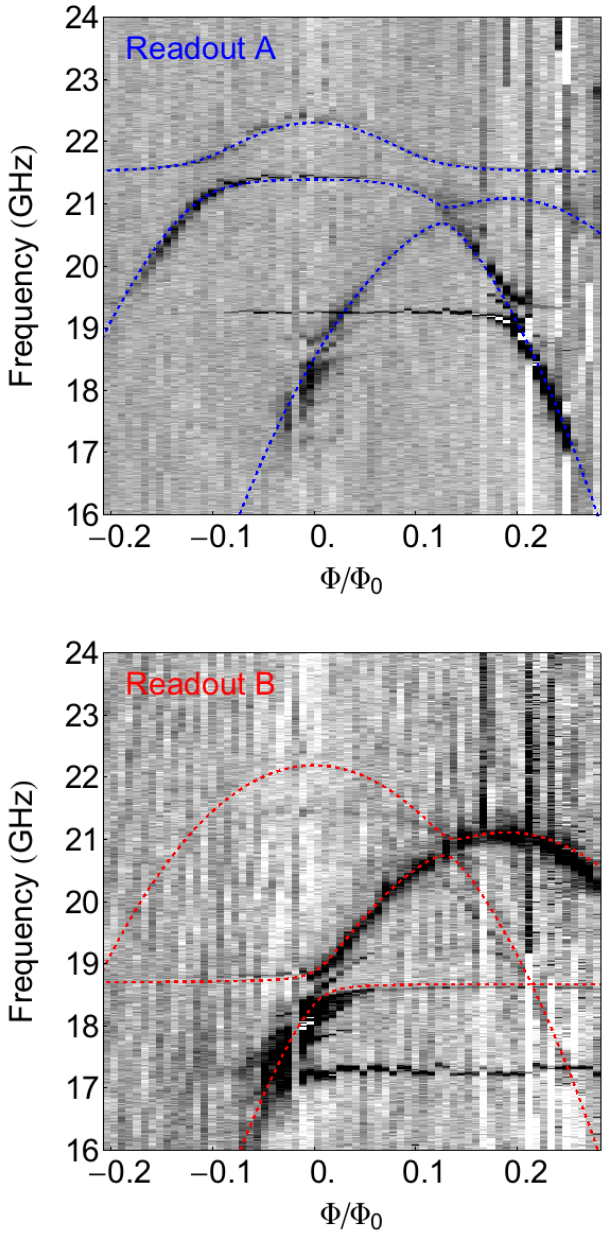

Fig. G.1. Spectroscopic measurements of the two qubits A (top) and B (bottom) of sample QS 4.1. Using a model consisting in two coupled qubits A and B, and two TLSs (note TLS,A and TLS,B) coupled to qubit A and B respectively, we plot the different transition frequencies of the system using parameters $E_{J_A} = 1.35 k_B$K, $E_{C_A} = 0.59 k_B$K, $E_{J_B} = 1.32 k_B$K, $E_{C_B} = 0.53 k_B$K, $\nu_{cc} = 0.15$ GHz, $\nu_{TLS,A} = 21.5$ GHz, $\nu_{cc,TLS,A} = 0.6$ GHz, $\nu_{TLS,B} = 18.7$ GHz, and $\nu_{cc,TLS,B} = 0.5$ GHz.

Quantum nondemolition readout using a Josephson bifurcation amplifier

N. Boulant,[1] G. Ithier,[1,*] P. Meeson,[1,*] F. Nguyen,[1] D. Vion,[1] D. Esteve,[1] I. Siddiqi,[2,†] R. Vijay,[2] C. Rigetti,[2] F. Pierre,[2,‡] and M. Devoret[2]

[1]*Quantronics Group, Service de Physique de l'Etat Condensé, CEA-Saclay, 91191 Gif-sur-Yvette, France*

[2]*Department of Applied Physics and Physics, Yale University, New Haven, Connecticut 06520-8284, USA*

(Received 4 April 2007; published 26 July 2007)

We report an experiment on the determination of the quantum nondemolition (QND) nature of a readout scheme of a quantum electrical circuit. The circuit is a superconducting quantum bit measured by microwave reflectometry using a Josephson bifurcation amplifier. We perform a series of two subsequent measurements, record their values and correlation, and quantify the QND character of this readout.

DOI: 10.1103/PhysRevB.76.014525 PACS number(s): 74.78.-w, 85.25.Cp, 85.25.Am, 03.65.Yz

I. INTRODUCTION

Performing repeated measurements on a single quantum object has become possible with the technological advances of the last 30 years. When the state of the system is destroyed by the measuring apparatus, the quantum object has to be prepared and measured in an identical manner a large number of times so that the ensemble description of the experiment is adequate.[1] It was while developing methods and techniques to detect gravitational waves with accuracy levels exceeding the standard quantum limits[1] that experiments with repeated measurements were first envisioned. It is within this context that the special kind of "quantum nondemolition" (QND) measurement was designed and first coined by Braginsky and Vorontsov in 1975.[2] A QND measurement is defined as a projective measurement where the output state of the measured quantum object is unaffected by subsequent measurements[1,3] and by its free evolution (see mathematical definitions in Sec. IV). When the state, however, is disturbed by the measuring apparatus or by other degrees of freedom during the measurement, one can still quantify the disturbance by measuring the QND "fractions"—i.e., the probabilities of leaving each possible projected state unaffected by the measurement.

Here we report an experiment on a quantum electrical circuit, the quantronium,[4] where the QND fraction left by the readout apparatus—namely, the Josephson bifurcation amplifier (JBA),[5] coupled to a split Cooper pair box—was measured. We first start with a review of the quantronium and its different components. Second, we describe the JBA measurement principles and motivate its QND aspect. We then describe the experimental setup and present the experimental results. Our data and model provide lower bounds on the QND fractions of the JBA in this particular setup.

II. QUANTRONIUM CIRCUIT

The basic element of the quantronium circuit is a split Cooper pair box (Fig. 1). It consists of a low-capacitance superconducting electrode, called the island, connected to a superconducting reservoir by two parallel Josephson junctions with capacitances $C_j/2$ and Josephson energies $E_J(1\pm d)/2$, where d is the asymmetry factor quantifying the difference between the two junctions $(0\leqslant d\leqslant 1)$,[4,6] $E_J=\varphi_0 I_0$, I_0 is the sum of the critical currents of the junctions, and $\varphi_0=\hbar/2e$ is the reduced flux quantum. The island is biased by a voltage source V_{g0} in series with a gate capacitance C_g. The second energy scale of the box is the Coulomb energy $E_{CP}=(2e)^2/2(C_g+C_j)$. For readout purposes, a larger Josephson junction is inserted in the superconducting loop formed by the island, the two junctions, and the reservoir. The quantronium qubit is then described by the Hamiltonian

$$H=E_{CP}(\hat{N}-N_g)^2-E_j\left(\cos\frac{\delta}{2}\cos\hat{\theta}-d\sin\frac{\delta}{2}\sin\hat{\theta}\right), \quad (1)$$

where $\hat{N}$ is the operator associated with the number of excess Cooper pairs in the island, $N_g=C_gV_{g0}/2e$ is the reduced gate charge, $\hat{\theta}$ is the superconducting phase operator ("conjugate" to $\hat{N}$—i.e., $[\hat{\theta},\hat{N}]=i$), and δ is the superconducting phase

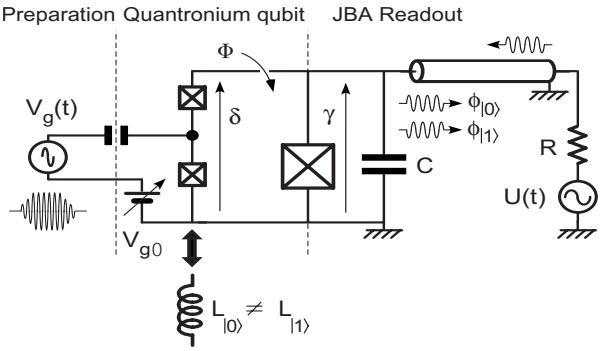

FIG. 1. Quantronium circuit with preparation and readout ports. The qubit consists of two Josephson junctions delimiting an island (black node) and inserted in a superconducting loop. Its eigenstates are tuned using the dc gate voltage V_{g0} and the magnetic flux Φ through the loop. Resonant microwave pulses $V_g(t)$ are applied to the gate to manipulate the qubit state. A larger junction and a shunt capacitor C forming an anharmonic oscillator are inserted in the loop for readout. A microwave readout pulse is sent to the system by a microwave generator with internal impedance $R=50\ \Omega$. The state-dependent inductive behavior of the qubit affects the plasma resonance of the oscillator and modifies the phase ϕ of the microwave readout pulse reflected by the system. In the case of large driving amplitudes, the dynamics of the superconducting phase γ across the readout junction can bifurcate between two distinct dynamical states, leading to a jump of ϕ.

across the series combination of the two small junctions. Hence this Hamiltonian can be tuned using the N_g and δ control knobs (considered as classical parameters for most applications of interest). For most values of (N_g, δ), the Hamiltonian has a strongly anharmonic energy spectrum, allowing a qubit—i.e., a quantum two-level system—to be encoded into the first two energy levels.[4,6] In addition, by symmetry, the system possesses in this parameter space points where $\partial\nu_{01}/\partial N_g = \partial\nu_{01}/\partial\delta = 0$. At these optimal working points, the qubit is immune to dephasing arising from fluctuations of N_g and δ, up to first order.[7]

III. JOSEPHSON BIFURCATION AMPLIFIER READOUT

To implement a QND readout, we use a dispersive method based on the reflection of a microwave pulse on the parallel combination of the qubit with a nonlinear oscillator made of the readout Josephson junction and an on-chip capacitance. This scheme is called the Josephson bifurcation amplifier[5] (see Fig. 1). Its operating principle relies on the fact that the dynamics of the phase γ across the readout junction depends on the total inductance of the circuit, itself dependent on the qubit state. The phases δ and γ are linked by the relation $\delta = \gamma + \Phi/\varphi_0$, where Φ is the flux threading the quantronium loop. When sending a microwave signal onto the circuit, the classical equation of motion of the phase across the readout junction, assuming the qubit remains in one of the instantaneous qubit eigenstates $|0(\delta(t))\rangle$ or $|1(\delta(t))\rangle$ (adiabatic limit[8]), is

$$RC\varphi_0\ddot{\gamma} + \varphi_0\dot{\gamma} + R\left(I_0 \sin\gamma + \frac{1}{\varphi_0}\frac{\partial E_{0,1}}{\partial\delta}\right) = U(t), \qquad (2)$$

where the reader can refer to Fig. 1 to identify the different variables and $E_{0,1}$ denote the energies for the ground and first excited states $|0\rangle$ and $|1\rangle$, respectively. In this paper, the circuit is operated only at $\Phi = 0$, which implies $\delta = \gamma$ and corresponds to an optimal point for $\gamma = 0$. Taylor-expanding eigenenergies to second order yields

$$\frac{\partial E_{0,1}}{\partial\delta} = \underbrace{\left.\frac{\partial E_{0,1}}{\partial\delta}\right|_0}_{=0} + \delta \left.\frac{\partial^2 E_{0,1}}{\partial\delta^2}\right|_0 = \delta(\varphi_0^2 L_{0,1}^{-1}), \qquad (3)$$

where $L_{0,1}$ denote the effective qubit inductances corresponding to the states $|0\rangle$ and $|1\rangle$. This scheme therefore constitutes a dispersive measurement in the sense that the second derivative of the energy with respect to δ is measured. For small excursions of the phase γ, the dynamics is the one of a damped harmonic oscillator. As the microwave power is increased, one enters the nonlinear regime of the oscillator. When the detuning of the microwave frequency with respect to the plasma frequency ω_p of the readout junction, $\Delta\omega = \omega_p - \omega$, is such that $\Delta\omega > (\sqrt{3}/2Q)\omega_p$ and when the drive current $U/R > I_B$, where I_B is the bifurcation current given in Ref. 9 and $Q = \omega_p RC$ is the quality factor of the readout junction, the resonator switches from a small-amplitude to a large-amplitude state, these two dynamical states having different phases ϕ of oscillation.[10] This phenomenon has a probabilistic nature in both quantum and thermal regimes. In our experiment, it occurs at the thermal to quantum crossover $k_B T = \hbar\omega_p$,[11] and the frequency and amplitude of the drive current can be tuned so that the system bifurcates with a high (low) probability when the qubit is in state $|1\rangle$ ($|0\rangle$). This bifurcation is detected by measuring the phase ϕ using homodyne demodulation. The method allows single-shot discrimination of the inductances $L_{0,1}$ and hence of the qubit states.

IV. QND CHARACTER OF THE JBA MEASURING THE QUANTRONIUM

When studying a measurement problem quantum mechanically, the total system is often conveniently described with the following Hamiltonian:[1,3,12]

$$H_{tot} = H_S + H_P + H_I, \qquad (4)$$

where H_S, H_P, and H_I are the system, the probe (the measuring apparatus), and their interaction Hamiltonians, respectively. When trying to measure an observable A_S, one should obviously have $\partial H_I/\partial A_S \neq 0$. The standard conditions to have a QND measurement are the following.[3]

(i) $[H_I, A_S] = 0 \Rightarrow$ there is no back action of the measuring device on the measured observable.

(ii) $[H_S, A_S] = 0 \Rightarrow$ a subsequent free evolution after the measurement leaves the projected state of the system unaffected.

After the projection of the first measurement, subsequent free evolutions and measurements always yield the same outcome. When $[H_S, H_I] \neq 0$, determining the basis into which the wave function collapses, the so-called pointer states basis,[12] can be a difficult task. Cucchietti *et al.* indeed show the rotation of that pointer basis with the relative strengths of the system and interaction Hamiltonians in the case of a central spin system coupled to a spin environment.[13] We now show, however, that for the JBA with a low-asymmetry factor d there is no ambiguity in the two-level approximation.

We now write the total Hamiltonian of the quantronium coupled to the readout junction under irradiation:

$$H_{tot} = E_{CP}(\hat{N} - N_g)^2 - E_J\left[\cos(\hat{\theta}) \otimes \cos\left(\frac{\hat{\delta}}{2}\right) - d\sin(\hat{\theta}) \otimes \sin\left(\frac{\hat{\delta}}{2}\right)\right] + \frac{\hat{Q}^2}{2C} - E_{J0}\cos(\hat{\delta}) - \frac{U(t)}{R}\varphi_0\hat{\delta}, \qquad (5)$$

where E_{J0} is the Josephson energy of the readout junction and $[\varphi_0\hat{\delta}, \hat{Q}] = i\hbar$. Note that the dissipation of the anharmonic oscillator was not included here for the sake of simplicity. The structure of H_{tot} should make the correspondence with Eq. (4) obvious. However, because the coupling between the system and the measuring apparatus is strong—i.e., $E_J \approx E_{CP}$—and because under no irradiation $\langle\cos(\hat{\delta}/2)\rangle \approx 1$, we recast the Hamiltonian as

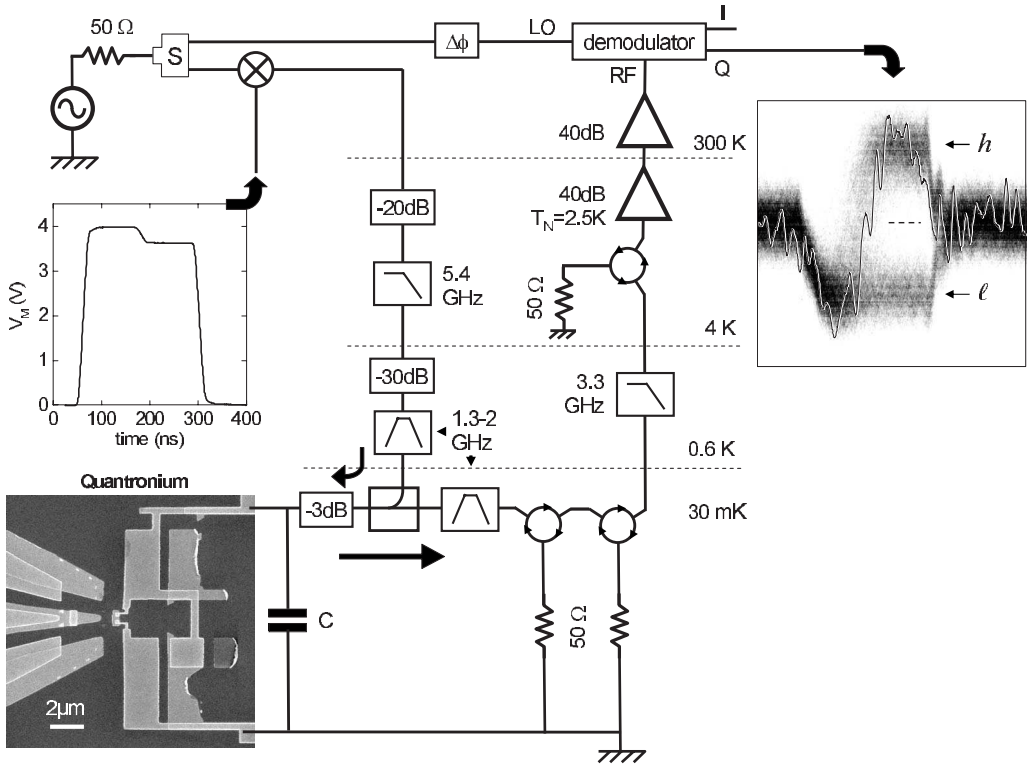

FIG. 2. Experimental setup of the JBA readout. The probing pulses come from the continuous microwave source mixed with a dc pulse $V_M(t)$ (middle left inset), consisting of a first plateau aimed at inducing the bifurcation or not and of a latching period for measuring the phase φ. The resulting microwave pulses propagate to the microfabricated circuit (bottom left SEM micrograph) along a filtered attenuated line and a directional coupler. The reflected pulse travels through the coupler and to the amplification stage via three cascaded circulators. Then it undergoes a homodyne demodulation; one of the quadratures is recorded with respect to time. The top right inset shows in gray levels thousands of superposed records, with one of them emphasized (shaded line). The observed quadrature either follows the envelope of the readout pulse when no bifurcation occurs (bottom traces, readout outcome $r=l$) or switches upwards in the opposite case (readout outcome $r=h$), corresponding to a phase jump. A threshold (dashed line) is used to count the switching events and deduce a switching probability.

$$H_{Tot} = \underbrace{E_{CP}(\hat{N}-N_g)^2 - E_J\cos(\hat{\theta})}_{\text{system Hamiltonian}} \underbrace{- E_J\left\{\cos(\hat{\theta})\otimes\left[\cos\left(\frac{\hat{\delta}}{2}\right)-1\right] - d\sin(\hat{\theta})\otimes\sin\left(\frac{\hat{\delta}}{2}\right)\right\}}_{\text{interaction Hamiltonian}} \underbrace{+\frac{\hat{Q}^2}{2C} - E_{J0}\cos(\hat{\delta}) - \frac{U(t)}{R}\varphi_0\hat{\delta}}_{\text{probe Hamiltonian}}. \tag{6}$$

To simplify our analysis, we now restrict ourselves to the first two energy eigenstates of the system, supposed to be biased at the optimum $N_g=1/2$. With this truncation, the Hamiltonian can be conveniently reexpressed as Eq. (4) with

$$H_S = -\frac{\hbar\omega_{01}}{2}\sigma_z,$$

$$H_I = -\left\{\alpha\sigma_z\otimes\left[\cos\left(\frac{\hat{\delta}}{2}\right)-1\right] - \beta\sigma_y\otimes\sin\left(\frac{\hat{\delta}}{2}\right)\right\},$$

$$H_P = \frac{\hat{Q}^2}{2C} - E_{J0}\cos(\hat{\delta}) - \frac{U(t)}{R}\varphi_0\hat{\delta}, \tag{7}$$

where $\sigma_{z,y}$ denote the Pauli spin matrices, $\alpha=E_J(\langle 0|\cos\hat{\theta}|0\rangle - \langle 1|\cos\hat{\theta}|1\rangle)/2$, and $\beta=idE_J(\langle 0|\sin\hat{\theta}|1\rangle - \langle 1|\sin\hat{\theta}|0\rangle)/2$. With $A_S=\sigma_z$, the QND conditions are fulfilled in the limit $d=0$. By symmetry, when d is not strictly equal to zero, we expect a correction to the QND fraction of order d^2.

V. MEASURING THE QND FRACTIONS

A. Experimental setup

The sample (see SEM inset of Fig. 2) was fabricated on an oxidized Si chip using standard double-angle evaporation and oxidation of aluminum through a shadow mask patterned by e-beam lithography. The sample was mounted on the cold plate of a dilution refrigerator and wired as indicated in Fig. 2. The JBA setup used at CEA is similar to the one described in Ref. 5. The plasma frequency of the sample was lowered in the 1–2 GHz bandwidth by adding an on chip capacitor equal to 33 pF in parallel with the junction. It is then easier to control the macroscopic electromagnetic environment in this frequency range than at higher frequencies. Furthermore,

the thermal population of the resonator is still negligible ($\hbar\omega_p/k_BT=3$). For generating and demodulating the microwave pulses, the output of a microwave generator is split into two channels. One of the channels is used for the homodyne detection of the reflected signal on the system, while the other one is mixed (using Minicircuit ZEM-4300MH mixers) with pulses coming from an arbitrary wave-form generator. The resulting microwave pulses are then sent to the microwave excitation line, which is strongly attenuated in order to use the full dynamical range of the microwave generator, and thus increase the signal-to-noise ratio at the level of the sample. At 30 mK, this line is coupled to the sample through a directionnal coupler (−16 dB coupling) via a 3-dB attenuator to avoid standing waves between the sample and the directional coupler. This main line is strongly filtered (bandwidth of 1.2–1.8 GHz) in order to avoid spurious excitation in the qubit by the external noise. After going through two circulators at 30 mK, the signal is amplified by a cryogenic amplifier (Quinstar L-1.5-30 H) with a noise temperature $T_N=2.2$ K at 1.5 GHz. A third circulator completes the total isolation of the line to 75 dB which provides a strong attenuation of the room-temperature noise in the bandwidth of interest. A second stage of amplification is required and is provided by an amplifier (Miteq AFS4) placed at room temperature. The amplified signal goes through a bandpass filter (K&L-5BT-1000/2000) centered at a tunable frequency and having a bandwidth of about 100 MHz in order to suppress the main part of the noise generated by the amplifier and which could saturate the demodulation card. This demodulation card (Analog Device AD8347) provides the in-phase and quadrature components of the reflected microwave with respect to the carrier reference. Demodulated signals showing no bifurcation (readout outcome $r=l$) or bifurcation (readout outcome $r=h$) are shown in Fig. 2.

The parameters of the sample, determined by electrical measurements and by spectroscopy of the qubit, were $E_{CP}=1.12$ K, $E_J=0.39$ K, $d\leqslant 0.1$, $E_{J0}=20.3$ K, and $C=33$ pF, which led to $\alpha\approx 0.2$ K, $\beta\leqslant 0.02$ K, and $\omega_{01}/2\pi\approx 8.1$ GHz. We have coherently manipulated the quantronium state, achieving 55%-contrast Rabi oscillations as opposed to 40% with the dc switching readout scheme previously used.[14,15] The discrepancy between the experimental contrast and the one expected theoretically [≈90% (Ref. 15)] can be partially attributed to spurious relaxation during the readout pulse. Indeed, the ac Stark shift of the qubit due to the applied microwave modifies the transition frequency and can make it cross electromagnetic resonances able to relax the qubit very efficiently.[5]

B. Experimental results

To measure the two QND fractions of the JBA, we prepared the states $|0\rangle$ and $|1\rangle$ in distinct experiments, then sent two successive nominally identical measurement pulses, recorded the switching events for both measurements, and extracted their correlations. The $|1\rangle$ state was prepared by applying a π pulse, whose power and duration were deduced from the analysis of Rabi oscillations, while the $|0\rangle$ state was simply obtained by letting the system relax to the ground state. The experiment schematics is provided in Fig. 3. The probabilities $p(|i\rangle, r_A, r_B)$ of the possible outcomes r_A and r_B ($r=l$ or $r=h$) for the two readouts A and B, starting from state $|i\rangle$ ($|0\rangle$ or $|1\rangle$) before readout, were measured over 2×10^4 events [see Fig. 3(c)]. If the readout discrimination between both qubit states was perfect, one could infer the QND fraction directly from the second answer r_B. The situation here, however, is a bit more complex due to the imperfect fidelity of the readout. We thus introduce the probabilities

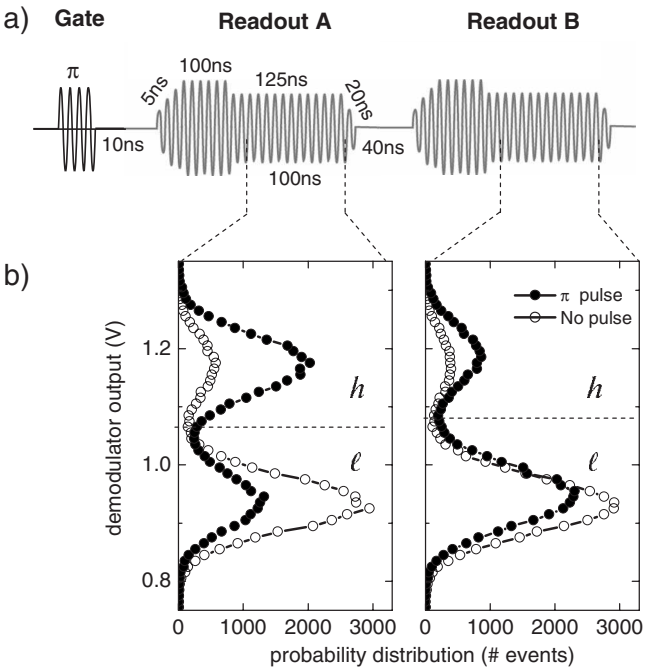

c)

Gate / state |i>	response r_A	response r_B	Probability $p(\|i\rangle, r_A, r_B)$
NO π pulse |0>	ℓ	ℓ	73 %
	ℓ	h	10 %
	h	ℓ	14 %
	h	h	3 %
π pulse |1>	ℓ	ℓ	30 %
	ℓ	h	9 %
	h	ℓ	42 %
	h	h	19 %

FIG. 3. Measurement of the QND fractions of the quantronium-JBA system. Panel (a): the qubit is prepared in state 1 (0) by applying a gate π pulse (no π pulse). Then two adjacent readout pulses A and B are applied. The two successive output quadrature voltages are averaged during the last 100 ns of the latching period of the pulses. Panel (b): bivalued histograms of the quadrature voltages (open symbols, no π pulse; solid symbols, π pulse). The top and bottom peaks correspond to bifurcation (readout $r=h$) and no bifurcation (readout $r=l$), respectively. A threshold (dashed horizontal line) leads to the determination of the bifurcation probabilities. Panel (c): the eight probabilities of getting two successive responses (r_A, r_B).

$$P^A(|i\rangle, r, |f\rangle) \tag{8}$$

for getting the response r at readout A starting from state $|i\rangle$ before and leaving the qubit in state $|f\rangle$ after. Like the data set p, the probability set P^A contains eight variables constrained by two normalization relations—i.e., six independent variables. We also introduce for both states the probability $P^{A,B}(|i\rangle, r)$ to obtain a given answer, whatever the final state. Although the pulses A and B are nominally identical, the switching rate is so sensitive to small changes of the microwave amplitude a of the readout pulses that it is necessary to introduce a small uncontrolled amplitude difference δa between both pulses. In order to deal with this complication, we have independently measured (data not shown) the derivative of the switching probabilities $\partial P^A(|i\rangle, r=h)/\partial a$, which allows us to evaluate the effect of a small amplitude change. Besides, direct observation of the microwave pulses with an oscilloscope provides an upper bound $|\delta a/a| < 0.5\%$ for such uncontrolled amplitude differences between the two readout pulses. The set of equations linking the probabilities introduced in the model is

$$p(|i\rangle, r_A, r_B) = \sum_{f=0,1} P^A(|i\rangle, r_A, |f\rangle) P^B(|f\rangle, r_B), \tag{9}$$

where

$$P^B(|f\rangle, r_B) = P^A(|f\rangle, r_B) + \partial P^A(|f\rangle, r_B)/\partial a \, \delta a. \tag{10}$$

The probabilities $P^A(|i\rangle, r_B)$ are readily obtained from Eq. (9) by summing over the possible outcomes of the second measurement:

$$P^A(|i\rangle, r_A) = \sum_{r_B=l,h} p(|i\rangle, r_A, r_B). \tag{11}$$

The system to solve is thus a linear system depending on the parameter δa. We find that it yields acceptable solutions—i.e., with positive values in the range $[0,1]$—only for $\delta a/a < -0.4\%$. Taking into account the upper bound already mentioned, $|\delta a/a| < 0.5\%$, and the error bars in the measured probabilities, we obtain the solution given in Fig. 4, which yields the following QND fractions for both qubit states:

$$q_1 = \sum_{r_A=l,h} P^A(|1\rangle, r_A, |1\rangle) = 34\,\% \pm 2\,\%, \tag{12}$$

$$q_0 = \sum_{r_A=l,h} P^A(|0\rangle, r_A, |0\rangle) = 100\,\% \,{}^{+0}_{-2}\,\%. \tag{13}$$

The large departure from perfect QND readout observed in this experiment cannot be attributed to the nonzero asymmetry factor $d < 0.1$, which would yield corrections of at most 1%. Besides, our results are to be compared with the ones obtained in similar JBA readout experiments performed on a quantronium at Yale [$q_0 = 100\%$, $q_1 = 55\% \pm 5\%$ (Ref. 16)] and on a flux-qubit at T.U. Delft [$q_0 = 100\%$ and $q_1 > 76\%$ (Ref. 17)]. The difference between the couplings of these two circuits to their environments may explain the differences observed for the QND character and for the readout fidelity. Although the theory in the two-level approximation predicts the JBA measurement to be a QND process, it is clear that during the measurement itself, other environmental

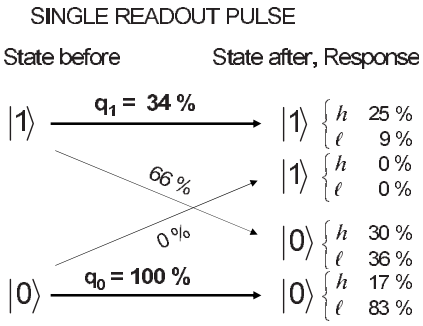

FIG. 4. Readout outputs and qubit state evolution in a measurement by a single readout pulse. The kets $|\psi=0,1\rangle$ indicate the qubit state before (left) and after (right) the measurement. The arrows and their associated probabilities correspond to the different possible qubit evolutions. The QND fractions are indicated in bold. The different readout responses for each different scenario are indicated on the right with their probabilities.

degrees of freedom interact with the system and cause it to relax, thus reducing the contrast of the Rabi oscillations.[7] As a consequence, all we can directly characterize is the combined action of the measurement itself and the environment on the qubit. Whether the JBA scheme itself is fully QND or not can be eventually inferred using additional independent relaxation time, T_1, measurements. Using the T_1 value at the optimal point, one can estimate the QND fraction, correcting for the relaxation that would occur if no readout pulse was applied—i.e., for $\delta=0$. The zeroth-order loss being $1-\exp(-t/T_1)=0.20$, with $T_1=1.3$ μs, the corrected QND fraction for state $|1\rangle$ is thus $54\% \pm 2\%$. However, this value must be considered with caution since there is no proof that relaxation during the readout pulse is the same as during free evolution. Indeed, one should bear in mind that T_1 greatly depends on the spectral density of the available states for qubit decay. This density can vary significantly with the qubit frequency,[7] which is changed by the Stark shift due to the ac excitation.[9]

VI. CONCLUSION

We have analyzed and characterized the quantum nondemolition aspect of the JBA readout scheme for the quantronium. For vanishing asymmetry, in the two-level approximation, the theory predicts a QND measurement. We have carried out an experiment consisting of preparing two orthogonal qubit states and then sending a series of two subsequent measurement pulses in order to measure both outcomes and their correlation. Using our model and data, we were able to obtain bounds on the QND fractions of this measurement scheme. The results obtained show that the QND character of the JBA readout of the quantronium is less perfect than expected, but the reasons for this discrepancy are not understood presently. Additional measurements of the T_1 dependence on the control parameters and a better control of the measurement pulse shapes in our experimental setup should lead to a more precise estimation of the QND fractions and of the parameters that affect it.

ACKNOWLEDGMENTS

This work was supported by the European projects Eurosqip and RSFQubit. We thank A. Lupascu for valuable discussions and P. Sénat, P. F. Orfila, and J. C. Tack for technical help. This work was also supported by NSA through ARO Grant No. W911NF-05-1-0365, the Keck Foundation, and the NSF through Grant No. DMR-0325580.

*Current address: Royal Holloway, Department of Physics, Egham, Surrey, TW20 0EX, UK.

†Present address: Department of Physics, U.C. Berkeley, 94720 California, USA.

‡Present address: LPN, Route de Nozay, 91460 Marcoussis, France.

[1] V. B. Braginsky and F. Ya. Khalili, *Quantum Measurement* (Cambridge University Press, Cambridge, England, 1992).

[2] V. B. Braginsky and Yu I. Vorontsov, Sov. Phys. Usp. **17**, 644 (1975).

[3] M. O. Scully and M. S. Zubairy, *Quantum Optics* (Cambridge University Press, Cambridge, England, 1997).

[4] D. Vion, A. Aassime, A. Cottet, P. Joyez, H. Pothier, C. Urbina, D. Esteve, and M. H. Devoret, Science **296**, 886 (2002).

[5] I. Siddiqi, R. Vijay, F. Pierre, C. M. Wilson, M. Metcalfe, C. Rigetti, L. Frunzio, and M. H. Devoret, Phys. Rev. Lett. **93**, 207002 (2004); I. Siddiqi, R. Vijay, M. Metcalfe, E. Boaknin, L. Frunzio, R. J. Schoelkopf, and M. H. Devoret, Phys. Rev. B **73**, 054510 (2006).

[6] A. Cottet, Ph.D. thesis, Université Paris VI, 2002 [available at http://tel.ccsd.cnrs.fr (in English)].

[7] G. Ithier, E. Collin, P. Joyez, P. J. Meeson, D. Vion, D. Esteve, F. Chiarello, A. Shnirman, Y. Makhlin, J. Schriefl, and G. Schon, Phys. Rev. B **72**, 134519 (2005).

[8] This assumption is valid as long as the qubit transition frequency is large compared to the driving frequency, which is the case here.

[9] I. Siddiqi, R. Vijay, F. Pierre, C. M. Wilson, L. Frunzio, M. Metcalfe, C. Rigetti, and M. H. Devoret, arXiv:cond-mat/0507248 (unpublished).

[10] L. D. Landau and E. M. Lifchitz, *Mechanics* (Reed, Oxford, 1981).

[11] M. I. Dykman, Phys. Rev. E **75**, 011101 (2007).

[12] W. H. Zurek, Phys. Rev. D **24**, 1516 (1981); **26**, 1862 (1982).

[13] F. M. Cucchietti, J. P. Paz, and W. H. Zurek, Phys. Rev. A **72**, 052113 (2005).

[14] E. Collin, G. Ithier, A. Aassime, P. Joyez, D. Vion, and D. Esteve, Phys. Rev. Lett. **93**, 157005 (2004).

[15] G. Ithier, Ph.D. thesis, Université Paris VI, 2005 [available at http://tel.ccsd.cnrs.fr (in English)].

[16] R. Vijay (unpublished).

[17] A. Lupascu, S. Saito, T. Picot, P. C. de Groot, C. J. P. M. Harmans, and J. E. Mooij, Nat. Phys. **3**, 119 (2007).

Current to Frequency Conversion in a Josephson Circuit

F. Nguyen, N. Boulant, G. Ithier,* P. Bertet, H. Pothier, D. Vion, and D. Esteve†

Quantronics Group, Service de Physique de l'État Condensé (CNRS URA 2464), DSM/DRECAM/SPEC, CEA-Saclay, 91191 Gif-sur-Yvette, France

(Received 13 March 2007; published 1 November 2007)

The voltage oscillations which occur in an ideally current-biased Josephson junction were proposed to make a current standard for metrology. We demonstrate similar oscillations in a more complex Josephson circuit derived from the Cooper pair box: the quantronium. When a constant current I is injected in the gate capacitor of this device, oscillations develop at the frequency $f_B = I/2e$, with e the electron charge. We detect these oscillations through the sidebands induced at multiples of f_B in the spectrum of a microwave signal reflected on the circuit, up to currents I exceeding 100 pA. We discuss the potential interest of this current-to-frequency conversion experiment for metrology.

DOI: 10.1103/PhysRevLett.99.187005 PACS numbers: 74.50.+r, 74.25.Fy, 74.45.+c, 74.78.Na

Exploiting the quantum properties of a current-biased Josephson junction to make a current standard suitable for metrology was proposed by Averin, Zorin, and Likharev [1]. This system has a simple mechanical analog: the phase difference φ across the junction is equivalent to the position of a particle moving in the Josephson potential $-E_J \cos\varphi$, the voltage across the junction to the particle velocity, and the bias current I to an applied force. The dynamics of such a particle is well explained within the framework of the Bloch energy bands $\epsilon_i(p)$ formed by the eigenstates of the particle, with p its quasimomentum [2]. It was predicted, in particular, that the voltage across the junction (particle velocity) oscillates at the Bloch frequency $f_B = I/2e$ [1]. These Bloch oscillations, which provide a direct link between time and current units, would be of fundamental interest for electrical metrology. However, it is extremely difficult to current-bias a junction because it requires one to embed it in a circuit with a high impedance over a wide frequency range [3,4]. On the other hand, it is easy to force Bloch oscillations [5] by imposing the quasimomentum, that is the total bias charge Q delivered to the junction [1], by connecting it to a small gate capacitor C_g in series with a voltage source V_g, so that $Q = C_g V_g$. This scheme cannot impose a constant current, but can deliver alternatively two opposite values of the current $dQ/dt = \pm I$. In this Letter, we report experiments using this procedure and demonstrating oscillations at the Bloch frequency $f_B = I/2e$ in a Josephson circuit that allows their detection. Our setup, shown in Fig. 1(a), is based on a modified Cooper pair box [6], the quantronium [7]. We show how this new current-to-frequency conversion method exploits the quantum properties of the circuit. We also discuss its interest in metrology of electrical currents, for which electron pumping [8,9] and electron counting [10] have also been proposed.

The quantronium device [7,11] is a split Cooper pair box that forms a loop including also a probe junction. The box island with total capacitance C is defined by two small junctions having Josephson energies $E_J(1+d)/2$ and $E_J(1-d)/2$, d being an asymmetry coefficient. The superconducting phase $\hat{\theta}$ of this island, conjugated to the number $\hat{N}$ of extra Cooper pairs inside, forms the single degree of freedom of the box [12]. The third larger junction with critical current I_0, in parallel with an added on-chip capacitor C_a, forms a resonator with plasma frequency f_p in the 1–2 GHz range [13]. Since this frequency is always smaller than the box transition frequency, we treat the phase difference γ across the probe junction as a clas-

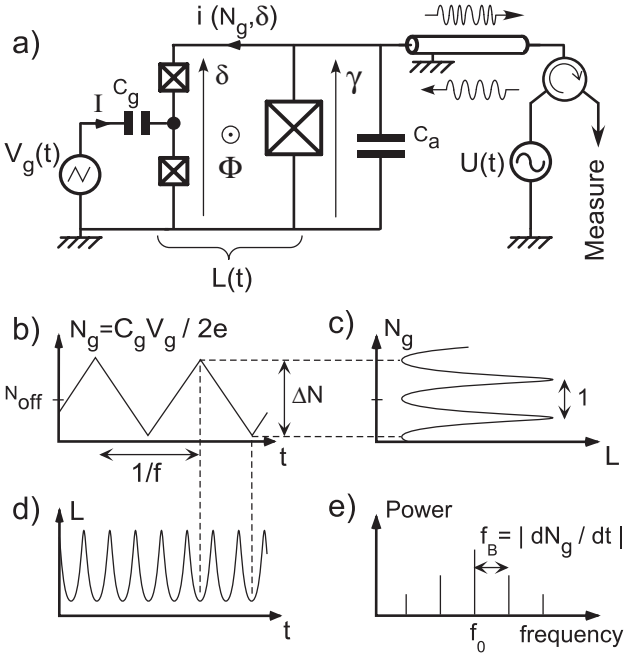

FIG. 1. Operating principle of the quantronium circuit for the production and detection of Bloch-like oscillations. The circuit (a) is a split Cooper pair box with a probe junction for the detection of the oscillations that develop when the gate charge is swept linearly. When the linear sweep is replaced by a triangular sweep (b) with extrema corresponding to symmetry points of the inductance modulation pattern (c), the time variations of the inductance (d) are the same as for a continuously increasing linear sweep. This modulation manifests itself as sidebands in the spectrum (e) of a microwave signal reflected onto the circuit.

sical variable. The same thus holds for the phase difference $\delta = \gamma + \phi/\varphi_0$ across the two box junctions in series, with ϕ the magnetic flux applied through the loop, and $\varphi_0 = \hbar/2e$. The control parameters of the split-box are δ and the reduced gate charge $N_g = C_g V_g/2e$, with C_g the island gate capacitance and V_g the gate voltage. The Hamiltonian of the box writes

$$\hat{H} = E_C(\hat{\mathbf{N}} - N_g)^2 - E_J \cos\frac{\delta}{2}\cos\hat{\boldsymbol{\theta}} + dE_J \sin\frac{\delta}{2}\sin\hat{\boldsymbol{\theta}}, \tag{1}$$

with $E_C = (2e)^2/2C$.

The eigenenergies $\epsilon_i(N_g, \delta)$ vary periodically with N_g (period 1) and δ (period 2π) [11]. The experiment consists in imposing a linear variation of the reduced quasimomentum N_g that induces a periodic evolution of the quantum state along the first Bloch band $\epsilon_0(N_g, \delta)$, at the Bloch frequency $f_B = dN_g/dt = I/2e$. Therefore, the current $i(N_g, \delta) = \varphi_0^{-1}\partial\epsilon_0(N_g, \delta)/\partial\delta$ through the two small junctions, the associated effective inductance for small phase excursions

$$L(N_g, \delta) = \varphi_0^2\left(\frac{\partial^2\epsilon_0(N_g, \delta)}{\partial\delta^2}\right)^{-1}, \tag{2}$$

and hence the admittance $Y(\omega) = j[C_a\omega - I_0/\varphi_0\omega - 1/L(N_g, \delta)\omega]$ as seen from the measuring line, vary periodically. We measure this admittance $Y(\omega)$ by microwave reflectometry, as for the rf-SET [14]. In our experiment, we apply a triangular modulation of the gate signal centered on $N_g = N_{\text{off}}$, with peak to peak amplitude ΔN, and with frequency f_g. Because of the symmetry properties of the quantum states with respect to N_g, the inductance varies as for a linear sweep, as shown in Fig. 1, provided that the extremal values of N_g are integer or half-integer, with a Bloch frequency $f_B = 2\Delta N f_g$. In order to obtain the largest gate-charge modulation of the inductance, the phase is adjusted at $\delta \approx \pi$ with the flux ϕ. When a small microwave signal at frequency f_0 is sent on the measuring line, the periodic modulation of the reflection factor yields sidebands in the spectrum of the reflected signal [14], shifted from the carrier by multiples of f_B, and called Bloch lines [15]. Because of the periodic excitation, the stationary outgoing amplitude can be written as a series:

$$v_{\text{out}}(t) = \sum_k v_k \exp[2i\pi(f_0 + kf_g)t]. \tag{3}$$

The circuit equations and the loop-current expression [7,11] allow to calculate all sideband amplitudes v_k, which get smaller and become asymmetric ($v_{-k} \neq v_k$) when the sideband frequencies depart from the resonance.

The sample was fabricated using electron-beam lithography [7,11] and aluminum deposition and oxidation. In order to avoid quasiparticle poisoning, the island was made thinner than the leads (13 and 42 nm, respectively), and gold quasiparticle traps were used [16]. In the present experiment, a sizeable asymmetry d was introduced on purpose in order to maintain a large gap $G_0 = \epsilon_1 - \epsilon_0$ at ($N_g = 1/2$, $\delta = \pi$), which avoids microwave driven transitions towards excited bands. The sample was placed in a sample holder fitted with microwave transmission lines, at a temperature $T \simeq 30$ mK. The gate was connected to a 250 MHz-bandwidth RF line. The microwave signal, after reflecting on the probe junction, went through 3 circulators before being amplified by a cryogenic amplifier with noise temperature $T_N = 2.2$ K, and a room temperature amplifier. The signal was then either demodulated with the cw input signal, or sent to a spectrum analyzer. In the latter case, the applied power was ≈ -132 dBm, corresponding to phase excursions smaller than ± 0.1 rad, and the total measurement gain was ≈ 88 dB. As a function of N_g and δ, the plasma resonance varied in the range 1.11–1.21 GHz, slightly below the circulator bandwidth, which yielded an extra attenuation of the signal due to a spurious interference with the leakage signal through circulator [17]. Fitting the variations of the resonance yielded $f_p = 1.19$ GHz, $Q \approx 17$, $E_C = 1.42 \pm 0.2 k_B K$, $E_J = 2.88 \pm 0.2 k_B K$, and $d = 0.15 \pm 0.03$ leading to $G_0 \approx 7hf_0$.

The reflected signal demodulated with the carrier is shown in Fig. 2 for a triangular gate voltage corresponding to $f_B = 8$ kHz. Because of noise, such time-domain measurements could only be performed within a 100 kHz bandwidth [18]. In the following, the reflectometry spectra are taken with a 1 Hz bandwidth resolution.

A series of spectra recorded at $f_0 = 1.14$ GHz with $f_g = 200$ Hz, and taken with progressively tuned gate sweep signal amplitude and offset, is shown in Fig. 3: when ΔN and N_{off} are tuned as sketched in Fig. 1, the spectrum consists only of Bloch lines, as predicted, with linewidth limited by the spectrum analyzer.

An example of comparison between the measured and predicted sideband amplitudes when N_{off} or ΔN is varied is shown in Fig. 4 for $f_g = 1$ kHz. The measured amplitudes are well accounted for by the solution of Eq. (3), but for the carrier, which suffers from the spurious interference effect

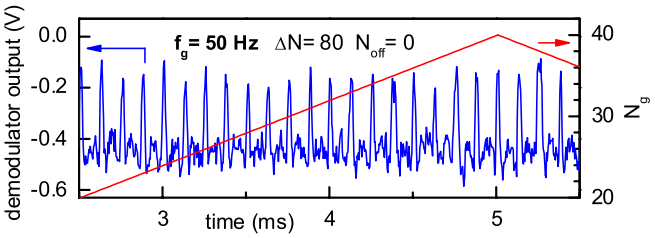

FIG. 2 (color online). Demodulated output signal (left scale) recorded with a 300 Hz—30 kHz bandwidth during a 3 ms time window, when a triangular wave voltage corresponding to a Bloch frequency $f_B = 8$ kHz is applied to the gate (right scale). Each period corresponds to the injection of one extra Cooper pair.

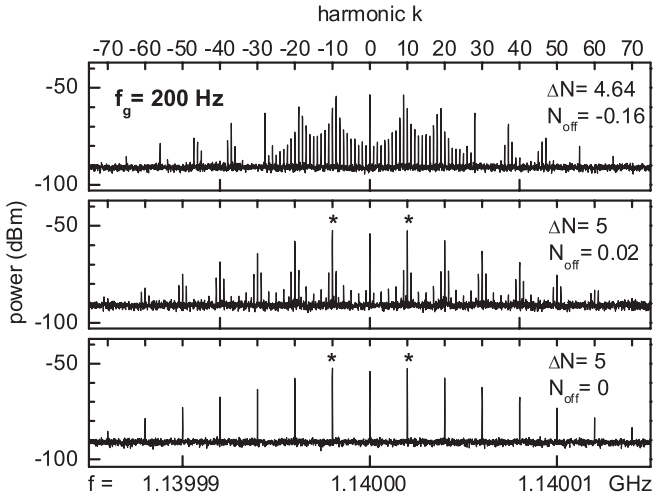

FIG. 3. Spectrum of a reflected cw signal at 1.14 GHz for different triangular wave gate modulation patterns, at frequency $f_g = 200$ Hz. The spectrum consists of sidebands shifted by kf_g from the carrier. Progressive tuning of the amplitude ΔN and of the offset N_{off} yields a spectrum consisting only of Bloch lines shifted from the carrier by a multiple of $f_B = 2\Delta N f_g$. The Bloch lines of order 1 ($k = \pm 2\Delta N$) are marked by an asterisk.

already mentioned [17]. Although the overall agreement for the sidebands, and, in particular, the cancellation of some of them at particular offsets and amplitudes, demonstrate the phase-coherence of the measured signal, it does not prove that the quantronium undergoes a perfect coherent adiabatic evolution of its ground state while N_g and δ are varied: incoherent excitation or deexcitation processes are for instance not excluded. Because of the opposed inductance modulation in the excited state, they would only reduce the amplitude of the Bloch lines in proportion of the time spent in this state.

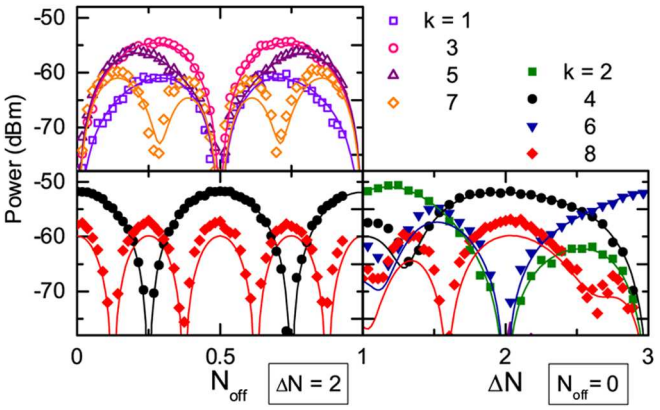

FIG. 4 (color online). Comparison of the measured (symbols) and calculated (lines) sideband amplitudes as a function of the sweep offset N_{off} and amplitude ΔN, for $f_g = 1$ kHz. Left panels: Offset dependence for $\Delta N = 2$; the observed sidebands correspond as predicted to odd multiples of f_g (top) and to the Bloch line $k = 4$ and its harmonics $k = 4n$, with period $1/(2n)$ in N_{off} (bottom). Right panel: ΔN amplitude dependence for $N_{\mathrm{off}} = 0$. The Bloch line corresponds to harmonic 4 at $\Delta N = 2$, and to harmonic 6 at $\Delta N = 3$. Calculated curves were shifted by 45 dB (estimated value was 44 dB) to best match the experimental Bloch line of order 1.

Spectra obtained at larger frequencies f_g and larger amplitudes ΔN, corresponding, respectively, to currents and Bloch frequencies $I = 32$ pA, $f_B = 100$ MHz, and $I = 130$ pA, $f_B = 408$ MHz, are shown in Fig. 5. These results demonstrate that Bloch oscillations persist at Bloch frequencies larger than the resonator bandwidth $f_p/Q \approx 70$ MHz, even though Bloch lines become weaker. The successful current-to-frequency conversion performed up to currents $I > 100$ pA using Bloch oscillations is the main result of this work. However, the amplitudes of the Bloch lines at these high frequencies are smaller than predicted by the model, and additional sidebands are present, which we attribute to the rounding of the gate triangular wave signal at its turning points, and to drifts of the gate-charge due to background charge noise. In principle, the theoretical maximum current is limited by two fundamental phenomena. First, the conversion mechanism requires $f_B \ll f_0$, with $f_0 \ll G_0/h$ to avoid multiphoton excitations. Second, the current must be low enough to avoid Zener transitions at $N_g = 1/2$ where the gap is minimum. For the present experiment, the Zener probability $p_Z = \exp(-\pi^2 G_0^2/hsf_B) \approx \exp(-13\ \mathrm{GHz}/f_B)$, with s the slope of $\epsilon_1(N_g) - \epsilon_0(N_g)$ away from $N_g = 1/2$, is negligible.

An important application of these experimental results could be to establish a direct link between a dc current and a frequency through the Bloch frequency $f_B = I/2e$, in order to close the triangle of quantum metrology [19]. Such an experiment would aim at measuring the current I_H

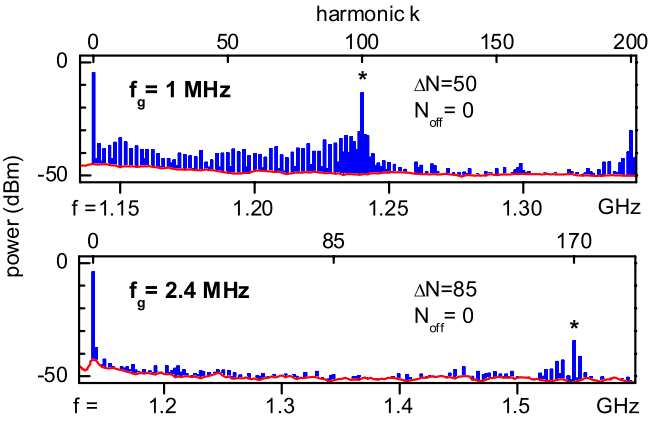

FIG. 5 (color online). Amplitude of the sidebands at positive harmonics (top scale) of the gate frequency f_g. Top panel: $\Delta N = 50$, $f_g = 1$ MHz ($I = 32$ pA, $f_B = 100$ MHz); bottom panel: $\Delta N = 85$, $f_g = 2.4$ MHz ($I = 130$ pA, $f_B = 408$ MHz). The Bloch line of order 1 is marked by an asterisk. The continuous line is the noise level. We attribute the presence of non-Bloch lines to the imperfections in the gate signal, and to charge noise.

passing through a Quantum Hall bar device in terms of a rate $\dot{N}_H$ of transferred Cooper pairs, in order to check the consistency of the Quantum Hall effect (QHE) with the ac Josephson effect. Using this latter effect, the Hall voltage $V_H = (h/e^2)I_H$ across a QHE bar can indeed be related to a frequency f_H through the relation $(h/e^2)I_H = (h/2e)f_H$. If the description of both QHE and Josephson experiments is exact, one predicts $\dot{N}_H = f_H/4$. A consistency check of this relation at the 10^{-8} level is presently a major goal in metrology because, in conjunction with a metrological realization of the mass unit by a Watt-balance experiment [20], it would provide a serious basis for a redetermination of the SI unit system in terms of electrical experiments involving only fundamental constants. The large current $I_H \approx 1\ \mu$A, needed for QHE experiments, can be transposed to a smaller range 0.1–1 nA using topologically defined transformers [21]. This current range, which is still beyond reach of single electron pumps [8] or of direct electron counting experiments [10], can be accessed with the sluice Cooper pair pump [9], with Bloch oscillations in a single Josephson junction [3], or with the method demonstrated here provided it can be used with a true dc current. In the last two cases, the impedance of the current source as seen from the single junction or from the box needs to be larger than $R_Q = h/4e^2$ to preserve single Cooper pair effects, and temporal fluctuations have to be small enough to obtain narrow Bloch lines enabling an accurate measurement of their frequency. Using for instance a resistive bias yields a Bloch linewidth of the order of the Bloch frequency [3], due to thermal fluctuations of the self-heated bias resistor. Developing a suitable current source for charge injection is thus a challenging prerequisite to metrology experiments based on Bloch physics. High impedance dissipative linear Josephson arrays have already been used to demonstrate indirectly Bloch oscillations [4]. Combining Ohmic, inductive, and Josephson elements, and possibly nonequilibrium cooling techniques [22], might provide an adequate low-noise high impedance.

In conclusion, we have demonstrated the conversion of a current $\pm I$ to a frequency $f_B = I/2e$ in a Josephson device biased through a small capacitor, through the production of ultra narrow sidebands in the spectrum of a reflected microwave signal. This new method, which reaches a current range $I > 0.1$ nA, would be extremely appealing for metrology if operated with a dc current.

We acknowledge discussions with M. Devoret, F. Piquemal, W. Poirier, N. Feltin, and within the Quantronics group, and technical support by P. Orfila and P. Senat. This work has been supported by the European project Eurosqip and by the C'nano grant 'signaux rapides'.

*Present address: Department of Physics, Royal Holloway, University of London, Egham, Surrey, TW20 OEX, UK
†Corresponding author: daniel.esteve@cea.fr

[1] D. V. Averin, A. B. Zorin, and K. K. Likharev, Sov. Phys. JETP **61**, 407 (1985); K. K. Likharev and A. B. Zorin, J. Low Temp. Phys. **59**, 347 (1985).
[2] F. Bloch, Z. Phys. **52**, 555 (1928).
[3] L. S. Kuzmin and D. B. Haviland, Phys. Rev. Lett. **67**, 2890 (1991); L. Kuzmin *et al.*, Physica B (Amsterdam) **203**, 376 (1994).
[4] S. Corlevi *et al.*, Phys. Rev. Lett. **97**, 096802 (2006).
[5] M. Büttiker, Phys. Rev. B **36**, 3548 (1987).
[6] V. Bouchiat *et al.*, Phys. Scr. **T76**, 165 (1998); Y. Nakamura, C. D. Chen, and J. S. Tsai, Phys. Rev. Lett. **79**, 2328 (1997).
[7] D. Vion *et al.*, Science **296**, 886 (2002); E. Collin *et al.*, Phys. Rev. Lett. **93**, 157005 (2004).
[8] M. W. Keller, J. M. Martinis, and R. L. Kautz, Phys. Rev. Lett. **80**, 4530 (1998); N. M. Zimmerman and M. W. Keller, Meas. Sci. Technol. **14**, 1237 (2003).
[9] J. J. Vartiainen *et al.*, Appl. Phys. Lett. **90**, 082102 (2007).
[10] J. Bylander, T. Duty, and P. Delsing, Nature (London) **434**, 361 (2005).
[11] A. Cottet, Ph.D. thesis, Université Paris VI, 2002, available at http://tel.ccsd.cnrs.fr (in English).
[12] In contrast to the case of a current-biased junction, the phase $\hat{\theta}$ is defined on a circle due to the quantization of $\hat{N}$.
[13] A related setup was reported recently in J. Könemann *et al.*, arXiv:cond-mat/0701144 [Phys. Rev. B (to be published)].
[14] R. J. Schoelkopf, Science **280**, 1238 (1998); A. Aassime *et al.*, Appl. Phys. Lett. **79**, 4031 (2001).
[15] N. Boulant *et al.*, *International Symposium on Mesoscopic Superconductivity and Spintronics 2006* (MS + S2006), edited by H. Takayanagi (World Scientific, Singapore, 2006).
[16] O. Naaman and J. Aumentado, Phys. Rev. B **73**, 172504 (2006); A. J. Ferguson *et al.*, Phys. Rev. Lett. **97**, 106603 (2006).
[17] The circulator leakage requested to explain our data varied from −7 dB to −23 dB over the plasma frequency excursion range, which is compatible with room temperature measurements.
[18] Note that a larger bandwidth was recently obtained in related electrometry setups [16].
[19] M. W. Keller *et al.*, Science **285**, 1706 (1999); F. Piquemal and G. Geneves, Metrologia **37**, 207 (2000); F. Delahaye and B. Jeckelmann, Metrologia **40**, 217 (2003).
[20] G. Geneves *et al.*, IEEE Trans. Instrum. Meas. **54**, 850 (2005).
[21] I. K. Harvey, Metrologia **12**, 47 (1976).
[22] O.-P. Saira *et al.*, Phys. Rev. Lett. **99**, 027203 (2007), and refs. therein.

J Low Temp Phys (2008) 151: 1034–1042
DOI 10.1007/s10909-008-9774-x

Tunable Resonators for Quantum Circuits

A. Palacios-Laloy · F. Nguyen · F. Mallet · P. Bertet · D. Vion · D. Esteve

Received: 26 November 2007 / Accepted: 6 December 2007 / Published online: 25 January 2008

Abstract We have designed, fabricated and measured high-Q $\lambda/2$ coplanar waveguide microwave resonators whose resonance frequency is made tunable with magnetic field by inserting a DC-SQUID array (including 1 or 7 SQUIDs) inside. Their tunability range is 30% of the zero field frequency. Their quality factor reaches up to 3×10^4. We present a model based on thermal fluctuations that accounts for the dependence of the quality factor with magnetic field.

Keywords Stripline resonators · Superconducting quantum devices · SQUIDs

PACS 74.78.-w · 84.40.Dc · 85.25.Am · 85.25.Dq

1 Introduction

On-chip high quality factor superconducting resonators have been extensively studied in the past years due to their potential interest for ultra-high sensitivity multi-pixel detection of radiation in the X-ray, optical and infrared domains [1–3]. They consist of a stripline waveguide of well-defined length, coupled to measuring lines through input and output capacitors. The TEM modes they sustain have quality factors defined by the coupling capacitors and reaching in the best cases the 10^6 range [3].

It has also been demonstrated recently [4] that superconducting resonators provide very interesting tools for superconducting quantum bit circuits [5–8]. Indeed, a resonator can be used to measure the quantum state of a qubit [4, 9–11]. Moreover, another resonator may serve as a quantum bus and mediate a coherent interaction between the qubits to which it is coupled. The use of resonators might thus lead to

A. Palacios-Laloy · F. Nguyen · F. Mallet · P. Bertet (✉) · D. Vion · D. Esteve
Quantronics Group, Service de Physique de l'Etat Condense (CNRS URA 2464),
DSM/DRECAM/SPEC, CEA-Saclay, 91191 Gif-sur-Yvette, France
e-mail: patrice.bertet@cea.fr

a scalable quantum computer architecture [9]. The coupling of two qubits mediated by a coplanar waveguide (CPW) resonator has already been demonstrated [12, 13]. In experiment [13], each qubit needs to be tuned in and out of resonance with the resonator for the coupling to be effective. Reference [14] proposed an alternative solution that consists in tuning the *resonator* in and out of resonance with each qubit. Here we report on the measurement of high quality factor resonators whose frequency can be tuned. Measurements similar to ours have been reported by other groups on lumped element [15] and distributed [16, 17] resonators.

2 Tunable Resonator with DC SQUID: Model

Our tunable resonators consist of $\lambda/2$ coplanar waveguides with an array of N DC-SQUIDs in series inserted in the middle of the central strip (see Fig. 1a). Each DC SQUID is a superconducting loop with self-inductance L_l intersected by two nominally identical Josephson junctions of critical current I_{c0}; the loop is threaded by a magnetic flux Φ. The SQUID array behaves as a lumped non-linear inductance that depends on Φ, which allows to tune the resonance frequency.

A CPW resonator without any SQUID consists of a transmission line of length l, capacitance and inductance per unit length $\mathcal{C}$ and $\mathcal{L}$, and characteristic impedance $Z_0 = \sqrt{\mathcal{L}/\mathcal{C}}$. We consider here only the first resonance mode that happens when $l = \lambda/2$ at a frequency $\omega_r = \pi/\sqrt{LC}$, where $L = \mathcal{L}l$ and $C = \mathcal{C}l$ are the total inductance and capacitance of the resonator. The quality factor Q results from the coupling of the resonator to the $R_0 = 50\,\Omega$ measurement lines through the input and output capacitors C_c, leading to

$$Q_c = \frac{\pi}{4Z_0 R_0 C_c^2 \omega_r^2}, \tag{1}$$

from internal losses (Q_{int}), and from possible inhomogeneous broadening mechanisms (Q_{inh}). These combined mechanisms yield

$$Q^{-1} = Q_c^{-1} + Q_{int}^{-1} + Q_{inh}^{-1}. \tag{2}$$

As shown in Fig. 2, we model a SQUID as a non-linear inductance $L_J(\Phi, i)$ that depends on Φ and on the current i passing through it, so that the voltage across the SQUID is

$$V = L_J(\Phi, i)\frac{di}{dt}. \tag{3}$$

All SQUID properties are periodic in Φ with a period $\Phi_0 = h/2e$, the superconducting flux quantum. Introducing the reduced flux quantum $\varphi_0 = \Phi_0/2\pi$, the SQUID frustration $f = \pi\Phi/\Phi_0$, the effective critical current $I_c(\Phi) = 2I_{c0}|\cos f|$ of the SQUID at zero loop inductance, and the parameter $\beta = L_l I_{c0}/\varphi_0$, our calculation of $L_J(\Phi, i)$ to first order in β and to second order in $i/I_c(\Phi)$ yields for $f \in]-\pi/2, \pi/2[$

$$L_J(\Phi, i) = L_{J0}(\Phi) + A(\Phi)i^2, \tag{4}$$

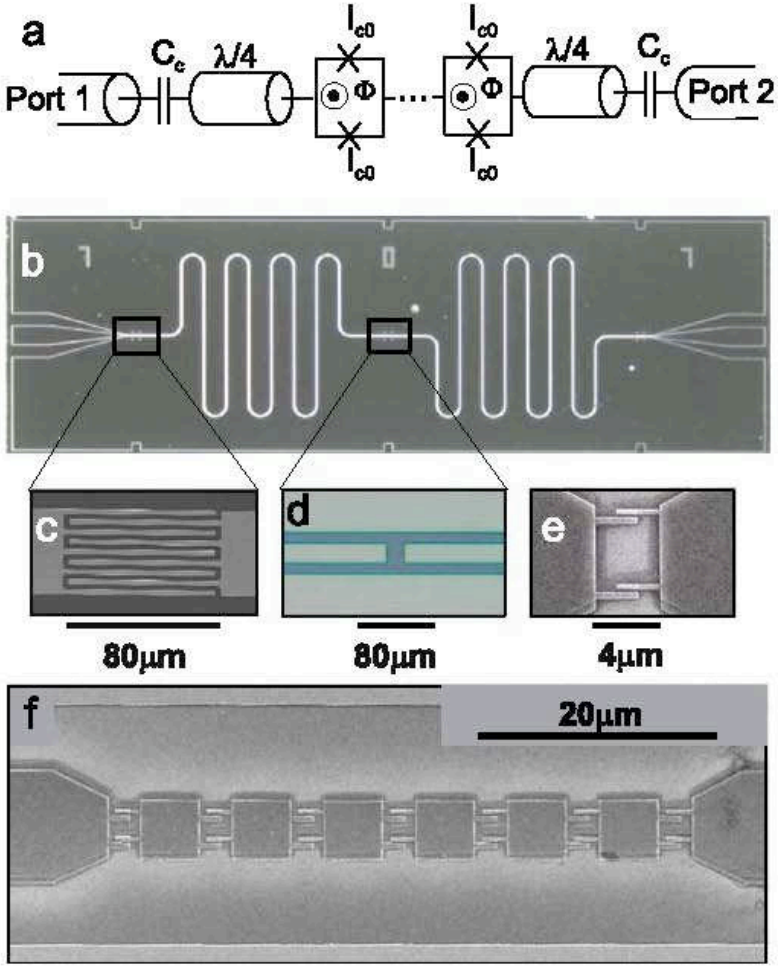

Fig. 1 (**a**) Tunable resonator scheme: a DC SQUID array is inserted between two $\lambda/4$ waveguides coupled to a 50 Ω measurement line through input and output capacitors C_c. (**b**) Optical micrograph of a CPW niobium resonator. (**c**) Typical coupling capacitor (design value: $C_c = 27$ fF). (**d**) Gap in the middle of the resonator, before SQUID patterning and deposition. (**e**) Electron micrograph of an aluminum SQUID (sample A), fabricated using electron-beam lithography and double-angle evaporation. (**f**) Electron micrograph of a 7-SQUID array (sample B)

with

$$L_{J0}(\Phi) = \frac{\varphi_0}{I_c(\Phi)}\left(1 + \beta\frac{\cos 2f}{2\cos f}\right), \tag{5}$$

$$A(\Phi) = \frac{\varphi_0}{2I_c^3(\Phi)}. \tag{6}$$

Equation (4) shows that the SQUID can be modelled as the series combination of a lumped inductance $L_{J0}(\Phi)$ and of a series non-linear inductance SNL(Φ) [18] (see Fig. 2).

In the linear regime $i \ll I_c(\Phi)$ corresponding to low intra-cavity powers, one can neglect the non-linear term in (4). The N-SQUID array then simply behaves as a lumped inductance $NL_{J0}(\Phi)$. The device works in that case as a tunable harmonic oscillator. Introducing the ratio $\varepsilon(\Phi) = L_{J0}(\Phi)/L$ between the total effective induc-

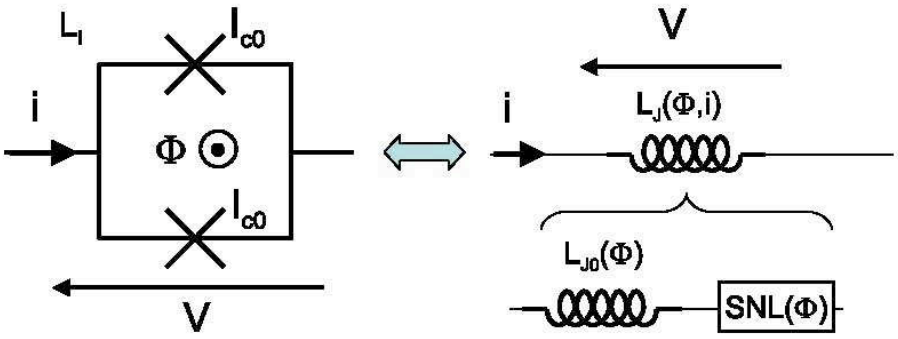

Fig. 2 A DC SQUID with two junctions of critical current I_{c0} and loop inductance L_l, biased by a magnetic flux Φ and by a current i, is equivalent to a lumped flux-dependent non-linear inductance $L_J(\Phi, i)$ that can be decomposed in an inductance $L_{J0}(\Phi)$ and a non-linear element SNL(Φ) in series

tance of the SQUID and the resonator inductance, the frequency and quality factor are

$$\omega_0(\Phi) = \omega_r \frac{1}{1 + N\varepsilon(\Phi)}, \tag{7}$$

$$Q_{ext}(\Phi) = Q_c[1 + 4N\varepsilon(\Phi)]. \tag{8}$$

At larger peak current in the resonator $i \lesssim I_c(\Phi)$, the non-linear element SNL(Φ) has to be taken into account. The equation of motion of the oscillator acquires a cubic term, similar to that of a Duffing oscillator [19]. This leads to a small additional shift of the resonance frequency $\delta\omega_0(E)$ proportional to the total electromagnetic energy E stored in the resonator. Retaining first order terms in $\varepsilon(\Phi)$, we find

$$\frac{\delta\omega_0(\Phi, E)}{\omega_0(\Phi)} = -N\left(\frac{2\omega_0(\Phi)}{\pi R_0[1 + 2N\varepsilon(\Phi)]}\right)^2 \frac{\varphi_0}{8I_c^3(\Phi)}E. \tag{9}$$

As shown by (7), a resonator including an array of N SQUIDs of critical current NI_{c0} has approximately the same resonant frequency and same tunability range as a resonator including one SQUID of critical current I_{c0}. However, an interesting advantage of using an array is to obtain a linear regime that extends to larger currents, allowing measurements at larger powers and therefore higher signal-to-noise ratios.

3 Sample Fabrication

The design and fabrication of our resonators closely followed Ref. [20]. The coupling capacitors were simulated using an electromagnetic solver. Test niobium resonators without any SQUIDs were first fabricated. They were patterned using optical lithography on a 200 nm thick niobium film sputtered on a high-resistivity ($> 1000\ \Omega$ cm) oxidized 2-inch silicon wafer. The niobium was etched away using either dry or wet etching. Dry etching was done in a plasma of pure SF_6 at a pressure of 0.3 mbar and at a power such that the self-bias voltage was 30 V and the etching rate 1.3 nm/s. We observed that adding oxygen to the plasma gave consistently lower quality factors.

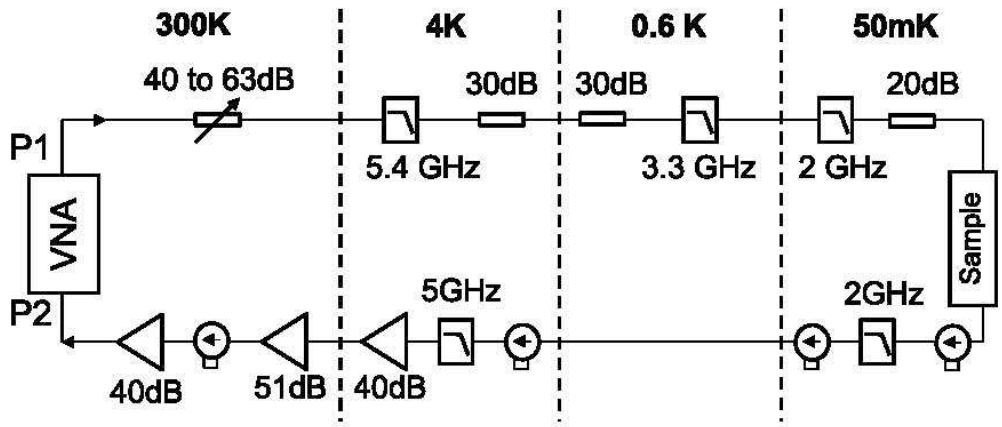

Fig. 3 Experimental setup. The sample is thermally anchored at the mixing chamber of a dilution refrigerator with temperature 40–60 mK. It is connected to a vector network analyzer (VNA) at room-temperature that measures the amplitude and phase of the S_{21} coefficient. The input line (*top*) is strongly attenuated (120 to 160 dB in total) with cold attenuators to protect the sample from external and thermal noise, and filtered above 2 GHz. The output line (*bottom*) includes a cryogenic amplifier with a 3 K noise temperature and 3 cryogenic isolators

Wet etching was done in a solution of HF, H_2O, and $FeCl_3$ having an etching rate of approximately 1 nm/s at room-temperature. A typical resonator and its coupling capacitor are shown in panels (b) and (c) of Fig. 1. Its 3.2 cm length yields a resonance frequency around 1.8 GHz.

In addition to these test structures, some resonators had a gap in the middle (see Fig. 1d) used in a later step to fabricate a SQUID array by e-beam lithography and double-angle aluminum deposition (see panels (e) and (f) in Fig. 1). Before depositing the aluminum, the niobium surface was cleaned by argon ion-milling (dose $\lesssim 10^{18}$ neutralized 500 eV ions per square centimeter). The Nb/Al contact resistance was found to be in the ohm range, yielding tunnel junctions of negligible inductance compared to that of the SQUID.

4 Experimental Setup

The chips were glued on a TMM10 printed-circuit board (PCB). The input and output port of the resonator were wire-bonded to coplanar waveguides on the PCB, connected to coaxial cables via mini-SMP microwave launchers. The PCB was mounted in a copper box. The S_{21} coefficient (amplitude and phase) of the scattering matrix was measured as a function of frequency using a vector network analyzer. Test resonators were measured in a pumped ^{4}He cryostat reaching temperatures of 1.3 K, with typical input power of -50 dBm and using room-temperature amplifiers. We measured internal quality factors up to 2×10^5 with both etching methods.

The tunable resonators were measured in a dilution refrigerator operated at 40–60 mK, using the microwave setup shown in Fig. 3. The input line includes room-temperature and cold attenuators. The output line includes 3 cryogenic isolators, a cryogenic amplifier (from Berkshire) operated at 4 K with a noise temperature of 3 K, and additional room-temperature amplifiers. The attenuators and isolators protect the

Table 1 Summary of sample parameters. See text for definitions

	Design				Measurements		
	C_c	Q_c	L_l	N	I_{c0}	$\omega_r/2\pi$	Q $(\Phi = 0)$
Test	2 fF	6×10^5		0		1.906 GHz	2×10^5
Sample A	27 fF	3.4×10^3	40 ± 10 pH	1	330 nA	1.805 GHz	3.5×10^3
Sample B	2 fF	6×10^5	20 ± 10 pH	7	2.2 μA	1.85 GHz	3×10^4

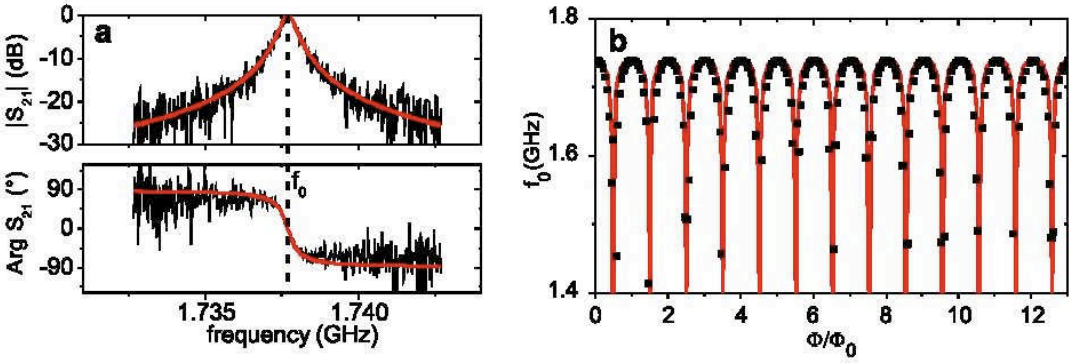

Fig. 4 (Color online) (**a**) Measured (*thin line*) amplitude (*top*) and phase (*bottom*) transmission of sample A for $\Phi = 0$ and fit (*bold line*) yielding the resonance frequency f_0 and a quality factor $Q = 3300$. (**b**) Measured f_0 of sample A (*squares*) as a function of applied magnetic flux, and corresponding fit (*full line*) according to (7)

sample from external and thermal noise. This setup allows to measure the sample with intra-cavity energies as small as a few photons in order to operate in the linear regime corresponding to typical input powers of −140 dBm at the sample level.

5 Experimental Results

Two tunable resonators were measured: sample A has only one SQUID (see Fig. 1e) and large coupling capacitors (27 fF) so that its total quality factor is determined by $Q_c = 3.4 \times 10^3$. Sample B has an array of 7 SQUIDs in series (see Fig. 1f) and smaller coupling capacitors (2 fF) so that its quality factor is likely to be dominated by internal losses or inhomogeneous broadening. Relevant sample parameters are listed in Table 1.

A typical resonance curve, obtained with sample A at $\Phi = 0$ for an input power of −143 dBm corresponding to a mean photon number in the cavity $\overline{n} \approx 1.2$, is shown in Fig. 4. The $|S_{21}|$ curve was normalized to the maximum measured value. By fitting both the amplitude and the phase response of the resonator, we extract the resonance frequency and the quality factor Q. When the flux through the SQUID is varied, the resonance frequency shifts periodically as shown in Fig. 4b, as expected.

The resonance frequency $f_0(\Phi)$ and quality factor $Q(\Phi)$ are shown for both samples in Fig. 5 over one flux period. The $f_0(\Phi)$ curves in panels (a) and (c) are fitted with (7). The agreement is good over the whole frequency range, which extends from

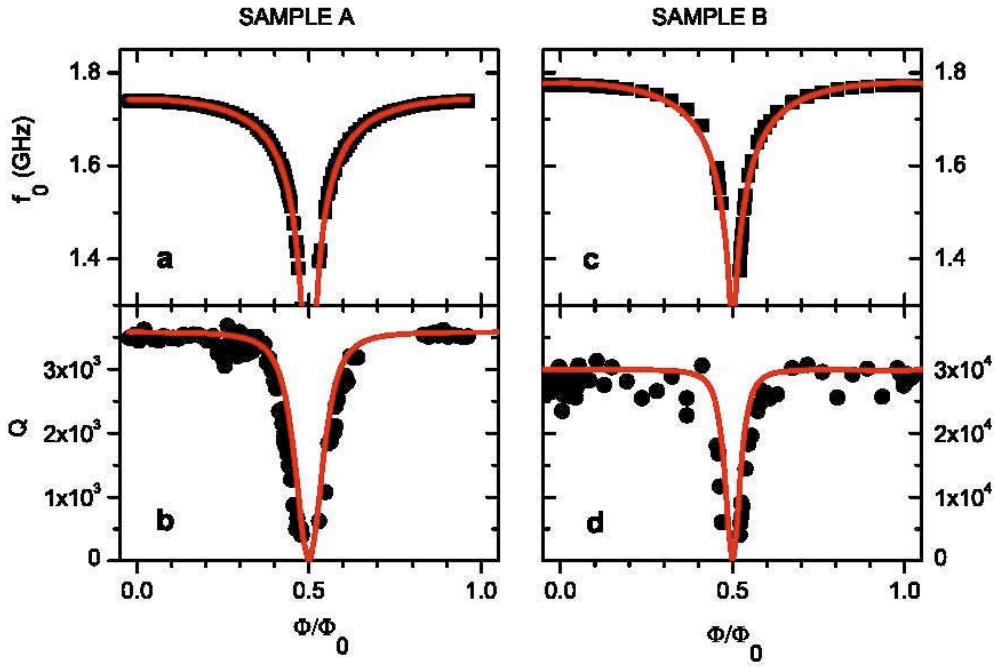

Fig. 5 (Color online) (**a**, **c**) Measured resonance frequency f_0 as a function of Φ/Φ_0 (*squares*) for samples A and B, respectively, and fit according to (7) (*solid line*). (**b**, **d**) Measured quality factor Q (*disks*) as a function of Φ/Φ_0. The *solid line* is calculated according to the model (see text) for a temperature $T = 60$ mK

1.3 to 1.75 GHz, yielding a tunability range of 30%. The small discrepancy observed for sample B might be due to a dispersion in the various SQUID loop areas that is not taken into account in our model. The parameters obtained by this procedure for both samples are shown in Table 1; they are in good agreement with design values and test-structure measurements.

The $Q(\Phi)$ dependence for both samples is shown in panels (b) and (d) of Fig. 5. Both samples show a similar behaviour: the quality factor depends weakly on Φ when the flux is close to an integer number of flux quanta, whereas it shows a pronounced dip around $\Phi_0/2$.

The largest quality factors are 3.5×10^3 for sample A and 3×10^4 for sample B. This difference is due to the different coupling capacitors. For sample A, the maximum quality factor is the same as measured on test resonators with similar capacitors and corresponds to the expected Q_c for $C_c = 27$ fF. Therefore sample A quality factor is limited by the coupling to the 50 Ω lines around integer values of Φ_0. The situation is different for sample B: the measured value is one order of magnitude lower than both the quality factor $Q_c = 6 \times 10^5$ expected for $C_c = 2$ fF and the measured Q of test resonators with the same capacitors (see Table 1). This unexplained broadening of the resonance in presence of a SQUID array might be due either to the presence of low-frequency noise in the sample, or to a dissipation source specifically associated with the SQUIDs. We note that flux-noise is not plausible since our measurements show no clear correlation with the sensitivity of the resonator to flux-noise. However, critical-current noise could produce such effect. Another possibility could be dielectric losses in the tunnel barriers.

We now turn to the discussion of the dip in $Q(\Phi)$ observed around $\Phi_0/2$, which we attribute to thermal noise. Indeed, as discussed in Sect. 2, the resonance frequency depends on the energy stored in the resonator. At thermal equilibrium, fluctuations in the photon number translate into a fluctuation of the resonance frequency and cause an inhomogeneous broadening. At temperature T, the resonator stores an average energy given by Planck's formula $\overline{E} = \hbar\omega_0(\Phi)\overline{n}$, $\overline{n} = 1/\{\exp[\hbar\omega_0(\Phi)/kT] - 1\}$ being the average photon number. The photon number and energy fluctuations are $\overline{n^2} - \overline{n}^2 = \overline{n}(\overline{n} + 1)$ and

$$\sqrt{\overline{\delta E^2}} = \sqrt{\overline{E}^2 + \hbar\omega_0(\Phi)\overline{E}}. \tag{10}$$

The characteristic time of these energy fluctuations being given by the cavity damping time Q/ω_0 with $Q \gg 1$, a simple quasi-static analysis leads to an inhomogeneous broadening $\delta\omega_{inh} = |d\omega_0/dE|\sqrt{\overline{\delta E^2}}$. Using (9), we get

$$Q_{inh}^{-1}(\Phi) = \frac{\delta\omega_{inh}(\Phi)}{\omega_0(\Phi)} = N\left\{\frac{2\omega_0(\Phi)}{\pi R_0[1 + 2N\varepsilon(\Phi)]}\right\}^2 \frac{\varphi_0}{8I_c^3(\Phi)}\sqrt{\overline{\delta E^2}}. \tag{11}$$

The resulting quality factor is $Q^{-1} = Q_{inh}^{-1} + Q_{ext}^{-1}$, which is plotted as full curves in panels (b) and (d) of Fig. 5, for $T = 60$ mK. The agreement is good, although (11) results from a first-order expansion that is no longer valid in the close vicinity of $\Phi_0/2$. We have also observed that Q values significantly degrade around $\Phi_0/2$ when the samples are heated, while remaining unchanged around integer numbers of Φ_0. These observations suggest that thermal noise is the dominant contribution to the drop of Q. Note that our model does not take into account flux-noise, which evidently contributes to Q_{inh} and could account for the residual discrepancy between experimental data and theoretical curves in panels (b) and (d) of Fig. 5.

6 Conclusion

We have designed and measured SQUID-based stripline resonators that can be tuned between 1.3 and 1.75 GHz, with a maximum $Q = 3 \times 10^4$ limited by an unknown mechanism. The quality factor degrades due to thermal noise around $\Phi_0/2$. This limitation would be actually lifted with higher frequency resonators matching typical Josephson qubit frequencies. Their tunability range at high Q would then be wide enough to couple a large number of qubits.

Acknowledgement This work has been supported by the European project EuroSQIP and by the C'nano grant "Signaux rapides". We acknowledge technical support from P. Sénat, P.F. Orfila and J.C. Tack, and fruitful discussions within the Quantronics group and with A. Lupascu, A. Wallraff, M. Devoret, and P. Delsing.

References

1. P. Day et al., Nature **425**, 817 (2003)
2. R. Barends et al., IEEE Trans. Appl. Supercond. **17**, 263 (2007)

3. B. Mazin, PhD thesis, California Institute of Technology (2004)
4. A. Wallraff et al., Nature **431**, 162 (2004)
5. Y. Nakamura, Yu.A. Pashkin, J.S. Tsai, Nature **398**, 786 (1999)
6. D. Vion et al., Science **296**, 886 (2002)
7. J.M. Martinis et al., Phys. Rev. Lett. **89**, 117901 (2002)
8. I. Chiorescu et al., Science **299**, 1869 (2003)
9. A. Blais et al., Phys. Rev. A **69**, 062320 (2004)
10. A. Lupascu et al., Nat. Phys. **3**, 119 (2007)
11. I. Siddiqi et al., Phys. Rev. B **73**, 054510 (2006)
12. J. Majer et al., Nature **449**, 443 (2007)
13. M.A. Sillanpaa, J.I. Parks, R.W. Simmonds, Nature **449**, 438 (2007)
14. M. Wallquist, V.S. Shumeiko, G. Wendin, Phys. Rev. B **74**, 224506 (2006)
15. K.D. Osborn et al., IEEE Trans. Appl. Supercond. **17**(2), 166 (2007)
16. M. Sandberg et al., (2008, to be published)
17. M.A. Castellanos-Beltran, K. Lehnert, Appl. Phys. Lett. **91**, 083509 (2007)
18. V.E. Manucharyan et al., Phys. Rev. B **76**, 014524 (2007)
19. L.D. Landau, E.M. Lifshitz, *Mechanics* (Pergamon, Oxford, 1969)
20. L. Frunzio et al., IEEE Trans. Appl. Supercond. **15**, 860 (2005)

References

1. F. London, On the bose-einstein condensation, Phys. Rev. **54**, 947 (1938), [url].
2. L. Landau, Theory of the superfluidity of helium ii, Phys. Rev. **60**, 356 (1941), [url].
3. L. Landau, On the theory of superfluidity, Phys. Rev. **75**, 884 (1949), [url].
4. J. Bardeen, L. N. Cooper, and J. R. Schrieffer, Theory of superconductivity, Phys. Rev. **108**, 1175 (1957), [url].
5. J. Bardeen, L. N. Cooper, and J. R. Schrieffer, Microscopic theory of superconductivity, Phys. Rev. **106**, 162 (1957), [url].
6. A. Einstein, B. Podolsky, and N. Rosen, Can quantum-mechanical description of physical reality be considered complete?, Phys. Rev. **47**, 777 (1935), [url].
7. A. Aspect, P. Grangier, and G. Roger, Experimental tests of realistic local theories via bell's theorem, Phys. Rev. Lett. **47**, 460 (1981).
8. M. H. Devoret, J. M. Martinis, D. Esteve, and J. Clarke, Resonant activation from the zero-voltage state of a current-biased josephson junction, Phys. Rev. Lett. **53**, 1260 (1984).
9. K. v. Klitzing, G. Dorda, and M. Pepper, New method for high-accuracy determination of the fine-structure constant based on quantized hall resistance, Phys. Rev. Lett. **45**, 494 (1980).
10. T. Ando, Y. Matsumoto, and Y. Uemura, Theory of hall effect in a two-dimensional electron system, J. Phys. Soc. Jpn **39**, 279 (1975), [url].
11. C. Bennett *et al.*, Quantum cryptography: Public key distribution and coin tossing, **175** (1984), [url].
12. D. Deutsch, Quantum theory, the church-turing principle and the universal quantum computer, Proceedings of the Royal Society of London. Series A, Mathematical and Physical Sciences (1934-1990) **400**, 97 (1985), [url].
13. P. W. Shor, Polynomial-time algorithms for prime factorization and discrete logarithms on a quantum computer, SIAM J.SCI.STATIST.COMPUT. **26**, 1484 (1997), řllinklabel.
14. D. Vion *et al.*, Manipulating the quantum state of an electrical circuit, Science **296**, 886 (2002), [url].
15. Y. Nakamura, Y. A. Pashkin, and J. S. Tsai, Coherent control of macroscopic quantum states in a single-cooper-pair box, Nature **398**, 786 (1999), [url].

16. A. Cottet, *Implementation of a Quantum Bit in a Superconducting Circuit*, PhD thesis, Université de Paris 6, 2002, [url].
17. G. Ithier, *Manipulation, readout and analysis of the decoherence of a superconducting quantum bit*, PhD thesis, Université de Paris 6, 2005, [url].
18. A. Wallraff *et al.*, Strong coupling of a single photon to a superconducting qubit using circuit quantum electrodynamics, Nature **431**, 162 (2004), [url].
19. M. Metcalfe, *New microwave readout scheme for superconducting qubit*, PhD thesis, Yale University, 2008.
20. D. Averin, A. Zorin, and K. Likharev, Bloch oscillations in small Josephson junctions, Sov. Phys.-JETP (Engl. Transl **61** (1985).
21. M. Büttiker, Zero-current persistent potential drop across small-capacitance josephson junctions, Phys. Rev. B **36**, 3548 (1987), [url].
22. B. D. Josephson, Possible new effects in superconductive tunnelling, Physics Letters **1**, 251 (1962), [url].
23. M. A. Nielsen and I. L. Chuang, *Quantum Computation and Quantum Information* (Cambridge University Press, 2000).
24. Y. Nakamura, C. D. Chen, and J. S. Tsai, Spectroscopy of energy-level splitting between two macroscopic quantum states of charge coherently superposed by josephson coupling, Phys. Rev. Lett. **79**, 2328 (1997), [url].
25. T. Duty, D. Gunnarsson, K. Bladh, and P. Delsing, Coherent dynamics of a josephson charge qubit, Physical Review B (Condensed Matter and Materials Physics) **69**, 140503 (2004), [url].
26. E. Collin *et al.*, Nmr-like control of a quantum bit superconducting circuit, Phys. Rev. Lett. **93**, 157005 (2004), [url].
27. G. Ithier *et al.*, Decoherence in a superconducting quantum bit circuit, Physical Review B (Condensed Matter and Materials Physics) **72**, 134519 (2005), [url].
28. I. Siddiqi *et al.*, Rf-driven josephson bifurcation amplifier for quantum measurement, Phys. Rev. Lett. **93**, 207002 (2004), [url].
29. A. Fay *et al.*, Strong Tunable Coupling between a Superconducting Charge and Phase Qubit, Physical Review Letters **100**, 187003 (2008), [url].
30. J. Majer *et al.*, Coupling superconducting qubits via a cavity bus, Nature **449**, 443 (2007), [url].
31. V. Ambegaokar and A. Baratoff, Tunneling between superconductors, Phys. Rev. Lett. **10**, 486 (1963), [url].
32. I. I. Rabi, Space quantization in a gyrating magnetic field, Phys. Rev. **51**, 652 (1937), [url].
33. Y. Nakamura, Y. A. Pashkin, T. Yamamoto, and J. S. Tsai, Charge echo in a cooper-pair box, Phys. Rev. Lett. **88**, 047901 (2002), [url].
34. M. Steffen *et al.*, State tomography of capacitively shunted phase qubits with high fidelity, Phys. Rev. Lett. **97**, 050502 (2006), [url].
35. L. Frunzio, A. Wallraff, D. Schuster, J. Majer, and R. Schoelkopf, Fabrication and characterization of superconducting circuit qed devices for quantum computation, Applied Superconductivity, IEEE Transactions **15**, 860 (2005).
36. A. Cottet *et al.*, Implementation of a combined charge-phase quantum bit in a superconducting circuit, Physica C **367**, 197 (2002), [url].
37. I. Siddiqi *et al.*, Direct observation of dynamical bifurcation between two driven oscillation states of a josephson junction, Physical Review Letters **94**, 027005 (2005), [url].

38. R. J. Schoelkopf, P. Wahlgren, A. A. Kozhevnikov, P. Delsing, and D. E. Prober, The radio-frequency single-electron transistor (rf-set): A fast and ultrasensitive electrometer, Science **280**, 1238 (1998), [url].
39. A. Aassime, G. Johansson, G. Wendin, R. J. Schoelkopf, and P. Delsing, Radio-frequency single-electron transistor as readout device for qubits: Charge sensitivity and backaction, Phys. Rev. Lett. **86**, 3376 (2001), [url].
40. T. A. Fulton and L. N. Dunkleberger, Lifetime of the zero-voltage state in josephson tunnel junctions, Phys. Rev. B **9**, 4760 (1974), [url].
41. M. I. Dykman and M. A. Krivoglaz, Fluctuations in nonlinear systems near bifurcations corresponding to the appearance of new stable states, Physica A: Statistical and Theoretical Physics **104**, 480 (1980), [url].
42. N. Boulant *et al.*, Quantum nondemolition readout using a josephson bifurcation amplifier, Physical Review B (Condensed Matter and Materials Physics) **76**, 014525 (2007), [url].
43. A. Lupascu, C. J. M. Verwijs, R. N. Schouten, C. J. P. M. Harmans, and J. E. Mooij, Nondestructive readout for a superconducting flux qubit, Phys. Rev. Lett. **93**, 177006 (2004).
44. A. Lupascu, E. F. C. Driessen, L. Roschier, C. J. P. M. Harmans, and J. E. Mooij, High-contrast dispersive readout of a superconducting flux qubit using a nonlinear resonator, PRL **96**, 127003 (2006), [url].
45. O. Astafiev, Y. Pashkin, Y. Nakamura, T. Yamamoto, and J. Tsai, Temperature square dependence of the low frequency 1/f charge noise in the josephson junction qubits, Physical Review Letters **96**, 137001 (2006), [url].
46. J. A. Schreier *et al.*, Suppressing charge noise decoherence in superconducting charge qubits, Physical Review B (Condensed Matter and Materials Physics) **77**, 180502 (2008), [url].
47. A. A. Houck *et al.*, Controlling the spontaneous emission of a superconducting transmon qubit, Cond-Mat **0803**, 4490 (2008), [url].
48. M. Metcalfe *et al.*, Measuring the decoherence of a quantronium qubit with the cavity bifurcation amplifier, Physical Review B (Condensed Matter and Materials Physics) **76**, 174516 (2007), [url].
49. Y. Makhlin, G. Schön, and A. Shnirman, Quantum-state engineering with josephson-junction devices, Rev. Mod. Phys. **73**, 357 (2001), [url].
50. Y. Makhlin and A. Shnirman, Dephasing of solid-state qubits at optimal points, Phys. Rev. Lett. **92**, 178301 (2004), [url].
51. R. C. Bialczak *et al.*, 1/f flux noise in josephson phase qubits, Physical Review Letters **99**, 187006 (2007), [url].
52. R. W. Simmonds *et al.*, Decoherence in josephson phase qubits from junction resonators, Phys. Rev. Lett. **93**, 077003 (2004), [url].
53. J. M. Martinis *et al.*, Decoherence in josephson qubits from dielectric loss, Phys. Rev. Lett. **95**, 210503 (2005), [url].
54. P. Bertet *et al.*, Dephasing of a superconducting qubit induced by photon noise, Phys. Rev. Lett. **95**, 257002 (2005), [url].
55. M. Neeley *et al.*, Transformed dissipation in superconducting quantum circuits, Physical Review B **77**, 180508 (2008), [url].
56. G. Falci, A. D'Arrigo, A. Mastellone, and E. Paladino, Dynamical suppression of telegraph and 1/f noise due to quantum bistable fluctuators, Phys. Rev. A **70**, 040101 (2004), [url].
57. K. Rabenstein, V. Sverdlov, and D. Averin, Qubit decoherence by gaussian low-frequency noise, JETP Letters **79**, 646 (2004), [url].

58. T. Yamamoto, Y. A. Pashkin, O. Astafiev, Y. Nakamura, and J. S. Tsai, Demonstration of conditional gate operation using superconducting charge qubits, Nature **425**, 941 (2003), [url].
59. R. McDermott *et al.*, Simultaneous state measurement of coupled josephson phase qubits, Science **307**, 1299 (2005), [url].
60. M. Steffen *et al.*, Measurement of the entanglement of two superconducting qubits via state tomography, Science **313**, 1423 (2006), [url].
61. J. H. Plantenberg, P. C. de Groot, C. J. P. M. Harmans, and J. E. Mooij, Demonstration of controlled-not quantum gates on a pair of superconducting quantum bits, Nature **447**, 836 (2007), [url].
62. J. Lantz, M. Wallquist, V. S. Shumeiko, and G. Wendin, Josephson junction qubit network with current-controlled interaction, Phys. Rev. B **70**, 140507 (2004), [url].
63. T. Yamamoto *et al.*, Spectroscopy of superconducting charge qubits coupled by a josephson inductance, Phys. Rev. B **77**, 064505 (2008).
64. T. Hime *et al.*, Solid-state qubits with current-controlled coupling, Science **314**, 1427 (2006), [url].
65. A. O. Niskanen, Y. Nakamura, and J.-S. Tsai, Tunable coupling scheme for flux qubits at the optimal point, Physical Review B **73**, 094506 (2006), [url].
66. M. A. Sillanpaa, J. I. Park, and R. W. Simmonds, Coherent quantum state storage and transfer between two phase qubits via a resonant cavity, Nature **449**, 438 (2007), [url].
67. B. Yurke and J. S. Denker, Quantum network theory, Phys. Rev. A **29**, 1419 (1984), [url].
68. M. H. Devoret, *Quantum fluctuations in electrical circuits, published in "Quantum Fluctuations" S. Reynaud, E. Giacobino, J. Zinn-Justin, eds. Les Houches, France, 27 June- 28 July* (Elsevier Science, 1997).
69. G. Burkard, R. H. Koch, and D. P. DiVincenzo, Multilevel quantum description of decoherence in superconducting qubits, Phys. Rev. B **69**, 064503 (2004).
70. S. R. Hartmann and E. L. Hahn, Nuclear double resonance in the rotating frame, Phys. Rev. **128**, 2042 (1962), [url].
71. E. Schrödinger, An undulatory theory of the mechanics of atoms and molecules, Phys. Rev. **28**, 1049 (1926), [url].
72. C. Rigetti, A. Blais, and M. H. Devoret, Protocol for universal gates in optimally biased superconducting qubits, Physical Review Letters **94**, 240502 (2005), [url].
73. P. Bertet, C. Harmans, and J. Mooij, Parametric coupling for superconducting qubits, Physical Review B **73**, 64512 (2006), [url].
74. C. Zener, Non-adiabatic crossing of energy levels, Proceedings of the Royal Society of London Series A **137**, 696 (1932).
75. H. A. Kramers, Brownian motion in a field of force and the diffusion model of chemical reactions, Physica **7**, 284 (1940), [url].
76. H. Grabert, Escape from a metastable well: The kramers turnover problem, Phys. Rev. Lett. **61**, 1683 (1988), [url].
77. S. Linkwitz, H. Grabert, E. Turlot, D. Estève, and M. H. Devoret, Escape rates in the region between the kramers limits, Phys. Rev. A **45**, R3369 (1992), [url].
78. K. Lang, S. Nam, J. Aumentado, C. Urbina, and J. Martinis, Banishing quasiparticles from josephson-junction qubits: why and how to do it, Applied Superconductivity, IEEE Transactions on **13**, 989 (2003), [url].

79. H. le Sueur and P. Joyez, Microfabricated electromagnetic filters for millikelvin experiments, Review of Scientific Instruments **77**, 115102 (2006), [url].
80. N. Corp, Li 75 a low-noise preamplifier, `1`inklabel.
81. N. Corp, Sa- series low-noise preamplifier, [url].
82. S. R. System, Sr 560 amplifier, [url].
83. P. Townsend, S. Gregory, and R. G. Taylor, Superconducting behavior of thin films and small particles of aluminum, Phys. Rev. B **5**, 54 (1972), [url].
84. P. Santhanam, S. Wind, and D. E. Prober, Localization, superconducting fluctuations, and superconductivity in thin films and narrow wires of aluminum, Phys. Rev. B **35**, 3188 (1987), [url].
85. M. T. Tuominen, J. M. Hergenrother, T. S. Tighe, and M. Tinkham, Even-odd electron number effects in a small superconducting island: Magnetic-field dependence, Phys. Rev. B **47**, 11599 (1993), [url].
86. M. Chauvin, *The Josephson effect in superconducting atomic contacts*, PhD thesis, Université de Paris 6, 2005, [url].
87. A. Fay, *Couplage variable entre un qubit de charge et un qubit de phase*, PhD thesis, UniversitÕ Joseph-Fourier - Grenoble I, 2008, [url].
88. J. Koch *et al.*, Charge-insensitive qubit design derived from the Cooper pair box, Physical Review A **76**, 42319 (2007), [url].
89. C. Cohen-Tannoudji, J. Dupont-Roc, and G. Grynberg, *Atom-photon interactions* (Wiley-VCH Verlag GmbH & Co. KGaA, 1998).
90. A. Wallraff *et al.*, Approaching Unit Visibility for Control of a Superconducting Qubit with Dispersive Readout, Physical Review Letters **95**, 60501 (2005).
91. F. Nguyen and P. Ribeiro, Readout of a superconducting quantum bit by microwave reflectometry, Unpublished (2005).
92. M. Dykman and M. Krivoglaz, Theory of fluctuational transitions between stable states of a nonlinear oscillator, Journal of Experimental and Theoretical Physics **50** (1979).
93. M. I. Dykman and V. N. Smelyanski, Fluctuational transitions between stable states of a nonlinear oscillator driven by random resonant force, Phys. Rev. A **41**, 3090 (1990), [url].
94. M. Marthaler and M. Dykman, Switching via quantum activation: A parametrically modulated oscillator, Physical Review A **73**, 42108 (2006), [url].
95. D. Schuster *et al.*, ac Stark Shift and Dephasing of a Superconducting Qubit Strongly Coupled to a Cavity Field, Physical Review Letters **94**, 123602 (2005).
96. T. Picot, A. Lupascu, S. Saito, C. Harmans, and J. Mooij, Role of relaxation in the quantum measurement of a superconducting qubit using a nonlinear oscillator, Arxiv preprint arXiv:0808.0464 **78**, 132508 (2008), [url].
97. A. Lupascu *et al.*, Quantum non-demolition measurement of a superconducting two-level system, Nat Phys **3**, 119 (2007), [url].
98. B. D. Josephson, The discovery of tunnelling supercurrents, Rev. Mod. Phys. **46**, 251 (1974).
99. G. Geneves *et al.*, The BNM Watt balance project, Instrumentation and Measurement, IEEE Transactions on **54**, 850 (2005), [url].
100. I. K. Harvey, Cryogenic ac josephson effect emf standard using a superconducting current comparator, Metrologia **12**, 47 (1976), [url].
101. H. Pothier, P. Lafarge, C. Urbina, D. Esteve, and M. Devoret, Single-electron pump based on charging effects, Europhys. Lett **17**, 249 (1992).
102. J. J. Vartiainen, M. Möttönen, J. P. Pekola, and A. Kemppinen, Nanoampere pumping of cooper pairs, Applied Physics Letters **90**, 082102 (2007), [url].

103. N. M. Zimmerman and M. W. Keller, Electrical metrology with single electrons, Measurement Science and Technology **14**, 1237 (2003), [url].
104. M. W. Keller, J. M. Martinis, and R. L. Kautz, Rare errors in a well-characterized electron pump: Comparison of experiment and theory, Phys. Rev. Lett. **80**, 4530 (1998), [url].
105. J. P. Pekola *et al.*, Hybrid single-electron transistor as a source of quantized electric current, Nat Phys **4**, 120 (2008), [url].
106. L. J. Geerligs *et al.*, Frequency-locked turnstile device for single electrons, Phys. Rev. Lett. **64**, 2691 (1990).
107. K. Likharev and A. Zorin, Theory of the bloch-wave oscillations in small josephson junctions, Journal of Low Temperature Physics **59**, 347 (1985), [url].
108. L. Kuzmin, Y. Pashkin, A. Zorin, and T. Claeson, Linewidth of bloch oscillations in small josephson junctions, Physica B: Condensed Matter **203**, 376 (1994), [url].
109. L. S. Kuzmin and D. B. Haviland, Observation of the bloch oscillations in an ultrasmall josephson junction, Phys. Rev. Lett. **67**, 2890 (1991), [url].
110. L. Landau and E. Lifshitz, Mechanics, (1960).
111. J. Aumentado, M. W. Keller, J. M. Martinis, and M. H. Devoret, Nonequilibrium quasiparticles and $2e$ periodicity in single-cooper-pair transistors, Phys. Rev. Lett. **92**, 066802 (2004).
112. Filmetrics, Filmetrics f20, [url].
113. Z. Kim *et al.*, Anomalous Avoided Level Crossings in a Cooper-Pair Box Spectrum, in *American Physical Society, 2008 APS March Meeting, March 10-14, 2008, abstract# H15. 008*, 2008.